University of Namur

DOCTOR OF SCIENCES

Elaboration of Composite Materials based on Conducting Polymers and Their Application in Energy Conversion: Thermoelectricity

Bourenane Cherif, Younes

Award date:
2024

Awarding institution:
University of Namur

ELABORATION OF COMPOSITE MATERIALS BASED ON CONDUCTING POLYMERS AND THEIR APPLICATION IN ENERGY CONVERSION: THERMOELECTRICITY

YOUNES BOURENANE CHERIF

Jury

Prof. Guillaume Berionni
University of Namur, Belgium
Prof. Catherine Michaux
University of Namur, Belgium
Prof. Noureddine Nasrallah
University of Science and Technology – Houari Boumediene, Algeria
Prof. Nacira Naar
University of Science and Technology – Houari Boumediene, Algeria
Prof. Zineb Mekhalif
University of Namur, Belgium

A thesis submitted in partial fulfillment of the requirements for the degree of Doctor of Philosophy in the subject of Chemistry

Supervised by Prof. Zineb Mekhalif

University of Namur
Department of Chemistry
Laboratory of Chemistry and Electrochemistry of Surfaces

UNIVERSITÉ DE NAMUR

ABSTRACT

The increasing worldwide energy demand as well as the environmental concerns related to traditional energy sources, presses the urgency of the exploration of sustainable alternatives. This thesis investigates the potential of thermoelectric energy, focusing on conducting polymer–based composites. Traditional thermoelectric materials, while efficient, face limitations such as toxicity and limited availability. Conducting polymers offer a promising solution due to their good electrical conductivity, low thermal conductivity, and modulable Seebeck coefficient associated with their flexibility and processability. By forming composites with materials like carbon nanotubes and graphene, their thermoelectric performance can be significantly enhanced. Surface treatment and functionalization play a crucial role in optimizing composite properties by monitoring the interaction of the fillers with the polymer matrix, offering avenues for improving TE efficiency. Through a comprehensive exploration, material synthesis, and their performance evaluation, this research contributes to advancing thermoelectric technology and paving the way for sustainable energy solutions.

The thesis manuscript begins with an exploration of the global energy investment and the environmental impacts associated with traditional energy sources, highlighting the imperative for sustainable alternatives. It explores the principles of thermoelectricity, the Seebeck and Peltier effects, which govern thermoelectric energy. Furthermore, it provides a detailed review of traditional thermoelectric materials and their limitations, setting the stage for the investigation of conducting polymers as viable alternatives.

The research methodology involves the synthesis and characterization of conducting polymer–based composites, with a focus on surface treatment and functionalization techniques to enhance thermoelectric performance. Various composites, including those incorporating graphene, carbon nanotubes, and metal oxides (bismuth oxide or nickel oxide) nanoparticles, are synthesized and evaluated for their thermoelectric properties. The influence of surface modifications on composite morphology, charge transport, and thermoelectric parameters is systematically studied.

The findings reveal significant improvements in thermoelectric efficiency achieved through surface treatment and composite formation. Functionalization of graphene and carbon nanotubes enhances their compatibility with polymer matrices, leading to improved dispersion and interfacial bonding. This results in enhanced electrical conductivity, reduced thermal conductivity, and ultimately, increased thermoelectric efficiency. Moreover, the incorporation of metal oxides (bismuth oxide or nickel oxide) nanoparticles leads to a remarkable enhancement of the power factor, highlighting the potential for hybrid composites in thermoelectric applications.

The findings of this research not only enhance our fundamental understanding but also provide valuable practical insights for the development of sustainable energy technologies. By addressing the challenges in designing and optimizing thermoelectric materials, this work advances thermoelectric technology, which has significant implications for waste heat recovery, renewable energy generation, and environmental sustainability.

Keywords: thermoelectricity, conducting polymers, graphene, carbon nanotubes, surface treatment, functionalization, metal oxides nanoparticles

RÉSUMÉ

La demande croissante en énergie, associée aux préoccupations environnementales mondiales liées aux sources d'énergie traditionnelles, souligne l'urgence d'explorer des alternatives durables. Cette thèse examine le potentiel de la conversion d'énergie thermique en électrique, en se concentrant sur les composites à base de polymères conducteurs. Les matériaux thermoélectriques traditionnels, bien qu'efficaces, sont confrontés à des défis de surmonter leurs inconvénients tels que la toxicité et la disponibilité limitée. Les polymères conducteurs offrent une solution prometteuse en raison de leurs propriétés modulables (conductivité électrique, effet Seebeck et conductivité thermique) associées à leur flexibilité. En formant des composites avec des matériaux tels que les nanotubes de carbone et le graphène dotés de propriétés de conductivité électrique et thermique, leur performance thermoélectrique peut être considérablement améliorée. Le traitement de surface et la fonctionnalisation jouent un rôle crucial dans l'optimisation des propriétés des composites, offrant des voies pour améliorer leur efficacité. À travers une exploration approfondie, une synthèse des matériaux et une caractérisation des performances, cette recherche contribue à faire progresser la technologie thermoélectrique, ouvrant la voie à des solutions énergétiques durables.

La thèse commence par une exploration de l'investissement énergétique mondial et des impacts environnementaux associés aux sources d'énergie traditionnelles, mettant en évidence l'impératif de rechercher des alternatives durables. Elle explore les principes de la thermoélectricité, les effets Seebeck et Peltier, qui régissent la conversion d'énergie thermoélectrique. De plus, elle offre une revue détaillée des matériaux thermoélectriques traditionnels et de leurs limitations, préparant le terrain pour l'étude des polymères conducteurs en tant qu'alternatives viables.

La méthodologie de recherche implique la synthèse et la caractérisation de composites à base de polymères conducteurs, en mettant l'accent sur les techniques de traitement de surface et de fonctionnalisation pour améliorer les performances thermoélectriques. Divers composites, y compris ceux incorporant du graphène, des nanotubes de carbone et des nanoparticules d'oxydes métalliques (oxyde de bismuth ou oxyde de nickel), sont synthétisés et évalués pour leurs propriétés thermoélectriques. L'influence des modifications de surface sur la morphologie des composites, le transport de charge et les paramètres thermoélectriques est étudiée de manière systématique.

Les résultats révèlent des améliorations significatives, par rapport aux matériaux préparés et ceux rapportés dans la littérature, de l'efficacité thermoélectrique obtenues grâce au traitement de surface et à la formation de composites. La fonctionnalisation du graphène et des nanotubes de carbone améliore leur compatibilité avec les matrices polymériques, conduisant à une dispersion et une liaison interfaciale améliorées. Cela se traduit par une conductivité électrique accrue, une conductivité thermique réduite et, finalement, une efficacité thermoélectrique plus élevée. De plus, l'incorporation de nanoparticules d'oxydes métalliques (oxyde de bismuth ou oxyde de nickel) démontre une amélioration remarquable du facteur de puissance, mettant en évidence le potentiel des composites hybrides dans les applications thermoélectriques.

Les conclusions de cette recherche améliorent non seulement notre compréhension fondamentale, mais fournissent également des perspectives pratiques précieuses pour le développement de technologies énergétiques durables. En abordant les défis de la conception et de l'optimisation des matériaux thermoélectriques, ce travail fait progresser la technologie thermoélectrique, ce qui a des implications significatives pour la récupération de la chaleur perdue, la génération d'énergie renouvelable et la durabilité environnementale.

Mots clés: thermoélectricité, polymères conducteurs, graphène, carbone nanotube, traitement de surface, fonctionnalisation, nanoparticules d'oxydes métalliques

ACKNOWLEDGEMENTS

The path to completing this PhD thesis was lengthy and filled with many twists and turns. Thanks to the assistance, encouragement, and advice from numerous individuals, I managed to reach the end of this journey.

First and foremost, I express my deepest appreciation to my supervisor, Prof. Zineb Mekhalif, for her guidance, confidence in me, advice, and encouragement throughout the four years of this PhD journey. It has been both a pleasure and an honor to work with you. I am particularly thankful for the freedom you gave me to explore my own thoughts. This trust helped me to develop both as a person and in my studies, encouraging me to take charge of my own research.

I extend my heartfelt thanks to the esteemed members of my supervisory committee – Prof. Guillaume Berionni, Prof. Catherine Michaux – and external examiners, Prof. Noureddine Nasrallah and Prof. Nacira Naar. I am grateful that you accepted the responsibility of being a part of my PhD committee. Your critiques and input on this thesis have been of enormous value and have contributed significantly to its refinement.

I am especially thankful to Prof. Ahmed Mekki for helping me to be in contact with Prof. M. Zineb, for his encouragements, support, sharing, and precious pieces of advice.

I am grateful for the funding grant from the "École Militaire Polytechnique" in Algeria, which made my PhD research possible. I extend my heartfelt thanks to all the teaching staff, officers, doctors, and professors at EMP, each of whom has contributed directly or indirectly to this dissertation.

I am deeply indebted to my co–authors and collaborators B.D.S. Zakaria, N. Linda, R. Souleymen. Your support, including performing thermoelectric analyses and meticulous proofreading, enriched my doctoral research experience.
A special thanks goes to my friend, colleague, and co–author Slimane Abdous.

I am especially appreciative of Tatiana, laboratory technician, who was available whenever I needed something, Sébastien, Paterne, Blinera, and all the CPB staff, each by their name. My time at UNamur was made enjoyable in large part due to your presence. I will never forget the friends with whom I have shared offices.

A special word of thanks to my family – my mother and my father Ammar, my sisters and brothers Rabie and Aissa. Your love and unwavering support provided a strong foundation that held me steady throughout this journey. A special thanks to my mother in–law and my sister in–law, your presence in my life is essential at the times when I first got to know you.

Above all, my deepest gratitude is reserved for my wife and our precious son, Ibrahim. Your decision to join me in Belgium, stands as one of my greatest blessings. Your constant love, support, and assistance were the pillars that upheld me throughout this journey.

I would like to thank as well my Algerian friends for their worry, care, and phone calls. These acknowledgements would not be complete without stating their names: Hamza Trirat, Okba Derardja, Yaakoub Righi, Fayçal Tiaiba, and Mohamed-Amine Yahiaoui. Thanks for your support, friendship, listening to me whenever I needed help and encouragements.

PUBLICATIONS

The contributions outlined in this thesis have been published in peer–reviewed journals and conferences. This section provides a list of these publications as well as the collaboration works.

Journal Papers

- Younes Bourenane Cherif, Nawel Matmat, Zakaria Bekkar Djelloul Sayah, Ahmed Mekki, Jean-Félix Durastanti, and Zineb Mekhalif. Influence of graphene oxide surface treatment by diazonium salts on thermoelectrical behavior of polypyrrole– based composites. **Journal of Materials Science: Materials in Electronics**, 33(18): 14938–14950, June 2022. ISSN 1573-482X. doi: 10.1007/s10854-022-08410-7. URL https://doi.org/10.1007/s10854-022-08410-7

- Younes Bourenane Cherif, Zineb Mekhalif, Ahmed Mekki, and Zakaria Bekkar Djelloul Sayah. Effect of MWCNTs surface functionalization group nature on the thermoelectric power factor of PPy/MWCNTs nanocomposites. **Synthetic Metals**, 291:117196, December 2022. ISSN 0379-6779. doi: 10.1016/j.synthmet.2022.117196. URL https://doi.org/10.1016/j.synthmet.2022.117196

- Younes Bourenane Cherif, Zineb Mekhalif, Ahmed Mekki, Zakaria Bekkar Djelloul Sayah, and Souleymen Rafai. Enhanced thermoelectric power factor of PPy–based nanocomposites: effect of decorated graphene nanoplatelets by bismuth oxide nanoparticles. **Journal of Materials Science**, 58(11):4809–4823, March 2023. ISSN 1573-4803. doi: 10.1007/s10853-023-08334-5. URL https://doi.org/10.1007/s10853-023-08334-5

- Younes Bourenane Cherif, Zineb Mekhalif, Slimane Abdous, Linda Nedjar, Ahmed Mekki, Zakaria Bekkar Djelloul Sayah, and Souleymen Rafai. Nickel Oxide Decorated MWCNTs Wrapped Polypyrrole: One Dimensional Ternary Nanocomposites for Enhanced Thermoelectric Performance. **ChemNanoMat**, 10(3):e202300486, 2024. ISSN 2199-692X. doi: 10.1002/cnma.202300486. URL https://doi.org/10.1002/cnma.202300486

List of Conferences

- Participated in the **Belgian Crystallography Symposium (BCS), Belgium**

- Participated in the **1st Japan France Virtual Workshop on Thermoelectrics (VWT2021), France**

- Oral Presentation: Younes Bourenane Cherif, Zineb Mekhalif, Ahmed Mekki, and Zakaria Bekkar Djelloul Sayah. Effect of decorated MWCNTs by bismuth oxide nanoparticles on the thermoelectric properties of polypyrrole–based nanocomposites. **The 1st International Conference on Renewable Materials and Energies ICRME2022** Ouargla, Algeria, October 2022, page 3. URL https://icrme2022.sciencesconf.org/

- Poster presentation: Younes Bourenane Cherif, Zineb Mekhalif, Ahmed Mekki and Zakaria Bekkar Delloul Sayah. Effect of decorated GNPs by bismuth oxide nanoparticles on the thermoelectric power factor of polypyrrole–based nanocomposites, in **2023 MAIN–NANOWAL**

- Digital Presentation: Younes Bourenane Cherif, Zineb Mekhalif, Slimane Abdous, Linda Nedjar and Ahmed Mekki. Synergistic Enhancement of Thermoelectric Performance through One-Dimensional Hybrid Nanocomposites: Wrapped Nickel Oxide–Decorated Multi–Walled Carbon Nanotubes with Polypyrrole, **ECS Meeting Abstracts MA2024-01** 1556. URL https://doi.org/10.1149/MA2024-01311556mtgabs

Collaborations

- Slimane Abdous, Mehdi Derradji, Zineb Mekhalif, Karim Khiari, Oussama Mehelli, and Younes Bourenane Cherif. Advances in Polymeric Neutron Shielding: The Role of Benzoxazine–h–BN Nanocomposites in Nuclear Protection. **Radiation Research**, 200(3):242–255, 07 2023. ISSN 0033-7587. doi: 10.1667/RADE-23-00060.1. URL https://doi.org/10.1667/RADE-23-00060.1

- Slimane Abdous, Mehdi Derradji, Zineb Mekhalif, Karim Khiari, Oussama Mehelli, and Younes Bourenane Cherif. Exploring the potential of benzoxazine-based nanocomposites for lightweight neutron shielding applications. **High Performance Polymers**, 35(8):812–826, 2023. doi: 10.1177/09540083231179114. URL https://doi.org/10.1177/09540083231179114

CONTENTS

LIST OF FIGURES

LIST OF TABLES

LIST OF ABBREVIATIONS

ABC	Ammonium Bismuth Citrate
DS–COOH	4–carboxybenzenediazonium tetrafluoroborate
DTG	Derivative ThermoGravimetry
EDOT	3,4–ethylenedioxythiophene
FTIR	Fourier Transform InfraRed Spectroscopy
FrGO	Functionalized Reduced Graphene Oxide
GNPs	Graphene Nanoplatelets
GO	Graphene Oxide
GP	Grafting Percentage
Gr	Graphene
MO	Methyl Orange
MWCNTs	Multi Walled Carbon Nanotubes
MWCNTs–COOH	COOH groups functionalized MWCNTs
MWCNTs–D1	Monocarboylic aryl functionalized MWCNTs
MWCNTs–D3	Tricarboxylic aryl functionalized MWCNTs
MWCNTs–NH_2	NH_2 groups functionalized MWCNTs
MWCNTs–SH	SH groups functionalized MWCNTs
NNH	Nickel (II) Nitrate Hexahydrate
O–MWCNTs	Oxidized MWCNTs
PANi	Polyaniline
PEDOT	Poly(3,4–ethylenedioxythiophene)
PEDOT:PSS	PEDOT:Polystyrene sulfonate
PF	Power Factor
PPy	Polypyrrole
p–MWCNTs	Purified MWCNTs
PTh	Polythiphene
PV	Photovoltaic
SDBS	Sodium DodecylBenzeneSulfonate
SEM	Scanning Electron Microscopy
SWCNTs	Single Walled Carbon Nanotubes
TE	Thermoelectric
TEGs	Thermoelectric Generators
TEM	Transmission Electron Microscopy
TGA	Thermal Gravimetric Analysis
XPS	X–ray Photoelectron Spectroscopy

XRD	X–Ray Diffraction
ZT	Figure of Merit
σ	Electrical conductivity
S	Seebeck Coefficient
κ	Thermal conductivity
ρ	Electrical resistivity

CHAPTER 1

INTRODUCTION

The global energy demand is continuously increasing, driven by industrial growth and technological advancements. Traditional energy sources, such as fossil fuels, have served as a global energy supply for over a century. These sources, including coal, oil, and natural gas, are not only finite but also contribute significantly to environmental pollution and climate change. The combustion of fossil fuels releases large amounts of carbon dioxide (CO_2) and other greenhouse gases into the atmosphere, leading to global warming and climatic changes [1].

Additionally, the extraction, transportation, and utilization of fossil fuels are associated with several environmental and ecological issues, such as habitat destruction, oil spills, and air and water pollution. These problems press the urgent need for a transition to cleaner and more sustainable energy sources. Renewable energy technologies, such as solar, wind, and hydroelectric power, have shown promise in reducing dependence on fossil fuels. However, these technologies face challenges related to energy storage, efficiency, and reliability, particularly in regions with variable weather conditions [2].

Therefore, there is a pressing need to explore and develop alternative energy sources and conversion technologies that are sustainable and environmentally friendly. One such promising technology is thermoelectricity [3], which can directly convert waste heat into electrical energy, thereby improving overall energy efficiency [4]. Thermoelectric devices have the potential to harness waste heat from various sources, such as industrial processes, automotive exhaust systems, and even human body heat, converting it into useful electrical power. This not only enhances energy utilization but also contributes to environmental conservation [5].

Thermoelectricity, a technology that directly converts heat into electrical energy and vice versa, offers a promising solution for energy conversion. The thermoelectric effect, which encompasses the Seebeck and Peltier effects, enables this direct conversion. Thermoelectric materials can generate electricity from temperature gradients, making them useful for waste heat recovery and renewable energy applications [6].

The Seebeck effect refers to the generation of an electric voltage when there is a temperature difference across a material. Conversely, the Peltier effect involves the absorption or emission of heat when an electric current passes through a junction of two different materials [7]. These principles form the basis of thermoelectric devices, which can function as both power generators and coolers. However, the efficiency of thermoelectric materials is determined by the dimensionless figure of merit, ZT, which depends on the Seebeck coefficient (S), electrical conductivity (σ), and thermal conductivity (κ), $ZT = (S^2 \cdot \sigma / \kappa) \cdot T$

Traditional thermoelectric materials, such as bismuth telluride (Bi_2Te_3), have demonstrated high efficiencies. However, their widespread application is hindered by several challenges, including high cost, toxicity, and limited availability of constituent elements. These limitations necessitate the development of new, sustainable materials with comparable or superior thermoelectric performance [8–10].

Bismuth telluride and its alloys have been the materials of choice for commercial thermoelectric applications due to their relatively high ZT values at room temperature. However, their environmental and health hazards, pose significant challenges. Moreover, these materials often require complex and expensive fabrication processes, limiting their scalability and practical deployment. Therefore, there is a strong impetus to explore alternative materials that are abundant, non–toxic, and cost–effective [11].

Conducting polymers have emerged as promising candidates for thermoelectric applications due to their properties. These materials are flexible, lightweight, and offer the potential for low–cost, large–scale production. Moreover, the electrical and thermal properties of conducting polymers can be tuned through chemical modifications and composite formation [12].

Polymers like polypyrrole (PPy), polyaniline (PANi), and poly(3,4–ethylenedioxythiophene) (PEDOT) have shown potential in thermoelectric applications due to their intrinsic electrical conductivity and processability. These polymers can be synthesized through relatively simple chemical or electrochemical methods, making them attractive for scalable production. Furthermore, their mechanical flexibility and low thermal conductivity are advantageous for applications where weight and flexibility are critical, such as in wearable electronics and flexible thermoelectric generators[13, 14].

The thermoelectric performance of conducting polymers can be significantly enhanced by forming composites with other materials, such as carbon nanotubes, graphene, and inorganic nanoparticles [15–17]. These composites leverage the synergistic effects of their constituents, leading to improved electrical conductivity, thermal stability, and overall thermoelectric efficiency. A critical aspect of this enhancement is the influence of surface treatments and functionalization, which can drastically alter the interfacial properties and, consequently, the thermoelectric performance of the composites [18–20].

Surface treatment and functionalization play a pivotal role in optimizing the properties of conducting polymer composites. By modifying the surface chemistry of materials like graphene and multi–walled carbon nanotubes (MWCNTs), it is possible to enhance their compatibility with polymer matrices, improve charge carrier mobility, and tailor the thermal and electrical conductivities of the composites.

Surface treatments techniques such as coating with functional groups can create active sites on the surface of carbon–based materials, facilitating better dispersion within the polymer matrix and improving interfacial bonding. This leads to enhanced electrical pathways and reduced thermal conductivity, which are crucial for efficient thermoelectric materials.

Functionalization is introducing functional groups (e.g., carboxyl, amine, thiol) onto the surface of graphene and MWCNTs can significantly improve their processability. Functionalization can also modulate the electronic structure of the composites, enhancing the Seebeck coefficient and overall power factor of the thermoelectric material.

For example, functionalizing MWCNTs with carboxyl groups (–COOH) or amine groups ($-NH_2$) can improve their dispersion in the polymer matrix, leading to a more homogeneous composite with enhanced thermoelectric properties. Similarly, surface treatment of graphene nanoplatelets can increase the number of active sites available for interaction with the polymer, thereby improving the composite's overall performance.

This thesis aims to explore the development of conducting polymer–based composites for thermoelectricity, with a focus on the impact of surface treatments by functionalization and decoration with nanoparticles. The primary objectives are to synthesize and characterize novel composites, investigate their thermoelectric properties, and optimize their performance for practical applications. Special emphasis is placed on understanding the role of surface treatments and functionalization in enhancing the thermoelectric efficiency of these composites.

The thesis is divided into three main parts to guide the reader through this research.

Part One: Background. Part one lays the foundation by providing essential background information to understand the research context and it contains two chapters (2 and 3). **Chapter two** offers an exploration into the generalities, principles, and practical applications of thermoelectricity. **Chapter three** presents a comprehensive review of various thermoelectric materials, shedding light on their properties and the challenges they present.

Part Two: Research Contributions. Part two presents the primary contributions of this research and it is subdivided into four chapters (4, 5, 6, and 7). **Chapter four** explores the impact of surface–treated graphene as a filler and different synthesis methods on the thermoelectric properties of ternary composites made from PPy and PEDOT or PEDOT:PSS. In **chapter five**, the focus shifts to examining how various functional groups (benzoic acid, benzene tricarboxylic acid, hydroxyl, carboxyl, amino, and thiol) grafted onto MWCNTs influence the thermoelectric performance of PPy–MWCNTs nanocomposites. **Chapter six** aims to improve the thermoelectric conversion efficiency of organic materials by developing a hybrid organic–inorganic material and investigates the influence of decorating MWCNTs and graphene nanoplatelets with bismuth oxide nanoparticles on the thermoelectric power factor of PPy–based nanocomposites, unraveling new avenues for enhanced materials. Lastly, **chapter seven** provides a detailed exploration of strategic design methodologies for achieving enhanced thermoelectric materials, employing nickel oxide–decorated MWCNTs wrapped with polypyrrole nanotubes.

Part Three: Closing Remarks. Part three serves as conclusion and final reflection on the thesis, containing two chapters (8 and 9). **Chapter eight** offers a cross–chapter examination, wrapping the various thermoelectric strategies explored throughout the thesis. Finally, **chapter nine** concludes the thesis by summarizing the key findings and offering insightful suggestions for future research directions.

The successful development of efficient conducting polymer–based thermoelectric composites could provide a sustainable and cost–effective solution for waste heat recovery and renewable energy generation. This research has the potential to contribute significantly to the advancement of thermoelectric technology and its practical applications in various industries.

Part I

Background and Literature Review

CHAPTER 2

THERMOELECTRICITY: GENERALITIES, PRINCIPLES AND APPLICATIONS

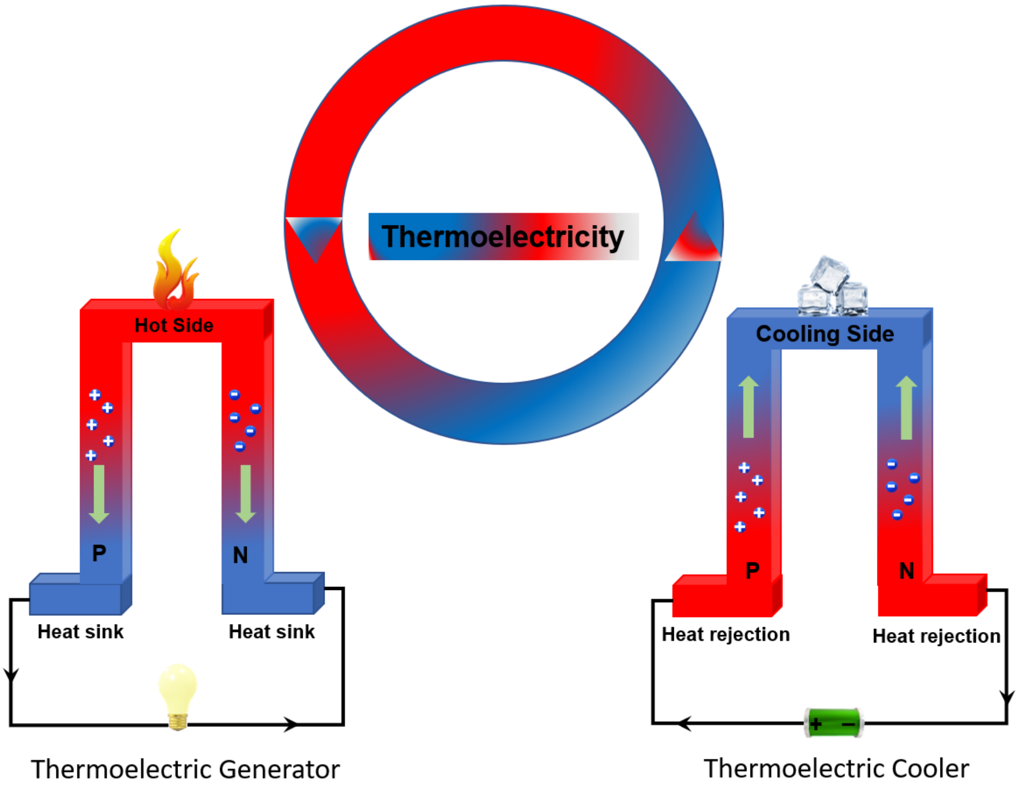

Thermoelectricity, covered in this chapter, is a very interesting field that connects physics, materials science, and engineering. It consists on the conversion of heat gradients into electrical power and, conversely, the conversion of electrical power into heat, with such applications as power generation and cooling systems. In this introductory chapter, we learn the principles and applications of thermoelectricity.

2.1 Fundamentals of Thermoelectricity

We begin the chapter with the basic ideas underlying all thermoelectric (TE) phenomena. In this respect, the chapter provides an understanding of heat–to–electricity conversion and thermoelectric transport phenomena.

2.1.1 Seebeck Effect

The principle of TE energy conversion is based on the fundamental TE effects discovered by Thomas Johann Seebeck in 1821, which can be better explained using the thermocouple scheme shown in Figure 2.1. The Seebeck effect is the physical basis of TE power generation devices [21]. One key feature of this effect is the Seebeck coefficient (S), which is also known as thermopower (α). The Seebeck coefficient provides a measure of the electromotive force developed across the ends of a thermocouple subjected to a temperature gradient [22]. In simpler terms, it is similar to a circuit containing two different conductors, or semiconductors, labeled as Material A and Material B. When the junctions of A and B are at dissimilar temperatures, T and T + ΔT respectively, an open circuit electromotive force V is obtained [4, 23]. Therefore, as one end of the thermocouple is hot and the other is cool, it can cause a flow of an electric current due to the frontal voltage difference ΔV.

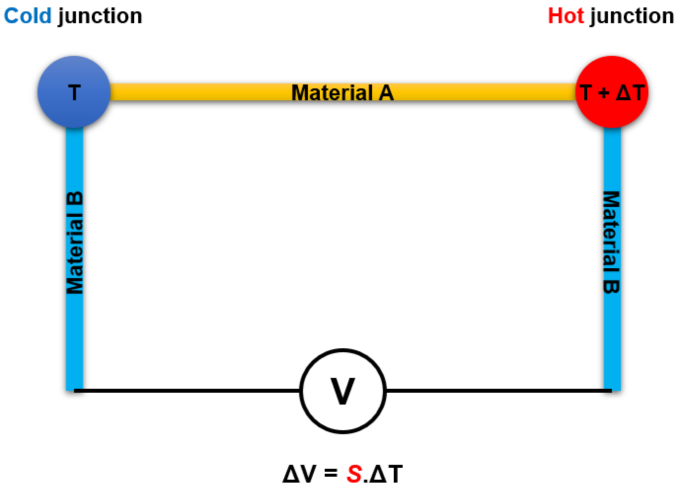

Figure 2.1: Schematic representation of the Seebeck effect in a thermocouple.

Subjecting a metal to a temperature gradient ΔT results in the establishment of an energy gradient across it due to the average energy of electrons on the hotter region necessarily exceeding that of the cooler region as heat is transferred from the former to the latter. The force driven by this energy gradient ensures the diffusion of electrons from the hot side to the cold side, Figure 2.2. Due to the temperature difference, the negative majority of carriers gather in the cooler region while the positive majority of carriers accumulate in the hotter area. As a result of this thermally–induced electron diffusion, Figure 2.2a, the hot region becomes positively charged compared to the opposite end of the conductor.

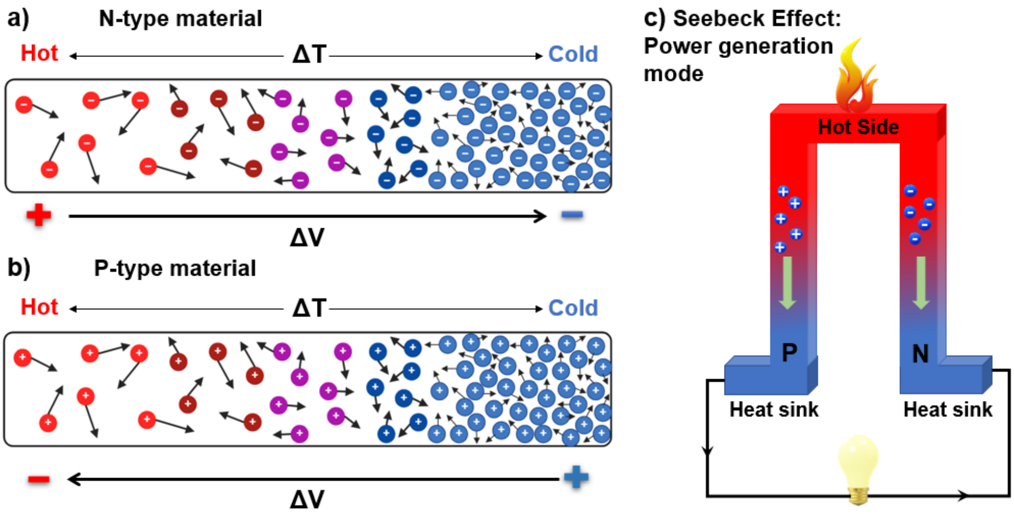

Figure 2.2: An overview of how temperature differences affect electron distribution from hot to cold, a) N–type material, b) P–type material and c) Seebeck effect (when N– and P–type materials are connected).

Conventionally in physics, the voltage difference known as ΔV (V) and generated by temperature difference ΔT (K) is quantified as the measure of the electrical potential observed on the colder side subtracted from that of the warmer side. The sign of the Seebeck coefficient (VK^{-1}) (Equation 2.1) depends on the type of primary charge carriers in the material: the main charge carriers are either electrons or holes.

$$S = -\frac{\Delta V}{\Delta T} \tag{2.1}$$

The Seebeck coefficient exhibits a direct correlated relationship to the type of charge carriers within the given material, being negative when electrons are the majority carriers as in N–type substrates as depicted in Figure 2.2a, yet positive when holes predominantly conduct as in the case of P–type substrates as shown in Figure 2.2b. P– and N–type semiconductors are usually used together in practical devices (Figure 2.2c) since they have Seebeck coefficients of opposite signs that add onto each other across the TE module. The negative sign indicates that the voltage generated is opposite in direction to the temperature gradient.

2.1.2 Peltier Effect

This fundamental TE phenomenon appears at the junction where two unlike materials meet whenever an electric current passes through, known as the Peltier effect. It is named after the French physicist Jean Charles Athanase Peltier, who discovered it in 1834 [24]. The Peltier effect is the basis for many TE refrigeration devices [21].

When an electrical current is passed through the junction of two materials with different Seebeck coefficients (which generate a voltage in response to a temperature gradient), the Peltier effect causes heat to either be absorbed or released at the junction. The direction of heat transfer depends on the direction of the electric current and the materials involved. If the direction of the electric current aligns with the direction of the Seebeck effect, the junction absorbs heat from the outside. Conversely, if the current flows in the opposite direction, the junction releases heat to the outside [25, 26].

Similarly, to the Seebeck coefficient, the Peltier coefficient (Π, V or JC^{-1}) is defined as the coefficient of the thermal current (Q, J) to the electrical current (I, C), given by Equation 2.2.

$$Q = \Pi \cdot I \tag{2.2}$$

Due to the flow of electrons across the junction resulting in a redistribution of energy levels within the constituent substances, a transfer of thermal energy occurs as a consequence. In other words, the electrical current induces a flow of charge carriers (electrons or holes), which, in turn, affects the thermal energy distribution at the junction, Figure 2.3.

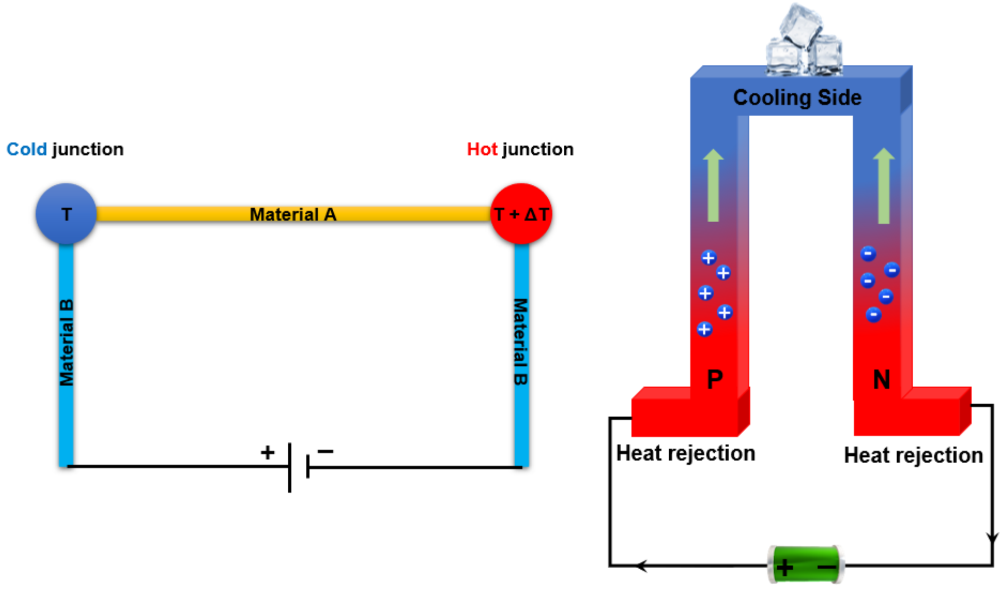

Figure 2.3: Peltier effect: refrigeration mode.

2.1.3 Thomson Effect

The Thomson effect, also known as the Thomson heat, is a TE phenomenon related to the transport of heat in a conductive material subjected to an electrical current and a temperature gradient. Named after the Scottish physicist William Thomson, who first described it in 1854, the Thomson effect occurs when an electric current flows through a homogeneous conductor that also has a temperature gradient along its length [27, 28].

In simple terms, the Thomson effect describes the generation or absorption of heat along a conductor due to the combined influence of electrical current and temperature gradient. The direction of heat transfer depends on the material's Thomson coefficient (Θ), which is a measure of the material's ability to generate or absorb heat [13].

The mathematical expression for the Thomson effect (Q_{Th}, W) can be given by Equation 2.3, which is related to the Thomson coefficient (Θ, $WA^{-1}K^{-1}$), the electrical current (I, A), and the temperature gradient (T, K) along the conductor's length [29].

$$Q_{Th} = -\Theta \cdot I \cdot \Delta T \tag{2.3}$$

2.2 Properties and Performance Metrics of TE Materials

In this section, we explore the key material properties, such as electrical conductivity, Seebeck coefficient, and thermal conductivity, which dictate the efficiency of thermoelectric conversion as well as the performance metrics of TE materials such as figure of merit and power factor.

2.2.1 Electrical Conductivity

Electrical conductivity (σ) is a crucial feature in TE materials as it determines their ability to transport electric current, which is essential for efficient TE energy conversion. In semiconductors, electrical conductivity comes from the movement of charge carriers (electrons or holes) through the material. Organic, carbon–based, semiconductors have similar behavior but unique properties compared to inorganic semiconductors [30].

At absolute zero temperature, semiconductors behave as insulators because their valence band is fully occupied, and their conduction band is empty, creating a bandgap between them [21, 31], Figure 2.4.

However, when sufficient energy is provided, electrons can be excited from the valence band to the conduction band, leaving behind holes in the valence band. These excited electrons and holes are referred to as charge carriers and contribute to electrical conductivity [32].

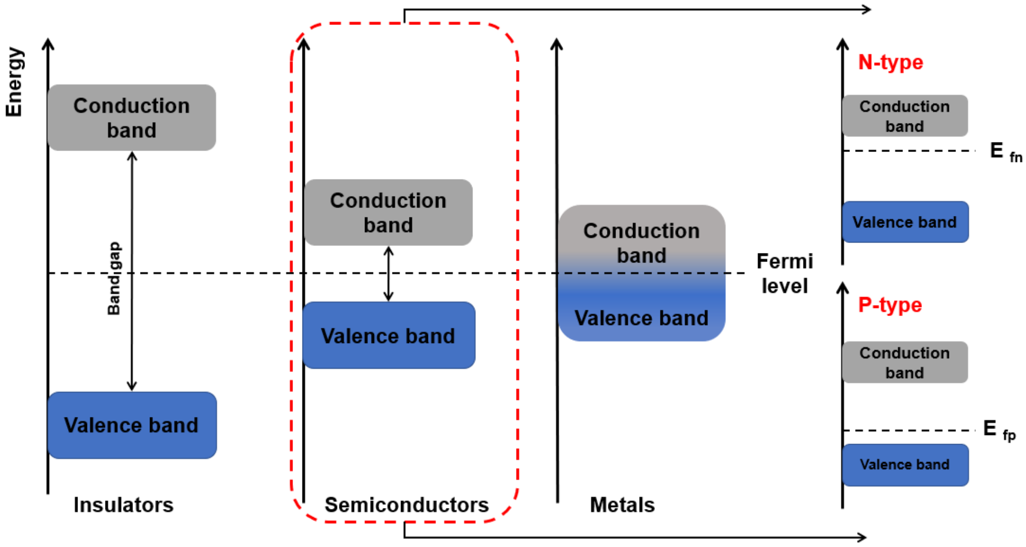

Figure 2.4: Band gap in insulators, semiconductors, and conductors.

In order to tune electrical conductivity, doping is the process of adding impurities (dopants) to a pure semiconductor so as to modify its electrical properties and increase its conductivity. There are two main types of doping [33, 34]:

N–type Doping: Introduces dopants with more valence electrons than the semiconductor. This adds extra electrons (negative charge carriers) to the conduction band (Figure 2.4), increasing conductivity.

P–type Doping: Introduces dopants with fewer valence electrons. This creates holes (positive charge carriers) in the valence band (Figure 2.4), also enhancing conductivity.

2.2.1.1 Key Factors Influencing Electrical Conductivity

The electrical conductivity of thermoelectric materials is influenced by several key factors. Firstly, the density of charge carriers (n) significantly impacts conductivity, as increasing the carrier concentration through methods such as doping enhances conductivity by providing more charge carriers for current flow. This relationship is described by Equation 2.4, where σ (Sm^{-1}) represents electric conductivity, n (m^{-3}) is the carrier concentration, μ ($m^2V^{-1}s^{-1}$) is the carrier mobility, and e (1.602×10^{-19} C) is the charge of the electron.

$$\sigma = n \cdot e \cdot \mu \tag{2.4}$$

Carrier mobility (μ) quantifies how easily charge carriers can move through the material when an electric field is applied, and higher carrier mobility results in improved conductivity. Additionally, the electronic band structure of the material is critical in determining conductivity, as the presence of bandgaps and the position of energy levels affect carrier transport properties [32, 35].

Defects and impurities (dopants) within the material can act as scattering centers, hindering the movement of charge carriers and reducing conductivity, making the minimization of defects and control of impurity concentrations essential for optimizing conductivity [36, 37]. Temperature also plays a role in influencing the mobility of charge carriers and affecting conductivity; generally, higher temperatures lead to increased conductivity due to enhanced carrier mobility [38, 39]. Furthermore, the arrangement and structure of the material at the microscopic level, known as microstructure and morphology, can impact conductivity by influencing charge carrier transport pathways and interface properties [40]. Understanding and optimizing these factors are crucial for designing TE materials with high electrical conductivity and overall performance.

2.2.2 Seebeck Coefficient

The Seebeck coefficient (Equation 2.1), also known as the TE power or thermopower, is a fundamental property of TE materials that characterizes their ability to convert temperature differences into electrical voltage and vice versa.

2.2.2.1 Key Factors Influencing Seebeck Coefficient

The Seebeck coefficient (S) of a material, a crucial parameter in TE applications, is primarily dictated by its electronic band structure. The Seebeck coefficient is inversely proportional to the carrier concentration (n). In materials with high carrier concentrations, such as metals, the Seebeck coefficient tends to be lower due to increased electron–electron scattering, while in semiconductors with lower carrier concentrations, the Seebeck coefficient is typically higher [41]. The Seebeck effect relies on the presence of a temperature gradient across the material; a larger gradient leads to a higher voltage generated and thus increases the Seebeck coefficient. The electronic band structure, including energy band positions and the presence of bandgaps, also influences the Seebeck coefficient [32]. Furthermore, lattice thermal conductivity (κ) indirectly affects the Seebeck coefficient. Higher lattice thermal conductivity promotes increased phonon transport, potentially reducing the temperature gradient and impacting the Seebeck coefficient [42]. Therefore, materials with low lattice thermal conductivity are preferable for TE applications, ensuring efficient energy conversion.

2.2.3 Thermal Conductivity

Thermal conductivity (κ, $Wm^{-1}K^{-1}$) is a measure of a material's ability to conduct heat. It quantifies how efficiently heat is transferred through the material when there is a temperature gradient. Mathematically, thermal conductivity is the sum of two components (Equation 2.5): one associated with electron conduction (κ_e), which correlates with charge carriers, and the other related to phonon propagation and atomic vibrations (κ_p) [24, 43].

$$\kappa = \kappa_e + \kappa_p \tag{2.5}$$

A material with high thermal conductivity transfers heat efficiently and has a low–temperature gradient for a given amount of heat flow. In contrast, a material with low thermal conductivity hinders heat transfer and exhibits a higher temperature gradient under the same conditions [44].

2.2.3.1 Key Factors Influencing Thermal Conductivity

The thermal conductivity of materials is influenced by several key factors. Firstly, the crystal structure and composition play a significant role [45], as the arrangement of atoms in the material's crystal lattice and its chemical composition determine thermal conductivity. Crystalline materials typically exhibit higher thermal conductivities compared to non–crystalline or amorphous materials due to the more ordered atomic arrangement [46]. Additionally, thermal conductivity may vary with temperature, with some materials showing temperature–dependent behavior. Impurities, defects, and grain boundaries within the material can scatter heat–carrying phonons, reducing thermal conductivity [43]. Moreover, material density is an important factor, as materials with higher densities generally have higher thermal conductivities due to more efficient phonon transport. Furthermore, some materials exhibit anisotropic thermal conductivity [47], meaning that thermal conductivity varies with direction due to differences in crystallographic structure.

2.3 Thermoelectric Efficiency

2.3.1 Figure of Merit

The optimal efficiency of an energy conversion process in a material is determined by the value of the dimensionless figure of merit (ZT) given by Equation 2.6 [8, 48–50]. This factor is directly proportional to temperature (T), electrical conductivity (σ), and the square of the Seebeck coefficient (S^2), while inversely proportional to thermal conductivity (κ). A good TE material should have high values of Seebeck coefficient and electrical conductivity, but low thermal conductivity.

$$ZT = \frac{\sigma \cdot S^2}{\kappa} \cdot T \tag{2.6}$$

2.3.2 Power Factor

The Power Factor (PF, $Wm^{-1}K^{-2}$) is the second key metric parameter that validates a TE material's efficiency where the measurement of thermal conductivity is difficult owing to the unavailability of equipment. It is defined as the product of the square of the Seebeck coefficient (S^2) and the electrical conductivity (σ) of the material. Mathematically, the PF can be expressed as:

$$PF = \sigma \cdot S^2 \tag{2.7}$$

2.4 Applications of Thermoelectricity

The versatility of TE devices extends across a wide spectrum of applications, each leveraging the unique capabilities of TE materials. From waste heat recovery in industrial processes to portable power generation in remote environments, TE generators offer sustainable solutions for energy harvesting. Conversely, TE coolers find applications in electronic devices and refrigeration systems offering compact and efficient thermal management solutions.

2.4.1 Waste Heat Recovery

Waste heat recovery using TE materials is a growing field of research aimed at improving energy efficiency and sustainability. Thermoelectric generators (TEGs) convert thermal energy into electrical energy. In industrial electronic devices, waste heat is a complex problem in many electronic devices such as central processing units (CPUs), integrated circuits, etc. The CPUs produce thermal power in the range of 6–320 W and generate a huge amount of wasted heat up to 110 °C [7]. This waste heat could be reused to supply other components in the device to activate the cooling fan or recharge the battery [51], which will lead to an increasing battery's performance and lifetime [52], Figure 2.5a. Moreover, TEGs can be designed with high flexibility and excellent performance for heat harvesting from the human body, with demonstrated capability to power wearable electronics and sensors [53–55], Figure 2.5b.

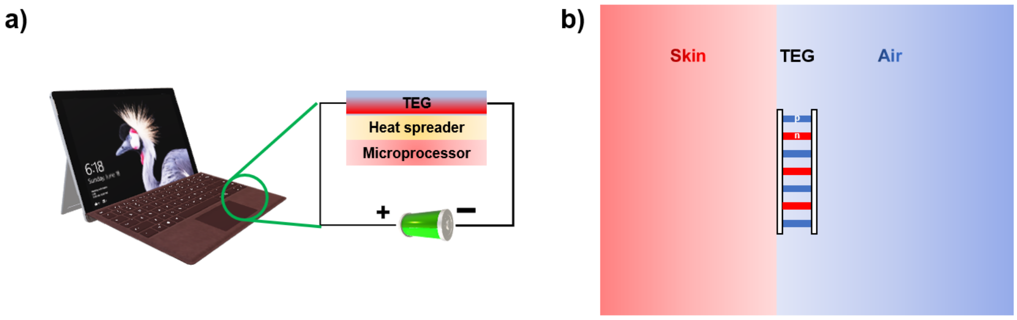

Figure 2.5: a) TEG used to recover wasted heat from a CPU to charge a battery, b) Wearable TEG as a TE energy harvesting using body heat.

2.4.2 Medical Wearable Devices

Given that body heat represents a sustainable energy source, its utilization holds the potential to power a wide array of emerging wearable and implanted medical devices. These devices can be employed across diverse applications, such as health monitoring and tracking systems, as well as sports and fitness wearable devices [56, 57].

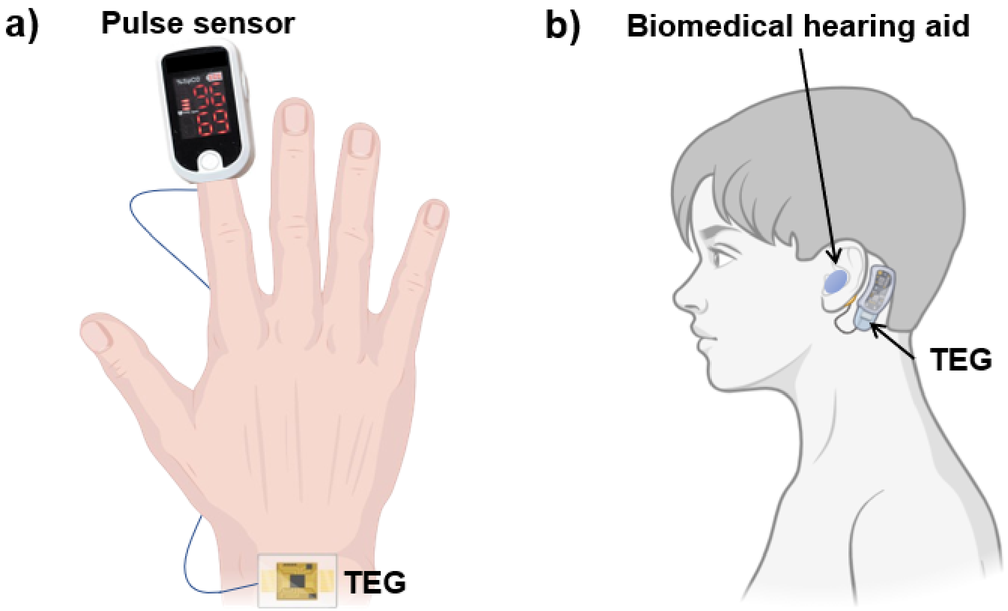

Figure 2.6: a) Wearable pulse sensor powered with a TEG, b) Biomedical hearing aid powered with a TEG.

2.4.3 Automobile Engines

More than two–thirds of the energy from fuel utilized by an automobile is dissipated as waste heat into the surrounding environment. To enhance fuel efficiency, TEGs can significantly improve the efficiency of internal combustion engines by recovering waste heat from exhaust pipes and radiators [58]. Experimental studies have demonstrated the potential for TEGs to improve fuel efficiency [59] and reduce environmental impact by generating electricity from automobile exhaust gases [60].

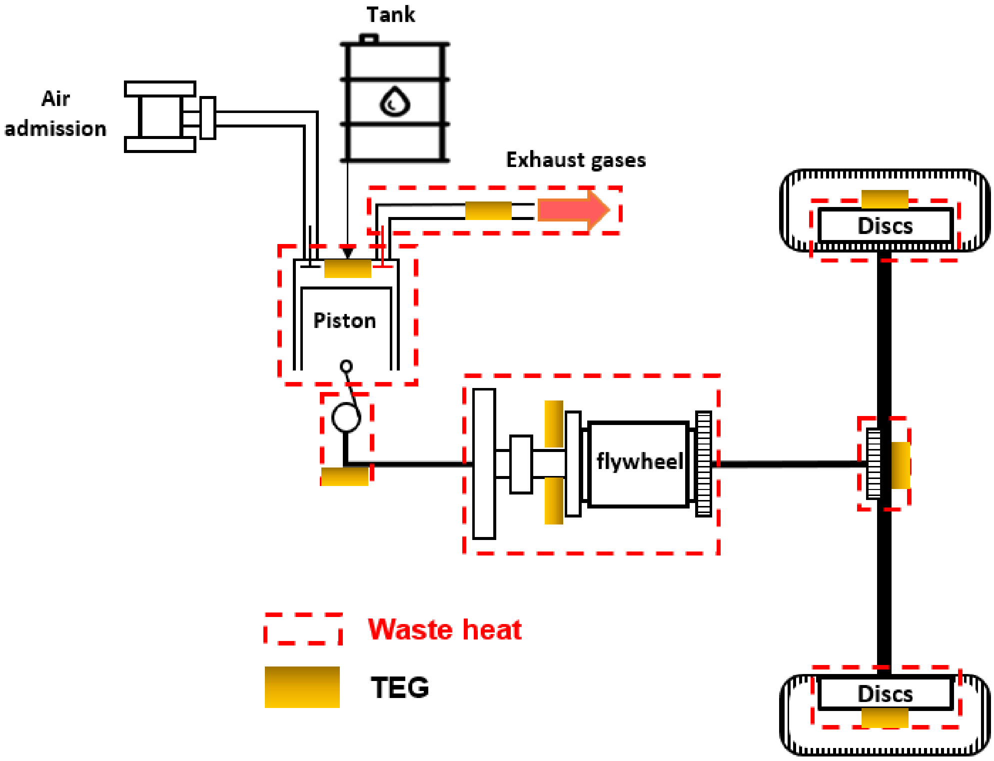

Figure 2.7: Schematic representation of waste heat recovery in automobile engines.

2.4.4 Renewable Energies

Solar photovoltaics constitutes one of the primary solar energy technologies. Photovoltaic (PV) cells function by directly converting solar radiation into electricity. However, it is worth noting that only approximately 10–15% of the absorbed solar radiation is effectively converted into electricity. The remaining portion is either reflected into the ambient environment (resulting in heat loss) or absorbed as heat, thereby elevating the operating temperature of the PV cell and subsequently diminishing its conversion efficiency [61, 62].

Therefore, integrating TE devices into PV modules would yield a hybrid device with improved overall performance, Figure 2.8. This synergy arises from the complementary nature of the two technologies (PV and TE) wherein the advantage of the TE can be used to compensate for the disadvantage of the PV. The TE devices can effectively serve a dual purpose: not only cooling the PV module but also generating supplementary energy [63], thus interconnecting photovoltaic and thermoelectric technology in a single structure improves efficiency and reduces temperature–related performance issues in solar panels [64].

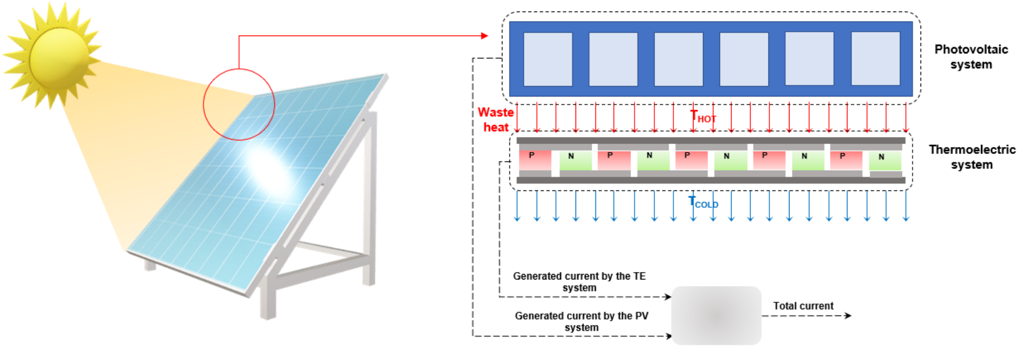

Figure 2.8: Schematic representation of a PV/TEG system.

2.5 Conclusion

As we conclude this introductory chapter, we reflect on the vast potential of thermoelectricity to address pressing challenges in energy sustainability. By understanding the principles and applications of thermoelectricity, we set the stage for further advancements in research and development. Moving forward, let us explore the materials utilized in thermoelectric applications, exploring their properties and potential in the upcoming chapter.

CHAPTER 3

THERMOELECTRIC MATERIALS

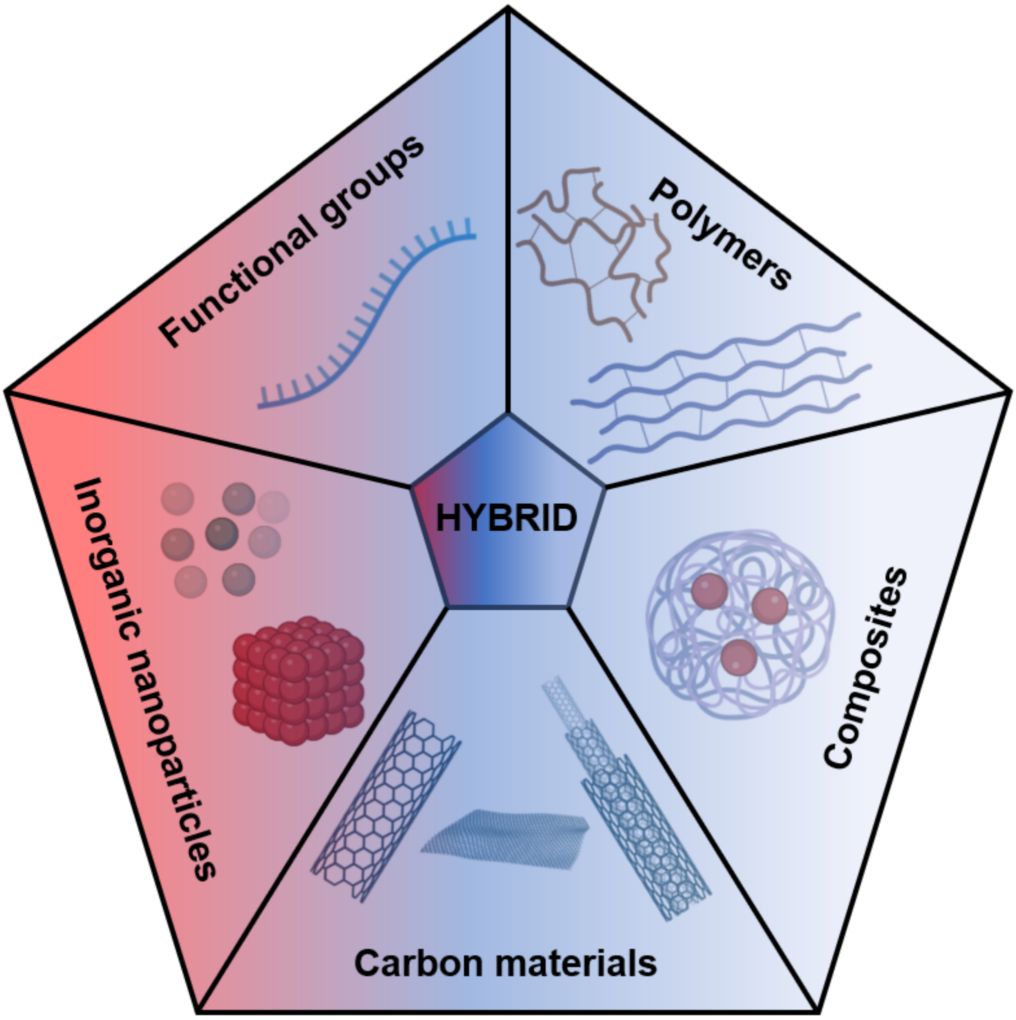

3.1 General Introduction

Building on the foundation of the previous chapter, which describes the general principles and applications of thermoelectricity, this chapter focuses specifically on the variety of materials used in thermoelectric (TE) applications.

The use of TE materials to convert waste heat into usable electrical energy is a significant advancement in improving energy sustainability and thermal management. This chapter focuses on TE materials, their properties, and methods of synthesis, with a focus on conductive polymers and their composites.

By examining the properties and performance characteristics of these materials, we aim to provide insight into the ongoing research efforts and the development of TE materials.

3.2 Thermoelectric Materials

To obtain a high figure of merit (ZT), both Seebeck coefficient (S) and electrical conductivity (σ) must be large, while thermal conductivity (κ) must be minimized [6]. The best materials satisfying these conditions are semiconductors, Figure 3.1 [15, 65].

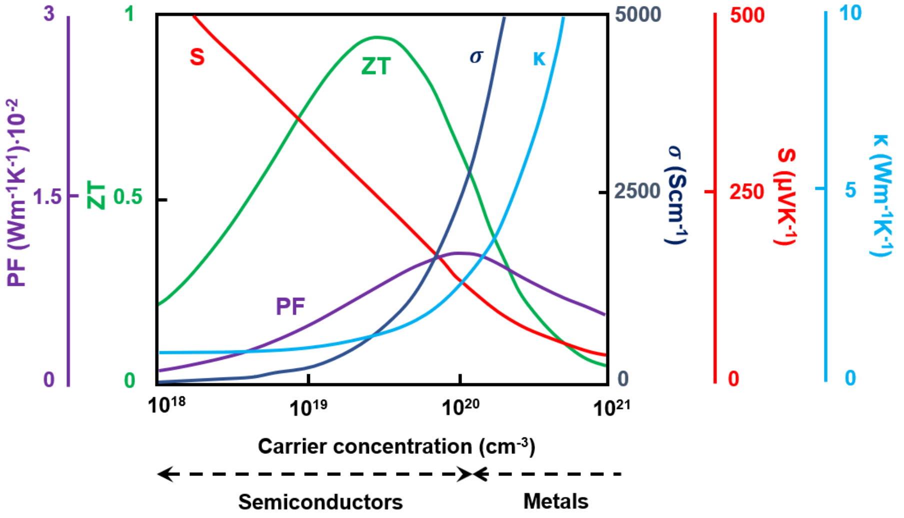

Figure 3.1: Thermoelectric properties according to changes in the carrier concentration.

Several studies [66–69] demonstrated that an efficient thermoelectric material exhibits the behavior of a PGEC (Phonon–Glass and Electron–Crystal), meaning it would have the thermal conductivity of glass and, conversely, the electrical conductivity of a conductive material. On the basis of their chemical composition [5], TE materials are classified in three categories: inorganic materials [11, 14, 70, 71], organic [30, 72–74], and hybrid materials [74–77].

3.2.1 Inorganic Thermoelectric Materials

Inorganic thermoelectric materials are solid–state materials composed of elements from the periodic table such as bismuth (Bi), tellurium (Te), lead (Pb), tin (Sn), selenium (Se), germanium (Ge), cobalt (Co) and nickel (Ni). These elements are typically used in combination to form compounds with desirable TE properties such as bismuth telluride (Bi_2Te_3) and lead telluride (PbTe) [78]. Inorganic TE materials are the classic and most widely used materials in the TE industry, and they can be subdivided into three categories depending on the temperature at the real application [11].

Near room temperature inorganic TE materials, which are extensively used to harvest the human body energy. Bi_2Te_3–based alloys are the most notable and widely used material in the TE industry and have been studied extensively since the 1960s [9, 70, 79, 80] reaching a ZT of 1.

TE materials are commonly employed in medium temperature range (600 to 1000 K), concern applications in automotive and other industries, where waste heat can be converted into electrical current directly from the engine (e.g., heat pipes). PbTe–based materials are the best since they have a ZT of 1.2 [81].

High–temperature range (up to 1000 K) TE materials, involve applications to harvest energy for space missions and exploration of outer space. Usually, PbSnTe is used as p–legs and $(GeTe)_{85}(AgSbTe_2)_{15}$ as n–legs. In the past, 18 SiGe–SiMo modules were mounted in a space–craft, the hot side operated at 1308 K and the cold ones at 566 K, the device provided 245 W of electrical power [5].

Other inorganic TE materials were investigated; transition metal oxides show potential for TE power harvesting due to their chemical and thermal stability at high temperatures. Wide–bandgap semiconductor oxides such as ZnO, SnO_2, and In_2O_3 exhibit high power factors of 10^{-3} $Wm^{-1}K^{-2}$ to 10^{-4} $Wm^{-1}K^{-2}$ [82].

N–type ZnO doped with Ga to reduce thermal conductivity and Al to increase electrical conductivity leading to $Zn_{0.96}Al_{0.02}Ga_{0.02}O$ material with a ZT of 0.47 at 1000 K [83]. P–type NiO doped with Li and Na exhibits TE PF of the order of 10^{-4} $Wm^{-1}K^{-2}$ at up to 1000 K [84]. Thin films based NiO were reported with S, σ of 101 μVK^{-1} and 10^{-2} Sm^{-1}, respectively at room temperature [85].

However, they often suffer from limitations such as high manufacturing costs and rigidity, which restrict their applications, particularly in flexible and wearable electronics.

These limitations can be overcome using organic materials such as conducting polymers (CPs), which will be discussed in the upcoming section.

3.2.2 Organic Thermoelectric Materials

The most popular organic TE materials are polymers. These materials are well–suited for flexible and lightweight TE applications conversely to inorganic TE materials. Conducting polymers (CPs) are a class of organic polymers that exhibit electrical conductivity. Unlike traditional insulating polymers, conducting polymers have a delocalized π–electron system along their backbone, which allows for the movement of charge carriers (electrons or holes) upon doping or oxidation/reduction processes [86]. This electronic structure is responsible for their semiconducting or metallic behavior which offers several advantages, including tunable electrical properties, in addition to their flexibility and processability. These properties make CPs attractive candidates for various applications, including organic electronics [87], energy storage [88] and conversion devices [74], sensors [89] and in our concern TE materials.

3.2.2.1 Electronic Configuration

The concept of conjugated bonding is intimately related to the hybridization state of carbon atoms, Figure 3.2. Carbon atoms can hybridize their orbitals to form σ bonds. In conjugated systems, carbon atoms typically adopt sp^2 hybridization, where one "s" orbital and two "p" orbitals combine to form three σ bonds in a trigonal planar geometry. The remaining "p" orbital, perpendicular to the plane of the σ bonds, is available for π bonding.

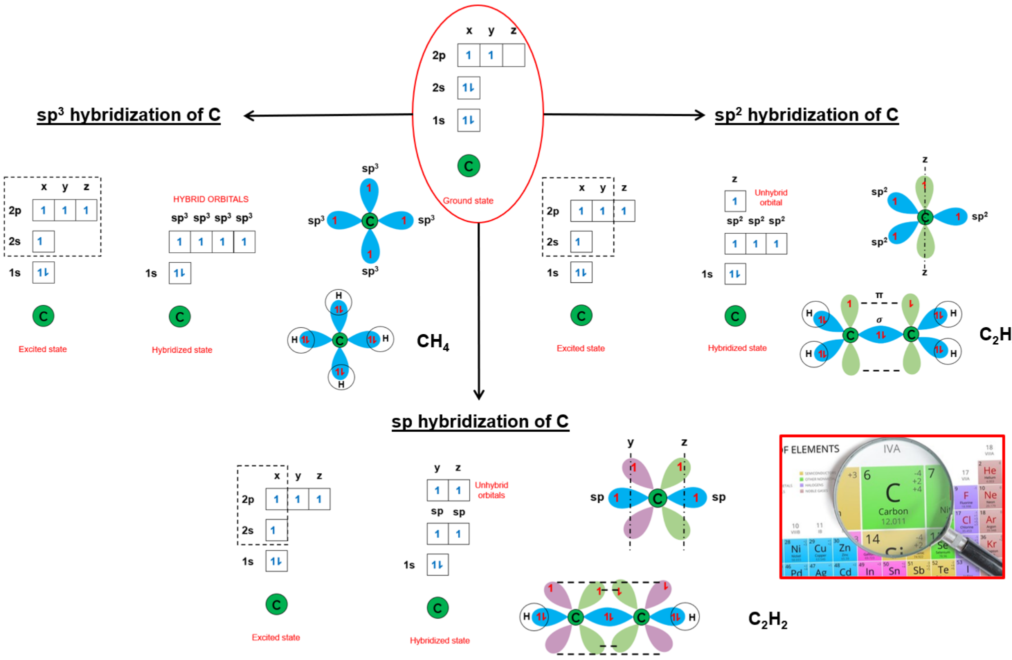

Figure 3.2: Hybridization of carbon atoms.

The bond model describes the structure of conjugated polymers. Indeed, the constituent units of a polymer possess discrete energy levels. As the effective conjugation length (number of monomers) increases, the energy levels of molecular orbitals also increase. In the π bond, two carbon atoms share their electrons. Quantum mechanics predicts the emergence of two molecular orbitals: a bonding orbital (π) and an anti–bonding orbital (π^*). For longer chains, additional bonding and anti–bonding orbitals have slightly different energies. As the chain length increases, the energy levels are no longer discrete and become valence (π) and conduction (π^*) bands. The highest occupied molecular orbital (HOMO) and the lowest unoccupied molecular orbital (LUMO) of the polymer are separated by a band gap, whose width ranges from 1 to 4 eV and is modulated by doping [90], as shown in Figure 3.3.

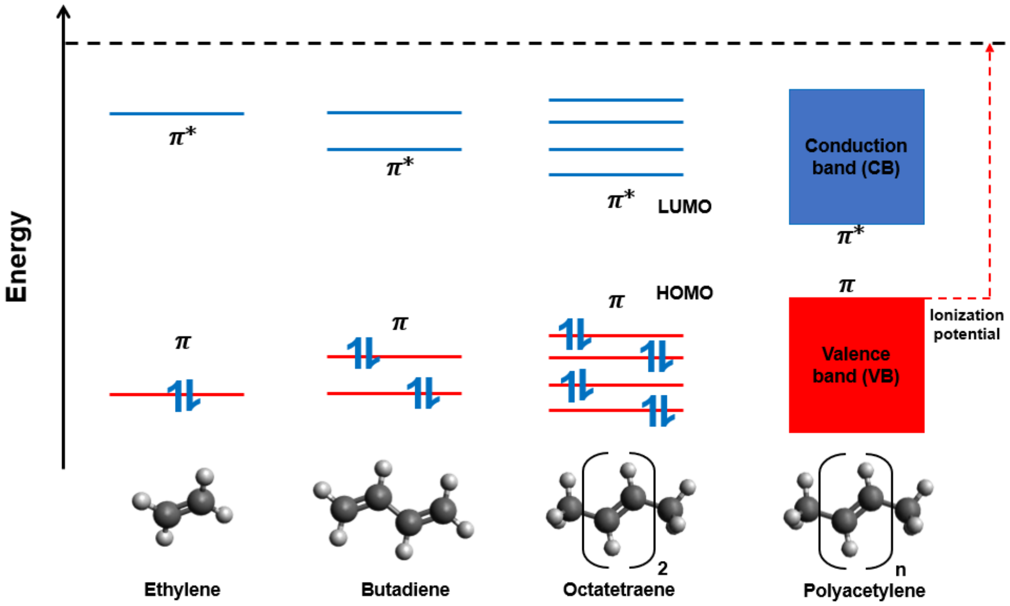

Figure 3.3: Energy levels changes according to chain length.

CPs have been investigated continuously, including polyaniline (PANi) [91–94], poly(3,4–ethylenedioxythiophene) (PEDOT) [95–98], PEDOT:poly(styrene sulfonate) (PEDOT:PSS) [99–102], polythiophene (PTh) [103] and polypyrrole (PPy) [104–107], Figure 3.4.

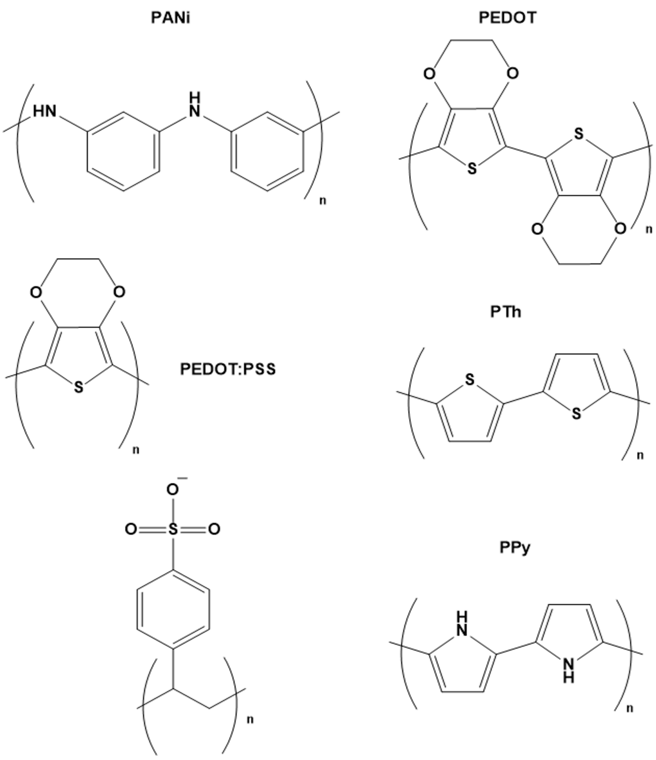

Figure 3.4: Chemical structure of common CPs.

In general, CPs possess a sequence of alternating single (σ) and double (π) bonds, known as π–conjugation, which provide them with distinctive optical, electrochemical, and electrical properties. Moreover, it is known that the key factors influencing the physical characteristics of CPs are their conjugation length, level of crystallinity, and interactions within and between polymer chains. Figure 3.5 shows the electrical conductivity of essential CPs.

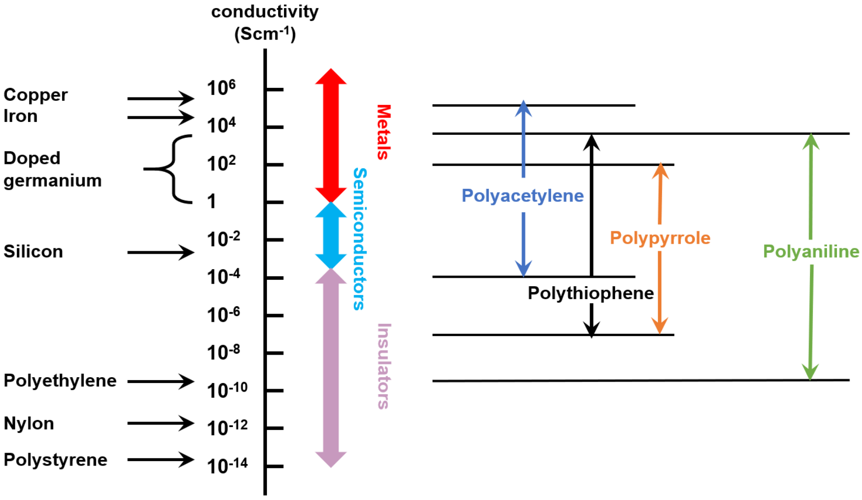

Figure 3.5: Electrical conductivity of some CPs.

3.2.2.2 Doping and Dedoping

Electron conduction in conducting polymers relies on the creation of structural defects incorporated within the macromolecular chains, which manifest as charge carriers (ions, polyions, radical ions, etc.). Doping is the process of introducing charge carriers into the macromolecule, thus creating structural defects that can move along the chains, facilitated by electronic conjugation, to ensure conductivity. This doping can be achieved through oxidation (electron extraction) or reduction (electron injection) of polymer films [108–110]. There are two types of doping: positive (p–type) doping and negative (n–type) doping. Conductivity increases with the level of doping in the polymer matrix. Consequently, the polymer transitions from a neutral state to a conductive state through doping and from a conductive state to a neutral state through dedoping.

In electronic CPs, the charge carriers are essentially defects within the polymer structure that possess an electrical charge. When these defects occur, they create energy states within the electronic band structure of the polymer. Specifically, these energy states are positioned between the conduction band, where electrons are free to move and carry electrical current, and the valence band, which represents the highest energy levels occupied by electrons. The presence of these energy states facilitates the movement of charge carriers, enabling the polymer to conduct electricity. Therefore, by introducing defects into the polymer chain, conducting polymers can exhibit enhanced electrical conductivity [111, 112]. Two types of defects can be distinguished: Polaron (or radical ion) corresponding to a charged defect (Figure 3.6b) and bipolaron corresponding to a double charged defect (Figure 3.6c) [86].

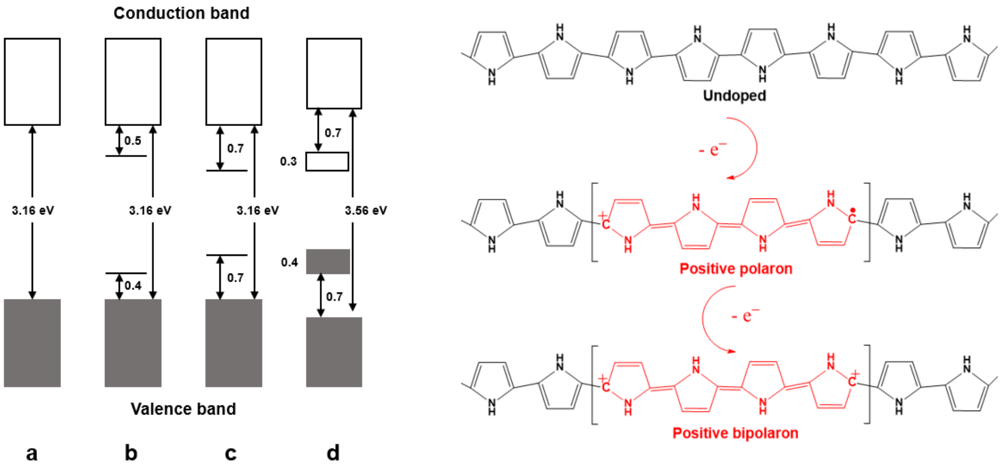

Figure 3.6: Electronic bands and chemical structures illustrating (a) undoped; (b) polaron; (c) bipolaron; and (d) fully doped states of PPy.

In the undoped state, PPy is an insulator with a large band gap of approximately 3.16 eV. Upon oxidation, the band gap shifted to 2.26 eV for polaron state and 1.76 eV for bipolaron state. The incorporation of ionic species follows to ensure electroneutrality to counteract the imbalance that could be created as regions of localized charge imbalance within the polymer.

3.2.2.3 Charge Transport Mechanism

Several studies [110, 113–116] to understand the charge transport mechanism in CPs were reported. The charge transport mechanism between chains in a polymer matrix is based on a microscopic level, on the overlap of various local transport modes: within the conjugated chain (intra–chain), from one chain to another (inter–chain), and from one fiber to another (inter–fiber). A schematic representation of a random polymer is presented in Figure 3.7 to illustrate the different charge transport mechanisms.

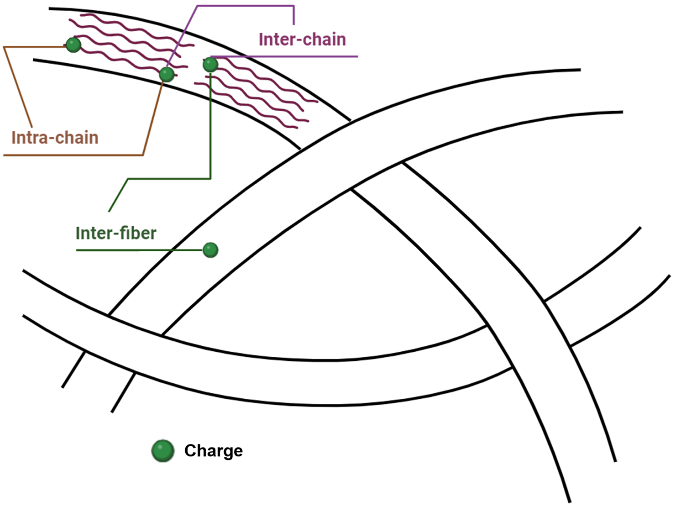

Figure 3.7: Schematic representation of charge transport mechanism within random polymer chains.

For inter–chain and fiber charge transport, hopping and tunneling models have been proposed by previous studies [117–120]. Charge carriers can move from one delocalized state to another via tunnels, and charge transport occurs through a random hopping mechanism of charge carriers between delocalized states of adjacent centers in the polymer chain.

3.2.2.4 Synthesis of Conducting Polymers

The synthesis of conducting polymers involves several methods to produce materials with specific properties for various applications. One common approach is chemical polymerization, where monomers are polymerized to form long chains with conjugated structures. This process often involves oxidative or reductive conditions to initiate polymerization and introduce charge carriers into the polymer backbone. The morphology of the polymer can be controlled by varying the parameters of the process, such as monomer/oxidizing agent concentration, temperature, pH, and reaction time [121, 122]. Figure 3.8 illustrates the chemical synthesis route of polypyrrole [123].

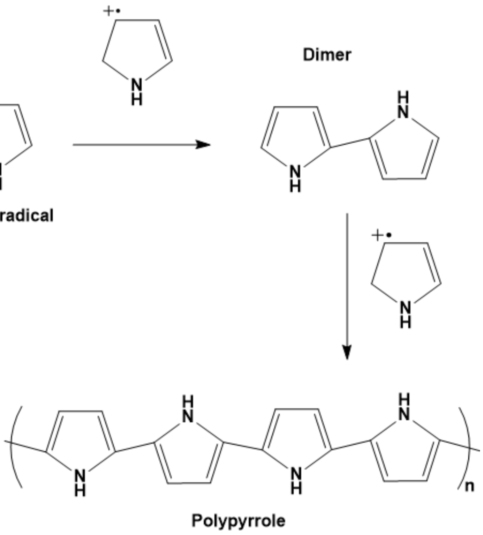

Figure 3.8: Chemical synthesis route of polypyrrole.

Another method that does not require an oxidizing chemical agent is the electrochemical polymerization, which allows for precise control over the polymerization process by applying a potential to an electrode immersed in a monomer solution. This method results in the synthesis of conducting polymers with specific morphologies and properties which is an efficient approach for depositing CPs on substrates, however, a high oxidation potential may lead to over–oxidation of the polymer [121, 122]. Figure 3.9 depicts the electrochemical synthesis mechanism of polypyrrole [124].

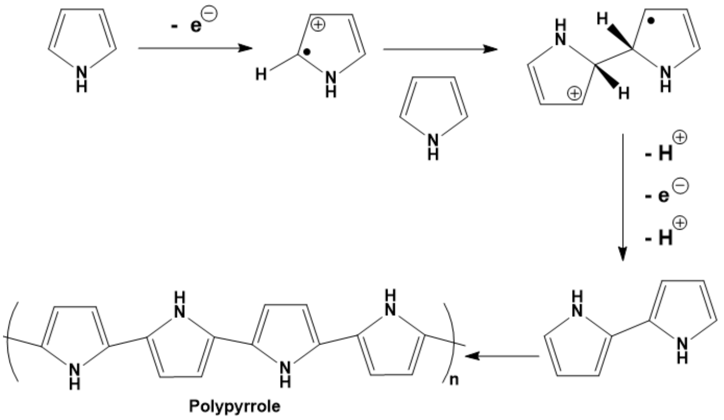

Figure 3.9: Electrochemical synthesis mechanism of polypyrrole.

Moreover, in order to solve the over–oxidation problem, another synthesis route was developed which is photo–polymerization where illumination is needed and the process can be controlled simply by turning the light on or off [121, 122]. Figure 3.10 shows a general presentation of photoinitiated polymerization, The choice of λ (and thus hν) depends on the specific photoinitiator being used, as different photoinitiators are activated by different wavelengths of light, ultraviolet (UV) ~365 nm, visible ~450 nm and infrared (IR) ~800 nm [125, 126].

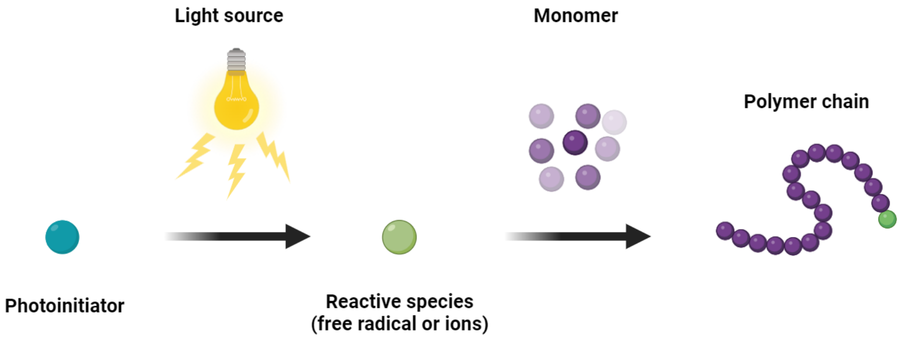

Figure 3.10: General representation of photo–polymerization route.

3.2.2.5 Ongoing Research in Organic Thermoelectric Materials

The field of polymer–based thermoelectric materials is making great progress, driven by the need to improve their efficiency, stability, and scalability. Researchers are exploring new polymer designs, better processing methods, and gaining a deeper understanding of how these materials work. These efforts aim to overcome challenges such as low efficiency, poor long–term stability, and difficulties in large–scale production.

Organic thermoelectric materials, including conducting polymers, small molecules, and carbon–based materials, offer unique advantages such as flexibility, low cost, and solution processability. They are particularly well–suited for applications requiring flexible and lightweight devices.

Nanostructured CPs are preferred in TE materials because their reduced dimensionality enhances their properties such as the Seebeck coefficient and decreases thermal conductivity. Research on the controlled synthesis of PPy nanostructures [104, 127–129] aims to optimize their properties by systematically adjusting experimental parameters. The type of oxidant (e.g., ferric chloride, ammonium persulfate), its concentration, the polymerization time, and the reaction medium (e.g., aqueous solutions, organic solvents) are all critical factors. High oxidant concentrations and extended polymerization time generally produce smaller, more uniform, and highly conductive nanostructures, while the choice of reaction medium influences solubility and stability.

Using PEDOT and PPy nanowires in blends, thermoelectric properties were enhanced by 20% (19.4 μVK^{-1}) regarding the Seebeck coefficient and 32% (18.2 $\mu Wm^{-1}K^{-2}$) in PF compared to neat PEDOT without sacrificing softness and flexibility, due to enhanced nanowire interfaces [130].

Compositing PEDOT:PSS with small nonpolar aromatic molecules such as naphthalene and pyrene significantly enhances its Seebeck coefficient 45.5 μVK^{-1} and a ZT value of 0.27 [131]. In this context, the overlap between the π–orbitals of the PEDOT chains and the π–orbitals of the aromatic molecules (naphthalene or pyrene) likely facilitating better charge transport. While other studies [132] report that post–treatments with common acids (H_2SO_4) and bases (NaOH) could reach an optimal PEDOT:PSS films with a Seebeck coefficient of 39.2 μVK^{-1} and a conductivity of 2170 Scm^{-1} at room temperature, and the corresponding power factor is 334 $\mu Wm^{-1}K^{-2}$. These treatments influence the polymer properties through modifying its morphology and oxidation level.

Another study [133] demonstrates the fabrication of PEDOT:PSS–PTh bilayered nanofilms on organic electrodes, resulting in stable and enhanced thermoelectric performances reaching a PF of 1.57 $\mu Wm^{-1}K^{-2}$.

Among several materials, 2D materials, such as graphene and related materials, show promise for thermoelectric applications due to their excellent transport properties leading to significant power factor. Graphene nanoplatelets (GNPs), carbon nanotubes (CNT), both single–walled (SWCNTs) and multi–walled (MWCNTs) carbon nanotubes are potentially under investigation in nanocomposites for TE applications. These materials have good electronic properties despite the high thermal conductivity compared to conducting polymers, good Seebeck coefficient, and surface area, which can lead to improved charge transfer and, thus, TE performance. Individual CNTs are not so promising as a TE material with high ZT values because of their intrinsic high thermal conductivity (2000–3000 $Wm^{-1}K^{-1}$) [134–138].

Introducing carbon–based materials to CPs matrix such as PPy is investigated in TE materials, PPy–MWCNTs composite synthesized using sodium dodecyl sulfate (SDS) as surfactant and ferric chloride as an initiator, resulted in a PF of 0.77 $\mu Wm^{-1}K^{-2}$ and a ZT of 10^{-3} [139]. Core–shell nanocomposites based on PPy–SWCNT were studied along with methyl orange (MO) as a surfactant and ferric chloride as an initiator [140]. The uniform coating and good interaction between PPy polymer chains and walls of the SWCNT through π–π stacking resulted in a PF and ZT of 360 $\mu Wm^{-1}K^{-2}$ and 0.09, respectively. As a result, incorporating SWCNTs results in better TE properties.

Ternary composites also have also been studied, as an example PEDOT:PSS–PPy–Graphene composites show excellent TE performance, with a maximum power factor of 82.22 $\mu Wm^{-1}K^{-2}$, at room temperature and 70% PPy–Graphene to PEDOT:PSS, attributed to its good crystallinity, while PEDOT:PSS–PPy–MWCNTs films show optimal power factor of 55.28 $\mu Wm^{-1}K^{-2}$ at only 5% PPy–MWCNT to PEDOT:PSS [141], which indicates that PPy–MWCNT result in better TE properties in PEDOT:PSS than PPy–Graphene.

The PPy–Graphene–PANi composite with 32 wt% graphene demonstrates good electrical conductivity, Seebeck coefficient, and high thermoelectric power factor, up to 52.5 $\mu Wm^{-1}K^{-2}$ [142].

Binary and ternary composites are promising approaches, since CPs offer good electrical conductivity and flexibility, while graphene and carbon nanotubes provide to the composite their electrical conductivity, thermal stability, and mechanical strength. A higher Seebeck coefficient can be achieved through optimized carrier concentration and mobility, and reduced thermal conductivity, leading to a high TE figure of merit (ZT). This synergistic effects lead to better charge carrier mobility and overall stability, making these nanocomposites efficient and suitable for diverse TE applications [14, 74, 143].

In summary, organic TE materials, with their flexibility, lightweight nature, and ease of processing, have shown considerable potential in the field of energy conversion. However, to further boost the performance and applicability of TE materials, the focus is now shifting towards hybrid TE materials. These combine the advantageous properties of both organic and inorganic components such as bismuth telluride, lead telluride and metal oxides, offering a promising avenue for achieving superior TE performance.

3.2.3 Thermoelectric Hybrid Materials

As mentioned above, hybrid materials increase TE materials versatility in various applications. They are typically elaborated by combining conducting polymers (CPs) with inorganic materials alone as bismuth or combined as bismuth telluride, lead telluride and metal oxides.

Composition, nano/micro size, and the way of elaboration, all are critical parameters that have to be optimized in hybrid TE materials. Smaller particles have a higher surface area–to–volume ratio, which can enhance interactions at the interfaces and improve overall material properties.

The main methods for preparing CPs–inorganic TE nanocomposites are physical mixing (PANi–Bi [144], PANi–$Bi_{0.5}Sb_{1.5}Te_3$ [145], PANi–SnO_2 [146] and PANi–$CuBO_2$ [147]), solution mixing (PANi–Bi_2Te_3 [148] and Te–PEDOT:PSS [149]) in situ oxidative polymerization/intercalation (PANi–PbTe [150] and PANi–TiO_2 [151]). All these composites exhibited enhanced TE properties due to several factors. Inorganic materials typically have higher electrical conductivity, which improves the overall conductivity of the composite. They also help optimize the Seebeck coefficient by adjusting carrier concentration and mobility. Additionally, while maintaining the polymer's low thermal conductivity, inorganics can further reduce thermal conductivity by scattering phonons. Inorganics also enhance the mechanical stability of the composite, making it more durable. Synergistic effects at the interface between CPs and inorganics lead to better charge transfer and reduced energy losses, resulting in more efficient and robust TE materials [16, 152].

A recent study [153] focused on compositing PPy with MWCNTs and metal hydroxides, for instance, $Sr(OH)_2$, $Zn(OH)_2$, $Ni(OH)_2$, and $Co(OH)_2$. This approach aimed to tackle the agglomeration problems at the nanoscale of metal oxides–CPs composites. The PF was approximately 0.2 $\mu Wm^{-1}K^{-2}$ at room temperature and the figure of merit for the nanocomposite incorporating $Ni(OH)_2$ was 0.6×10^{-3}. The observed enhancement was attributed to the strong interaction between PPy and metal hydroxides, facilitated by π–π stacking between the polymer chains and the metal hydroxides, as well as with MWCNTs.

Metal oxides have been also studied in the matter of hybrid composite with organic CPs matrix. To cite an example, aluminum doped zinc oxide–PANi hybrid was synthesized via sol–gel and in situ oxidative polymerization methods resulting in a simultaneous improvement in electrical conductivity which is attributed to carrier mobility and Seebeck coefficient due to scattering of low–energy carriers via energy–filtering effect leading to enhance the room temperature figure of merit (ZT = 0.0035) [93]. The energy–filtering effect aims to selectively allow high–energy charge carriers to pass through while scattering lower–energy carriers. This selective filtering is achieved at the interfaces between different materials in the composite, such as between the CP and inorganic nanoparticles. High–energy carriers have more energy and contribute more effectively to electrical conductivity, thus enhancing the overall TE performance of the material [154–156].

In conclusion, hybrid TE materials, which combine CPs and inorganic components, exhibit enhanced performance due to improved electrical conductivity, optimized Seebeck coefficient, and reduced thermal conductivity. The interface interactions and effects play a crucial role and the synergy results in more efficient, durable mechanical stability TE materials.

3.3 Characterization Techniques for Thermoelectric Materials

Characterization techniques are essential to evaluate the electrical, thermal, and structural properties of materials by providing valuable insights into thermoelectric behavior.

Conductivity measurements are used to assess charge transport properties. It is assessed with a Jandel four–probe instrument. This device measures the resistivity (ρ) and resistance (R) of semiconductor materials, thin films, and other conductive samples. It employs the four–point probe method, four equally spaced and in contact with the material. Composite powders were cold pressed at 7 tons into pellets using a hydraulic press (Specac) with 13 mm in diameter, and a loading duration of about 20–30 s each (Appendix A for further details).

Seebeck coefficient is measured using a designed system to measure the voltage generated in response to a temperature gradient across a material. Herein, the system is made in the laboratory of macromolecular chemistry at École Militaire Polytechnique in Algeria (Appendix B for further details).

Thermal conductivity is also a key parameter to calculate ZT of TE materials, Hot–Disk instrument is widely used to measure it for its non–destructive nature. Another device used in this thesis is conceptualized and carried out in the laboratory of macromolecular chemistry at École Militaire Polytechnique in Algeria (Appendix C).

Hall characterization is a useful technique used to determine various electronic properties of bulk semiconductors. This method involves measuring the Hall voltage generated when a magnetic field is applied perpendicular to the current flowing through a semiconductor sample. The Hall effect provides valuable insights into carrier concentration (n), mobility (μ), and the type of charge carriers in the material (holes or electrons). The measurments were assessed by a Hall effect system type Ecopia HMS–5000.

Microscopy techniques, including scanning electron microscopy (SEM–JEOL 7500–F) and transmission electron microscopy (TEM–TECNAI G^2 20), are used to assess material morphology and microstructure. Samples for TEM analysis were prepared by materials dispersion in ethanol and deposition of a drop of suspension on a carbon–coated copper grid. The electrons are accelerated with 80 kV voltage and 5 μA emission current. For SEM analysis, the microscope operates at 15 kV at a working distance between the final lens of the electron column and the sample surface of 4.2 mm.

The structural composition was determined using a Thermo–Fisher DXR 2 Raman spectrometer; excitation was at 532 nm from a He–Ne laser at room temperature and a Perkin Elmer Fourier Transform InfraRed spectroscopy (FTIR) in attenuated total reflection (ATR) mode in the wavenumber range 4000–600 cm^{-1} with a nominal resolution of 4 cm^{-1} over 50 scans. Powder X–Ray diffraction (PXRD) is performed using PAN analytical XPert PRO Bragg–Brentano diffractometer with tube current of 30 mA and an operating voltage of 45 kV with Cu K_α (λ = 1.5418 Å) in the 2θ range of 10–90°. XPS spectra are recorded on a Thermo Scientific K–Alpha spectrometer using monochromatized Al K_α radiation (1486.6 eV) and the photoelectrons collected at 0° with respect to the surface normal are analyzed using a hemispherical analyzer. The major peak of core level spectra is calibrated with respect to C1s level fixed at 284.6 eV.

Thermal analysis techniques are used to study thermal properties and stability. Thermogravimetric analysis (TGA) measurements were performed on a Perkin Elmer (STA 6000). The samples were heated at the rate of 10 °C/min in nitrogen.

3.4 Conclusion

In summary, this chapter provided an overview of thermoelectric materials, covering both inorganic and organic materials and their properties as well as synthesis methods. Organic TE materials, particularly CPs, show significant promise for flexible and lightweight applications due to their tunable electrical properties and ease of processing. However, their relatively low performance limits their practical use. To enhance TE efficiency, hybrid TE materials have been developed, combining the advantages of organic CPs with inorganic materials. These hybrids improve electrical conductivity and thermal stability while maintaining the flexibility and processability of polymers. They appear as promising materials for TE applications.

Part II

Contributions

CHAPTER 4

Optimizing Thermoelectric Potential: Graphene Surface Treatment and Conducting Polymers–based Ternary Composite Preparation

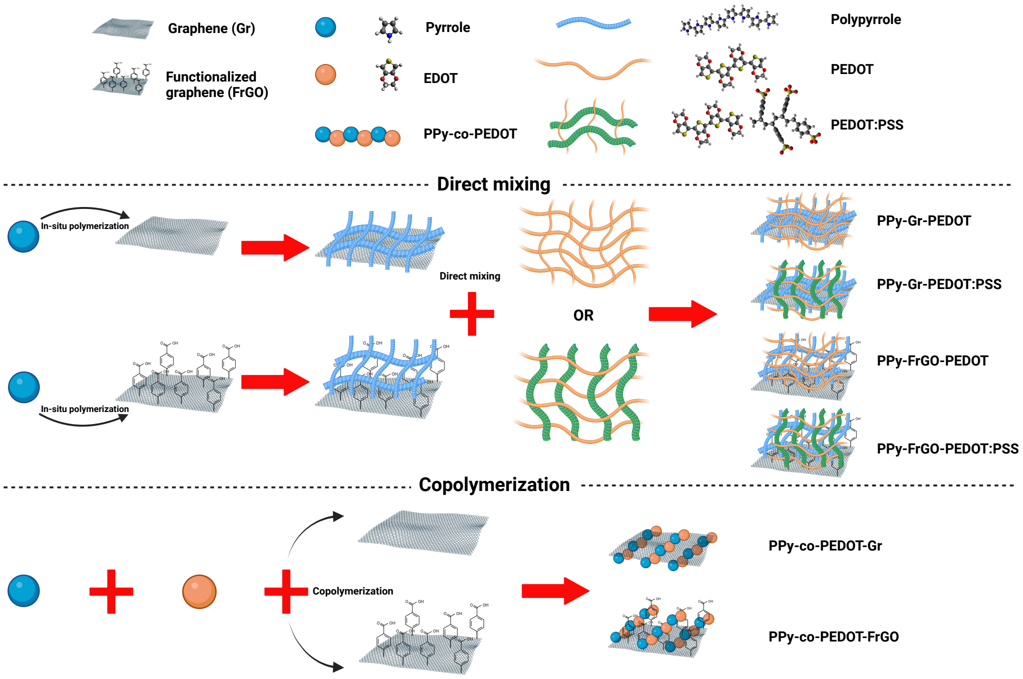

4.1 General Introduction

The preceding investigations detailed in the literature chapter have unveiled promising advancements in TE properties through the integration of graphene–based materials into polymer matrices [142, 157, 158]. Functionalization processes, such as oxidation and chemical modifications, have been pivotal in fine–tuning the thermal and electronic properties of graphene, as evident from studies elucidating the significant enhancement achieved in the figure of merit (ZT) [159–162]. Furthermore, the integration of graphene derivatives like reduced graphene oxide (rGO) and functionalized graphene (FrGO)–into polymer composites has exhibited a paradigm shift in achieving superior properties [14, 163].

Noteworthy advancements have also emerged from ternary composites, showcasing synergistic effects among constituent materials. Integrating PEDOT:PSS into composites, for instance, has demonstrated heightened electrical conductivity [99]. The amalgamation of PPy and PEDOT or PEDOT:PSS presents an opportunity for synergy, potentially elevating TE properties [164].

However, the methodologies employed in the preparation of ternary composites have been primarily limited to in situ chemical oxidization followed by physical mixing, with a lack of studies exploring simultaneous copolymerization techniques [14]. This gap forms the crux of the current investigation, aiming to compare the influence of surface treatment and preparation methods on the TE properties of ternary composites.

In this pursuit, the current study [165] explores the enhancement of PPy's TE properties through the incorporation of PEDOT and PEDOT:PSS, alongside with graphene and FrGO as fillers. A customized preparation methodology is introduced, involving copolymerization on graphene and functionalized reduced graphene oxide surfaces, serving as a departure from conventional preparation techniques. Comparative analyses between copolymerization and physical mixing of binary composites with a third component will provide valuable insights into optimizing TE properties.

4.1.1 Publications

The content of this chapter is based on the following peer–reviewed scientific publication "Reproduced with permission from Springer Nature":
Younes Bourenane Cherif, Nawel Matmat, Zakaria Bekkar Djelloul Sayah, Ahmed Mekki, Jean-Félix Durastanti, and Zineb Mekhalif. Influence of graphene oxide surface treatment by diazonium salts on thermoelectrical behavior of polypyrrole-based composites. **Journal of Materials Science: Materials in Electronics**, 33 (18):14938–14950, June 2022. ISSN 1573-482X. doi: 10.1007/s10854-022-08410-7. URL https://doi.org/10.1007/s10854-022-08410-7

This paper investigates a system "polymer1–filler–polymer2" where polymer1 and polymer2 are PPy and PEDOT or PEDOT:PSS and graphene as it is or functionalized constitutes the introduced filler. Using optimized formulations, six different ternary composites have been synthesized. The aim is to elucidate the effect of the filler surface modifications as well as the elaboration method of the composite on the thermoelectric properties of the final material. First, the surface treatment of graphene with diazonium salt compared to pristine graphene (Gr and FrGO) appears to play an essential role in dispersion in the composite, linking the two matrices and reducing hopping barrier potential. All together leads to an enhancement of TE properties of the final materials. Second, the synthesis method is a crucial key providing different properties of any material; herein, two methods were investigated between a direct mixing of polymers and copolymerization (PPy–PEDOT, PPy–co–PEDOT). Simultaneous improvements in the electrical conductivity and the Seebeck coefficient have been shown. Furthermore, among all composites, the figure of merit (ZT) value of PPy–FrGO–PEDOT is the highest (240 times higher than PPy) prepared by the mixing procedure. This evidences the critical contribution of graphene oxide functionalized with the diazonium salts in improving the polymer anchoring and distribution on the top of this latter.

4.1.2 Outline

The organization of this chapter is as follows: Section 4.2 provides insights into the used methodology and synthesis methods. Section 4.3 discusses the obtained results of different characterizations. Finally, Section 4.4 concludes the chapter by summarizing its key contributions.

4.2 Methodology

4.2.1 Materials

4–aminobenzoic acid ($H_2NC_6H_4CO_2H$, ≥ 99%), tetrafluoroboric acid (HBF_4, 52%) and sodium nitrite ($NaNO_2$, 97%) were purchased from Sigma–Aldrich and used to synthesize 4–carboxybenzenediazonium tetrafluoroborate denoted DS–COOH. For composites synthesis, monomers as pyrrole, EDOT, were purchased from Sigma–Aldrich as well as PEDOT:PSS, and graphite (> 98%) and the following chemicals: Dodecylbenzene sulfonic acid (DBSA, dopant, > 98%) and iron chloride hexahydrate ($FeCl_3$, oxidant, > 98%) were used to synthesis PPy and PEDOT. Potassium permanganate ($KMnO_4$, 98%), hydrogen peroxide (H_2O_2, 30%), hydrochloric acid (HCl, 37%), phosphoric acid (H_3PO_4, 85%), and sulfuric acid (H_2SO_4, 98%) were used in graphene oxide (GO) treatment. For reducing GO, hydrazine monohydrate ($NH_2NH_2.H_2O$, 60%) was used. Solvents were of analytical grade: deionized water (DI), diethyl ether, methanol, acetone, and N,N–dimethylformamide (DMF).

4.2.2 Fillers Preparation

4.2.2.1 Synthesis of Diazonium Salt

Preceding the functionalization of graphene sheets, a diazonium salt (DS–COOH) was meticulously prepared and isolated, rather than in–situ formed in the presence of the materials intended for functionalization. It was synthesized by dissolving 0.04 mol of 4–aminobenzoic acid in a solution containing 20 ml of HBF_4 and 70 ml of deionized water (DI) [166, 167]; and stirred at 0 °C for a duration of 15 min. Subsequently, 3 g of $NaNO_2$, dissolved in 10 ml of solution, was gradually introduced into the mixture, and the reaction was left for 2 h. The resulting product, observed as a white solid, was then filtered, washed with diethyl ether, and stored at a temperature of 4 °C denoted as DS–COOH.

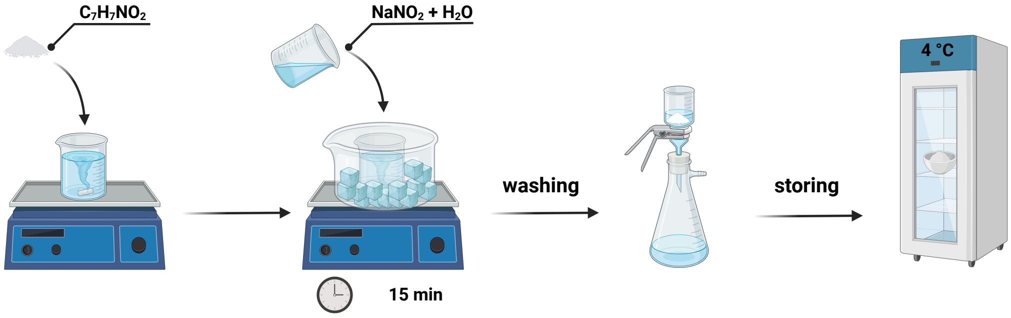

Figure 4.1: Schematic experimental protocol of DS–COOH preparation.

4.2.2.2 Preparation of Graphene Surface

Graphite, which is a three–dimensional crystal structure consisting of many layers of graphene stacked on top of each other. Each layer is weakly bonded to the adjacent layers through van der Waals forces. Ultrasonication is a method for exfoliating graphene from graphite. Initially, graphite is suspended in a liquid medium (ethanol) to form a stable suspension. The suspension is then subjected to ultrasonication to form graphene sheets. Secondly, graphene oxide (GO) was synthesized following a modified version of the Hummer's method [159]. In a concise summary of the procedure, 0.255 g of graphene powder were introduced into a mixture of H_3PO_4 and H_2SO_4 (3:27 ml) at room temperature. Subsequently, 1.32 g of $KMnO_4$ were gradually incorporated into the mixture, which was then allowed to stand for 6 hours until a dark green color appeared. The differentiation between the Hummer's and modified Hummer's methods lies in the substitution of $NaNO_3$ with H_2SO_4 and H_3PO_4, along with doubling the amount of $KMnO_4$. To eliminate excess $KMnO_4$, 0.675 ml of H_2O_2 were meticulously added to the mixture, followed by an additional 10 min reaction period and subsequent cooling. The resultant residue was subjected to centrifugation at 5000 rpm for 7 min, using a solution consisting of 10 ml of

HCl diluted in 30 ml of deionized water (DI). This centrifugation process was repeated three times to ensure the removal of any unreacted reagents. The final GO powder was obtained after drying at 90 °C for 24 h.

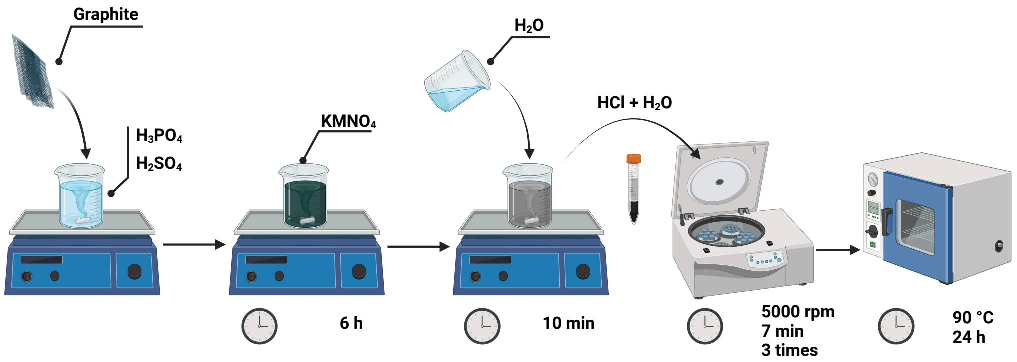

Figure 4.2: Experimental protocol of GO preparation.

When graphene is in its oxidized state form (GO), it exhibits reduced reactivity, mainly because of the presence of oxygen functional groups, resulting in electrical insulation [168]. To restore conductivity and reactivity, it is necessary to eliminate the oxygen and reinstate the double bonds in the carbon atoms of the aromatic structure through a reduction process using hydrazine. The exact procedure is as follows [169]: 0.1 g of GO was dispersed in 100 ml of DI under sonication, then 1 ml (32.1 mmol) of $NH_2NH_2.H_2O$ was added and refluxed at 100 °C for 24 h. The product was then filtered, washed with DI:methanol (50:50), dried and denoted rGO.

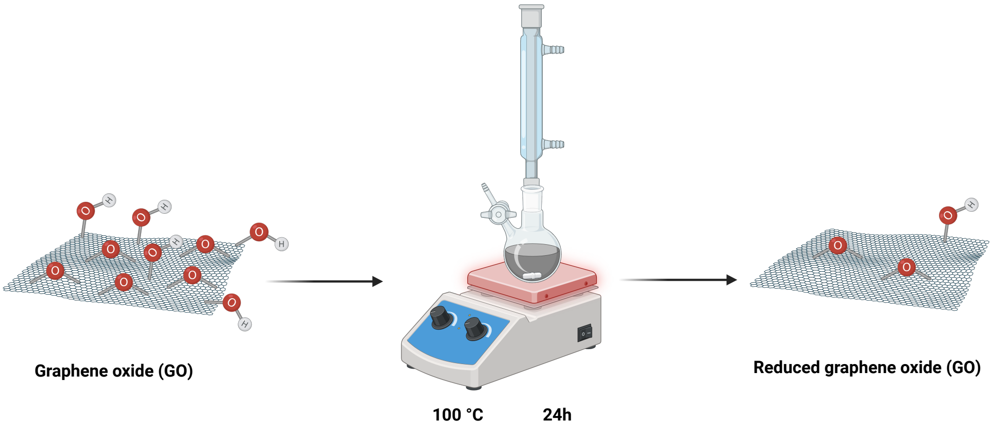

Figure 4.3: Experimental protocol of reduction of graphene oxide.

4.2.2.3 Graphene Functionalization

The functionalization process was in accordance with the procedure outlined by Lomeda et al. [170], a 20 ml dispersion of reduced graphene oxide (rGO) at a concentration of 1 mg/ml was combined with the previously prepared DS–COOH solution, which had a concentration of 0.33 mmol/ml in the rGO dispersion. This mixture was left to react for 1 h. Subsequently, the solution was diluted with 100 ml of acetone, subjected to filtration, and washed three times using a DI:acetone solution. The resulting powder was re–suspended in dimethylformamide (DMF) to eliminate the excess of diazonium salt, washed again with acetone, and then dried at 70 °C for 24 h.

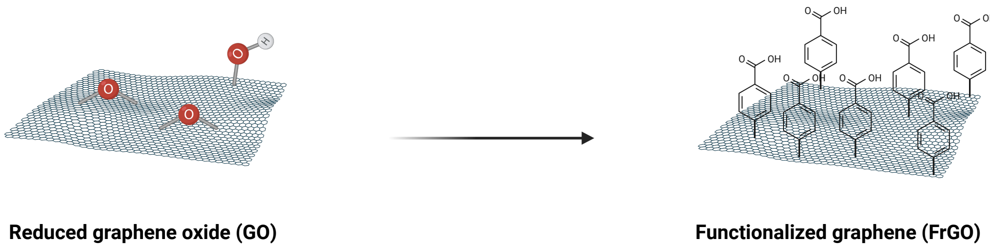

Figure 4.4: Functionalized graphene (FrGO).

4.2.3 Ternary Composites Preparation

To obtain different composites, PPy, PEDOT and PEDOT:PSS are used as matrices while Gr, FrGO are used as fillers.

PPy–Gr, PEDOT and ternary composites (PPy–Gr–PEDOT, PPy–Gr–PEDOT:PSS, PPy–FrGO–PEDOT, PPy–FrGO–PEDOT:PSS, PPy–co–PEDOT–Gr and PPy–co–PEDOT–FrGO) were synthesized as shown in Figure 4.5. First, following the procedure of Wang et al. [142], and optimizing the molar ratio between the dopant and the monomer according to Bekkar et al. [171], chemical polymerization of pyrrole in the presence of Gr and FrGO was achieved by sonicating 60 mg of Gr (or FrGO) in 50 ml of DI. Then 5 mmol of $FeCl_3$ (oxidant) and 0.5 mmol of DBSA (dopant) were added to the above solution and kept under stirring for 10 min. 5 mmol of pyrrole was then added dropwise to the previous mixture and kept at 0 °C for 20 min. The resulting product was filtered, washed, and dried at 70 °C. Denoted PPy–Gr and PPy–FrGO.

PEDOT was synthesized by introducing 3 ml of $FeCl_3$ in a 50 ml flask, adding 0.45 ml of EDOT monomer and stirring the mixture for 24 h. The final product, denoted PEDOT, was filtered, washed and dried at 65 °C [172].

To prepare ternary composites, two methods were adopted in this chapter. **Direct mixing** in ethanol under sonication of already prepared PPy–Gr (or PPy–FrGO) with PEDOT or PEDOT:PSS or **copolymerization** of pyrrole–EDOT in the presence of Gr (or FrGO), Figure 4.5.

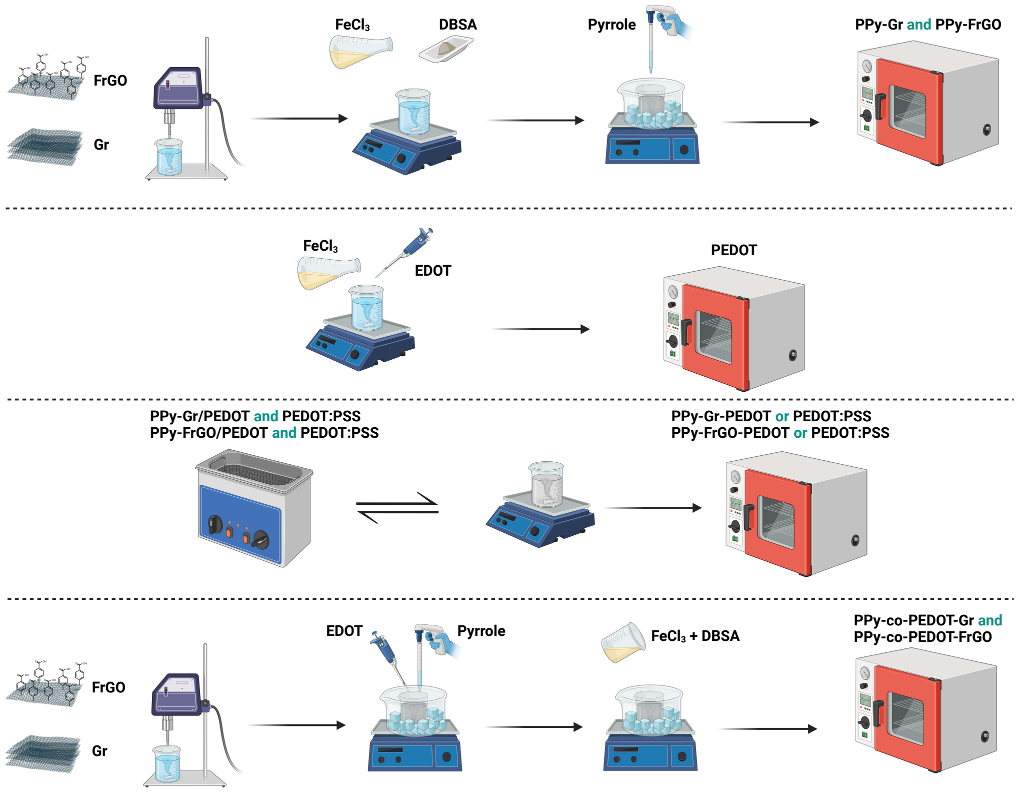

Figure 4.5: Experimental protocol for synthesizing all ternary composites.

The copolymerization protocol was carried out according to Munusamy et al. [173]. The filler, Gr or FrGO, was dispersed in DI under sonication and then an equimolar amount of both pyrrole and EDOT was added to the above solution. 1:10 DBSA and 1:1 $FeCl_3$ were added drop by drop to the mixture and left for 4 h at 0 °C. The resulting product was then washed, filtered, and dried at 70 °C, denoted as PPy–co–PEDOT–Gr and PPy–co–PEDOT–FrGO.

4.3 Results and Discussion

4.3.1 Structural Characterization

Raman and Fourier Transformer InfraRed techniques were used to investigate the structural behavior of the synthesized materials. The Raman spectra (Figure 4.6a) of the diazonium salt (DS–COOH), shows a peak at 1075 cm^{-1} attributed to C–H in–plane bending for para– and mono–substituted benzenes coupled with C–N stretching. The peaks at 1591 and both 1708 and 1732 cm^{-1} were associated with C=C and C=O stretching, respectively. The peak at 2308 cm^{-1} is typical of the N=N stretching bond. All these observations are in coherence with the literature [166].

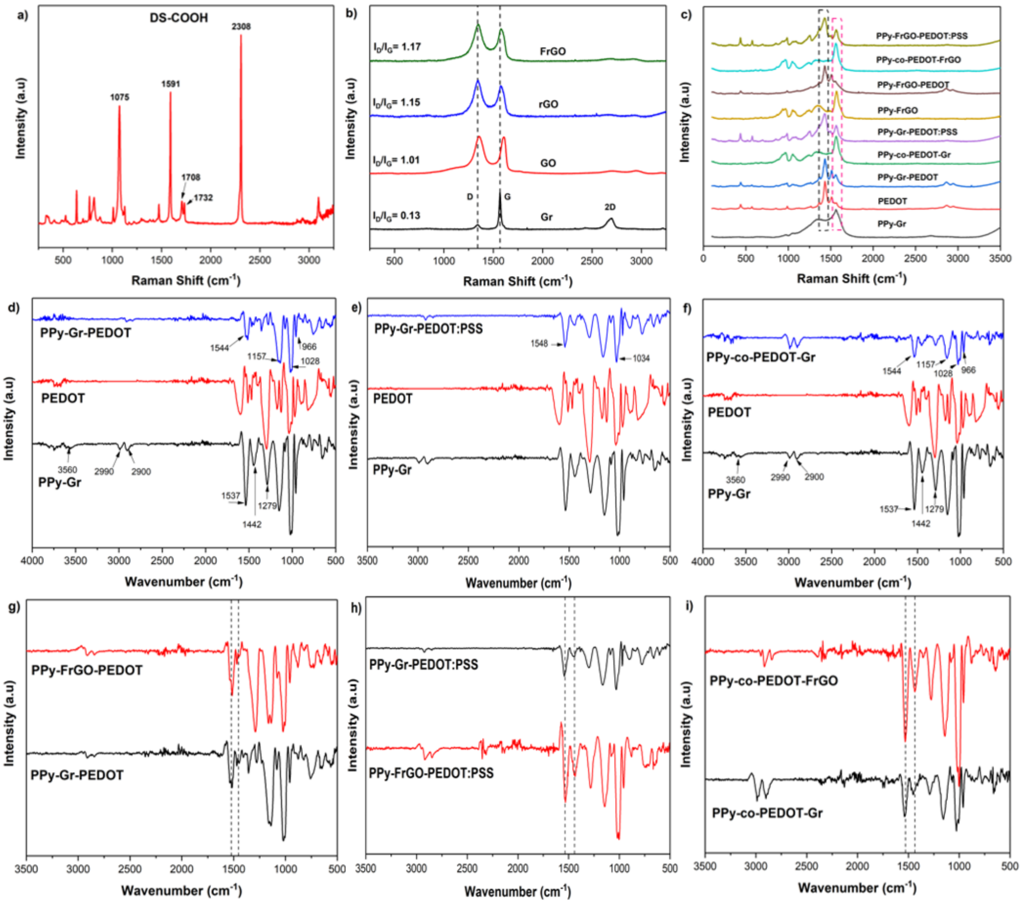

Figure 4.6: Raman and FTIR spectra of synthesized materials.

Regarding Gr, GO, rGO and FrGO, they were also characterized using Raman spectroscopy. As shown in Figure 4.6b, typical peaks of G and D band characteristic of graphitic materials were observed at 1561 and 1343 cm^{-1}, respectively. The D/G intensities ratio indicates structural modification of crude graphite at different chemical treatment steps, for instance: oxidation, reduction and functionalization with DS–COOH. The increased ratio from Gr to GO points out the reduction of the in–plane sp^2 sites, possibly due to extensive oxidation. The rGO and FrGO exhibit a D/G intensity ratio higher compared to GO. This change suggests a further decrease in the average size of sp^2 domains upon reduction and functionalization steps [169].

The comparative Raman spectra, Figure 4.6c, presents a comprehensive analysis of all synthesized materials, offering an intricate view of their structural characteristics. The distinctive peak patterns and spectral variations signify diverse chemical compositions to each material. These spectra serve as a valuable tool for discerning and characterizing the vibrational modes and molecular interactions within these materials. Here, the most intense peaks of polypyrrole and PEDOT are shown in red color and black color, respectively.

FTIR spectroscopy was used to further investigate the structural properties of the ternary composites. The first set of samples is prepared by mechanical mixing of PPy–Gr with PEDOT and PEDOT:PSS. Figure 4.6d shows FTIR spectra of PPy–Gr, PEDOT and PPy–Gr–PEDOT. Typical peaks of PPy at 1537 and 1442 cm^{-1} are attributed to symmetric and antisymmetric stretching of the pyrrole ring and stretching vibration of $C–N^{+}$ of the polaronic structure appears at 1279 cm^{-1} [127, 174, 175]. The presence of PEDOT is evidenced by its characteristic peaks at 1544, 1157, 1028 and 966 cm^{-1}. The band between 1138 and 1048 cm^{-1} refers to bending vibrations of C–O–C group. The bands at 972, 832 and 674 cm^{-1} are characteristic of stretching vibrations of C–S–C in the thiophene ring [176]. Characteristic bands of PPy–Gr–PEDOT:PSS and the aforementioned bands are depicted in Figure 4.6e. The vibration band at 1034 cm^{-1} is due to sulfone groups of the PSS, while the peak at 1548 cm^{-1} is typical of thiophene C=C stretching [127].

The second set is prepared by the pyrrole and EDOT copolymerization on the surface of Gr leading to PPy–co–PEDOT–Gr composite. Figure 4.6f shows the corresponding FTIR peaks typical of PPy–co–PEDOT [177]. The structural characterization does not show any difference between mechanical mixing and copolymerization preparation methods.

To evidence the role of the functionalization, set of samples based on FrGO was compared to Gr based ones. FTIR spectra (Figures 4.6g–i) show two peaks at 1573 and 1442 cm^{-1} attributed to the quinoid ring [178], with intensities significantly higher for FrGO composite. This presence of more quinoid units could predict higher electrical conductivity for the FrGO–based composites.

4.3.2 Morphological Characterization

The SEM technique was employed to analyze the morphology of the prepared materials, micrographs are displayed in Figure 4.7a–i. Here is a breakdown of the observed characteristics: Pure PPy (Figure 4.7a) showcases a compact morphology, appearing as dense and rough globules with non–uniform and irregular structures within the grains. The binary composite PPy–Gr (Figure 4.7b) illustrates thick graphene sheets enveloped by PPy. This coverage inhibits the aggregation of graphene sheets, promoting the formation of a homogeneous PPy–Gr composite with a structured appearance [142]. The morphology of PEDOT (Figure 4.7c) presents tightly compacted small particles, stacking atop each other to form a continuous structure.

Moreover, ternary composites PPy–Gr–PEDOT and PPy–co–PEDOT–Gr (Figure 4.7d and e) manifest as assemblies of multiple microparticles with varied sizes and shapes. In PPy–co–PEDOT–Gr, graphene occupies small cavities within the copolymer, resulting in a slightly closed structure that challenges granule differentiation.

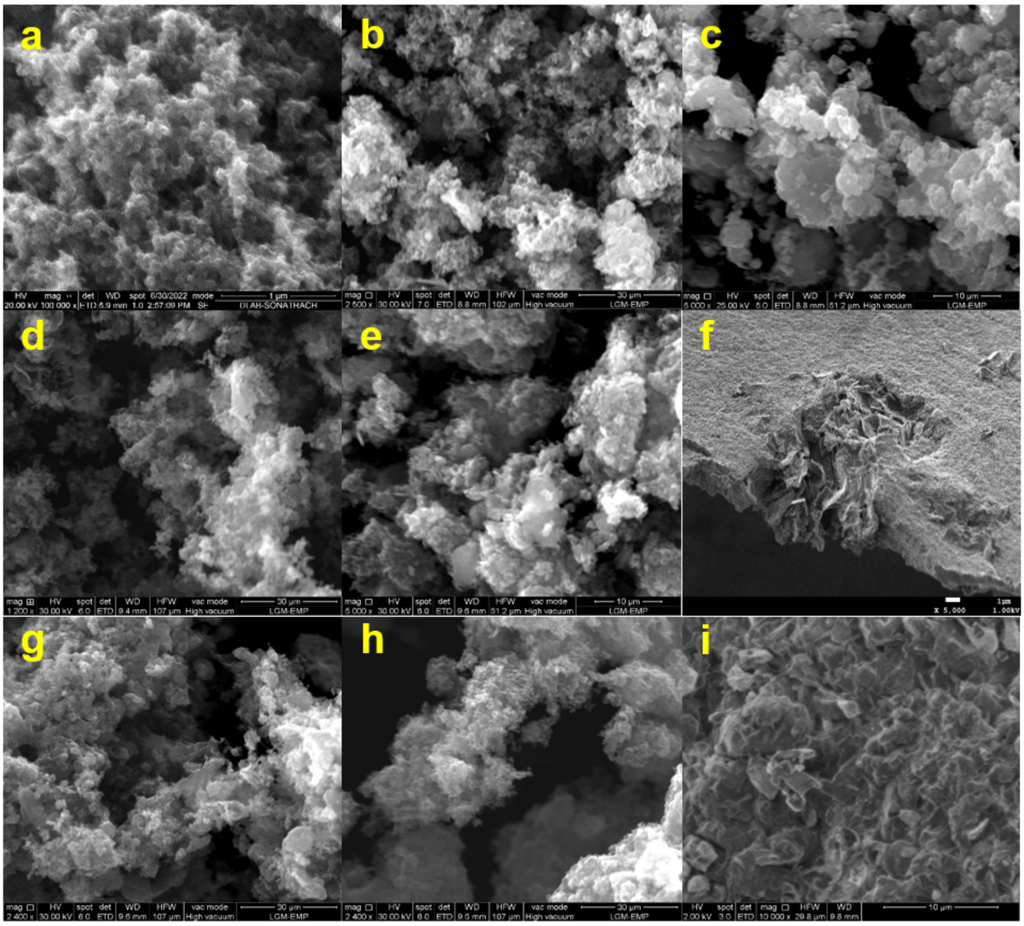

Figure 4.7: SEM micrographs of a) PPy, b) PPy–Gr, c) PEDOT, d) PPy–Gr–PEDOT, e) PPy–co–PEDOT–Gr, f) PPy–FrGO, g) PPy–FrGO–PEDOT, h) PPy– co–PEDOT–FrGO and i) PPy–FrGO–PEDOT:PSS.

The PPy–FrGO structure (Figure 4.7f) exhibits dispersion of small particles surrounded by a solid matrix, a consequence of incorporating FrGO filler into the PPy matrix. In Figure 4.7g, solid particle compaction forms a continuous structure which may contribute to the higher thermoelectric (TE) performance in the PPy–FrGO–PEDOT ternary composite. While PPy–co–PEDOT–FrGO (Figure 4.7h) displays an accumulation of grains with diverse geometries, representing the copolymer structure on the surface of FrGO. The PPy–FrGO–PEDOT:PSS resulted in a compact structure (Figure 4.7i) compared with the previous ternary composites which could be attributed to the presence of PSS.

These diverse morphological features across the different composites highlight the role of filler incorporation, its functionalization and polymer interactions, elucidating their influence on the resulting structure, crucial for achieving specific material properties, especially in the realm of thermoelectric performance.

4.3.3 Thermoelectric Characterization

Thermoelectric characterization involves essential measurements like the Hall effect, electrical conductivity, Seebeck coefficient, power factor, and ZT. These parameters collectively define a material's behavior and efficiency in converting heat into electricity. The Hall effect reveals charge carrier properties under a magnetic field, while conductivity measures the material's electrical flow. Seebeck coefficient relates temperature differences to voltage, crucial for understanding thermoelectric potential. The power factor balances conductivity and Seebeck coefficient, reflecting a material's power generation ability. Ultimately, ZT summarizes a material's thermoelectric efficiency, guiding the development of better energy conversion materials for various applications.

In this section, the materials were coded according to Table 4.1 in order to facilitate the graphical illustration.

Table 4.1: List of code given to each material for sake of clarity.

Pure or composite material	Code	Preparation method
PPy	C1	Chemical polymerization
PPy–Gr	C2	In–situ polymerization
PPy–Gr–PEDOT	C3	Direct mixing
PPy–co–PEDOT–Gr	C4	Copolymerization
PPy–Gr–PEDOT:PSS	C5	Direct mixing
PPy-FrGO–PEDOT	C6	Direct mixing
PPy–co–PEDOT–FrGO	C7	Copolymerization
PPy–FrGO–PEDOT:PSS	C8	Direct mixing

Hall Effect. The Hall effect provides valuable details about the nature, concentration, and mobility of charge carriers. It examines parameters such as charge density in both surface and volume, along with their mobility.

Hall coefficient is defined as $R_H = -\frac{1}{ne}$ if charge carriers are electrons and $R_H = +\frac{1}{pe}$ if charge carriers are holes. Hall mobility which measures how fast the charge carriers move under the influence of an electric field and a magnetic field. It is calculated using the formula: $\mu_H = \frac{\sigma}{ne}$ which is related to the electrical conductivity.

While the Hall effect and thermoelectric effects arise from different physical principles, they both provide important insights into the electronic properties of materials. The parameters characterizing the Hall effect (such as charge carrier density and mobility) may influence the thermoelectric properties, and vice versa. For example, the mobility of charge carriers affects both the Hall coefficient and the electrical conductivity of the material.

Figure 4.8 display the outcomes from measurements of the Hall effect in ternary composites (C3 to C8). The reduced mobility of charge carriers is a consequence of the disorder in the composite's morphology, which is closely linked to the material's structure [179].

A noticeable enhancement in mobility and the Hall coefficient is evident in FrGO–based composites (C6 to C8) compared to those based on Gr. This enhancement can be attributed to the alterations in morphology induced by the presence of FrGO layers. This latter tends to create pathways along which charge carriers, such as electrons, can travel with minimal resistance, contributing to increased mobility. Furthermore, the positive sign of the Hall coefficient confirms the doping type (p), thereby indicating that the charge carriers within the structure are positively charged holes (+).

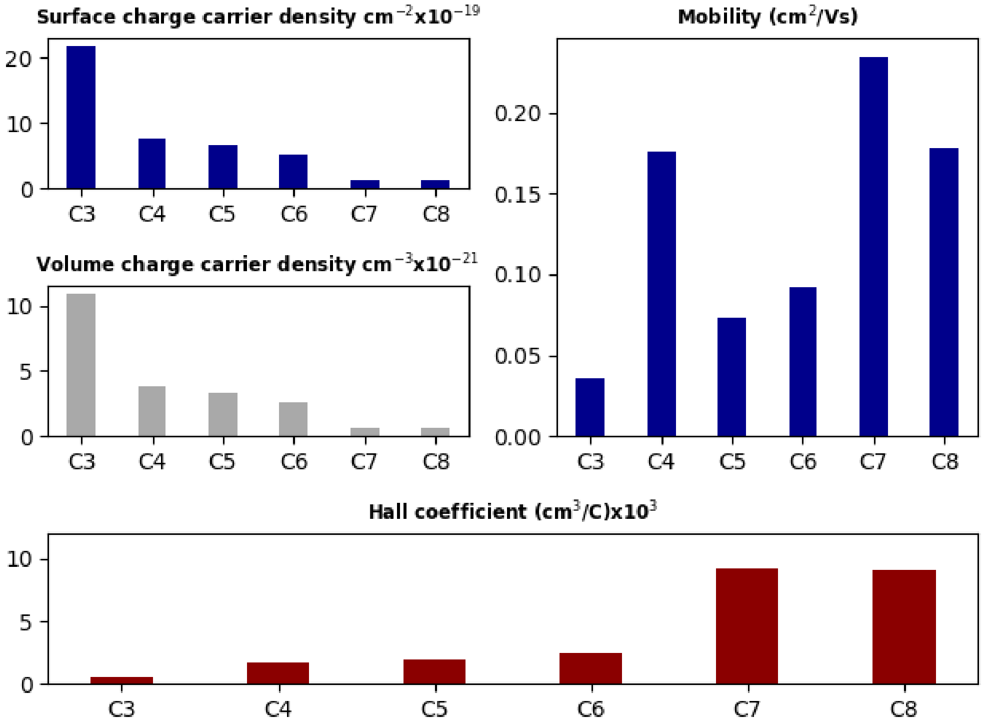

Figure 4.8: Hall effect parameters of PPy–based ternary composites.

Electrical Conductivity. The composites were compressed into pellets to evaluate their electrical conductivity using a four–point system (Appendix A). When pure PPy is in–situ polymerized on the surface of graphene (C2), its electrical conductivity is enhanced by a factor of 2 (16 Scm^{-1}). Notably, superior electrical conductivity is observed in FrGO–based materials compared to their corresponding Gr–based ones across all ternary composites, indicating the significance of the functionalization process.

Moreover, the electrical conductivity is influenced by the presence of either a limited number of highly mobile electrons or numerous electrons with lower mobility. The data presented in Figure 4.8 reveal that the inclusion of FrGO leads to a lower electron density with higher mobility compared to Gr–based materials. This higher mobility accelerates the movement of charge carriers, thereby increasing the electrical conductivity of the composite [180, 181].

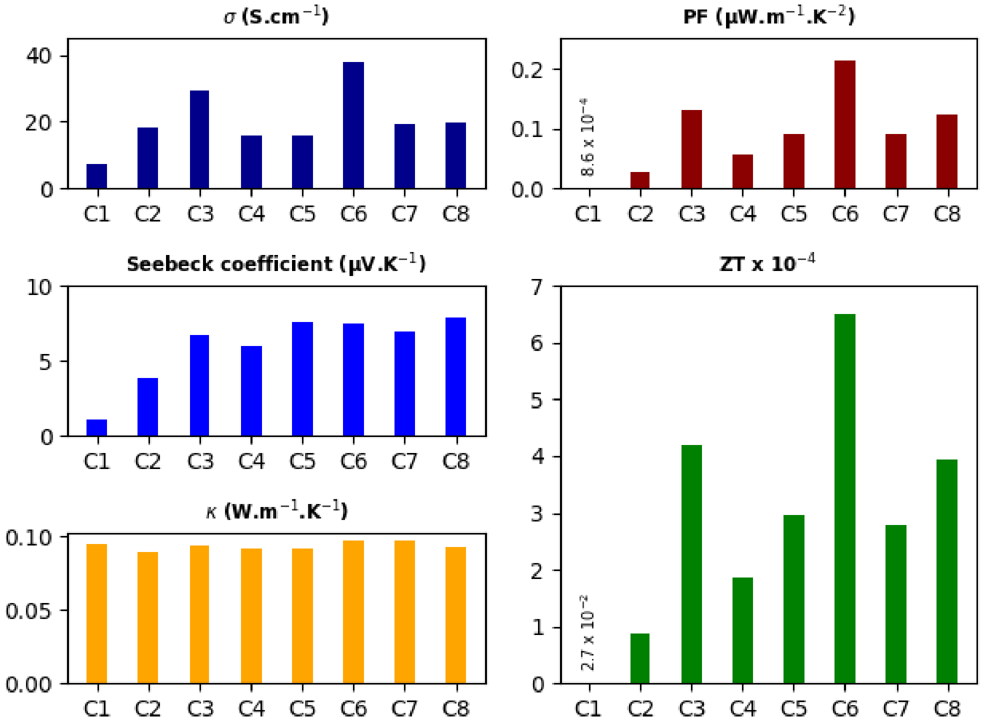

Figure 4.9: TE performance of the pure PPy and the prepared composites.

Introducing PEDOT enhances the electrical conductivity of the ternary composite (C3, C4 and C6, C7). Direct mixing (C3 and C6) appears to be a more promising method than copolymerization (C4 and C7). This is attributed to the effective dispersion of pure PEDOT through direct mixing, as opposed to PPy–co–PEDOT, along with its inherent electrical properties which could attributed to the increase of contact surfaces.

Seebeck Coefficient. The homemade instrument measured the Seebeck coefficient of pure PPy (Appendix B). Figure 4.9 showing a six–fold enhancement in ternary composites, elevating it from 1.34 to 8 μVK^{-1}. Remarkably, the FrGO–based composites exhibited the highest values, highlighting the critical role of functionalization [182]. Functional groups establish covalent bonds with the graphene surface, influencing the local hybridized bonding (from sp^2 to sp^3). This process reduces the charge carrier density (as seen in Figure 4.8) and increases the Seebeck coefficient.

Moreover, the inclusion of PEDOT favors π–π interactions between PPy–Gr and PEDOT, thereby augmenting both electrical conductivity and the Seebeck coefficient [183]. While copolymerized composites also display a commendable Seebeck coefficient, it tends to be lower than those achieved through direct mixing. This discrepancy might arise from fewer interactions and restricted mobility within copolymerized composites.

Thermal Conductivity. The thermal conductivity evaluations were conducted using the Hot Disk 2500S device, and the outcomes are visualized in Figure 4.9. Notably, all ternary composites exhibit low thermal conductivity, closely resembling that of pure PPy. This characteristic proves advantageous for thermoelectric (TE) applications.

Power Factor and Figure of Merit. Figure 4.9 illustrates the power factor (PF) and the figure of merit (ZT) for the various composites. Given the nearly unchanged thermal conductivity, the highest ZT value is attained by the PPy–FrGO–PEDOT ternary composite (6.51×10^{-4}) prepared via the mixing route. This value stands out significantly, being 240 times greater than that of pure PPy (2.71×10^{-6}).

These experiments underline the pivotal role of composite composition, incorporating PPy and PEDOT as conducting polymers alongside functionalized graphene as a filler. Moreover, they emphasize how the chosen preparation method significantly impacts the resulting thermoelectric properties. The intricate interplay between these components and the fabrication process profoundly influences the final characteristics essential for thermoelectric applications.

4.4 Conclusions

In this chapter, the experimental work involved the creation of ternary composites from polypyrrole (PPy) using a combination of mixing and copolymerization methods. These composites aimed to enhance the thermoelectric (TE) properties of PPy by incorporating various fillers such as graphene (Gr), functionalized graphene oxide (FrGO) or reinforcing the PPy matrix with other conducting polymers such as poly(3,4–ethylenedioxythiophene) (PEDOT), and PEDOT:PSS.

To evaluate the characteristics of these ternary composites, multiple analytical techniques were employed. Scanning electron microscopy (SEM) provided detailed images for visual inspection, allowing the examination of the surface morphology and structural features. Raman spectroscopy was employed to investigate the specific structures of graphene derivatives (Gr, GO, rGO, FrGO) and the successful synthesis of 4–carboxybenzenediazonium tetrafluoroborate (DS–COOH). Additionally, Fourier transform infrared (FTIR) spectroscopy was utilized to analyze the chemical composition and bonding within the composites.

Among the synthesized composites, the PPy–FrGO–PEDOT composite produced through the mixing method exhibited the highest figure of merit (ZT) value. Remarkably, this value was 240 times greater than that of the pristine PPy. This substantial improvement underscores the critical role played by functionalizing graphene oxide with diazonium salts. This functionalization process significantly enhanced the adhesion and distribution of the polymer atop the graphene oxide surface.

Consequently, it promoted better charge mobility, thereby elevating the overall conductivity of the composite and subsequently boosting its thermoelectric properties.

The achievement in synthesizing and characterizing these ternary composites opens up exciting possibilities for advancing materials with enhanced thermoelectric properties. These advancements may pave the way for exploring the impact of various functional groups on Multi–Walled Carbon Nanotubes (MWCNTs) alongside with PPy, shedding light on their collective effect on thermoelectric properties. This forthcoming chapter delves into a detailed study focused on understanding how different functional groups attached to MWCNTs influence the thermoelectric performance of the PPy–MWCNT nanocomposite.

Chapter 5

Surface Functionalization of MWCNTs Impact on Thermoelectric Power Factor in PPy–MWCNTs Nanocomposites: A Comparative Analysis

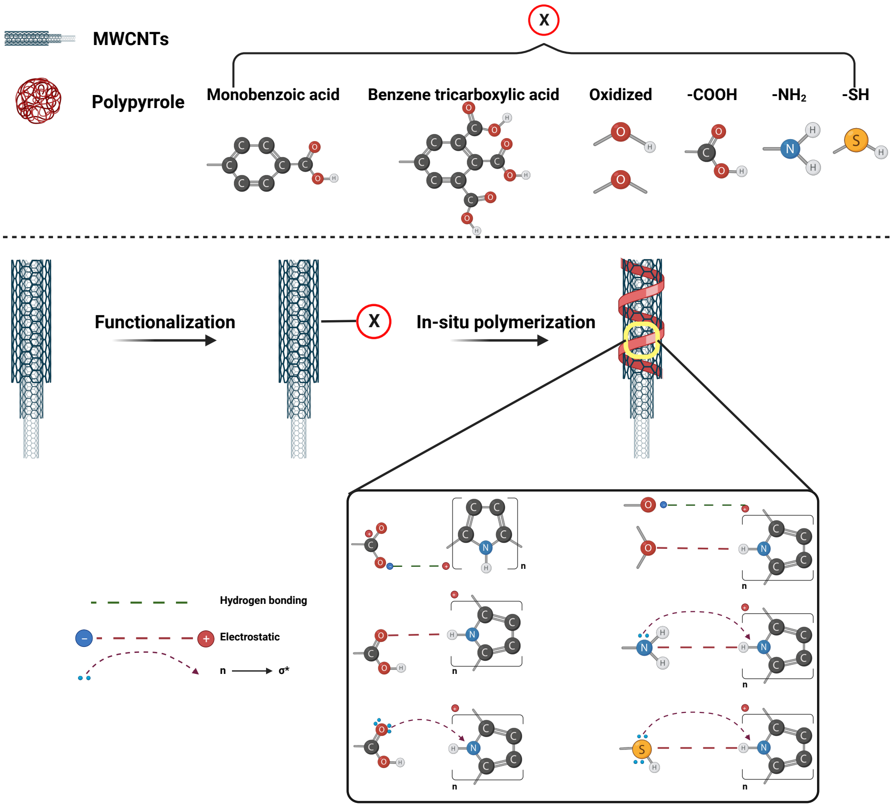

5.1 General Introduction

As the exploration into enhancing the thermoelectric properties within PPy–based composites draws to a close, significant insights emerge from the previous chapter. This chapter highlighted the profound impact of treating graphene oxide with diazonium salts, shedding light on the conductivity and thermoelectric behavior of these composites. Through meticulous exploration of preparation methods and surface modifications in ternary composites, promising pathways toward optimizing thermoelectric efficiencies have been unveiled.

Building upon these foundational insights, the subsequent chapter delves deeper into another critical aspect shaping the thermoelectric properties of PPy–based materials: the nature of surface functionalization groups in MWCNTs. Transitioning from the profound impact of graphene oxide modification, this chapter aims to elucidate the intricate interplay between various functionalization groups within MWCNTs and their consequential effects on the thermoelectric power factor of PPy–MWCNTs nanocomposites.

In this pursuit, the focus extends beyond graphene derivatives to examine the nuanced influence of distinct functionalization groups within MWCNTs on the thermoelectric behavior of resulting nanocomposites. Through meticulous analysis, this chapter role of surface functionalization of MWCNTs in augmenting the thermoelectric performance of PPy–based nanocomposites. By combining experimental exploration with insightful analyses, this chapter aims to establish a comprehensive understanding of how different surface functionalization groups within MWCNTs impact the thermoelectric power factor. The shift in focus from graphene oxide surface treatment to the intricate interplay of MWCNTs' functionalization groups signifies an evolutionary step in understanding and leveraging surface modifications to optimize thermoelectric efficiencies within PPy–based materials.

Thus, this field of research [184] aims to establish a coherent progression from the basic insights into changing graphene oxide to the intricate examination of MWCNTs' surface functionalization. Together, these investigations advance the quest for tailored thermoelectric materials crucial for sustainable energy applications.

5.1.1 Publications

The content of this chapter is based on the following peer–reviewed scientific publication "Reproduced with permission from Elsevier":
Younes Bourenane Cherif, Zineb Mekhalif, Ahmed Mekki, and Zakaria Bekkar Djelloul Sayah. Effect of MWCNTs surface functionalization group nature on the thermoelectric power factor of PPy/MWCNTs nanocomposites. **Synthetic Metals**, 291:117196, December 2022. ISSN 0379-6779. doi: 10.1016/j.synthmet.2022.117196. URL https://www.sciencedirect.com/science/article/pii/S0379677922001904

This research investigates the influence of distinct functional groups (benzoic acid, benzene tricarboxylic acid, hydroxyl, carboxyl, amino, and thiol) grafted into multi–walled carbon nanotubes (MWCNTs) on enhancing the thermoelectric properties of PPy–MWCNTs nanocomposites. Initially, the MWCNTs were either functionalized or remained unaltered. Subsequently, an in–situ oxidative polymerization of pyrrole occurred on the functionalized MWCNTs to wrap them with polypyrrole. The findings suggest that the functionalization process reduces electrical conductivity, depending on the nature and density of the functional groups. Moreover, it increases the Seebeck coefficient compared to PPy and PPy–purified–MWCNTs nanocomposites. Notably, among the various chemical functionalities explored, PPy–MWCNTs–SH exhibits the most promising outcomes, showcasing the highest power factor (0.51 $\mu Wm^{-1}K^{-2}$), marking an eightfold enhancement compared to pure PPy (0.064 $\mu Wm^{-1}K^{-2}$).

5.1.2 Outline

This chapter is structured as follows: Section 5.2 presents a detailed explanation of the methodology and synthesis techniques employed. In Section 5.3, the results derived from various characterizations are examined and discussed. Finally, Section 5.4 encapsulates the chapter by presenting a summary of its principal contributions.

5.2 Methodology

5.2.1 Materials

For crude MWCNTs purification, the thin MWCNTs (NC 7000, 0.1 – 10 µm, Ø10 nm, > 95%) is purchased from Nanocyl SA, Belgium and NaOH (> 98%) is purchased from Acros Organics. Functionalization process requires sodium nitrite ($NaNO_2$, 99.2%), 4–aminobenzoic acid (≥ 99%), 5–amino–1,2,3–benzene tricarboxylic acid (97%) which were purchased from Fisher Scientific UK as well as the perchloric acid ($HClO_4$, 70%) from Aldrich. Pentane (99%) and acetone (> 99%) are used for the washing process and are obtained from Chem–Lab. Already functionalized MWCNTs are received from Nanocyl SA, Belgium (MWCNTs–COOH, MWCNTs–NH_2 and MWCNTs–SH). For nanocomposites synthesis; pyrrole, sodium dodecylbenzene sulfonate (SDBS), ethanol and iron chloride ($FeCl_3$) are purchased from Sigma–Aldrich, Germany. All chemicals are of analytical grade or higher purity.

5.2.2 Fillers Preparation

Purification process. Prior to use crude MWCNTs, they were first purified using basic treatment in order to not alter their structure and chemical composition [185, 186]. MWCNTs were mixed with 500 ml of 12 M NaOH solution in a round–bottomed flask, Figure 5.1. The mixture was then refluxed under constant stirring at 170 °C for 12 h. The final product was washed with DI until pH ~7, dried at 60 °C and denoted as p–MWCNTs.

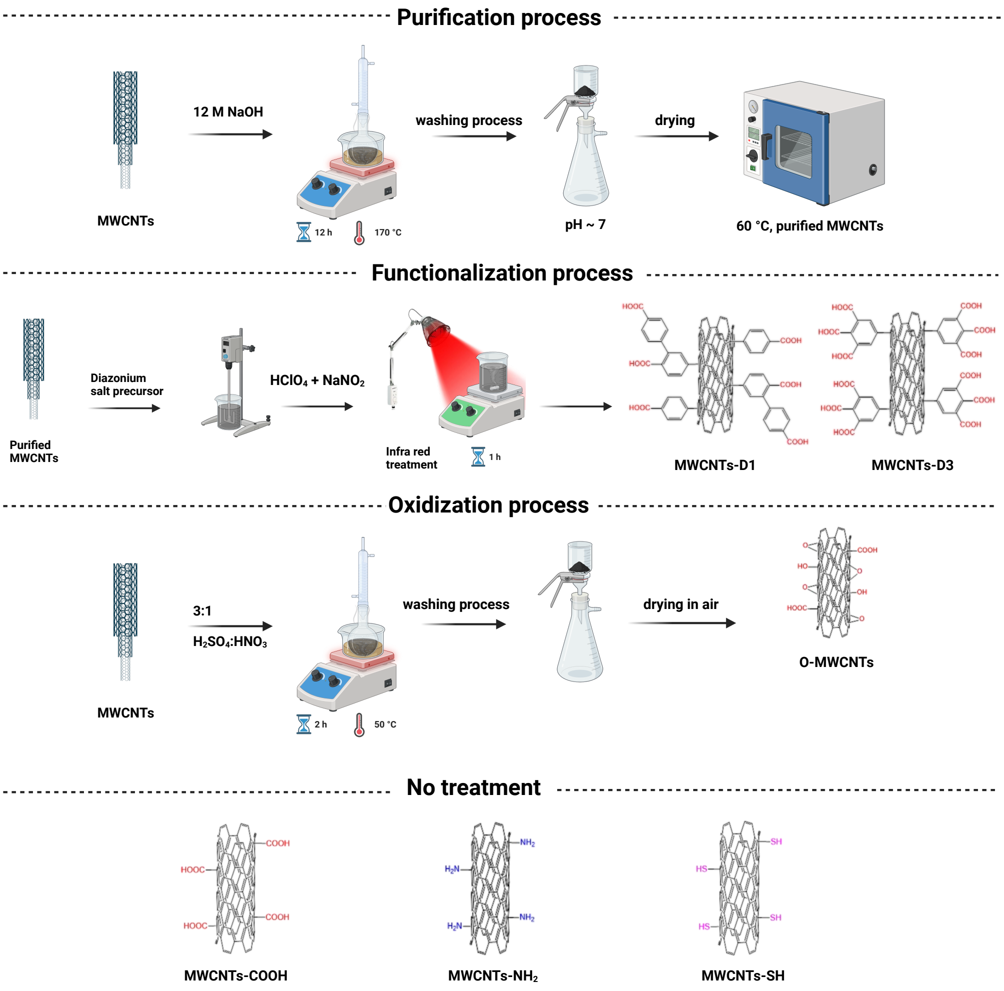

Figure 5.1: Experimental protocol of fillers preparation.

Functionalization process. Following the purification, post–treatment of p–MWCNTs involving diazonium salt was accomplished according to previous work [185], Figure 5.1. p–MWCNTs were mixed with a solution of diazonium salt precursor (4–aminobenzoic acid or 5–amino–1,2,3–benzene tricarboxylic acid) and put under sonication. Subsequently, perchloric acid and sodium nitrite were added under stirring. The above mixture was after infrared irradiated for 1 h to favor the grafting process as carbonaceous materials can absorb these latter which result in electronic excitations [187]. Finally, the washing process was carried out using both pentane and acetone and left drying at room temperature. Both products monocarboxylic and tricarboxylic aryl functionalized MWCNTs were denoted as MWCNTs–D1 and MWCNTs–D3, respectively.

Oxidization process. Separately, MWCNTs were dispersed in a mixture of 3:1 of H_2SO_4 and HNO_3 and refluxed at 50 °C for 2 h [188, 189]. The suspension was left to cool down at room temperature and then diluted with DI, filtered and washed, then left to dry in air. This latter was referred as O–MWCNTs.

Not treated. Additionally, other functionalized MWCNTs were used in this study as received. Herein, MWCNTs–COOH, MWCNTs–NH_2 and MWCNTs–SH (Figure 5.1).

5.2.3 Nanocomposites Preparation

Binary nanocomposites (PPy–MWCNTs) were prepared as illustrated in Figure 5.2. Initially, SDBS (dopant) was dissolved in absolute ethanol and subsequently diluted with DI. Purified or functionalized MWCNTs were dispersed in the prepared mixture and stirred.

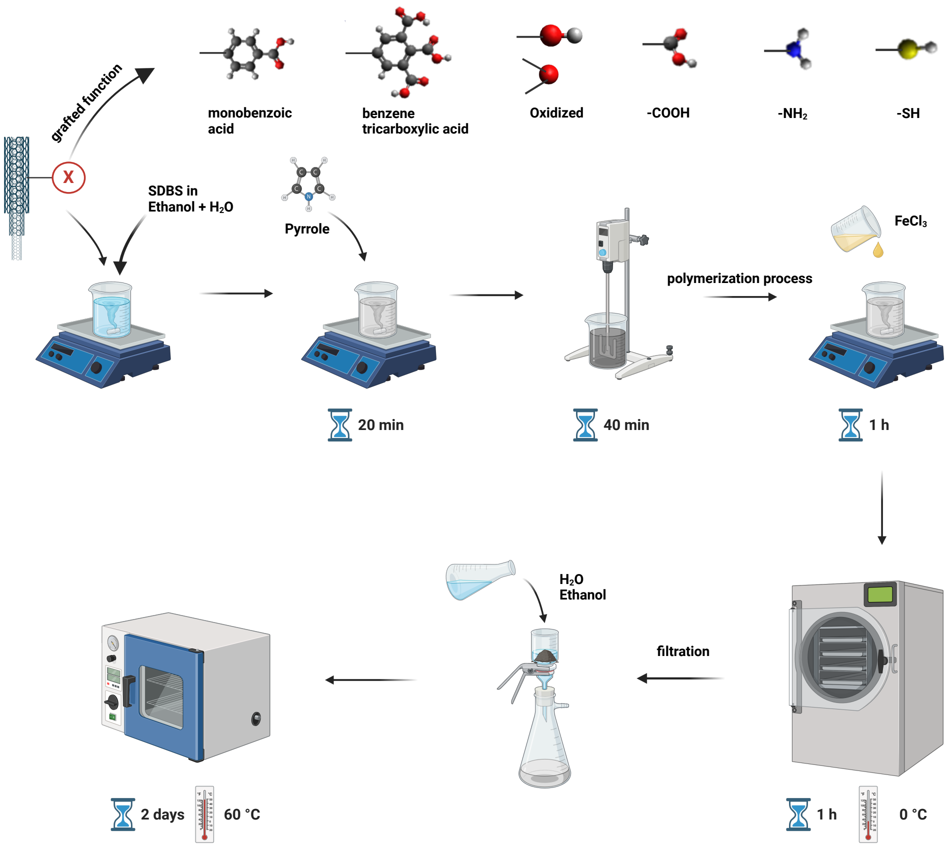

Figure 5.2: Experimental setup for preparation of nanocomposites.

Pyrrole was then added and left under magnetic stirring for 20 min. A crucial 40 min sonication process was followed to ensure the dispersion of MWCNTs and pyrrole monomer, after which $FeCl_3$ (oxidant) was added to initiate the polymerization process which continued for 1 h. The resulting suspension was stored at 0 °C for 1 h, washed with DI and ethanol, filtered and dried at 60 °C for 2 days [139, 190]. Pure PPy was synthesized following the same protocol but without the addition of MWCNTs.

5.3 Results and Discussion

5.3.1 Structural Characterization

Raman spectroscopy and Fourier–transform infrared (FTIR) techniques were employed to analyze the structural characteristics of the synthesized materials. To provide an insight into the structure of MWCNTs and the resulted binary nanocomposites, Raman technique was used. Figure 5.3a shows the Raman spectra of crude, purified and functionalized MWCNTs. All samples exhibit three distinctive peaks: D, G and 2D. The D band, appearing at 1347 cm^{-1}, is attributed to sp^3 hybridized carbon and structural defects.

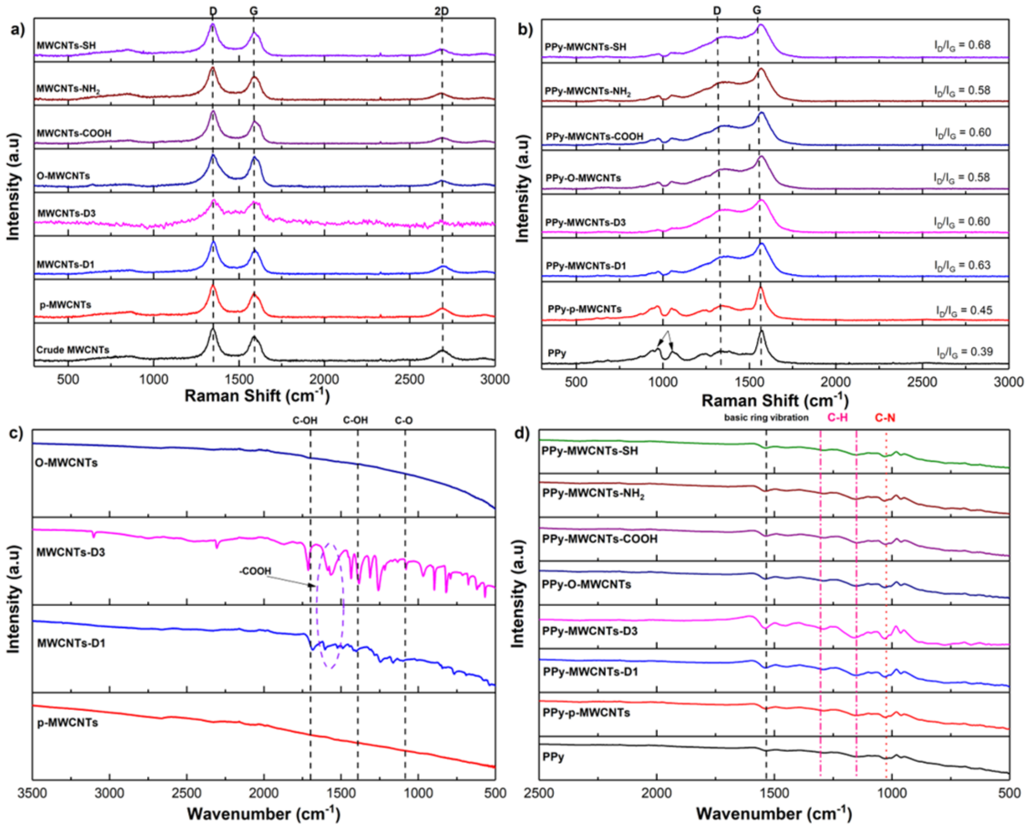

Figure 5.3: Raman and FTIR spectra.

Whereas the G band which occurs at 1588 cm^{-1} represents the vibration of sp^2 carbon atoms and the 2D band, observed at 2688 cm^{-1}, appears broadened due to the presence of multiple layers within the nanotube structure [191, 192].

The preservation of the D and G bands following functionalization suggests that the graphitic structure of carbon nanotubes remained intact, as there were no shifts observed in these peaks after the functionalization process. Previous studies [193–195] demonstrated that an increase in the D band intensity indicates the shift from sp^2 to sp^3 hybridization on the sidewalls due to covalent bonding of various functional groups. Table 5.1 displays the D to G band intensity ratio showing notable alterations that indicate disruptions in the electron delocalization along the nanotubes. These changes serve as evidence of different degrees of functionalization in the MWCNTs [191, 196]. The reduction in I_D/I_G post–purification indicates an improvement in the quality of MWCNTs, likely achieved by removing carbonaceous impurities and metallic catalysts like alumina. This supports the efficacy of the purification process. On the other hand, the alteration of I_D/I_G due to functionalization demonstrates changes depending on the degree of functionalization, revealing that the process maintains the overall integrity of MWCNTs.

Table 5.1: I_D/I_G ratio of different MWCNTs.

Material	**Crude MWCNTs**	**p–MWCNTs**	**MWCNTs –D1**	**MWCNTs –D3**	**O–MWCNTs**	**MWCNTs –COOH**	**MWCNTs –NH_2**	**MWCNTs –SH**
I_D/I_G	1.37	1.21	1.45	1.08	1.10	1.40	1.42	1.47

Figure 5.3b displays the Raman structural characteristics of both pure PPy and binary nanocomposites. Two prominent broad bands were identified at 1564 and 1337 cm^{-1}, attributed to MWCNTs (presence of D and G bands) and the vibration modes of C–C and C=C within the PPy backbone ring [197]. The existence of bipolaronic and polaronic structures in the synthesized PPy was evidenced by the observed two weak peaks at 910 and 1080 cm^{-1} [197, 198]. Furthermore, a slight shift towards higher wavenumbers of the two band D and G is probably due the role of functional groups on MWCNTs as a dopant to the PPy backbone and the π–π interaction between the PPy and MWCNTs [199]. Lower ratio values for all nanocomposites are observed compared to functionalized MWCNTs; this may be due to the uniform coating of the surface of MWCNTs with PPy chains, which results in a minor concentration of defects on the MWCNTs surface [200].

FTIR analysis was extended to investigate the structural properties of chemically modified MWCNTs, pure PPy, and their resulting nanocomposites. In Figure 5.3c, distinct characteristic bands corresponding to polar functional groups post–functionalization (MWCNTs–D1, MWCNTs–D3, and O–MWCNTs) are depicted. The spectra reveal intense bands related to COOH groups, distinctive of carboxyl functional groups, on the surfaces of MWCNTs–D1 and MWCNTs–D3 at 1730, 1380, and 1100 cm^{-1} [201, 202], along with bands of notably lower intensity on O–MWCNTs indicative of C–OH and C–O functionalities.

Additionally, the intense band at 1500 – 1600 cm^{-1} range is typical of benzene ring vibrations present in MWCNTs–D1 and MWCNTs–D3 [203].

Pure PPy and the binary nanocomposites were also investigated using FTIR spectroscopy. Figure 5.3d show the characteristic peaks of PPy and MWCNTs. The fundamental ring vibration of PPy occurs at 1546 cm^{-1}, while vibrations associated with C–H plane, C–N stretching occur at 1310, 1045 cm^{-1} and 1184 cm^{-1}, respectively. Observable changes in peak intensities, notably in PPy–MWCNTs–D1 and PPy–MWCNTs–D3, along with a slight shift towards higher wavenumbers, suggest interaction between NH groups in the PPy backbone and surface groups of modified MWCNTs, in addition, the noncovalent π–π bonds between these latter [204, 205].

Furthermore, research has established a correlation between the length of conjugation in PPy chains and the ratio of intensities observed in the two bands at 1546 and 1452 cm^{-1} in FTIR spectra [206]. As the conjugation length changes, it affects the relative intensities of these bands, allowing for inference about the polymer's structural properties via FTIR analysis. Variations in intensity indicate varied conjugation lengths among different samples. This relationship strongly influences the material's electrical conductivity since longer PPy chains tend to demonstrate enhanced electrical conductivity.

5.3.2 Morphological Characterization

The TEM technique was utilized to examine the morphology structure of the functionalized MWCNTs and the prepared binary nanocomposites. The obtained images are depicted in Figure 5.4.

The analysis of the crude MWCNTs' surface treatment, from purification to aryl diazonium functionalization, revealed that the MWCNTs remained undamaged, indicating the efficacy of the purification and functionalization techniques. However, the surface of MWCNTs treated solely with oxidation (O–MWCNTs) showed a slight alteration compared to those treated with aryl diazonium [189].

Considering the synthesis conditions involving the oxidation of pyrrole using $FeCl_3$ and doping with SDBS in a mixture of water and ethanol as a co–solvent, the resulting PPy particles exhibit a spherical shape [207], as depicted in Figure 5.4. Their average diameter, estimated using Image J software, measures around 68 nm.

The morphological analysis of all nanocomposites indicates complete coverage of MWCNTs by PPy nanoparticles, as marked by arrows in the images of PPy–MWCNTs–D1 and PPy–MWCNTs–D3. A distinct and uniform coating is evident, although the presence of functionalized MWCNTs affects the growth of PPy on their sidewalls, resulting in varying thicknesses.

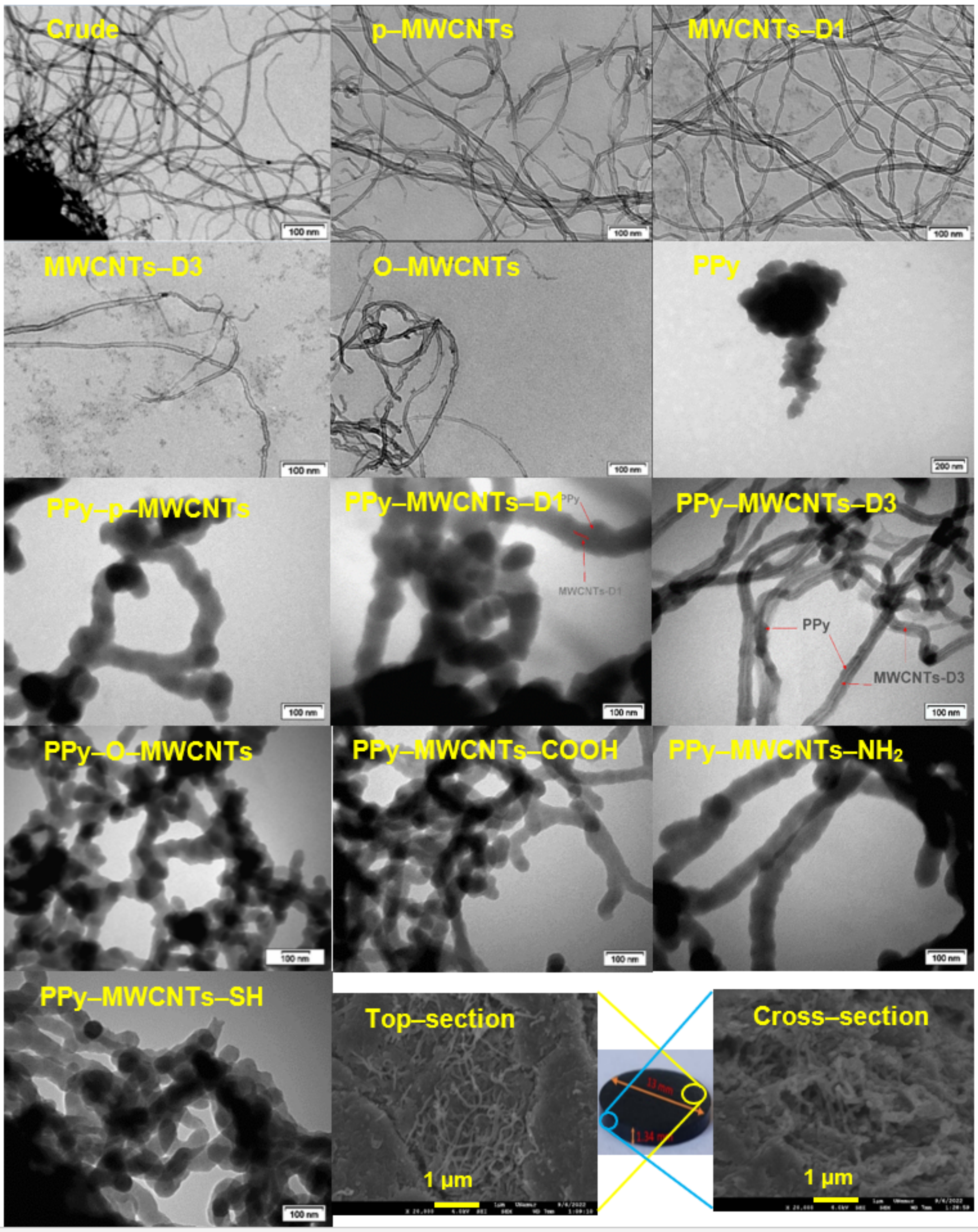

Figure 5.4: TEM images of surface treated MWCNTs, pure PPy, PPy–MWCNTs nanocomposites and SEM top– and cross–sections of a PPy–MWCNTs–SH pressed pellet.

Utilizing Image J software, the thickness of each nanocomposite layer was measured, revealing discrepancies in diameters compared to MWCNTs (~10 nm), PPy–p–MWCNTs (~60 nm), PPy–MWCNTs–D1 (~74 nm), PPy–MWCNTs–D3 (~33 nm), PPy–O–MWCNTs (~53 nm), PPy–MWCNTs–COOH (~38 nm), PPy–MWCNTs–NH_2 (~66 nm), and PPy–MWCNTs–SH (~30 nm).

These variations can be attributed to several factors: the formation of monolayers, notably evident in PPy–MWCNTs–D1 and PPy–MWCNTs–D3, wherein MWCNTs–D3 only can develop a single aryl layer while MWCNTs–D1 can evolve multiple layers; the nature and concentration of functional groups along the MWCNTs' surface impacting the interfacial interactions (such as hydrogen bonding, electrostatic forces and π–π stacking) between PPy and the functionalized MWCNTs [19]. These interactions prove pivotal in binding PPy to MWCNTs, facilitating uniform coatings. This simple and fast process highlights the effectiveness of in–situ polymerization of PPy on functionalized MWCNTs.

SEM images of the top and cross–section view clearly show dense pellet and a random distribution of a 1D nanocomposite structure. This random orientation demonstrates no preferential orientation along or vertical to the length of PPy–MWCNTs nanocomposite which validates the isotropy of the pellets.

5.3.3 Thermogravimetric Characterization

In order to confirm the grafting rate of different functions on the surface of MWCNTs, thermal gravimetric analysis (TGA) is performed. The weight loss was studied as a function of temperature, Figure 5.5.

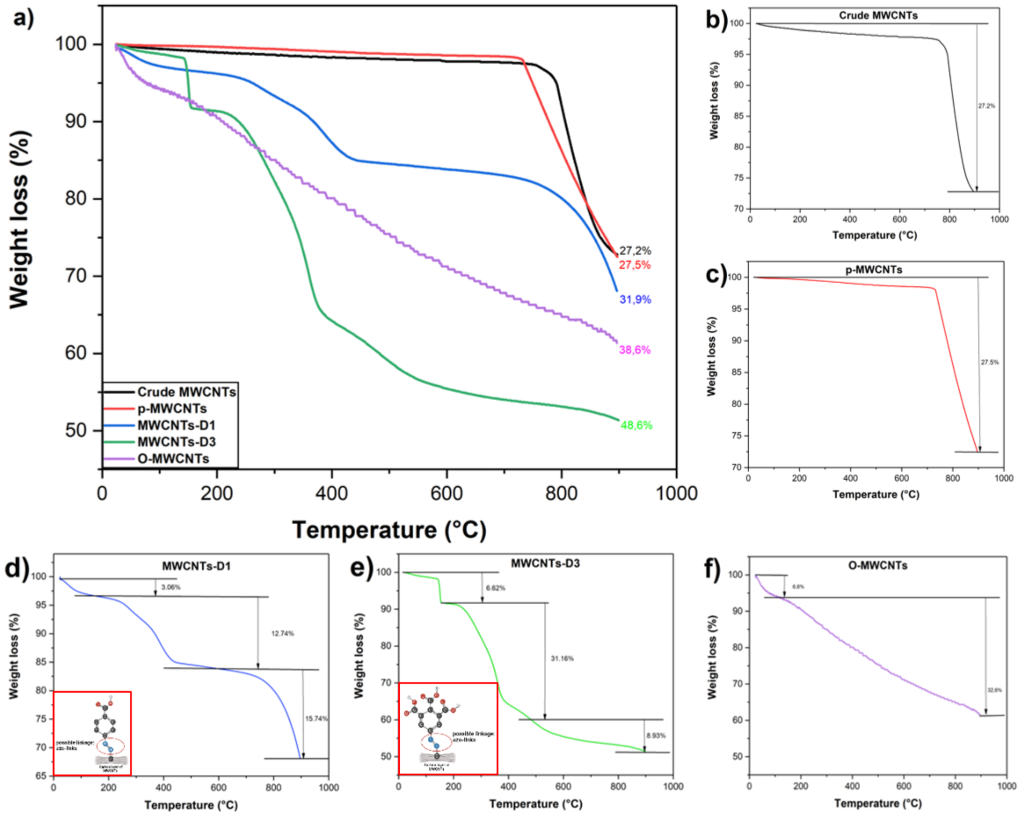

Figure 5.5: TGA curves of the chemically treated MWCNTs.

The samples were exposed to a temperature range 25 – 900 °C with a 10 °C/min rate under N_2 gas. Crude MWCNTs showed a final weight loss of 27.2%, while the purified MWCNTs exhibited a slightly higher weight loss of 27.5% due to the purification process likely removed some impurities present in the crude MWCNTs leading to a slightly higher weight loss. Both of them (Figures 5.5b and 5.5c) exhibit one step weight loss.

However, aryl diazonium functionalized MWCNTs (Figure 5.5d and 5.5e) show 3 steps weight loss. An initial decomposition which starts at 180 °C is due to moisture loss, followed by another decomposition below 400 °C associated with benzene mono– and tricarboxylic acid groups where the weight loss in MWCNTs–D3 is 31.16% (Figure 5.5e) which is approximately 3 time of MWCNTs–D1 (12.74%, Figure 5.5d) [208]. The final weight loss at 500 °C is attributed to the start of the degradation of the graphitic structure of MWCNTs.

O–MWCNTs (Figure 5.5f) start decomposing before 200 °C and continue until total decomposition which can be attributed to the presence of functional groups from oxidization process.

The grafting percentage (GP) of the chemically treated MWCNTs was determined using the Equation 5.1. Regarding the as received MWCNTs–COOH, MWCNTs–NH_2 and MWCNTs–SH the GP was given > 8%.

$$GP = (\Delta W_{\text{Functionalized MWCNTs}} - \Delta W_{\text{Crude MWCNTs}}) \times 100\% \tag{5.1}$$

$\Delta W_{\text{Functionalized MWCNTs}}$ and $\Delta W_{\text{Crude MWCNTs}}$ are the percentage of weight loss of chemically treated MWCNTs and crude MWCNTs, respectively.
It follows from the above equation, the percentage of functions on MWCNTs–D1 is about 4.7%, MWCNTs–D3 is about 21.4% and on O–MWCNTs is about 11.4%.

5.3.4 Thermoelectric Characterization

In this section, the materials were coded according to Table 5.2 in order to facilitate the graphical illustration which presents the codes to each material or composite material.

Table 5.2: List of code given to each material for sake of clarity.

Pure or composite material	**Code**
PPy	C1
PPy–p–MWCNTs	C2
PPy–MWCNTs–D1	C3
PPy–MWCNTs–D3	C4
PPy–O–MWCNTs	C5
PPy-MWCNTs–COOH	C6
PPy–MWCNTs–NH_2	C7
PPy–MWCNTs–SH	C8

Electrical Conductivity. The electrical conductivity of PPy is around 973 Sm^{-1} (Figure 5.6). MWCNTs' electrical conductivity is strongly dependent on their purification and functionalization nature and degree. The purification enhances the MWCNTs electrical conductivity from 455 Sm^{-1} to 833 Sm^{-1} which is in agreement with the values reported in previous research [189], however it is lower compared to other studies [209], this may be dependent on the MWCNTs supplier and the procedure by which they were synthesized.

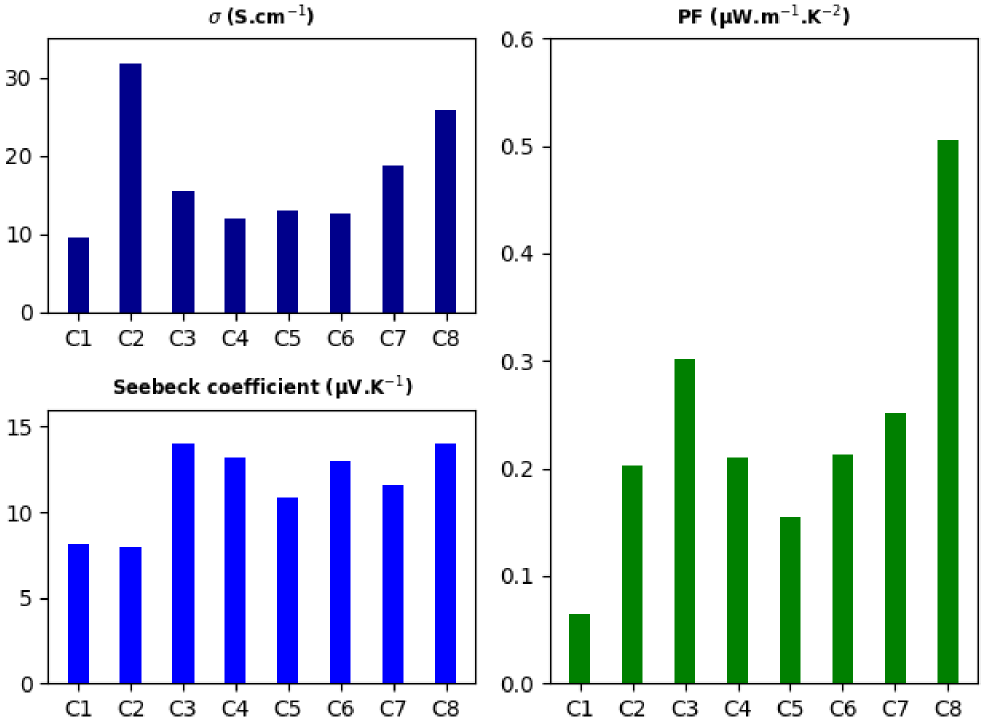

Figure 5.6: Thermoelectric properties of the synthesized materials.

The electrical conductivity of PPy–MWCNTs relies on both the conjugation degree of PPy and the presence of MWCNTs. When PPy coats the MWCNTs, it creates a nanocomposite (C2) with significantly enhanced electrical conductivity (3171.7 Sm^{-1}) compared to their individual components. However, the inclusion of functional groups reduces the mobility of charge carriers, diminishing the conductivity compared to C2 (Figure 5.6).

As a result, nanocomposites with fewer charge carriers but higher concentrations of functional groups on MWCNT surfaces exhibit reduced conductivity. Additionally, the introduction of functional groups leads to sp^2–sp^3 carbon hybridization, which depends on the degree of MWCNT functionalization, creating defects that increase resistance [210]. Furthermore, conductivity within the PPy arises from both intramolecular conjugation and intermolecular contributions due to π–π stacking between PPy chains and MWCNTs.

However, TE performance does not depend merely on electrical conductivity. As far as semiconductor materials are concerned, conductivity depends on the efficiency of charge transfer within the material; in this case, it depends on electrons in the π orbital, which can pass to the conductive bands and leave holes in the valence band [211].

Seebeck Coefficient. As the functionalization of MWCNTs decreases the electrical conductivity; it increases slightly the Seebeck coefficient. The highest values (14 μVK^{-1}) are obtained for C3 (PPy–MWCNTs–D1) and C8 (PPy–MWCNTs–SH) as a consequence of the high density of –COOH and –SH functions at the MWCNTs surface shown in Raman spectra by the highest intensity ratio (I_D/I_G).

The grafting method (–COOH linked directly to the nanotubes by oxidation or via the aryl group) makes a difference in TE properties (electrical conductivity and Seebeck coefficient). Aryldiazonium functionalization provides more functions at the surface (S of C3 is higher than C6). It also allows the control of the –COOH densities (C3/C4) and the thickness of the aryl layer (monolayer or multilayers).

As shown in Figure 5.6, the Seebeck coefficient exhibits different values strongly related to the MWCNTs functional groups in the nanocomposites. S values follow the following order, C8≃C3>C4>C6>C7>C5>C2. It is also related to their density, and the interactions between the PPy chains and MWCNTs.

Power Factor. The PF values of the prepared nanocomposites are shown in Figure 5.6. As PF is the square of S multiplied by σ, the PPy–MWCNTs–SH (C8) has the highest value among all nanocomposites. Therefore, the classification of TE properties has to be done considering both σ and S.

Figure 5.7 is a schematic presentation of the possible molecular interactions between the MWCNTs surface and the PPy positively charged backbone due to the oxidative polymerization.

Although not covalent, these interfacial interactions are sufficiently strong to keep PPy anchored to the MWCNTs via the functions layer. We can distinguish electron acceptor groups in PPy–MWCNTs–D1, PPy–MWCNTs–D3, PPy–O–MWCNTs, and PPy–MWCNTs–COOH, the nitrogen–containing electron–donor groups in PPy–MWCNTs–NH_2, and sulfur–containing electron–donor groups in PPy–MWCNTs–SH. These interactions enhance the Seebeck coefficient and mobility of charges providing PPy–MWCNTs–SH with the more significant power factor of 0.51 $\mu Wm^{-1}K^{-2}$ which is 8 times superior to pure PPy.

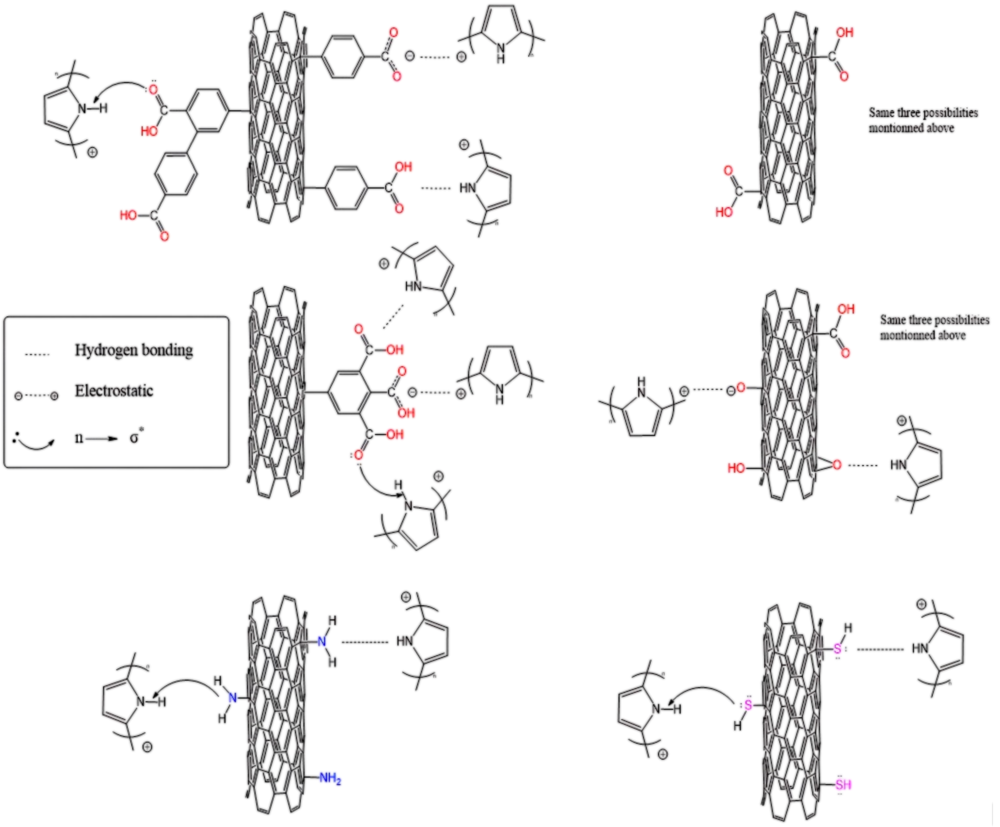

Figure 5.7: Possible molecular interactions between polypyrrole backbone and different MWCNTs.

5.4 Conclusions

The investigation of various functional groups on MWCNTs has revealed their impact on enhancing the thermoelectric (TE) properties of PPy–MWCNTs nanocomposites. These functionalized MWCNTs exhibit a nuanced influence, reducing electrical conductivity based on the nature (electron donor/acceptor) and density of functional groups while concurrently elevating the Seebeck coefficient compared to PPy–p–MWCNTs composites. Notably, both purified and functionalized MWCNTs demonstrate an enhancement in TE performance relative to pure PPy, with PPy–MWCNTs–SH emerging as the most promising function, displaying the highest power factor.

The exploration of functionalized MWCNTs' influence prompts the investigation of a new avenue: the grafting of metal oxides onto the surface of these modified graphitic materials to serve as fillers within the PPy matrix. These upcoming chapters delve into the strategic incorporation of metal oxides onto the surface of functionalized GNPs and MWCNTs, exploring their potential for further optimizing TE properties through controlled density and improved grafting methodologies, aiming to regulate electrical conductivity and enhance overall TE performance.

Chapter 6

Investigation of the Effect of Decorated Multi–Walled Carbon Nanotubes and Graphene Nanoplatelets by Bismuth Oxide Nanoparticles on the Thermoelectric Power Factor of PPy–based Nanocomposites

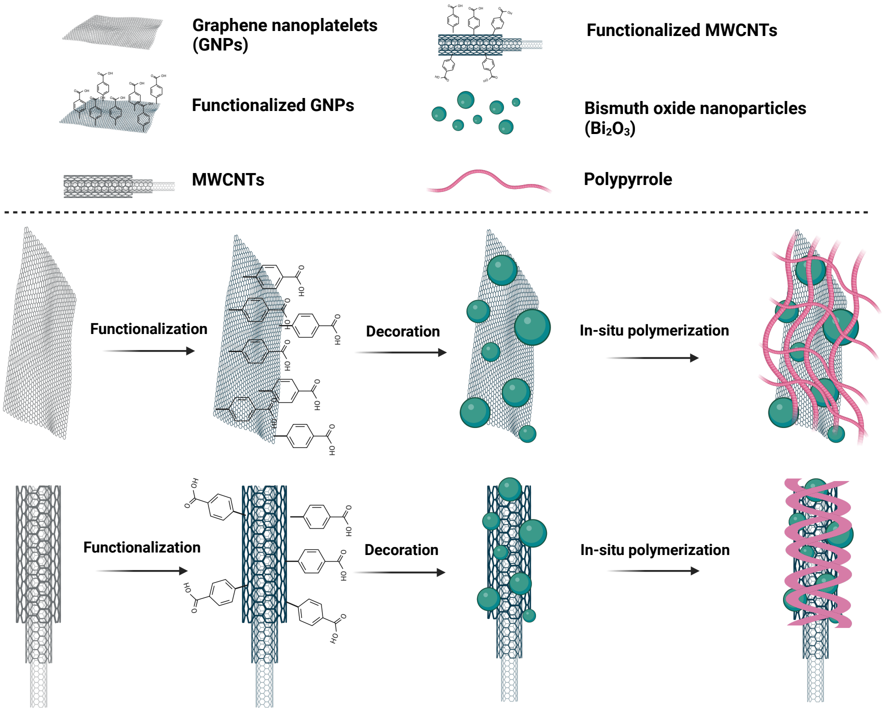

6.1 General Introduction

Continuing our pursuit to enhance the thermoelectric properties of composite materials; the preceding chapter investigated the influence of various functionalized MWCNTs on the thermoelectric characteristics of PPy–based nanocomposites. The investigation of various functional groups on MWCNTs has revealed their impact on enhancing the thermoelectric (TE) properties of PPy–MWCNTs nanocomposites. Both purified and functionalized MWCNTs demonstrate an enhancement in TE performance relative to pure PPy, with PPy–MWCNTs–SH as the most promising function, displaying the highest power factor.

Expanding upon these insights, this chapter explores a new trajectory in composite design. Our focus pivots towards GNPs–Bi_2O_3–based PPy [212] and MWCNTs–Bi_2O_3–based PPy nanocomposites [213], a kind of fusion of organic and inorganic constituents, to open new avenues for enhanced thermoelectric performance. Starting from conventional methodologies where metal oxide nanoparticles are incorporated ex–situ, our new approach explores the in–situ generation of Bi_2O_3 nanocrystals anchored onto functionalized GNPs and MWCNTs surfaces.

The transition from exploring the nuanced effects of functionalized graphitic materials to GNPs–Bi_2O_3– and MWCNTs–Bi_2O_3–based PPy nanocomposites highlights a progressive continuum in our quest to engineer better thermoelectric materials. This chapter aims to demonstrate the synergistic interplay between organic and inorganic components, shedding light on the impact of the fillers' (MWCNTs, GNPs) functionalization and their decoration with Bi_2O_3 on the thermoelectric performance of these new nanocomposites.

6.1.1 Publications

The content of this chapter is based on the following peer–reviewed scientific publication "Reproduced with permission from Springer Nature":
Younes Bourenane Cherif, Zineb Mekhalif, Ahmed Mekki, Zakaria Bekkar Djelloul Sayah, and Souleymen Rafai. Enhanced thermoelectric power factor of PPy-based nanocomposites: effect of decorated graphene nanoplatelets by bismuth oxide nanoparticles. **Journal of Materials Science**, 58(11):4809–4823, March 2023. ISSN 1573-4803. doi: 10.1007/s10853-023-08334-5. URL https://doi.org/10.1007/s10853-023-08334-5

> This study aims to develop a hybrid organic–inorganic material comprising polypyrrole (PPy), graphene nanoplatelets (GNPs), and bismuth oxide nanoparticles (Bi_2O_3) to address the limitations in the thermoelectric (TE) conversion efficiency of organic materials. GNPs were coated with Bi_2O_3 nanoparticles through a straightforward method involving infrared irradiation and diazonium chemistry. Various characterization techniques—such as X–ray diffraction, transmission electron microscopy,

Raman spectroscopy, Fourier transform infrared spectroscopy, and X–ray photoelectron spectroscopy—were employed to assess the structural and physical properties of the synthesized nanocomposites.

The study revealed an enhancement in the electrical conductivity (σ) and Seebeck coefficient (S) of PPy–GNPs–Bi_2O_3 in comparison to pure PPy making this nanocomposite as promising TE materials. This improvement was attributed to the π–π stacking interaction between PPy chains and the GNPs' surface. Additionally, Bi_2O_3 played a crucial role in enhancing the TE behavior by improving charge transport and binding both PPy and GNPs. At room temperature, the power factor exhibited an 11–fold increase (1 $\mu Wm^{-1}K^{-2}$) compared to pure PPy. The potential for further enhancement in TE performance at higher temperatures suggests avenues for further exploration.

Younes Bourenane Cherif, Zineb Mekhalif, Ahmed Mekki, and Zakaria Bekkar Djelloul Sayah. Effect of decorated MWCNTs by bismuth oxide nanoparticles on the thermoelectric properties of polypyrrole–based nanocomposites. **The 1st International Conference on Renewable Materials and Energies ICRME2022** Ouargla, Algeria, October 2022, page 3. URL https://icrme2022.sciencesconf.org/

This study investigates the fabrication of composite materials by merging polypyrrole (PPy) with multiwalled carbon nanotubes (MWCNTs) and bismuth oxide nanoparticles (Bi_2O_3). PPy synthesis involved an in–situ oxidative polymerization method using $FeCl_3$ as an oxidant and sodium dodecylbenzene sulfate (SDBS) as a dopant. MWCNTs–Bi_2O_3 were created by modifying MWCNTs and adding bismuth oxide particles. Nanocomposites of PPy–MWCNTs and PPy–MWCNTs–Bi_2O_3 were synthesized and characterized using FTIR and TEM. Their thermoelectric properties showed better performance in the power factor at room temperature for PPy–MWCNTs–Bi_2O_3 compared to pure PPy and PPy–MWCNTs composites.

6.1.2 Outline

This chapter is structured in three sections: Section 6.2 describes the methodology, the synthesis procedures and the characterization techniques. Section 6.3 displays the outcomes and related discussions. Section 6.4 gives the essential conclusions.

6.2 Methodology

6.2.1 Materials

MWCNTs were prepared according to similar procedures as described in Chapter 5 (section § 5.2.2). GNPs (750 $m^2.g^{-1}$) were purchased from Sigma Aldrich. Their functionalization process was done using 4–aminobenzoic acid (99%) as an initiator for the corresponding diazonium derivative, sodium nitrite ($NaNO_2$, 99.2%) and perchloric acid ($HClO_4$, 70%), all were purchased from Fisher Scientific UK. For nanocomposites syntheses, pyrrole, sodium dodecylbenzene sulfonate (SDBS), ethanol, and iron chloride ($FeCl_3$) were used. All the aqueous solutions were prepared using ultra–pure milli–Q (18.2 MΩ).

6.2.2 Fillers Preparation

GNPs and MWCNTs fillers were prepared in three steps: first, functionalization with appropriate diazonium salts bearing carboxylic acid functions, then their impregnation with a bismuth precursors salt and then finally the calcination step to create the bismuth oxide nanoparticles on the fillers surfaces.

6.2.2.1 Functionalization of GNPs and MWCNTs

The functionalization step was conducted on both GNPs and MWCNTs following the procedures outlined in our previous studies (Chapter 5 § 5.2.2) [184]. In brief, 0.2 g of GNPs (or MWCNTs) were mixed with 2.33 g of 4–aminobenzoic acid, 1.15 g of sodium nitrite, and 1.74 ml of perchloric acid and 100 ml of water. The resulting solution underwent 1 h of IR irradiation with constant magnetic stirring, followed by cooling and filtration. The IR treatment is applied because carbonaceous materials absorb infrared irradiation and efficiently convert electronic excitations into molecular vibration energies, generating heat. These photo–adsorption and thermal properties are conducive to the grafting process [187]. The covalently functionalized GNPs (or MWCNTs) with diazonium benzoic acids were then washed with deionized water (DI) and acetone, dried at room temperature, and designated as GNPs–D1 and MWCNTs–D1, Figure 6.1.

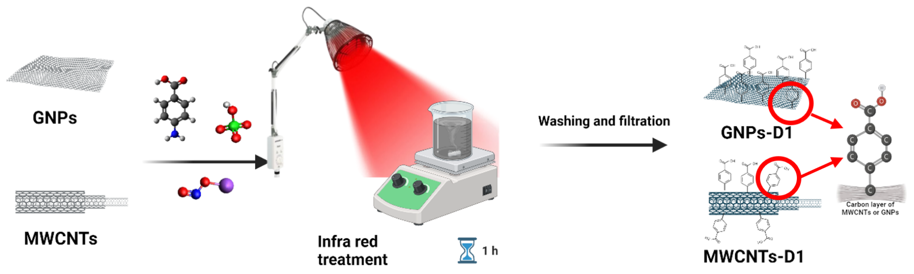

Figure 6.1: Functionalization pathway of GNPs and MWCNTs using Infrared irradiation.

6.2.2.2 Decoration of GNPs and MWCNTs with Bismuth Oxide Nanoparticles

To decorate GNPs–D1 (or MWCNTs–D1) with Bi_2O_3 nanoparticles [71], 0.21 g of ammonium bismuth citrate (ABC) was dissolved in 100 ml of water. GNPs–D1 (or MWCNTs–D1) powder (GNPs–D1 (or MWCNTs):ABC at 1:0.2) was introduced into the solution, sonicated for 5 min, and then subjected to 2 h of IR irradiation with constant magnetic stirring. The presence of acidic groups on the surface of GNPs (or MWCNTs) resulted in deprotonation, producing negatively charged ions that interact favorably with positively charged metal ions during the impregnation step. The resulting material was filtered, washed with DI and acetone, and subsequently calcined at 250 °C for 30 min in the air to convert the attached chemicals into bismuth oxide. Further calcination at 350 °C under argon gas flow for 30 minutes led to the development of a crystalline phase. The resulting materials were denoted as GNPs–D1–Bi_2O_3 and MWCNTs–D1–Bi_2O_3, Figure 6.2.

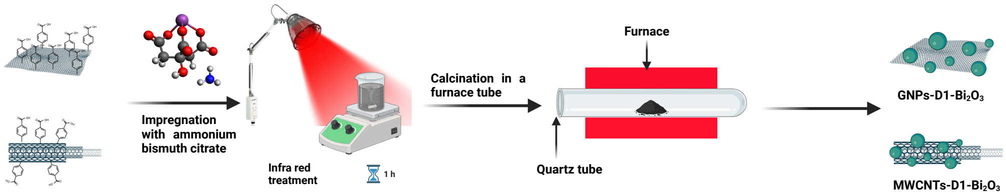

Figure 6.2: Experimental protocol of GNPs and MWCNTs decoration with bismuth oxide nanoparticles.

6.2.3 Nanocomposites Preparation

The prepared nanocomposites based on PPy in–situ formed on the fillers are denoted: PPy–GNPs, PPy–GNPs–D1, PPy–GNPs–D1–Bi_2O_3, PPy–MWCNTs, PPy–MWCNTs–D1 and PPy–MWCNTs–D1–Bi_2O_3. They were synthesized through the following procedure: At room temperature, 1.24 g of SDBS was dissolved in 35 ml of absolute ethanol and then diluted to 140 ml with water. 0.2 g of the prepared fillers were then introduced into the prepared mixture and allowed to react for 20 min. To each solution, 1.04 ml of pyrrole monomer was added and sonicated for 40 minutes. Following this, 56 ml of $FeCl_3$ (4.54 g) dropwise was added, stirred with a magnetic stirrer for 1 h, and stored at 0 °C for 1 h. The filler–to–pyrrole ratio was maintained at 20%. Washing of the resulting materials was carried out using deionized water (DI) and ethanol. Finally, the synthesized materials were dried at 60 °C for a period of 2 days [139, 184]. The proposed interactions between the fillers and the polymer are shown in Figure 6.3.

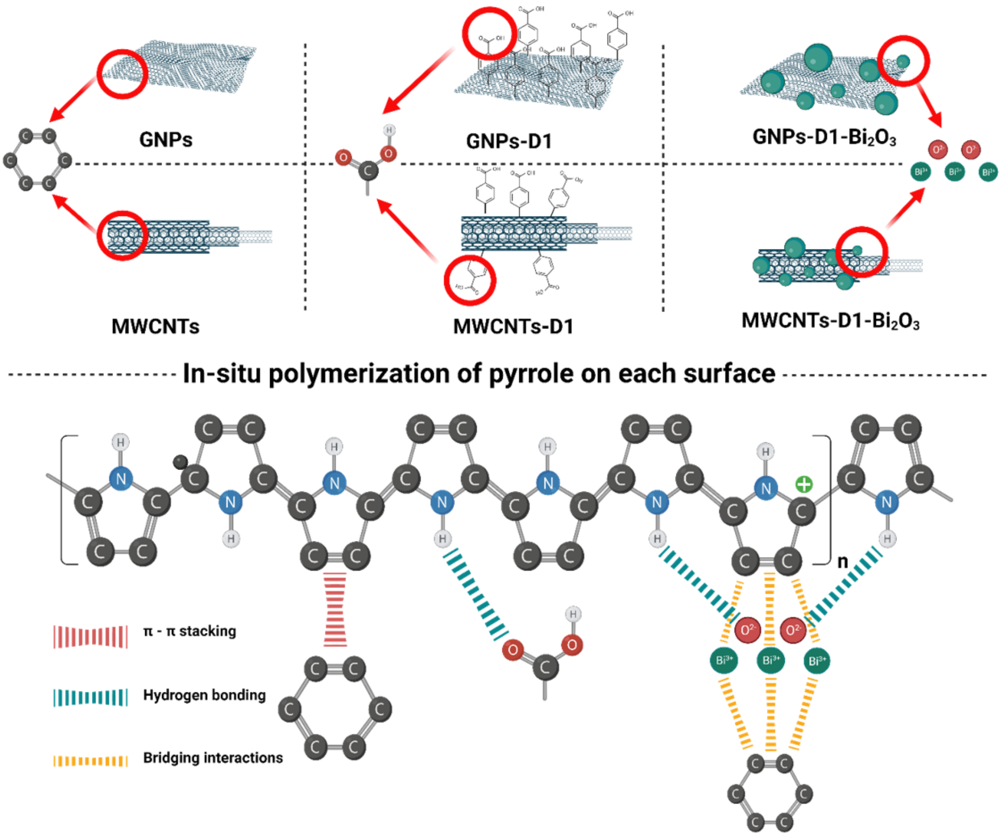

Figure 6.3: Proposed interactions between fillers' surface and polypyrrole chains.

6.3 Results and Discussion

6.3.1 Structural Characterization

The structure of GNPs and MWCNTs before and after the various modifications was analyzed using the P–XRD. As shown in Figure 6.4, GNPs, and MWCNTs have similar structure presented as one intense peak (002) and two peaks with lower intensities (100) (004) at $2\theta = 26°$, 43°, and 54°, respectively [214, 215]. An interlayer spacing (d–spacing) for GNPs is of value 3.43 Å was determined using Bragg's law (Equation 6.1) where $\lambda = 0.154$ nm is the wavelength of the X–ray beam, θ is the diffraction angle ($\theta = 13°$).

$$2 \cdot d \cdot \sin\theta = \lambda \tag{6.1}$$

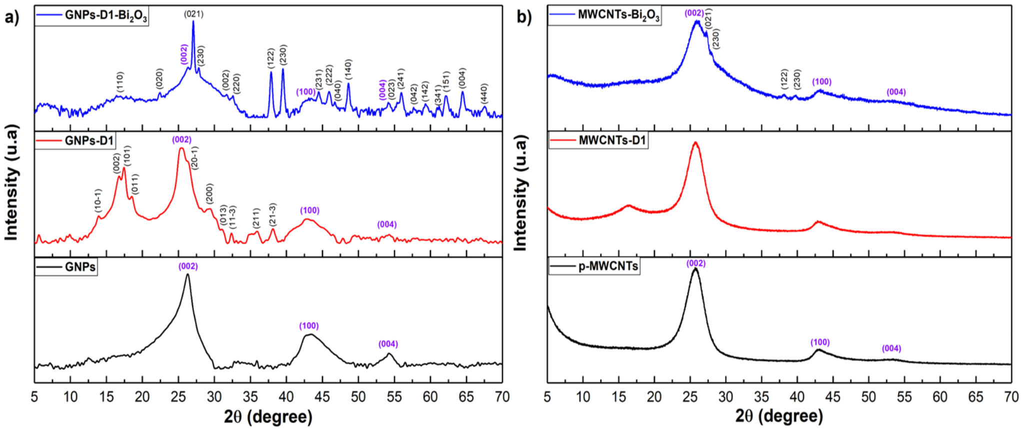

Figure 6.4: XRD patterns of a) GNPs, GNPs–D1, and GNPs–D1–Bi_2O_3, b) MWCNTs, MWCNTs–D1, and MWCNTs–D1–Bi_2O_3.

The functionalized fillers, GNPs–D1 (Figure 6.4a) and MWCNTs–D1 (Figure 6.4b) patterns show the structure of GNPs and MWCNTs, and additional broad peaks similar to the XRD pattern of 4–aminobenzoic acid [216, 217] indicating a crystalline–like structure of the grafted organic layer. Moreover, the functionalization of GNPs is accompanied by a shift towards lower degrees ($2\theta = 25°$) which indicates a larger interlayer spacing (3.56 Å) than that of GNPs.

The GNPs–D1–Bi_2O_3 (Figure 6.4a) pattern indicates the disappearance of the diazonium salt peaks due to the decomposition of the aryl layer of monocarboxylic aryl diazonium functionalized GNPs by the annealing process. However, distinct sharp peaks typical of the formation of a tetragonal β–phase bismuth oxide nanocrystals on the GNPs surface space group: P–421c; space group number: 114; a (Å) = 7.743; b (Å) = 7.743; c (Å) = 5.631; α (°) = 90.00; β (°) = 90.00; γ (°) = 90.00 [189].

In case of MWCNTs–D1–Bi_2O_3 pattern (Figure 6.4b), broadening in certain peaks may suggest structural defects indicating the amorphous structure on the side wall of MWCNTs [218].

In case of GNPs, nanoparticle crystalline sizes ‘τ’ were obtained by applying the Scherrer equation (Equation 6.2) where K (0.9) is a constant and β is the FWHM (full width at half maximum). The size of the crystalline particles obtained from the most intense peak is 14.3 nm.

$$\tau = \frac{K \cdot \lambda}{\beta \cdot \cos\theta} \tag{6.2}$$

Henceforth, we will exclusively feature the results of GNPs–based nanocomposites rather than both GNPs– and MWCNTs–based nanocomposites. This decision is grounded in the identical graphitic structures observed in Raman and FTIR spectroscopies for both materials.

Raman spectroscopy emerges as a robust tool for the analysis of carbon–based materials, as illustrated in Figure 6.5, which depicts the Raman spectra of GNPs–based materials (a) and nanocomposites (b). GNPs reveal distinctive bands, specifically the D–band at ~1346 cm^{-1} and the G–band at ~1586 cm^{-1}. The D band is indicative of disorder defects within graphene sheets or nanotube lattice, while the G band mode corresponds to the stretching mode in graphene or nanotube walls, prevalent in sp^2 carbon materials. The intensity ratio between these two bands serves as an indicator of defects, suggesting, as shown in Figure 6.5, that GNPs–based materials exhibit fewer defects compared to MWCNTs–based materials from our previous work [184]. Remarkably, post–functionalization leads to an increased I_D/I_G ratio due to heightened sp^3 content. Following annealing and Bi_2O_3 nanoparticles decoration, the ratio decreases below pristine GNPs levels. This shift signifies that functionalization induces sp^2 to sp^3 conversion, introducing defects, disrupting electron delocalization. Conversely, annealing restores the sp^2 structure, resulting in a decreased I_D/I_G ratio.

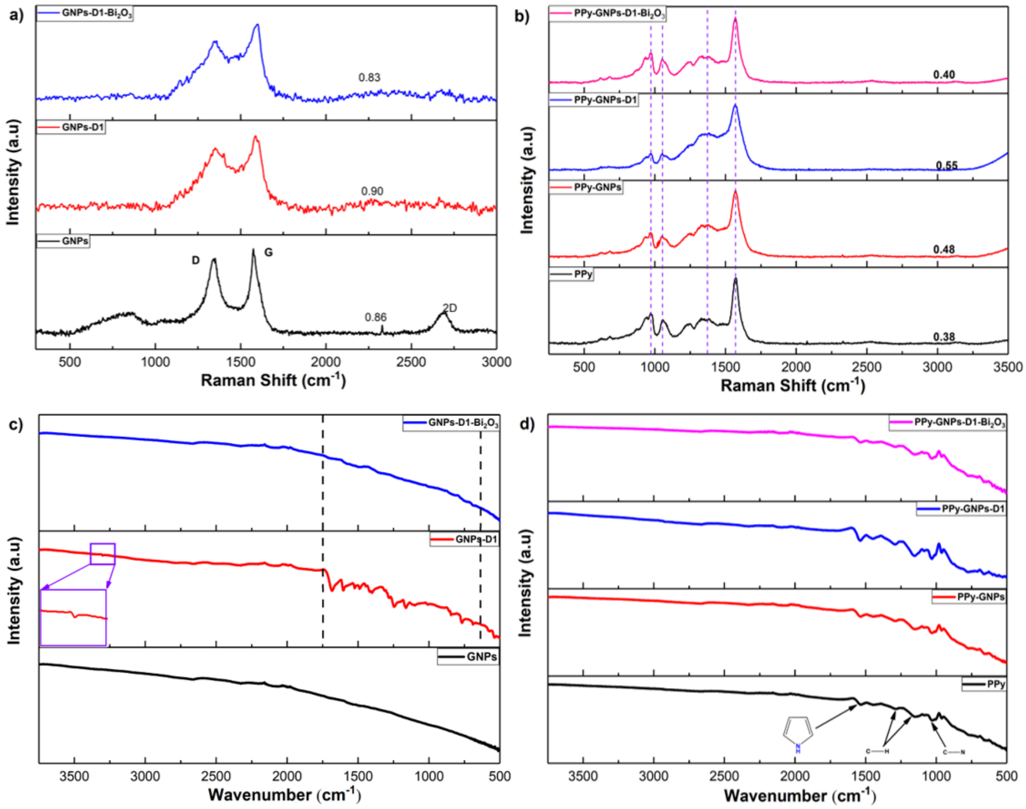

Figure 6.5: a, b) Raman and c, d) FTIR spectra.

Raman analysis conducted on PPy and PPy–based nanocomposites (Figure 6.5b) revealed a spectrum with multiple Raman bands within the 620 to 1600 cm^{-1} range, consistent with previous research [219]. The distinctive bands of pure PPy are visible at 1347 cm^{-1} and 1588 cm^{-1}.

Additionally, two weak peaks appear at 910 cm^{-1} and 1080 cm^{-1}, corresponding to the bipolaron and polaron structures within the PPy chain. Notably, the I_D/I_G values of PPy–GNPs nanocomposites are nearly identical, emphasizing the highly effective hybridization between PPy and GNPs–based materials. Meanwhile, these nanocomposites exhibit lower I_D/I_G values compared to pure GNPs, implying that the introduction of PPy contributes to a reduction in physical defects within GNPs–based materials, as inferred from the Raman data.

The FTIR data depicted in Figures 6.5c and 6.5d demonstrate the chemical composition of GNPs and PPy–based nanocomposites, respectively. Characteristic bonds of GNPs are evident in the FTIR spectra, with a superficial band at 3300 cm^{-1} in functionalized GNPs. The spectral range from 1750 to 600 cm^{-1} affirms the functionalization of GNPs, showcasing the vibrations of COOH, C–OH, and C–O. The disappearance of peaks in decorated GNPs is attributed to thermal annealing, partially restoring the GNPs structure, and the influence of anchored Bi_2O_3 nanoparticles confirmed with XRD.

All nanocomposites (Figure 6.5d) exhibit PPy's distinctive bands, including vibrations of the basic ring at 1540 cm^{-1}, the C–H plane at 1305 and 1048 cm^{-1}, and C–N stretching at 1180 cm^{-1} [184]. Consequently, the TE performance can be anticipated by calculating the intensity ratio between the two bands at 1544 and 1450 cm^{-1}, inversely proportional to the length of PPy chain conjugation [206]. Table 6.1 indicates that PPy–GNPs–D1 exhibits the lowest ratio value, reflecting an extended conjugation chain, a result substantiated by subsequent electrical conductivity measurements of the samples.

Table 6.1: Intensities ratio of 1544 cm^{-1} and 1450 cm^{-1} FTIR bands.

Sample	**PPy**	**PPy–GNPs**	**PPy–GNPs–D1**	**PPy–GNPs–D1–Bi_2O_3**
$I_{1544/1450}$	2.85	2.70	2.44	2.54

6.3.2 Morphological Characterization

The investigation of morphological structure through TEM analysis revealed micrographs of different materials. Figure 6.6 showcases typical Bi_2O_3 particles with an average diameter of 40 nm. Additionally, the successful synthesis and in–situ generation of Bi_2O_3 onto both functionalized GNPs and MWCNTs surfaces are depicted in Figure 6.6, highlighting the surfaces of GNPs and MWCNTs decorated with Bi_2O_3 nanoparticles. These nanoparticles, highlighted in red circles, exhibit a uniform distribution, with nanocrystals displaying a smaller size range of 2–7 nm (mean size of 4 nm) and larger nanocrystals in the range of 10–60 nm (mean size of 30 nm). The calculated size of the crystalline particles was determined to be 17 nm [(4 + 30)/ 2], closely matching the measurement from XRD analysis (14.3 nm). Additionally, free–standing bismuth oxide nanoparticles were observed in MWCNTs–Bi_2O_3.

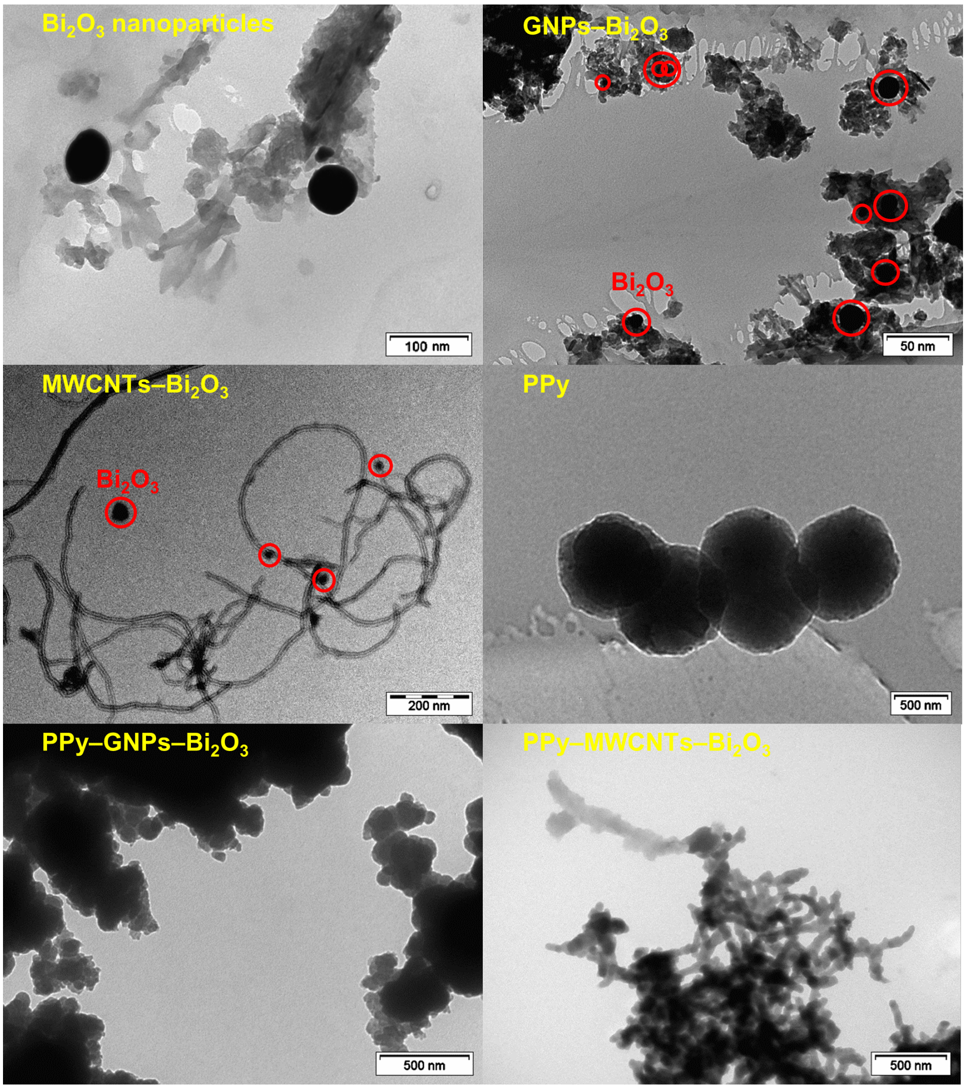

Figure 6.6: TEM images of Bi_2O_3 nanoparticles, GNPs–Bi_2O_3, MWCNTs–Bi_2O_3, PPy, PPy–GNPs–Bi_2O_3 and PPy–MWCNTs–Bi_2O_3.

Utilizing water and ethanol as co–solvent and employing an in–situ oxidative pyrrole method with $FeCl_3$ as an oxidizer and SDBS as a dopant, TEM images of the resulting PPy reveal a distinctive globular morphology with a spherical shape of PPy particles. These particles developed on the GNPs–Bi_2O_3 sheets, forming films; however, a few small blocks are aggregated between the GNPs layers [220].

Furthermore, the in–situ polymerization on the GNPs–Bi_2O_3 surface played a significant role in reducing the particle size of PPy in the PPy–GNPs–Bi_2O_3 nanocomposite compared to pure PPy. This reduction is attributed to the presence of Bi_2O_3 nanoparticles, acting as a secondary dopant to the PPy backbone. Additionally, MWCNTs–Bi_2O_3 were uniformly coated with PPy as illustrated in Figure 6.6 which enhances the interactions between PPy chains and MWCNTs–Bi_2O_3.

6.3.3 Chemical Characterization

X–ray Photoelectron Spectroscopy (XPS) is employed for analyzing the surface atomic composition and chemical states of materials. Henceforth, we will exclusively feature the results of GNPs–based nanocomposites rather than both GNPs– and MWCNTs–based nanocomposites. This decision is grounded in the identical graphitic structure for both materials. Figure 6.7a presents the elemental composition of various GNPs samples and PPy in the corresponding survey spectra. During XPS fitting, the primary peak in the core level spectra was adjusted to the C1s level (284.6 eV). Thermo Avantage software was used for the XPS peak fitting process.

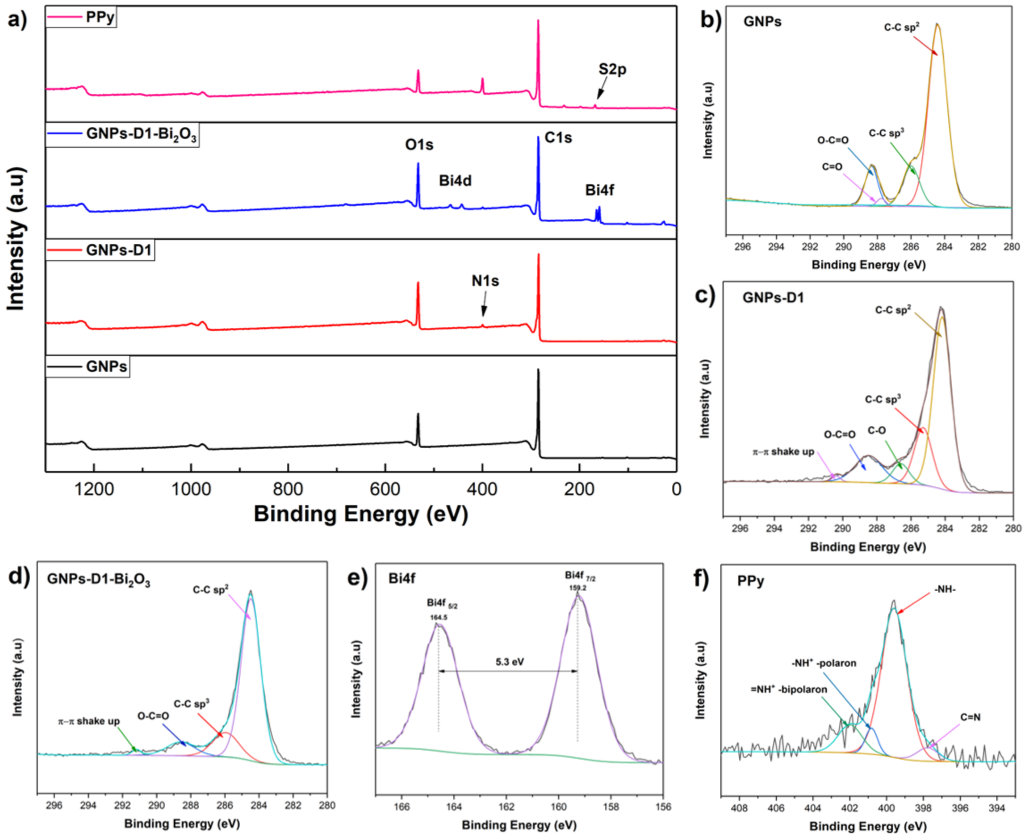

Figure 6.7: XPS survey spectra and high–resolution C1s, N1s, and Bi4f core–levels.

Following the functionalization process, an augmentation in oxygen content is observed. Nitrogen presence is evident, attributed to the azo connection in the GNPs–D1 sample. Post–treatment with ammonium bismuth citrate and subsequent calcination reveal peaks corresponding to bismuth, with the disappearance of the nitrogen peak indicating the removal of aryl connections. In the case of PPy, the XPS spectra displays carbon, oxygen, nitrogen, and even sulfur originating from the dopant.

The successful functionalization is substantiated by a notable increase in the intensity of the C–C sp^3 peak, indicating structural defects on the GNPs' surface due to covalent functionalization. Figures 6.7b, 6.7c, and 6.7d illustrate a peak at 284.4 eV attributable to graphitic carbon sp^2–hybridization and another at 285.7 eV signifying sp^3–hybridization characteristic of carbon. This suggests the presence of structural defects in GNPs [185].

The concentration of sp^2–hybridized carbon, as determined by XPS (Table 6.2), serves as an indicator of both graphitization and functionalization degrees. In its pristine state, GNPs exhibited 64% sp^2–hybridized carbon. However, upon functionalization, this percentage decreased to 46%, implying that functionalization leads to a reduction in sp^2–hybridized carbon content. This reduction suggests a higher defect density in the lattice structure of GNPs [221].

Table 6.2: Oxygen and sp^2–carbon concentrations, as determined by XPS.

Sample	sp^2–carbon [%]	Oxygen [%]
GNPs	64.56	13.14
GNPs–D1	46.02	18.21

Additionally, peaks corresponding to different carbon–oxygen bonds are identified in the XPS spectra. Carbon attached to single oxygen bonds (C–O), carbon linked to oxygen double bonds (C=O), and carbon associated with two oxygen atoms (O–C=O) appear at 286.5, 287.7, and 288.5 eV, respectively [185].

In the high–resolution XPS spectra of bismuth oxide within GNPs–D1–Bi_2O_3 (Figure 6.7e), a doublet is observed. Peaks at 159.2 and 164.5 eV, separated by 5.3 eV, are assigned to Bi $4f_{7/2}$ and Bi $4f_{5/2}$, indicating the Bi^{3+} oxidation state in the Bi_2O_3 form [222]. Figure 6.7f illustrates the deconvoluted N1s spectra of pure PPy. The major peak at 399.5 eV is attributed to neutral amine nitrogen (N–H). Additionally, higher binding energy components at 400.8 and 401.9 eV correspond to positively charged nitrogen ($-N^+$) polaron and ($=N^+$) bipolaron, respectively. The lower binding energy component at 397.7 eV is associated with imine nitrogen (–N=) [223]. As demonstrated by Gence et al. [224], the ratios of $-N^+/N$ can be utilized to quantify the doping level of PPy, here estimated at 26%.

6.3.4 Thermoelectric Characterization

In this section, the materials were coded according to Table 6.3 in order to facilitate the graphical illustration.

Table 6.3 presents the codes of each material or composite material to facilitate the data analysis.

Table 6.3: List of code given to each material for the sake of clarity.

Pure or composite material	**Code**
PPy	C1
PPy–MWCNTs	C2
PPy–GNPs	C3
PPy–MWCNTs–D1	C4
PPy–GNPs–D1	C5
PPy–MWCNTs–Bi_2O_3	C6
PPy–GNPs–Bi_2O_3	C7

In the specific case of a PPy, GNP (or MWCNTs), and Bi_2O_3 nanocomposite:

- Bridging interactions could involve Bi^{3+} ions or surface oxygen atoms in Bi_2O_3 connecting PPy and GNPs (or MWCNTs).
- π–π stacking would occur between the PPy and GNPs (or MWCNTs), contributing to their electronic synergy.
- Hydrogen bonding might further stabilize the matrix, particularly with oxygen–containing groups on GNPs (or MWCNTs) or Bi_2O_3 interacting with PPy.

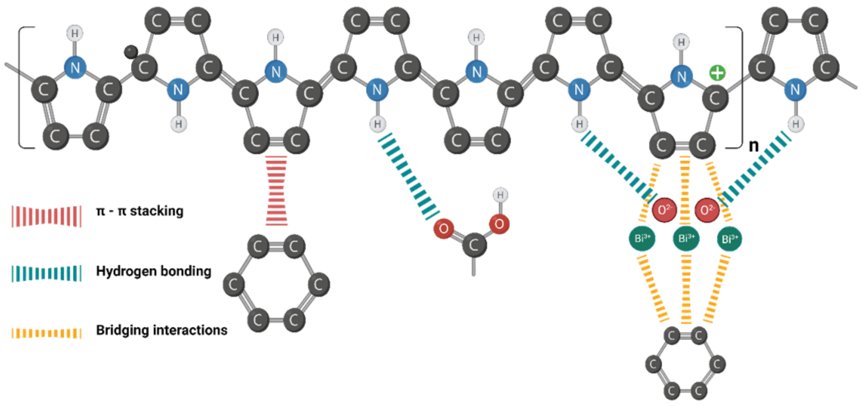

Figure 6.8: Different interactions between PPy, GNP (or MWCNTs), and Bi_2O_3.

Electrical Conductivity. The four–probe instrument was used to measure the in–plan electrical conductivity of the samples, as depicted in Figure 6.9. The results reveal that all nanocomposites exhibit a greater electrical conductivity compared to pure PPy. This enhancement is ascribed to the effective dispersion of MWCNTs and GNPs in PPy, facilitated by favorable interfacial interactions, particularly through π–π stacking [184, 190, 225].

The interfacial interaction in 2D GNPs extends to both sides, unlike on MWCNTs where only the outer shell is implicated [184]. This distinction accounts for the increased electrical conductivity observed in GNPs–based nanocomposites (C3 compared to C2). While covalent functionalization of carbon–based materials, demonstrated by the transformation of carbon's hybridized state [225].

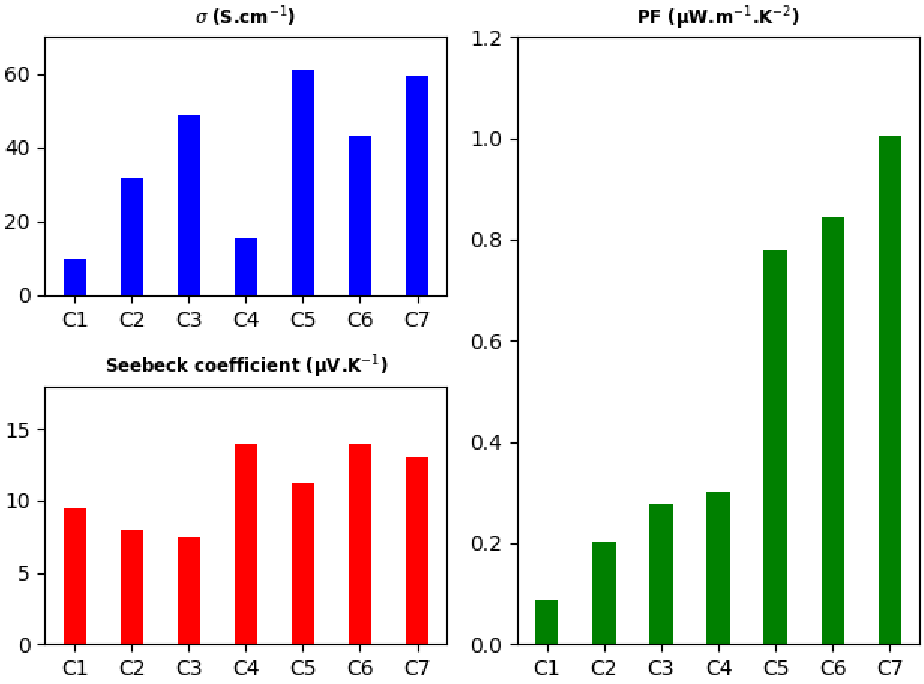

Figure 6.9: Thermoelectric properties of synthesized materials.

However, in GNPs–based nanocomposites (C5 compared to C4), this deficiency appears to be compensated by the presence of π–π stacking and orbital hybridization with the interfacing PPy backbone.

Furthermore, the incorporation of Bi_2O_3 nanoparticles onto MWCNTs and GNPs (C6 and C7) holds the potential to enhance the electrical conductivity of the nanocomposites. This improvement stems from both the inherent conducting characteristics of Bi_2O_3 nanoparticles and the annealing process applied to MWCNTs and GNPs, facilitating the formation of the crystalline phase of Bi_2O_3 nanoparticles on GNPs and amorphous phase on MWCNTs. The difference in conductivity between decorated GNPs (C7) and MWCNTs (C6) –based nanocomposites can be attributed to this distinction in the crystalline phases formed during the annealing process. This annealing process, in turn, serves as another method to tune the TE performance of carbon–based materials. It achieves this by altering the interfacial structure, increasing sp^2 hybridized bonds, and decreasing sp^3 hybridized bonds simultaneously, thus influencing the transport properties [226].

The slight decrease in conductivity observed in PPy–GNPs–D1–Bi_2O_3 (C7) compared to PPy–GNPs–D1 (C5) can be attributed to the limited interaction between GNPs and Bi_2O_3 nanoparticles since the primary factor influencing electrical conductivity remains the structural integrity and distribution of GNPs [227]. Poor dispersion is also responsible for decreasing electrical conductivity [228]. This decrease can be attributed to the decoration of GNPs with Bi_2O_3 nanoparticles, which interrupts the uniform dispersion of GNPs.

These conductivity findings align with the data extracted from FTIR, particularly the conjugation length inferred from the intensity ratio (Table 6.1). On the other hand, an increase in conductivity in PPy–MWCNTs–D1–Bi_2O_3 (C6) compared to PPy–MWCNTs–D1 (C4) is observed, which can be attributed to the perfect coating of MWCNTs–D1–Bi_2O_3 by PPy, as seen in TEM images, thus a good structural integrity resulting in an increased electrical conductivity.

Seebeck Coefficient. The in–plane Seebeck coefficient of the nanocomposites was determined using a homemade setup, and the results at room temperature are illustrated in Figure 6.9. The incorporation of MWCNTs and GNPs appears to marginally decrease the Seebeck coefficient in the PPy–MWCNTs and PPy–GNPs (C2 and C3) nanocomposites, possibly due to the untreated surface leading to less hybridization between PPy and MWCNTs or GNPs surfaces. Conversely, this effect is accentuated when using MWCNTs–D1, GNPs–D1 (C4, C5) and MWCNTs–D1–Bi_2O_3, GNPs–D1–Bi_2O_3 (C6, C7), attributed to the surface functionalities of MWCNTs–D1, GNPs–D1 and Bi_2O_3 nanoparticles, as well as their intrinsic properties related to the Seebeck coefficient. The latter nanocomposites exhibit the highest Seebeck coefficient among all nanocomposites. The slight distinction between MWCNTs– and GNPs–based nanocomposites may be attributed to the fact that MWCNTs are entirely coated by PPy, creating a uniform coverage. In contrast, TEM images reveal that in the case of GNPs, there are some agglomerated spots. These agglomerations could influence the Seebeck coefficient, as they potentially introduce non–uniformities in the nanocomposite structure. The varying distribution of PPy on MWCNTs versus the presence of agglomerates in GNPs may contribute to the observed differences in the Seebeck coefficient between the two types of nanocomposites.

These findings can be summarized based on three key parameters: Doping effect, where Bi_2O_3 acts as a dopant for PPy and MWCNTs or GNPs, serving as a bridge to enhance charge transport and carrier dynamics [229]. Interfacial effect, where the presence of Bi_2O_3 improves the interface between PPy and MWCNTs or GNPs. Synergistic effect, where the combination of PPy and GNPs or MWCNTs decorated Bi_2O_3 results in a synergistic effect, elevating the properties of the nanocomposites beyond the sum of their individual components.

Power Factor. Based on the electrical conductivity and Seebeck coefficient results, the power factor of all samples was calculated, Figure 6.9, and a maximum value of 1 $\mu Wm^{-1}K^{-2}$ was reached, attributed to PPy–GNPs–D1–Bi_2O_3 (C7) which is 11 folds that of pure PPy ~0.087 $\mu Wm^{-1}K^{-2}$, while PPy–MWCNTs–D1–Bi_2O_3 (C6) has reached 0.843 $\mu Wm^{-1}K^{-2}$. These results at room temperature, given the low percentage of bismuth oxide (~4%), is more important than other values reported using the incorporation of nickel oxide nanoparticles (0.435 $\mu Wm^{-1}K^{-1}$ at 60 °C) [229] and even better than tellurium powder (1.064 $\mu Wm^{-1}K^{-2}$, 1 wt.% at a temperature difference of 100 °C) [230], or by incorporating 5 wt.% of SWCNTs at 408 K (~0.980 $\mu Wm^{-1}K^{-2}$) [114].

6.4 Conclusions

The in–situ generation of Bi_2O_3 nanoparticles on the surface of GNPs and MWCNTs marks a strategic advancement in enhancing the TE performance of organic–based nanocomposites. The synthesis involved the formation of Bi_2O_3 on GNPs or MWCNTs, followed by the in–situ polymerization of pyrrole to yield GNPs–Bi_2O_3– or MWCNTs–Bi_2O_3–coated PPy nanocomposites. This novel preparation method demonstrated a remarkable improvement in both electrical conductivity (σ) and Seebeck coefficient (S) when compared to pure PPy. The observed enhancement is attributed to the synergistic effects of π–π stacking and orbital hybridization between the PPy backbone and both GNPs and MWCNTs surfaces. Additionally, the introduced Bi_2O_3 nanoparticles play a dual role by its intrinsic properties and acting as a bridge between PPy chains and GNPs, thereby enhancing charge transport properties. As a result, the surface decoration of graphitic fillers with Bi_2O_3 leads to an impressive 11–fold increase in the power factor (PPy–GNPs–Bi_2O_3, 1 $\mu Wm^{-1}K^{-2}$) compared to pure PPy.

Building on the success of both PPy–GNPs–Bi_2O_3 and PPy–MWCNTs–Bi_2O_3 nanocomposites, the subsequent chapter delves into the exploration of a one–dimensional nanocomposite. This new nanocomposite is based on PPy and MWCNTs, further decorated with nickel oxide (NiO). The investigation into this one–dimensional structure aims to leverage the unique characteristics of MWCNTs and NiO, continuing the trajectory of enhancing thermoelectric performance. This seamless transition maintains a coherent link, showcasing the progressive development and optimization of polymer–based hybrid materials for thermoelectric applications.

Chapter 7

Strategic Design for Enhanced Thermoelectricity: Nickel Oxide–Decorated MWCNTs Wrapped with Polypyrrole Nanotubes

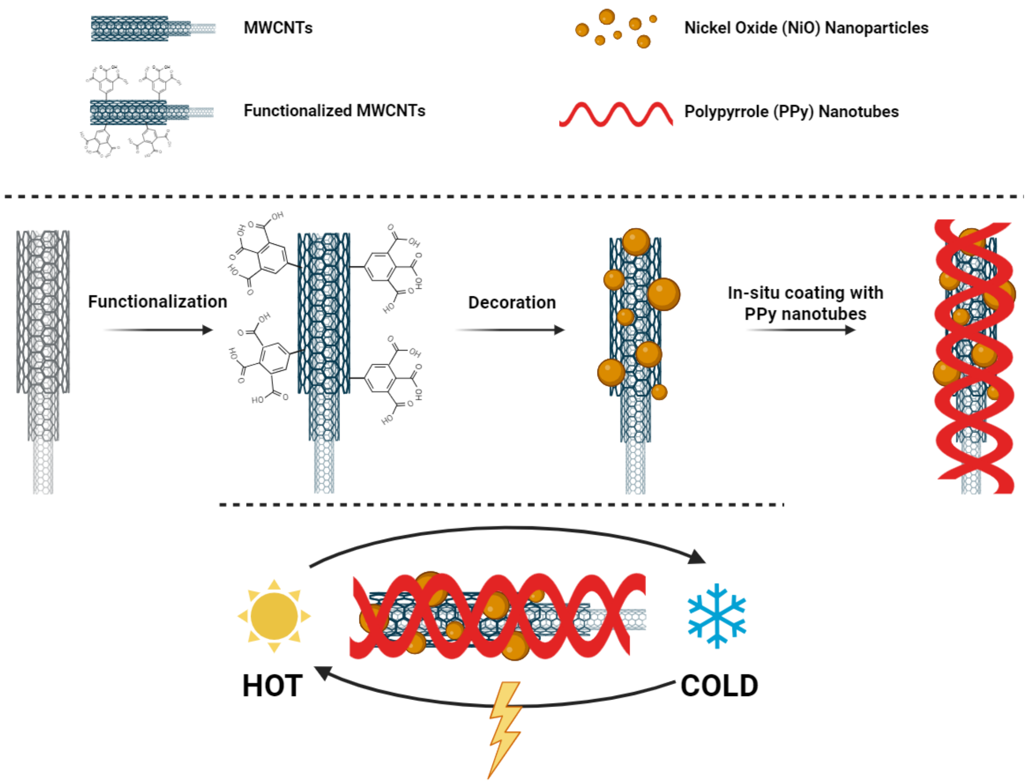

7.1 General Introduction

Transitioning from the trajectory explored in the previous chapter, where GNPs–Bi_2O_3–based PPy and MWCNTs–Bi_2O_3–based PPy nanocomposites opened new avenues for enhanced thermoelectric performance through in–situ generation of metal oxide nanoparticles, our current focus shifts to an exploration of the design of hybrid organic–inorganic thermoelectric materials.

In this chapter, our attention centers on the design of a PPy–MWCNTs–NiO nanocomposite, continuing the trend of hybrid materials for improved thermoelectric properties. The choice of polypyrrole (PPy) as the polymer matrix is highlighted by its stability, compatibility, and easy synthesis. Additionally, the commendable electrical conductivity of both MWCNTs and NiO enhances the overall performance of the composite.

The inclusion of nickel oxide (NiO) is a key feature of this study, driven by its good electrical conductivity and its status as a wide band–gap p–type semiconductor. This strategic choice aims to enhance conductivity and improve thermoelectric properties.

Like prior works (Chapter 6) the in–situ approach is also used as it has shown a high efficiency compared to other approaches such as the mechanical mixing to incorporate metal oxide nanoparticles. This customized methodology [231] not only contributes to the evolving landscape of hybrid organic–inorganic thermoelectric materials but also reflects a departure from conventional methods, offering a promising avenue for large–scale fabrication and waste heat recovery. The chapter's description progresses as a continuation of the exploration towards advanced thermoelectric composites, now with a focus on the synergistic integration of PPy, MWCNTs, and NiO in a meticulously designed nanocomposite.

7.1.1 Publications

The content of this chapter is based on the following peer–reviewed scientific publication "Reproduced with permission from Wiley":
Younes Bourenane Cherif, Zineb Mekhalif, Slimane Abdous, Linda Nedjar, Ahmed Mekki, Zakaria Bekkar Djelloul Sayah, and Souleymen Rafai. Nickel Oxide Decorated MWCNTs Wrapped Polypyrrole: One Dimensional Ternary Nanocomposites for Enhanced Thermoelectric Performance. **ChemNanoMat**, 10(3): e202300486, 2024. ISSN 2199-692X. doi: 10.1002/cnma.202300486. URL https://doi.org/10.1002/cnma.202300486

> This study reports on a customized and revised approach to fabricate "nickel oxide decorated MWCNTs wrapped PPy" nanocomposite with enhanced room–temperature TE properties. The nanocomposite is formed through three steps: MWCNTs functionalization via diazonium salt grafting of 5–amino–1,2,3–benzene tricarboxylic acid; in–situ generation on their surfaces of NiO nanoparticles with a homogenous distribution; the

chemical polymerization of pyrrole using methyl orange as templating and dopant to wrap the MWCNTs–D3–NiO. Various techniques were used as characterization tools, including XRD, TEM, FTIR, Raman, TGA, XPS, and TE measurements. The PPy–MWCNTs–D3–NiO nanocomposite exhibits significantly higher Seebeck coefficient, electrical conductivity, and power factor than PPy and PPy–MWCNTs–D3. The achieved enhancement in TE properties (figure of merit, $ZT_{\text{PPy–MWCNTs–D3–NiO}} = 1.51 \times 10^{-2}$) is attributed to the presence of NiO, which acts as a dopant and improves the charge carrier density in the nanocomposite.

7.1.2 Outline

The organization of this chapter unfolds as follows: Section 7.2 explores the applied methodology and synthesis techniques. In Section 7.3, we delve into the discussion of results obtained from diverse characterizations. Finally, Section 7.4 concludes the chapter by summarizing its key contributions.

7.2 Methodology

7.2.1 Materials

To obtain PPy–MWCNTs–D3–NiO nanocomposite, MWCNTs were prepared in the same way as explained in the previous chapters. The functionalization process of MWCNTs involves the use of 5–amino–1,2,3–benzene tricarboxylic acid (99%), sodium nitrite ($NaNO_2$, 99.2%), perchloric acid ($HClO_4$, 70%), all acquired from Fisher Scientific UK. The generation of nickel oxide (NiO) requires nickel (II) nitrate hexahydrate (NNH) salt precursor purchased from Sigma Aldrich. For the synthesis of nanocomposites, pyrrole, methyl orange (MO), ethanol, and iron chloride ($FeCl_3$) were used, they were obtained from Sigma Aldrich, Germany. All aqueous solutions were meticulously prepared using ultra–pure milli–Q (18.2 MΩ).

7.2.2 Fillers Preparation

The followed method relies on in–situ processes as follow: Initially, MWCNTs are functionalized with 5–amino–1,2,3–benzene tricarboxylic acid using diazonium chemistry. This enhances their dispersion in the polymer matrix, modifies their electronic properties, and facilitates the anchoring of NiO nanoparticles. Subsequently, the MWCNTs–D3 are impregnated with a nickel precursor (nickel (II) nitrate hexahydrate) thanks to the tricarboxylic functions introduced by the grafted molecules. The ensuing step involves high–temperature calcination, converting the nickel ions into NiO particles and resulting in the decoration of the MWCNTs' side wall with NiO nanoparticles.

7.2.2.1 Functionalization of MWCNTs

The functionalization of MWCNTs was performed as reported in previous works [184, 185]; briefly, a mixture of purified MWCNTs (0.2 g), 0.017 mol of both 5–amino–1,2,3–benzene tricarboxylic acid and sodium nitrite, 0.029 mol of perchloric acid and water (100 ml) was stirred and irradiated under IR irradiation for 1 h. The resulting powder (MWCNTs–D3) was filtered, washed with acetone, and dried in the oven at 60 °C for 12 h, Figure 7.1.

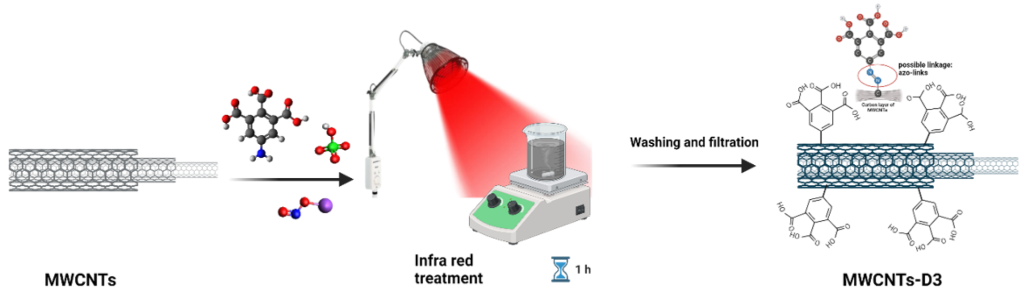

Figure 7.1: Functionalization pathway of MWCNTs using infrared irradiation.

7.2.2.2 Decoration of MWCNTs

The impregnation step was initiated by introducing the preceding prepared fillers (MWCNTs–D3) into a 1 M solution of NNH. Subsequently, a 5 M solution of NaOH (20 ml) was gradually added to the aforementioned mixture and stirred for a duration of 1.5 h. Following the filtration process, the filtrate was dried at 100 °C for 6 h. The subsequent calcination step, aimed at the formation of nickel oxide, was conducted in a tube furnace at 450 °C for 3 h, Figure 7.2.

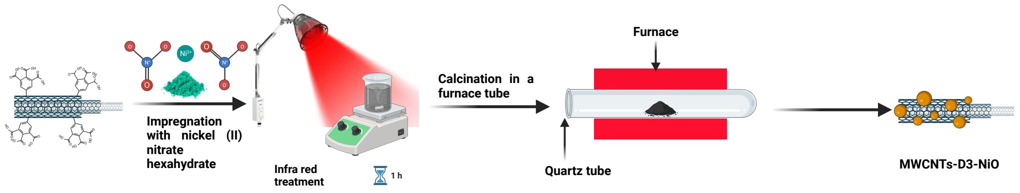

Figure 7.2: Experimental protocol of MWCNTs decoration with nickel oxide nanoparticles.

7.2.2.3 Nickel Oxide Nanoparticles

Following the same procedure (§7.2.2.2) but without MWCNTs, $Ni(OH)_2$ green powder was formed, and turned to black NiO nanocrystals after annealing at 450 °C [229].

7.2.3 Nanocomposites Preparation

PPy was produced through a series of steps involving the dissolution of 0.85 g of methyl orange (MO) in 25 ml of ethanol, followed by the addition of 75 ml of water to the mixture. In this process, MO serves both as a dopant and a template, guiding the growth of PPy by forming a complex with the PPy precursor molecules. Subsequently, pyrrole was introduced in an optimized ratio with MO (wt./wt.= 0.82) [232] and left under magnetic stirring for 30 min. $FeCl_3$, acting as an oxidant, was then gradually added to the solution, and the mixture was left for 2 h. The resulting dispersions were left overnight, followed by filtration and multiple washes with distilled water and ethanol to eliminate MO, unreacted species, and excess ferric chloride. The resultant nanocomposites were dried at 60 °C for 2 days. The synthesis of PPy–MWCNTs–D3 nanocomposite followed a similar procedure, where MWCNTs–D3 and MWCNTs–D3–NiO were added before the introduction of pyrrole, Figure 7.3.

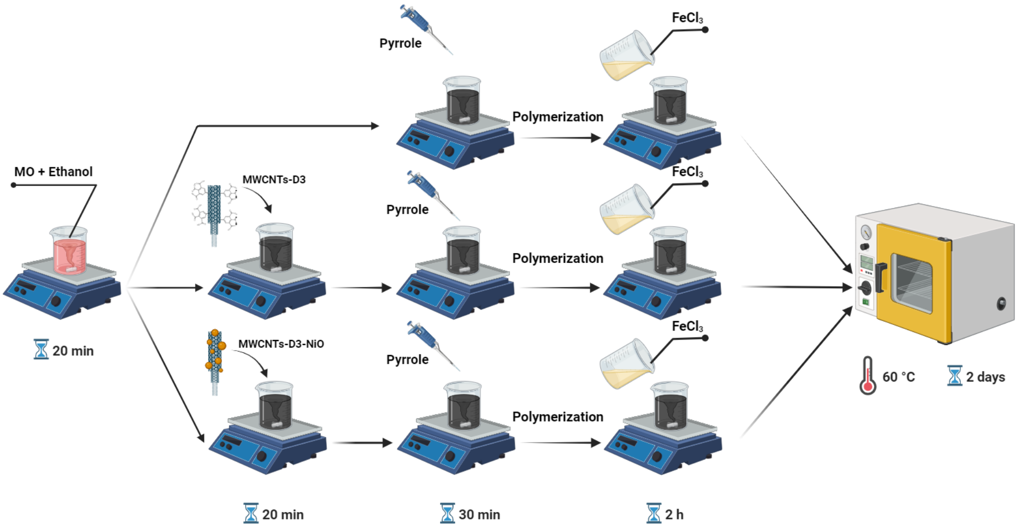

Figure 7.3: Synthesis routes of the nanocomposites.

7.3 Results and Discussion

This section presents the findings and discussions regarding the utilization of NiO–decorated MWCNTs wrapped with PPy as a TE material. To validate the functionalization and decoration of MWCNTs with NiO, X–ray diffraction (XRD), thermogravimetric analysis (TGA), and X–ray photoelectron spectroscopy (XPS) analyses are employed. The structural integrity, functional groups, and morphological characteristics of the targeted nanocomposite PPy–MWCNTs–D3–NiO are explored using Raman spectroscopy, Fourier transform infrared spectroscopy (FTIR), and transmission electron microscopy (TEM). Subsequently, the thermoelectric properties, including electrical conductivity, Seebeck coefficient, and thermal conductivity, are assessed.

7.3.1 Structural Characterization

Powder X–Ray Diffraction (XRD) was employed to investigate the crystal structures of MWCNTs, NiO nanoparticles, and MWCNTs–D3–NiO.

As illustrated in Figure 7.4, the diffraction pattern of MWCNTs (depicted by the black curve) exhibits a distinct peak at 2θ = 26°, corresponding to the (002) plan with an interlayer spacing of 3.423 Å (as indicated by Equation 6.1[1]) [233]. Additionally, three broader peaks at 2θ = 43°, 54°, and 79°are observed, suggesting the presence of disordered or amorphous structures within the MWCNTs [234]. Bragg's law, represented by Equation 6.1, defines the relationship between the wavelength (λ = 0.154 nm) of X–rays, the angle (θ = 13°) between the incident X–ray beam and the detector or sample, and the spacing between atomic planes (d), also known as the interlayer distance.

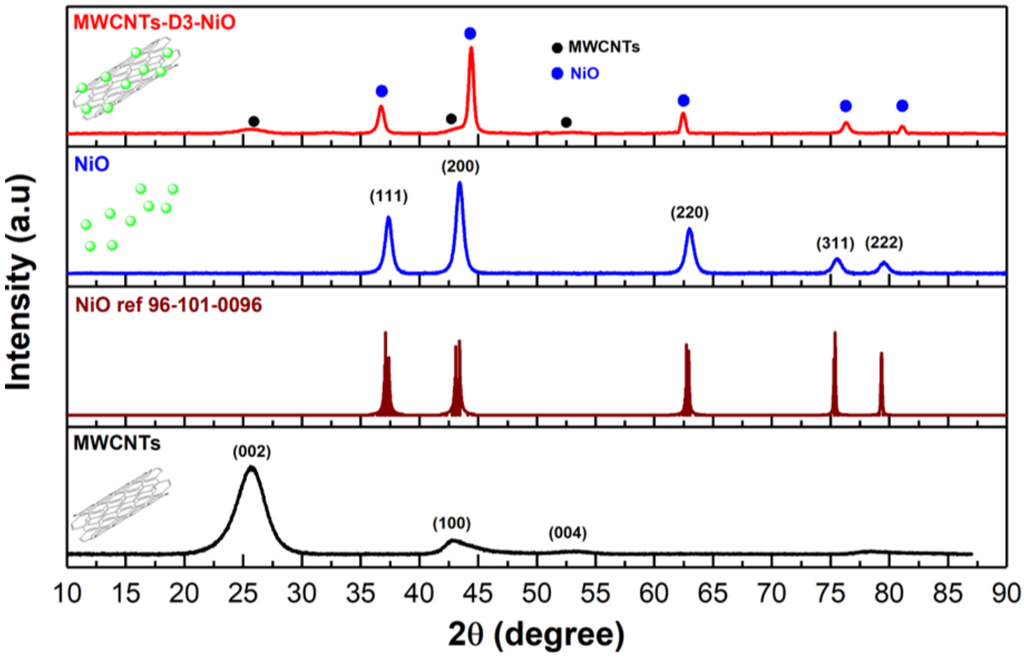

Figure 7.4: XRD patterns of MWCNTs, reference and synthesized NiO and MWCNTs–D3–NiO.

Nickel oxide particles were synthesized, and their XRD pattern (blue curve in Figure 7.4) aligns with the characteristic peaks of NiO. Sharp peaks at 2θ = 37.48°, 43.42°, 62.97°, 75.63°, and 79.60°correspond to the (111), (200), (220), (311), and (222) planes, respectively. These values concord with the reference sample (96–101–0096, garnet curve) provided by HighScore Plus software and match previously reported works [235–237]. According to the Scherrer equation (Equation 6.2[2]), the estimated mean size of NiO nanoparticles is 14.6 nm.

---

[1] $2 \cdot d \cdot \sin\theta = \lambda$

[2] $\tau = \frac{K \cdot \lambda}{\beta \cdot \cos\theta}$

When MWCNTs were functionalized and in–situ modified to generate NiO nanoparticles, the XRD peaks characteristic of both MWCNTs and NiO nanoparticles are observed (red curve in Figure 7.4). This confirms the efficiency of covalent functionalization of MWCNTs with tricarboxylic functions (MWCNTs–D3), effectively trapping nickel ions that subsequently convert to NiO during the calcination process.

In summary, XRD analysis has validated the crystal structures of MWCNTs, NiO nanoparticles, and MWCNTs–D3–NiO. The successful functionalization of MWCNTs and the conversion of trapped nickel ions into NiO are substantiated by the presence of characteristic peaks in the XRD analysis of both MWCNTs and NiO.

Moving beyond crystallography, Raman spectroscopy delves into the vibrational modes of the materials, providing information about their molecular structures and chemical compositions. In particular, Raman analysis can elucidate the structural integrity of the PPy–MWCNTs–D3–NiO nanocomposite and reveal any alterations in the carbon nanotube network due to functionalization and the incorporation of NiO nanoparticles. The shift or intensity changes in Raman peaks can offer insights into the interactions between the various components, reflecting the success of the synthesis process.

In Figure 7.5a, two distinct peaks at 1570 cm^{-1} (G band) and 1351 cm^{-1} (D band) are evident, corresponding to the C=C stretching vibration and the ring stretching mode of PPy, respectively. This assignment is consistent with previous studies [238, 239]. Additionally, two peaks appear at 1040 and 953 cm^{-1}, attributed to the polaron and bipolaron structures of the PPy backbone [184]. Notably, these peaks exhibit higher intensity in PPy–MWCNTs–D3–NiO, suggesting an increased presence of polarons and bipolarons in the composite structure. The peak at 1231 cm^{-1}, associated with the bipolaron structure, exhibits a well–resolved nature in PPy–MWCNTs–D3–NiO, indicating enhanced conductivity compared to PPy–MWCNTs–D3 nanocomposites [240].

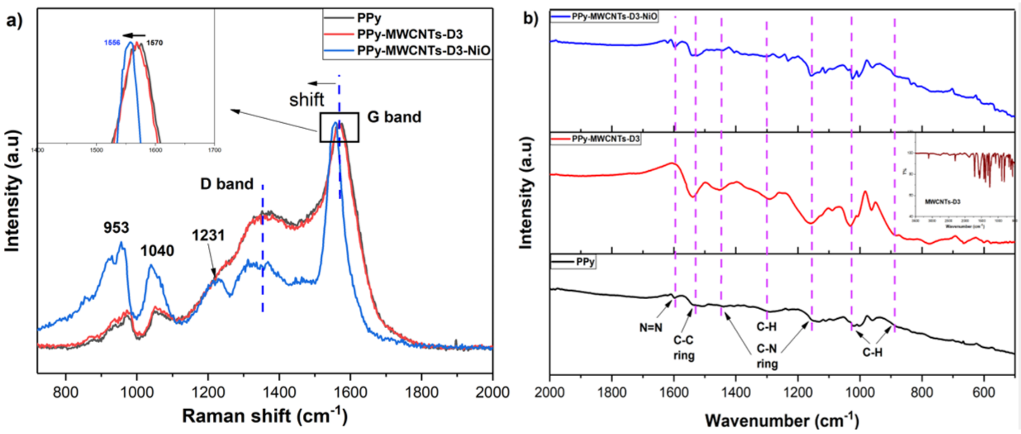

Figure 7.5: a) Raman and b) FTIR spectra of the prepared materials.

Furthermore, a noticeable peak shift from 1570 to 1556 cm^{-1} is observed, attributed to various factors such as π–π interactions, electrostatic interactions, and hydrogen bonding [241]. This shift provides valuable insights into the interactions between PPy, MWCNTs–D3, and NiO in the nanocomposite structure. These vibrational changes, especially the well–resolved bipolaron peak and the shift in the G band, signify the unique structural features and improved conductivity of PPy–MWCNTs–D3–NiO, highlighting its potential as a highly conductive material.

The examination of the intensity ratio between the D band and G band peaks in Raman analysis serves as a valuable indicator of changes in π–π conjugated defects within the composite materials. This ratio shifts from 0.61 in the case of PPy to 0.58 and 0.40 for PPy–MWCNTs–D3 and PPy–MWCNTs–D3–NiO, respectively. This shift strongly suggests a reduction in π–π conjugated defects, indicating the development of a more ordered structure within the composites.

In summary, Raman analysis not only provides insights into the interactions between PPy and MWCNTs–D3, both with and without NiO but also sheds light on the nature of π–π interactions, electrostatic interactions, and hydrogen bonding. Furthermore, the observed decline in the intensity ratio of the D band to the G band signifies a diminishing presence of π–π conjugated defects, confirming the establishment of a more organized structure in the composite materials.

In Figure 7.5b, distinct peaks characteristic of PPy are prominently displayed, offering valuable insights into the molecular structure of PPy. Notably, the vibrational modes associated with these peaks provide specific information about various bonds within the PPy structure. The C–C ring vibration manifests at 1543 cm^{-1}, while the C–N ring vibrations are observed at 1456 cm^{-1} and 1159 cm^{-1}, signifying the presence of carbon–carbon and carbon–nitrogen bonds in PPy. Additionally, C–H vibrations, both in and out of the plane, are identified at 1300 cm^{-1} and 1030 cm^{-1}, 889 cm^{-1}, respectively. These vibrational signatures contribute to the overall characterization of PPy's molecular composition [165, 212, 238, 242, 243].

Furthermore, the characteristic vibration of the dopant (MO) is evident in the N=N stretching mode at 1600 cm^{-1}, allowing for the identification of the dopant within the PPy structure [244]. Moreover, PPy–MWCNTs–D3 exhibits heightened peak intensities in the 1600–900 cm^{-1} range compared to pure PPy, indicating the incorporation of MWCNTs–D3. These enhanced peaks in this region are primarily attributed to the vibrational modes associated with the benzenetricarboxylic acid groups present in MWCNTs–D3, as highlighted in the inset of Figure 7.5b. This observation underscores the successful integration of MWCNTs–D3 into the PPy matrix, providing additional structural information through vibrational modes associated with the introduced functional groups.

7.3.2 Morphological Characterization

TEM analysis played a crucial role in evaluating the structure, morphology, and dimensions of the synthesized materials. MWCNTs–D3 (Figure 7.6) exhibit a morphology similar to pure MWCNTs, displaying a diameter ranging from 7 to 12 nm [184, 222]. This suggests the softness of the functionalization process, preserving the length and integrity of the nanotubes.

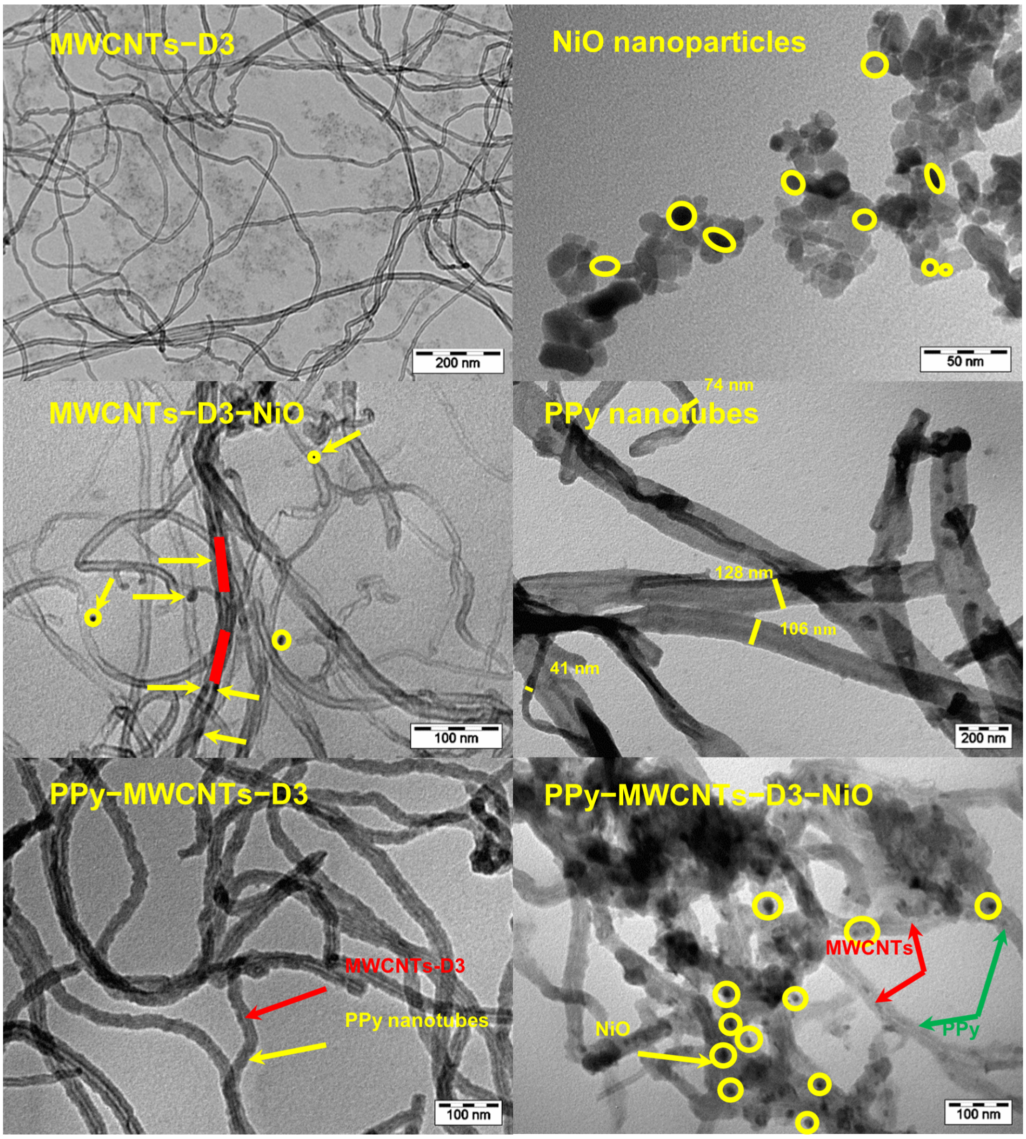

Figure 7.6: TEM images of MWCNTs–D3, NiO nanoparticles, MWCNTs–D3–NiO, PPy nanotubes, PPy–MWCNTs–D3 and PPy–MWCNTs–D3–NiO.

In Figure 7.6, NiO nanoparticles appear nearly spherical, with an average size of 8.3 nm, closely aligning with XRD measurements (14.6 nm). MWCNTs–D3–NiO clearly present NiO nanoparticles on the side walls of MWCNTs, effectively distributed and anchored, highlighting the efficacy of the synthesis procedure, involving proper functionalization, an appropriate salt precursor, and an optimized calcination temperature.

Figure 7.6 also illustrates the TEM image of PPy, revealing a nanotubular structure with a diameter ranging from 40 to 130 nm, a distinctive feature induced by the use of methyl orange (MO) as a dopant [232, 238]. This nanotubular morphology holds promise for thermoelectric applications due to its potential to enhance electron and hole movement, to minimize scattering events, and to improve material conductivity [245]. The tubular structure also offers a substantial surface area, promoting better environmental interaction and thus enhanced thermoelectric performance.

The in–situ polymerization of pyrrole on functionalized and decorated MWCNTs with NiO, utilizing MO as a dopant and $FeCl_3$ as an oxidant, resulted in a homogeneous structure of coated MWCNTs with PPy nanotubes (Figure 7.6). The observed diameter reduction, despite using the same polymerization conditions as PPy alone, suggests the templating role of MWCNTs–D3 in the growth of PPy.

In the presence of MWCNTs–D3–NiO, PPy nanotubes were found to coat the entire decorated nanotubes, as demonstrated in Figure 7.6, where each component is indicated with arrows (green: PPy, red: MWCNTs, and yellow: NiO).

This TEM analysis has provided crucial insights into the structure, morphology, and dimensions of the synthesized materials. It verified the preservation of nanotube integrity in the functionalization process, the uniform distribution and anchoring of NiO nanoparticles on MWCNTs, and the templating role of MWCNTs in the growth of PPy nanotubes in the nanocomposites. These observations significantly contribute to the comprehension of the materials' properties.

7.3.3 Thermogravemetric Characterization

Thermal gravimetric analysis was conducted to quantify the grafting amounts of both organic molecules and inorganic nanoparticles. The thermo–gravimetric (TG) curve, along with its differential curve (DTG), for NiO, MWCNTs, MWCNTs–D3, and MWCNTs–D3–NiO is presented in Figures 7.7 (a, b, c, and d) respectively.

In Figure 7.7a, a total weight loss of approximately 4.5% occurs within the temperature range of 80–600 °C. The initial sharp peak below 100 °C is attributed to the desorption of physically adsorbed water molecules. Subsequently, two broad peaks between 200–300 °C and 500–600 °C reflect the release of excess oxygen, impurities, and the thermal decomposition of $Ni(OH)_2$ to form NiO. These observations agree with previous studies on NiO thermal behavior [237, 246–248].

Figure 7.7b displays a singular sharp peak at around 740 °C, indicating the degradation of the graphitic structure of MWCNTs, resulting in a maximum weight loss of about 27.2%.

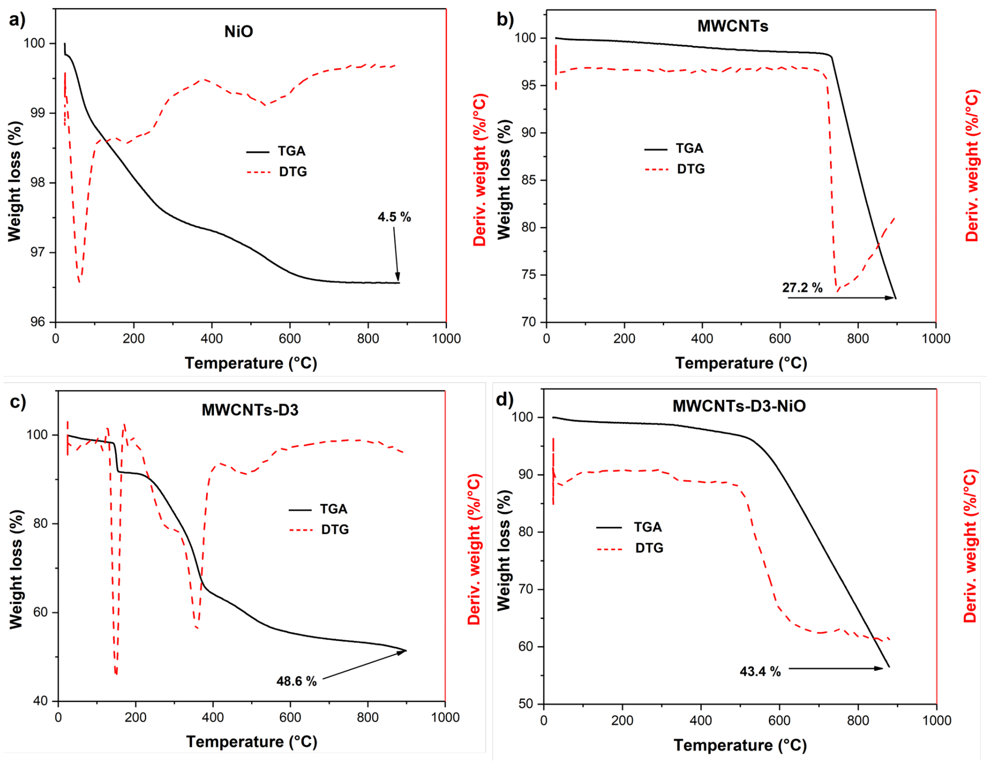

Figure 7.7: TGA–DTG curves of a) MWCNTs, b) NiO nanoparticles, c) MWCNTs–D3 and d) MWCNTs–D3–NiO.

Due to the thermal instability of introduced functional groups during the functionalization process, their decomposition occurs below 400 °C. As shown in Figure 7.7c, TGA and DTG curves of MWCNTs–D3 exhibit three decomposition peaks. The initial decomposition starts at 180 °C, attributed to moisture loss [208], followed by another decomposition below 400 °C associated with benzenetricarboxylic acid groups. The final weight loss at 500 °C is attributed to the initiation of the degradation of the graphitic structure of MWCNTs, resulting in a weight loss of 48.6%.

In Figure 7.7d, TGA–DTG curves of MWCNTs–D3–NiO reveal a late decomposition around 500–600 °C due to the presence of NiO nanoparticles. No early decomposition is observed compared to MWCNTs–D3, owing to the prior annealing process, creating a crystalline phase of NiO on the side wall of MWCNTs and destroying benzenetricarboxylic acid groups. This decomposition peak is associated with both the degradation of NiO nanoparticles and the graphitic structure of MWCNTs, resulting in a final weight loss of 43.4%.

The grafting percentage (GP) can be estimated using Equation 5.1[3] [249], revealing a GP of approximately 21.4% for MWCNTs–D3, indicative of its early decomposition compared to MWCNTs. For MWCNTs–D3–NiO, considering the absence of benzenetricarboxylic acid groups post–calcination, the GP value is calculated to be 16.2%. These findings shed light on the thermal properties and grafting efficiencies of the synthesized materials.

---

[3] $\mathrm{GP} = (\Delta W_{\text{Functionalized MWCNTs}} - \Delta W_{\text{Crude MWCNTs}}) \times 100\%$

7.3.4 Chemical Characterization

XPS analysis was employed for assessing the chemical surface composition, as depicted in Figure 7.8a. The survey spectrum of purified MWCNTs exhibits an oxygen O1s peak at 531.9 eV with relatively low intensity in comparison to the dominant C1s peak at 284.1 eV, mainly attributed to residual species.

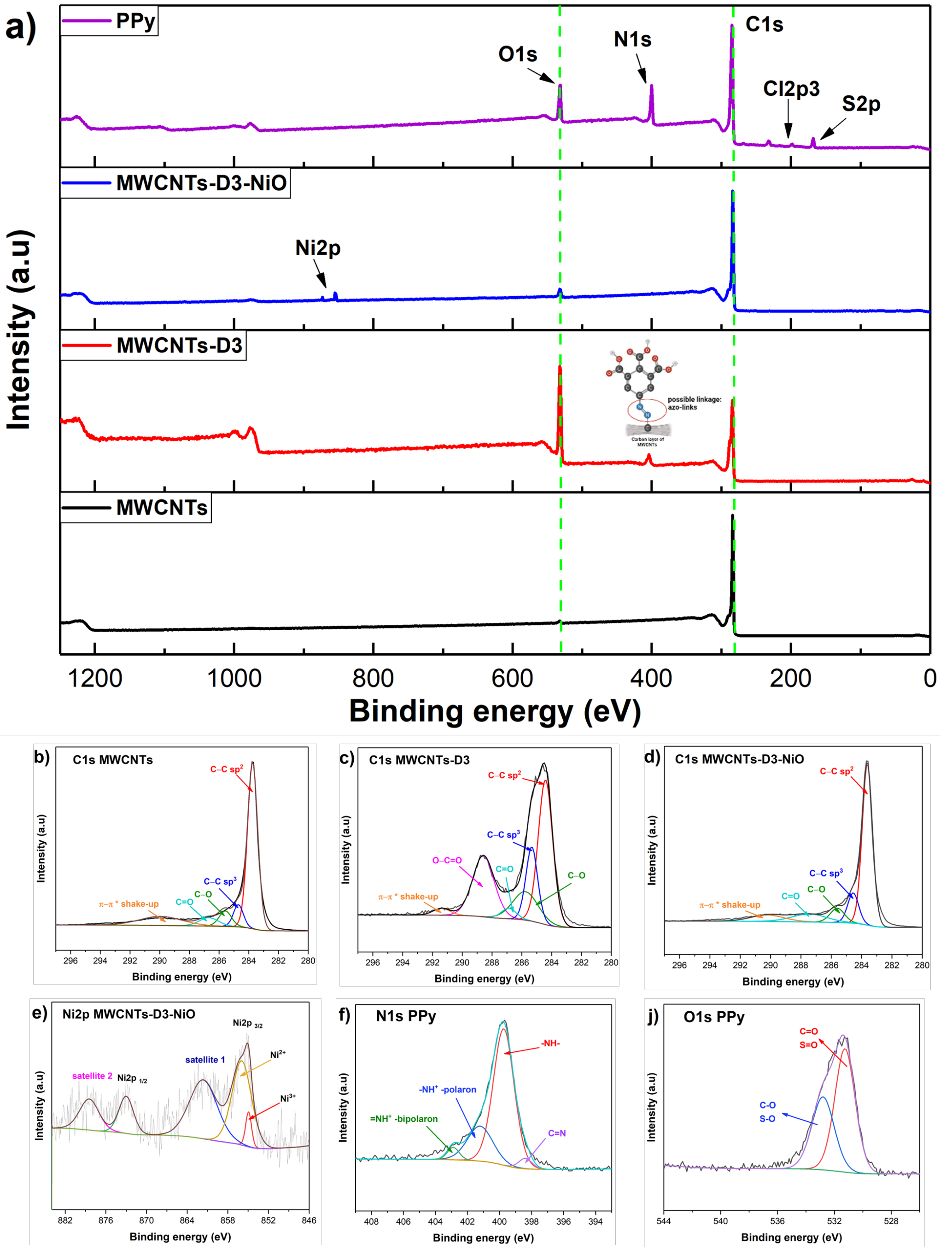

Figure 7.8: XPS survey spectra and high–resolution C1s, N1s and Ni2p core–levels.

The grafting of benzenetricarboxylic acid groups onto the side wall of MWCNTs leads to a notable increase in the O1s peak, accompanied by the appearance of a nitrogen (N1s) peak at 400 eV, characteristic of azo links. Additionally, this latter peak is associated with grafting via –C–N=N–C– covalent bond.

MWCNTs–D3–NiO shows a significant reduction in the O1s peak and the complete disappearance of the N1s peak due to the calcination process. This process eliminates organic molecules, leaving NiO nanoparticles firmly attached to the walls of MWCNTs.

The XPS atomic percentages of carbon, oxygen, nitrogen, and nickel for the samples are detailed in Table 7.1. The oxygen content ranges from 1.33% for MWCNTs to 27.9% and 3.81% after functionalization and calcination, respectively. The nitrogen associated with the azo links (–C–N=N–C–) is present only in MWCNTs–D3 at approximately 6.03%, while the nickel content in the NiO nanoparticles is around 1.28%.

Table 7.1: Atomic % of the samples found from XPS analysis.

Sample	**C%**	**O%**	**N%**	**Ni%**
MWCNTs	98.67	1.33	–	–
MWCNTs–D3	66.07	27.9	6.03	–
MWCNTs–D3–NiO	94.91	3.81	–	1.28

The XPS survey spectrum of PPy reveals the prominent presence of the primary constituents of the polymer, with carbon comprising 72.40% and nitrogen 13.66%. Additionally, lower–intensity elements such as chlorine (~1.31%) from the oxidant ($FeCl_3$), sulfur (~3.13%) from the MO dopant, and oxygen (9.49%) are detected. This suggests the successful incorporation of the dopant with the oxidant during the chemical synthesis of PPy.

The high–resolution C1s XPS spectra for all MWCNTs, MWCNTs–D3, and MWCNTs–D3–NiO are depicted in Figures 7.6b, 7.6c, and 7.6d. Purified MWCNTs predominantly display sp^2 carbon hybridization, characteristic of carbon nanotubes, with residual functionalities represented by C–O (285.68 eV) and C=O (268.78 eV) bonds. Figure 7.6c illustrates an increase in the sp^3 peak due to MWCNT functionalization, accompanied by C–O and C=O peaks. Notably, the appearance of O–C=O (288.68 eV) with high intensity confirms the functionalization of the MWCNTs' side wall with benzene tricarboxylic groups.

The sp^3 to sp^2 intensity ratio, presented in Table 7.2, provides a quantitative measure of the changes in carbon hybridization induced by functionalization and decoration processes. This ratio serves as a useful metric for assessing the extent of functionalization, the degree of graphitization, and the overall structural integrity of carbon–based materials. A higher sp^3 to sp^2 intensity ratio suggests an increase in the proportion of sp^3 hybridized carbon atoms, which could indicate functionalization or defects in the carbon structure.

Table 7.2: sp^3 to sp^2 ratio.

Sample	**sp^3 intensity**	**sp^2 intensity**	**sp^3/sp^2 ratio**
MWCNTs	5092.46	39388.31	0.13
MWCNTs–D3	1739.07	4158.45	0.42
MWCNTs–D3–NiO	5345.83	26771.82	0.20

Following calcination, there is a notable reduction in the carbon sp^3 hybridization peak, signifying the elimination of side wall functionalities and the integration of nickel oxide nanoparticles (Figure 7.6d). This transformation is confirmed by the high–resolution Ni2p spectra (Figure 7.6e), showing two major peaks at 855.3 eV and 873.2 eV corresponding to $Ni2p_{3/2}$ and $Ni2p_{1/2}$, respectively. Additionally, two satellite peaks at 861.8 eV and 879.1 eV indicate a shake–up event in the NiO structure [250–252], commonly associated with Ni^{2+} in NiO compounds [253–255]. The presence of Ni^{3+} ions may be attributed to an excess of oxygen, possibly in the form of NiOOH [256, 257].

In Figure 7.6f, the N1s high–resolution XPS spectra reveal the primary peak of neutral amine nitrogen (N–H) at 399.5 eV. Higher binding energy components at 401.2 eV and 402.8 eV are assigned to positively charged nitrogen, such as $–NH^+$ polaron and $=NH^+$ bipolaron, respectively [212, 223]. The O1s spectrum of PPy (Figure 7.6j) presents two deconvoluted peaks at 531 eV and 532.2 eV, attributed to C=O, S=O, and C–O, S–O, reflecting the presence of sulfur in the MO dopant structure [258].

XPS analysis provided insights into the surface composition of the samples. MWCNTs displayed a low oxygen content, and nitrogen was introduced through covalent grafting. Upon calcination, MWCNTs–D3–NiO showed reduced oxygen and nitrogen peaks. In the case of PPy, carbon, nitrogen, and elements from the dopant and oxidant were observed. High–resolution spectra confirmed functionalization and the presence of NiO nanoparticles on MWCNTs–D3–NiO, revealing characteristic peaks indicative of various bonding states.

7.3.5 Thermoelectric Characterization

Designing a high–performance thermoelectric material is a challenge as it requires a delicate balance among key factors: a high Seebeck coefficient, high electrical conductivity, and a low thermal conductivity. This complexity arises from the complex relationships between these parameters. Achieving a balance is particularly challenging because achieving a high Seebeck coefficient often correlates with lower electrical conductivity, while heightened electrical conductivity tends to increase thermal conductivity.

The effectiveness of thermoelectric parameters is linked to the electronic band structure, carrier concentration, and mobility. In ternary nanocomposites, each constituent, such as PPy, MWCNTs, and NiO, can contribute differently to these properties.

For example, PPy, functioning as a conductive polymer matrix in the composite, exhibits high electrical conductivity, playing a crucial role in facilitating charge transport within the material. Moreover, PPy can be doped to further enhance its electrical conductivity and adjust its charge carrier concentration.

Moreover, one–dimensional carbon nanostructures, MWCNTs, exhibit high electrical conductivity and distinctive mechanical properties. In the context of the composite, MWCNTs act as conductive fillers, forming a network that facilitates the movement of charge carriers, such as electrons, throughout the material. This network structure significantly enhances the overall electrical conductivity of the composite.

In the ternary nanocomposite, NiO plays a pivotal role by acting as a bridge between PPy and MWCNTs, as depicted in Figure 7.9. Serving as an interface modifier, NiO contributes to the enhancement of interactions between PPy and MWCNTs. The decoration of NiO nanoparticles on the surface of MWCNTs forms a strong connection between the two components. This bridge–like structure allows efficient charge transfer and facilitates electron transport across the composite through π–π and hydrogen bonding interactions, as illustrated in Figure 7.9. The weight percentages of PPy, MWCNTs, and NiO within the nanocomposite are critical, balancing their contributions is essential for achieving enhanced electrical conductivity and an improved Seebeck coefficient, ultimately optimizing the thermoelectric performance.

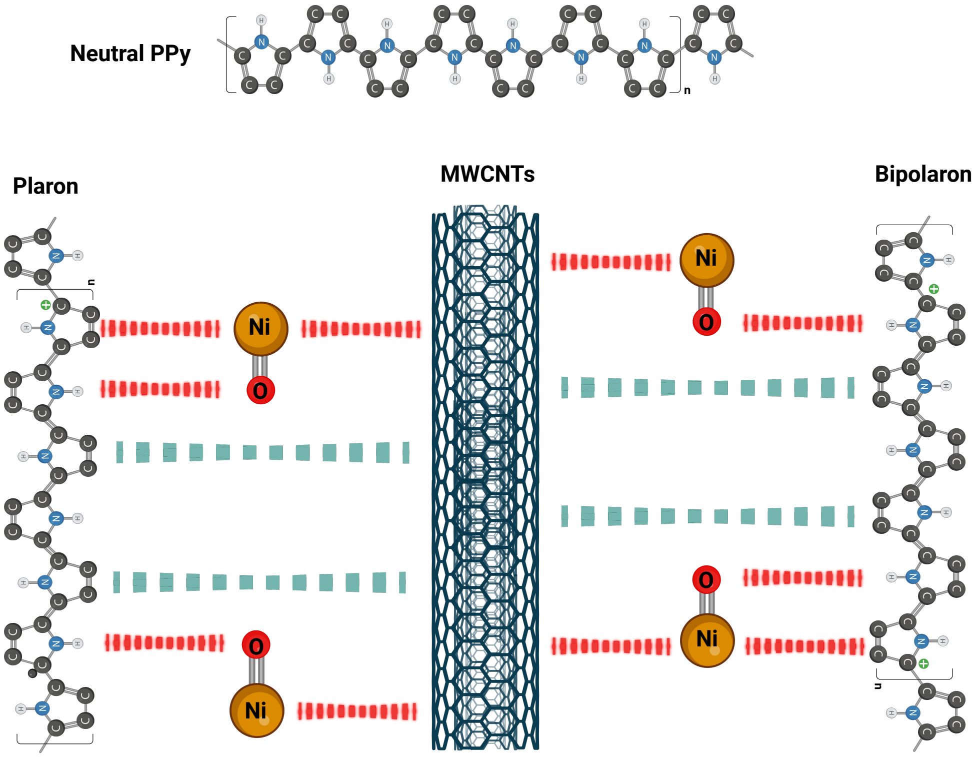

Figure 7.9: Schematic representation of the PPy, NiO and MWCNTs interactions in the PPy–MWCNTs–D3–NiO nanocomposite.

Electrical Conductivity. The electrical conductivity values, obtained through a four–point probe technique and illustrated in Figure 7.10, highlight significant insights. PPy in the form of nanotubes exhibits an impressive electrical conductivity of ~2160 Sm^{-1}, higher than reported values for PPy with a spherical morphology (~1000 Sm^{-1}, previous chapters) [238, 259] and agreeing with findings from other studies [232]. This difference is primarily attributed to the morphology, influencing the packing arrangement and interconnectivity. The more elongated shape of PPy nanotubes forms well–aligned structures, promoting efficient charge transfer pathways and enhancing electrical conductivity.

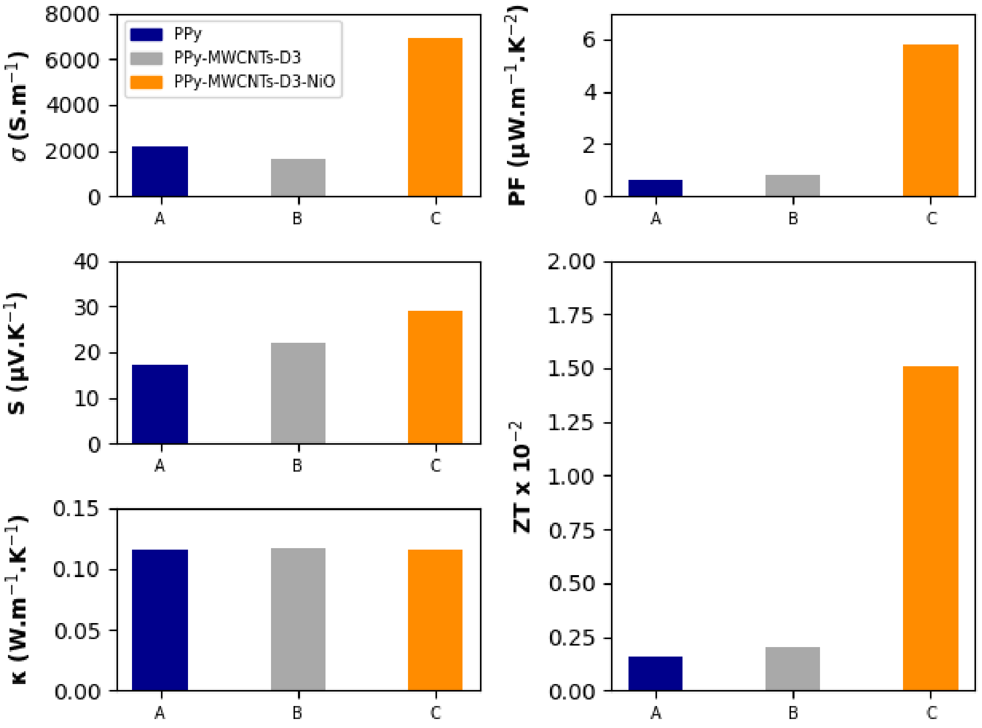

Figure 7.10: Thermoelectric properties of the synthesized materials.

However, when PPy nanotubes are combined with MWCNTs–D3, the electrical conductivity of the nanocomposite decreases to 1628 Sm^{-1}. This change is attributed to the presence of grafted benzenetricarboxylic acid groups on the sidewall of MWCNTs, which hinders charge carriers, as reported in Chapter 5 §5.3.4. The PPy–MWCNTs–D3–NiO nanocomposite, on the other hand, exhibits a substantially higher electrical conductivity (~6923 Sm^{-1}). This enhancement is likely attributed to the role of NiO in the charge transport mechanism, creating more interfaces between PPy nanotubes and MWCNTs. NiO acts as conductive pathways through which electrons can flow, thereby improving the overall conductivity of the nanocomposite.

Seebeck Coefficient. The Seebeck coefficient values, obtained using a homemade setup (Appendix B), are depicted in Figure 7.10, providing valuable insights into the thermoelectric performance. PPy nanotubes exhibit a Seebeck coefficient of 17 μVK^{-1}, aligning with reported values for PPy synthesized under similar conditions [232]. This is notably higher than the Seebeck coefficient reported for spherical PPy morphology (around 8–11 μVK^{-1}).

Upon introducing MWCNTs–D3 to PPy, the resulting Seebeck coefficient increases to ~22 μVK^{-1}. This enhancement can be attributed to the presence of benzenetricarboxylic acid groups, which maintain the wrapping of PPy nanotubes around MWCNTs, improving the interaction between the PPy chains and functionalized MWCNTs.

The incorporation of both MWCNTs and NiO nanoparticles in PPy significantly improves the overall Seebeck coefficient to 29 μVK^{-1}. This enhancement can be explained by the fact that the resulting PPy is p–doped and can act as an electron acceptor, allowing electrons to flow from MWCNTs–D3–NiO to PPy. This electron transfer mechanism contributes to the increased Seebeck coefficient in the composite.

Thermal Conductivity. The thermal conductivity (κ) results, presented in Figure 7.10 and detailed in Table 7.3, were determined using a homemade setup (Appendix C) by applying a current (1.31 A) and measuring thermal conductance (K), related to thermal conductivity by a linear equation ($K = A + \kappa \cdot B$). Interestingly, all samples exhibit similar thermal conductivities, ~0.116 $Wm^{-1}K^{-1}$. This no change agrees with other reported values [259, 260] and suggests that the incorporation of well–dispersed MWCNTs–D3 and MWCNTs–D3–NiO in the PPy matrix, facilitated by the templating effect, results in an ordered one–dimensional nanocomposite. The observed low κ is favorable for TE materials, highlighting the potential of the synthesized materials in TE applications.

Table 7.3: Thermal conductance and conductivity of the prepared samples.

Sample	ΔT (K)	ΔV (V)	K (WK^{-1}) $\times 10^{-3}$	κ ($Wm^{-1}K^{-1}$)
PPy	54.2	0.0315	0.761	0.1158
PPy–MWCNTs–D3	46.3	0.0352	0.996	0.1164
PPy–MWCNTs–D3–NiO	42.1	0.0209	0.650	0.1154

Power Factor and Figure of Merit. The power factor (PF) value, as illustrated in Figure 7.10, demonstrates the promising thermoelectric characteristics of the synthesized materials. PPy nanotubes exhibit a PF value of 0.62 $\mu Wm^{-1}K^{-2}$, higher than reported values for PPy with spherical particles (~0.08 $\mu Wm^{-1}K^{-2}$, Chapter 6). The introduction of MWCNTs–D3 and MWCNTs–D3–NiO further enhances the PF values to 0.79 $\mu Wm^{-1}K^{-2}$ and 5.82 $\mu Wm^{-1}K^{-2}$, respectively. The highest PF observed in PPy–MWCNTs–D3–NiO is attributed to its high electrical conductivity values and Seebeck coefficient, better than the PF values of the other samples and being 9 times that of pure PPy.

The calculated values of figures of merit, ZT, shown in Figure 7.10, further highlight the superior thermoelectric performance of PPy–MWCNTs–D3–NiO. With the highest ZT value of 1.51×10^{-2} observed at room temperature, it exhibits better performance compared to PPy–MWCNTs–D3 (0.20×10^{-2}) and PPy (0.16×10^{-2}) by 7.5 times and 9 times, respectively. These results highlight the substantial potential of PPy–MWCNTs–D3–NiO as a highly efficient thermoelectric material.

The combination of PPy's nanotube morphology and the effective dispersion and decoration of NiO on the MWCNTs sidewall has significantly boosted the TE properties of the composite. The attained TE value suggests that TE performance can be adjusted by modifying the morphology and precisely managing the decoration process of metal oxides on MWCNTs. It is important to note that the observed results at room temperature might see further improvements at higher temperatures.

7.4 Conclusions

Given the limitations of organic thermoelectric materials, this approach involved a customized and revised synthesis strategy to create a hybrid nanocomposite comprising PPy nanotubes, MWCNTs, and NiO nanoparticles. Leveraging the applicability of diazonium chemistry for surface functionalization, this method successfully formed NiO nanoparticles on MWCNTs. The sequential process involved the in–situ generation of a diazonium derivative from 5–amino–1,2,3–benzene tricarboxylic acid to functionalize MWCNTs, followed by nickel (II) nitrate hexahydrate (NNH) impregnation and material calcination at 450 °C. The choice of the dopant molecule, methyl orange (MO), in the chemical polymerization of pyrrole resulted in a tubular form. Comprehensive structural, morphological, and thermal analyses were conducted, highlighting the preservation of the nanotubular structure of the PPy backbone at all steps of materials' modification. This structure uniformly wrapped MWCNTs–D3–NiO, promoting good dispersion and enhanced interfacial interactions between the PPy backbone and MWCNTs. This strategic approach led to an enhanced Seebeck coefficient (S) and electrical conductivity (σ), while maintaining low thermal conductivity (κ). Consequently, the figure of merit (ZT) at room temperature reached 1.51×10^{-2} for PPy–MWCNTs–D3–NiO, which is nine times higher than that of PPy nanotubes.

As we move forward into the next chapter, we will bring together the findings from all experimental chapters to facilitate a comprehensive comparison. This collective analysis aims to provide a comprehensive understanding of the diverse strategies employed and their respective impacts on thermoelectric performance.

Part III

Closing Comments

CHAPTER 8

Unraveling Thermoelectric Strategies: A Cross–Chapter Examination

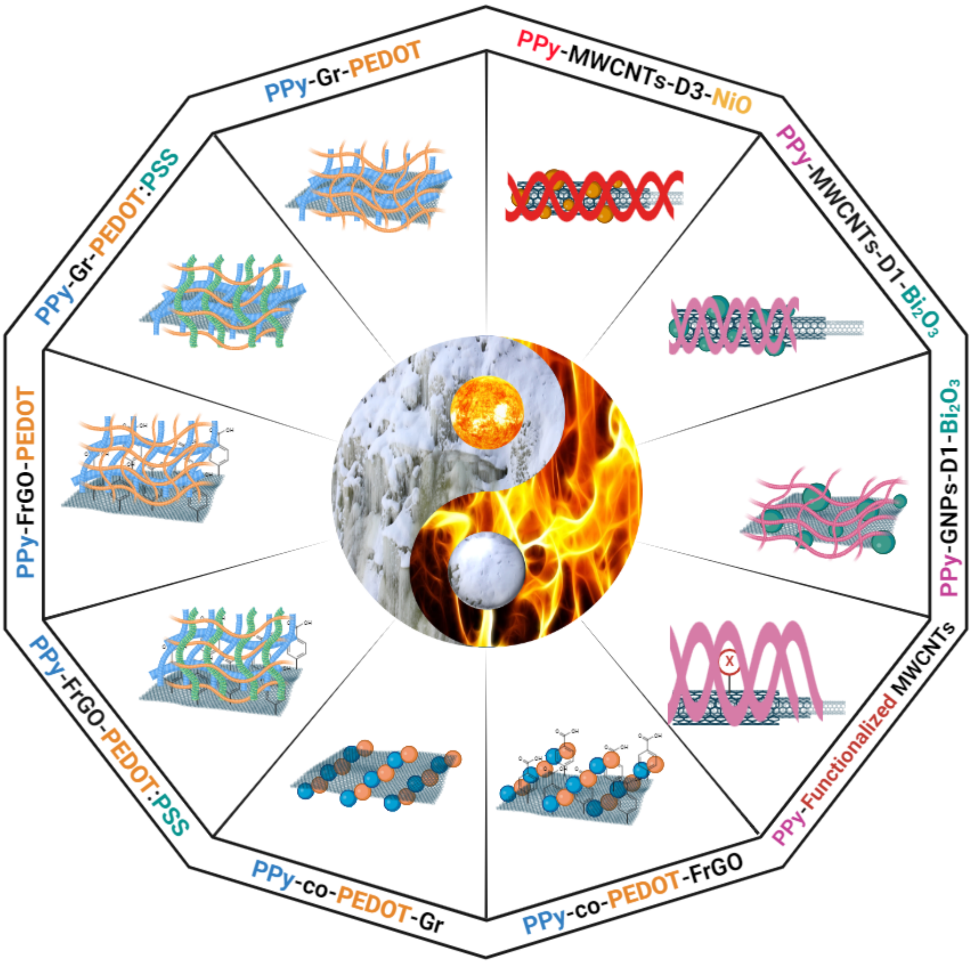

8.1 General Introduction

Building upon the foundation of previous chapters, this chapter explores a comprehensive examination of thermoelectric strategies, synthesizing insights from across our scientific findings. Our aim is to unravel the relationships between synthesis techniques, material properties, and thermoelectric performance.

Throughout the preceding chapters, we have explored diverse approaches to optimize thermoelectric potential, ranging from surface functionalization techniques to the incorporation of nanostructured additives. In this cross–chapter examination, we will analyze the collective findings, drawing parallels and contrasts to find the main principles governing thermoelectric enhancement.

Through a systematic review of experimental results, we will explain the synergistic effects of various optimization strategies on thermoelectric properties such as electrical conductivity, thermal conductivity, and Seebeck coefficient.

Through this cross–chapter examination, we aim not just to bring together the results from different studies, but also to discuss and compare the results of the different studies. Ultimately, our goal is to contribute to the collective effort towards sustainable energy solutions by unraveling the complexities of thermoelectric materials design.

8.1.1 Outline

The chapter begins by explaining how the structure and composition of thermoelectric materials affect their properties, known as the matrix effect (PPy, PEDOT, PEDOT:PSS). It then discusses the use of fillers (GNPs, MWCNTs, and their derivatives) to enhance these properties. Different methods for synthesizing thermoelectric materials are explored. The chapter also addresses current challenges and future research directions. Finally, it concludes by summarizing key findings.

8.2 Matrix Effect

Our investigation begins with polypyrrole–functionalized graphene oxide (PPy–FrGO) binary composite. Through systematic study, we have demonstrated the effects of adding PEDOT (Poly(3,4–ethylenedioxythiophene)) to PPy via two distinct methods: direct mechanical mixing (PPy–PEDOT) and copolymerization (PPy–co–PEDOT). The outcomes of these investigations illuminate the interplay between matrix engineering and thermoelectric (TE) performance. Furthermore, our examination extends to the inclusion of PEDOT:PSS (Poly(3,4–ethylenedioxythiophene) polystyrene sulfonate), a well–studied conductive polymer blend, to further explore its impact on TE properties. By summarizing the findings from previous chapters, we aim to provide a comprehensive understanding of how these modifications collectively influence the TE behavior of the composite materials.

As detailed in Chapter 4, the ternary composites were synthesized and their TE properties were measured. To investigate the influence of the matrix effect on the TE properties of materials, we used PPy–FrGO as a reference material and compared their properties with those of its ternary composite derivatives (PPy–FrGO–PEDOT, PPy–co–PEDOT–FrGO and PPy–FrGO–PEDOT:PSS), as shown in Figure 8.1.

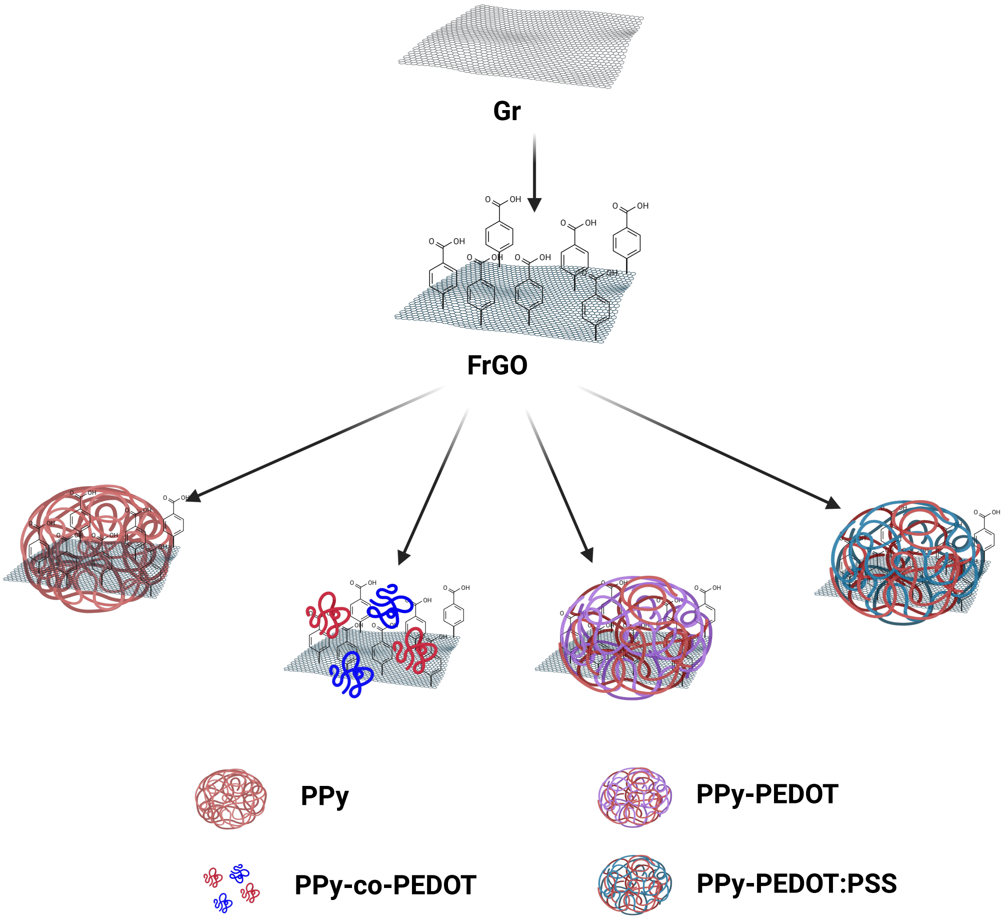

Figure 8.1: Schematic representation of different synthesized PPy–based nanocomposites.

The observed improvement in thermoelectric properties in ternary composites compared to binary reference composite suggests the pivotal role played by the blended matrix, Figure 8.2. This enhancement is driven by synergistic effects, where the ternary composites amalgamate multiple materials possessing complementary properties. For instance, the incorporation of PEDOT or PEDOT:PSS into the matrix can introduce additional charge carriers, thereby augmenting electrical conductivity.

Moreover, it is evident that directly mixing PEDOT leads to higher electrical conductivity than either PEDOT:PSS or copolymerized PEDOT with PPy. This disparity can be attributed to interface effects, wherein the junction between PEDOT and the host matrix (e.g., PPy) facilitates superior charge transfer. Consequently, the electrical conductivity is enhanced compared to instances where PEDOT is copolymerized with PPy or blended with PSS.

In addition to the enhanced electrical conductivity observed in ternary composites, the Seebeck coefficient, or thermopower, is another criterion to evaluate the thermoelectric properties. It quantifies a material's ability to generate a voltage difference when subjected to a temperature gradient. Adding to PPy, PEDOT or PEDOT:PSS to form new matrices can contribute to an increase in the Seebeck coefficient, thereby enhancing the overall thermoelectric performance of the composite.

Furthermore, while the electrical conductivity is notably improved, it is noteworthy that the thermal conductivity remains largely unchanged in these ternary composites. This aspect is crucial as a high thermal conductivity would facilitate excessive heat dissipation, diminishing the temperature gradient necessary for efficient thermoelectric conversion. Therefore, the maintenance of an unchanged thermal conductivity, alongside improvements in electrical conductivity and Seebeck coefficient, highlights the potential of these ternary composites for thermoelectric applications which are observed in ZT values.

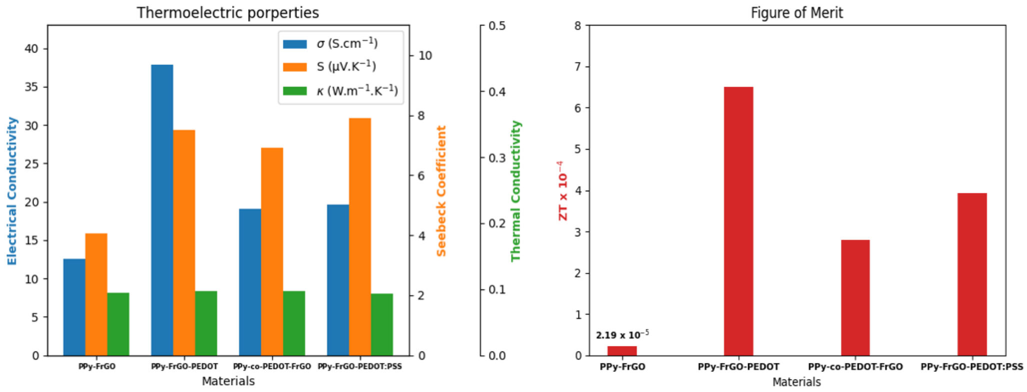

Figure 8.2: Thermoelectric properties of PPy–FrGO, PPy–FrGO–PEDOT, PPy–co–PEDOT–FrGO and PPy–FrGO–PEDOT:PSS.

8.3 Fillers Effect

The thermoelectric behavior of PPy–based composites can be significantly influenced by the incorporation of various fillers, including GNPs, functionalized GNPs, GNPs–Bi_2O_3 hybrids, MWCNTs, functionalized MWCNTs, MWCNTs–Bi_2O_3 hybrids, and MWCNTs–NiO hybrids. Each type of filler contributes differently to the overall thermoelectric performance of the composite materials, Figure 8.3.

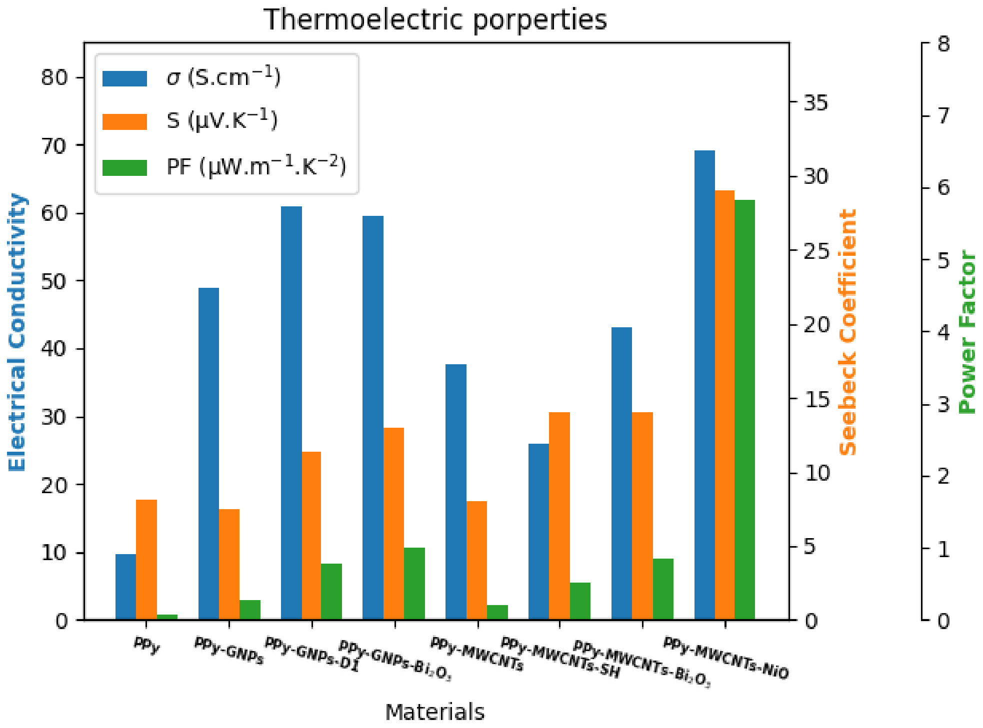

Figure 8.3: TE properties of binary and ternary PPy–based nanocomposites.

When GNPs are incorporated into PPy–based composites, electrical conductivity is enhanced due to their high surface area and excellent charge transport properties. This results in improved thermoelectric performance by facilitating efficient electron transport within the composite material. Furthermore, functionalization of GNPs improves the compatibility between GNPs and the PPy matrix, leading to better dispersion and stronger interfacial interactions, which further improve the electrical conductivity and thermoelectric properties.

Incorporating GNPs–Bi_2O_3 hybrids into PPy–based composites provides additional benefits for thermoelectric applications. Bi_2O_3 nanoparticles as they act as bridges, thereby facilitating the interface interactions and enhancing the thermoelectric power factor (PF). Moreover, the synergistic effects between GNPs and Bi_2O_3 nanoparticles can lead to enhanced electrical conductivity and thermoelectric performance compared to composites with individual fillers.

Similarly, the inclusion of MWCNTs in PPy–based composites improves electrical conductivity and TE performance due to their one–dimensional structure and high aspect ratio, which facilitate efficient charge transport. Functionalized MWCNTs further enhance compatibility with the PPy matrix, promoting better dispersion and interfacial adhesion, leading to improved thermoelectric properties.

Introducing MWCNTs–Bi_2O_3 hybrids or MWCNTs–NiO hybrids into PPy–based composites offers opportunities to simultaneously enhance electrical conductivity and reduce thermal conductivity. The choice of Bi_2O_3 and NiO among other metal oxides was based on their thermoelectric properties, compatibility with graphitic materials (GNPs and MWCNTs), and ease of synthesis. The incorporation of Bi_2O_3 or NiO nanoparticles scatter phonons, thereby lowering thermal conductivity, while GNPs and MWCNTs contribute to enhanced electrical conductivity. The combination of these fillers results in synergistic effects, leading to improved thermoelectric performance compared to composites with individual fillers.

In summary, as depicted in Figure 8.4, the choice and combination of fillers play a crucial role in tailoring the thermoelectric behavior of PPy–based composites. By carefully selecting and engineering fillers, it is possible to enhance electrical conductivity, reduce thermal conductivity, and improve the overall thermoelectric performance of these materials for various applications, including energy harvesting and waste heat recovery.

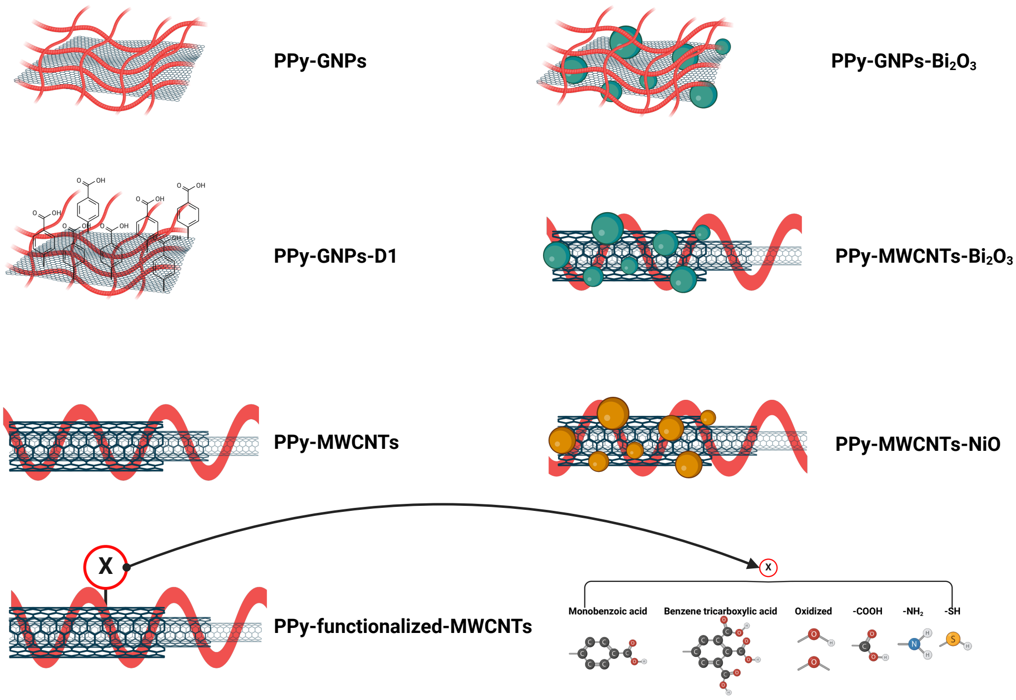

Figure 8.4: Schematic representation of PPy–based nanocomposites with different fillers.

In the context of in–situ generation of metal oxides, diazonium precursors serve as functionalization agents for carbon–based materials, such as carbon nanotubes or graphene, by covalently attaching metal oxide precursors onto their surfaces.

4–aminobenzoic acid (–D1) and 5–amino–1,2,3–benzene tricarboxylic acid (–D3) are both aromatic carboxylic acids commonly used as diazonium precursors in functionalization reactions. The choice between these two precursors depends on several factors, including the desired properties of the resulting material and the specific application requirements.

–D1 (used to anchor Bi_2O_3 on the surface of GNPs and MWCNTs), being a monofunctional aromatic carboxylic acid, typically leads to the attachment of a single metal oxide precursor moiety onto the carbon substrate. This results in a lower density of metal oxide functional groups on the surface of the carbon material. However, the use of –D1 can offer advantages such as improved dispersibility of the functionalized carbon material in solution and potentially better control over the functionalization process due to the presence of only one functional group per diazonium molecule. Moreover, in this case, multi–layers could be formed as the aryl diazonium radical can also react on the free positions of the phenyl, Figure 8.5.

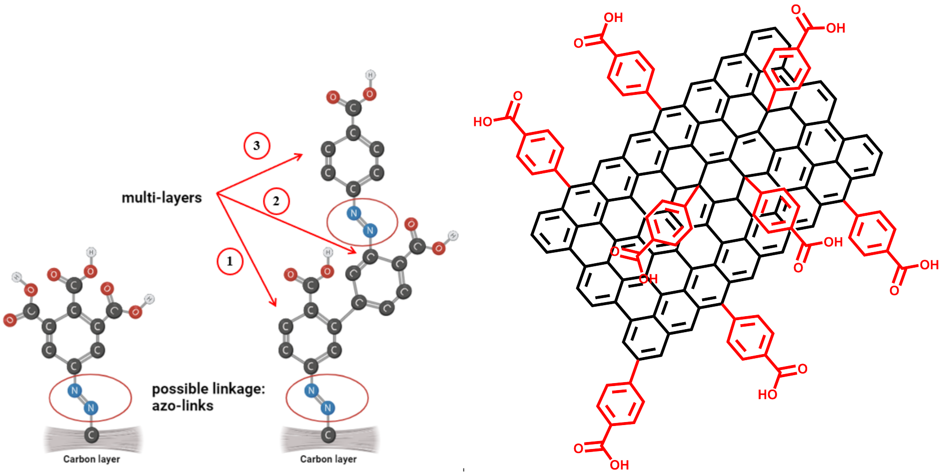

Figure 8.5: Possible linkage and 2D structure of functionalized GNPs.

Functional groups are covalently bonded to the carbon atoms [261], Figure 8.5, disrupting the material's π–conjugation by introducing sp^3 hybridization at the attachment sites. This breaks the continuous delocalized electron system, altering its electronic properties. While this disruption reduces conductivity, it enhances chemical reactivity and increases the material's potential for adsorbing metal ions or anchoring metal oxide nanoparticles.

On the other hand, –D3 (used to anchor NiO on the surface of MWCNTs), being a polyfunctional aromatic carboxylic acid with three carboxylic acid groups, allows the attachment of multiple metal oxide precursor moieties onto the carbon substrate.

This results in a higher density of metal oxide functional groups on the carbon surface compared to –D1. The increased density of functional groups can lead to enhanced chemical reactivity, improved interfacial interactions, and potentially higher loading of metal oxide species.

8.4 Conducting Polymer Synthesis Effect

Sodium dodecyl benzene sulfonate (SDBS) is a surfactant commonly used as a dopant agent in the synthesis of conductive polymers like PPy. When SDBS is employed, it typically leads to the formation of globular or spherical morphologies within the PPy structure, Figure 8.6. This globular morphology is formed due to the surfactant's ability to stabilize PPy chains and control their growth during polymerization. As a result, the PPy chains are distributed uniformly, and the material exhibits a higher surface area compared to other morphologies. The presence of globular structures facilitates efficient charge transport within the material, leading to enhanced electrical conductivity. Moreover, the boundaries and interfaces introduced by the globular morphology scatter phonons effectively, thereby reducing thermal conductivity and improving ZT. Additionally, the controlled growth of PPy chains in globular morphologies results in a more ordered structure, leading to higher Seebeck coefficients and improved thermoelectric performance.

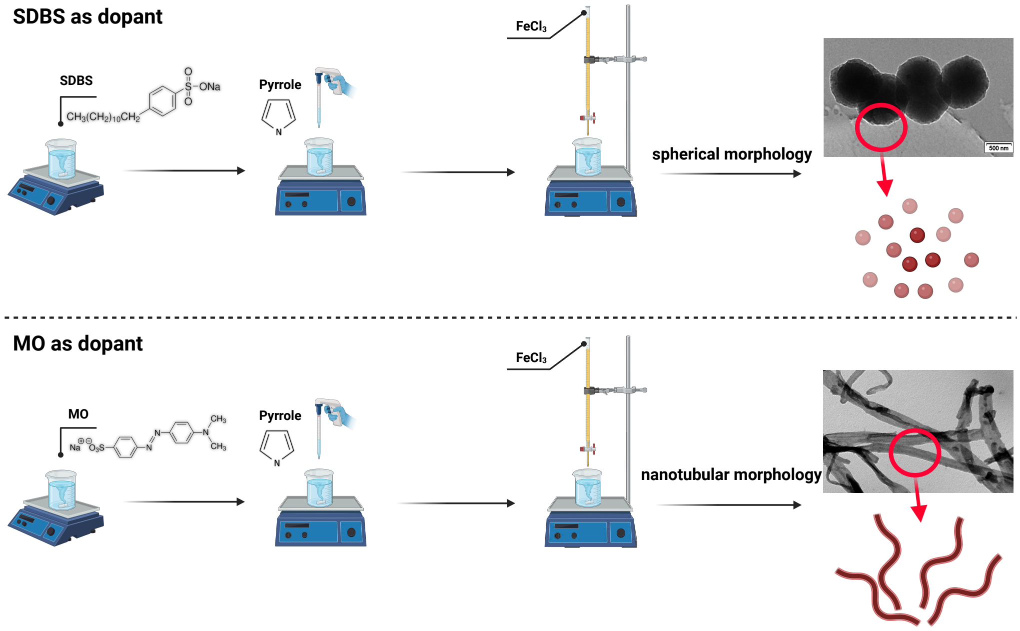

Figure 8.6: Illustration of different routes of synthesis of PPy.

In contrast, methyl orange (MO), another dopant agent used in PPy synthesis, induces the formation of tubular or fiber–like morphologies within the polymer structure, Figure 8.6.

The tubular morphology is formed due to the planar structure of MO, which influences polymerization chain growth, resulting in elongated or tubular structures. The tubular structure of PPy nanotubes allows more directional charge transport along the length of the tubes. Moreover, the elongated shape and specific orientation of PPy nanotubes provide effective phonon scattering sites, leading to reduced thermal conductivity thereby enhancing ZT.

Figure 8.7 shows the TE properties of both morphologies, PPy nanotubes demonstrate better TE properties compared to PPy globules due to their higher surface–to–volume ratio, allowing more efficient charge transport. Moreover, the directional charge transport along the length of the nanotubes leads to lower electrical resistance and improved conductivity, while their elongated shape provides effective phonon scattering sites, resulting in reduced thermal conductivity and enhanced ZT.

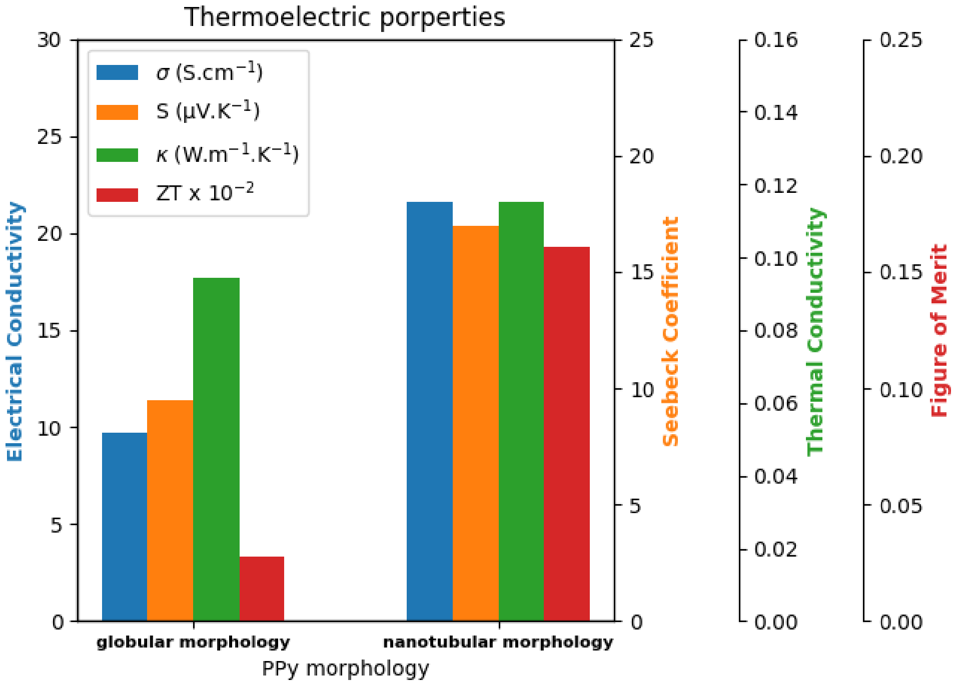

Figure 8.7: Thermoelectric behavior of PPy with two different morphologies.

8.5 Limitations and Future Directions

Limitations in the current study open potential areas for further optimization in blending ratios of PEDOT or PEDOT:PSS with the PPy matrix. The study has been confined to a limited range of ratios, possibly missing out on an optimal composition for maximizing thermoelectric performance.

Additionally, the characterization techniques utilized may not have fully captured the intricacies of the composite materials, suggesting a need for more sophisticated methods such as: High–Resolution TEM (HRTM), charge carrier and density measurements, and ZT–meter, to delve deeper into their nanostructure and thermoelectric behavior. The stability and durability of the ternary composites under real–world conditions were not investigated, leaving questions about their long–term performance and reliability unanswered.

Moreover, understanding the synergistic effects and trade–offs between various fillers in ternary or quaternary composites is crucial for optimizing the thermoelectric performance of PPy–based materials. Each filler type contributes unique properties to the composite, such as enhancing electrical conductivity, reducing thermal conductivity, or improving compatibility with the PPy matrix. However, when multiple fillers are combined, their interactions can lead to synergistic effects, where the overall thermoelectric performance is greater than the sum of its individual components. On the other hand, there are also trade–offs to consider when incorporating multiple fillers. For instance, increasing the loading of certain fillers to improve one aspect of thermoelectric performance, such as electrical conductivity, may inadvertently lead to an increase in thermal conductivity, counteracting the desired effect. Balancing these trade–offs requires a deep understanding of the interactions between fillers, the PPy matrix, and the resulting composite structure. Furthermore, optimizing the filler composition and distribution within the composite is essential to achieve the desired balance of properties for efficient thermoelectric conversion.

Furthermore, the use of dopant agents such as sodium dodecyl benzene sulfonate (SDBS) and methyl orange (MO) in the synthesis of conductive polymers like PPy significantly influences the resulting morphologies and, consequently, the TE properties of the materials. The differences between SDBS–induced globular morphologies and MO–induced tubular morphologies in PPy significantly impact the thermoelectric properties of the material. Globular morphologies offer advantages such as enhanced charge transport, reduced thermal conductivity, and higher Seebeck coefficients, leading to improved thermoelectric performance. Understanding these differences is crucial for tailoring the morphology of PPy–based materials to optimize their thermoelectric properties for various applications.

Moving forward, future research could focus on fine–tuning the nanostructure and morphology of ternary composites to optimize their thermoelectric properties. This could involve exploring alternative synthesis methods such as different dopants resulting in different morphologies, and alternative additives such as 0D (quantum dots), 1D (SWCNTs), 2D (MXene with the general formula of $M_{n+1}X_n$: M being an early transition metal, and X being carbon or nitrogen) or 3D (Metal–organic frameworks) materials to achieve enhanced performance. Furthermore, exploring a broader range of materials beyond PEDOT and PEDOT:PSS to form binary or ternary matrices could expand the design space for high–performance thermoelectric composites.

Moreover, further research is needed to explain the processes and optimize morphology control strategies for enhanced thermoelectric performance by focusing on the dopant effect on the TE properties. Integration of these composites into prototype thermoelectric devices and evaluating their performance under realistic conditions would be crucial for assessing their potential for practical applications.

8.6 Conclusions

In conclusion, our investigation into thermoelectric materials has yielded valuable insights into their optimization and potential applications. Through the synthesis of findings from various studies, we have identified fundamental principles (electrical conductivity, Seebeck coefficient, and thermal conductivity) governing thermoelectric enhancement, such as material composition and processing techniques.

Looking ahead, there remain challenges to be addressed, further research and innovation will be crucial in advancing thermoelectric technology and exploiting its full potential for sustainable energy solutions.

CHAPTER 9

CONCLUSION

To address the issue of the global demand for energy, there is a method that allows minimizing energy losses by recovering and directly converting residual heat into useful electrical energy. This method involves thermoelectric (TE) energy technology. This thesis investigates several challenges in enhancing the thermoelectric properties of conducting polymer–based composites.

The first part of this work involved a comprehensive literature review focused on the principles of thermoelectricity, traditional thermoelectric materials, and innovative approaches in conductive polymers and thermoelectric composites. This background and literature enhance the understanding of key challenges, backup the choice of studied polymers and fillers, and guide the development of their preparation methods. By exploring the physical concepts and recent advancements, the review aimed to address the limitations of existing materials and identify promising alternatives for efficient thermoelectric applications.

The second part explores four research questions to be addressed in this thesis. The first treats how do surface modifications of graphene and different synthesis methods (direct mixing or copolymerization) affect the thermoelectric properties of ternary composites based on polypyrrole (PPy) and either poly(3,4–ethylenedioxythiophene) (PEDOT) or PEDOT:polystyrene sulfonate (PEDOT:PSS). One significant finding was that functionalizing graphene with diazonium salts and employing a mixing procedure greatly improved the thermoelectric performance, particularly in the PPy–FrGO–PEDOT nanocomposite, which showed a remarkable enhancement in its power factor (PF) and figure of merit (ZT) of 0.21 $\mu W m^{-1} K^{-2}$ and 6.51×10^{-4}, respectively, while those of PPy are 8.6×10^{-4} $\mu W m^{-1} K^{-2}$ and 2.7×10^{-6}, respectively. This was attributed to better adhesion and distribution of the polymers atop the functionalized graphene and promoting better charge mobility.

The question aimed to be answered in the fifth chapter was about how do different functional groups (benzoic acid, benzene tricarboxylic acid, hydroxyl, carboxyl, amino, and thiol) grafted onto multi–walled carbon nanotubes (MWCNTs) influence the thermoelectric properties of PPy–MWCNTs nanocomposites. The grafting of functional groups involved the use of chemistry of diazonium and infrared irradiation approach. It was found that these functions generally reduce electrical conductivity, however increase the Seebeck coefficient. The composites were synthesized by adopting an in–situ oxidative polymerization of pyrrole on the functionalized MWCNTs to wrap them with polypyrrole. Among the functional groups tested, thiol–functionalized MWCNTs (MWCNTs–SH) demonstrated the most promising results, achieving a power factor significantly higher than that of pure PPy of 0.51 $\mu Wm^{-1}K^{-2}$ and 0.064 $\mu Wm^{-1}K^{-2}$, respectively. While the power factor achieved is comparable to that of some PPy composites, such as PPy Nanowire/Graphene at 0.61 $\mu Wm^{-1}K^{-2}$ [128], PPy/MWCNTs at 0.77 $\mu Wm^{-1}K^{-2}$ [139] and PPy/MWCNTs/Ni$(OH)_2$ at 0.2 $\mu Wm^{-1}K^{-2}$ [153], it is still lower than some materials reported in the literature, such as PPy/MWCNTs (68 wt.%) at 2.2 $\mu Wm^{-1}K^{-2}$ [262] and PPy:NPs and double–walled carbon nanotube–graphene oxide at 0.96 $\mu Wm^{-1}K^{-2}$ [263]. The power factor can vary depending on the specific composition (fillers concentration) and synthesis method of the composite, which opens avenues for further research and improvement.

Further research was conducted on elaborating hybrid composites by incorporating graphene nanoplatelets (GNPs) or MWCNTs and bismuth oxide nanoparticles (Bi_2O_3) to enhance the thermoelectric conversion efficiency of PPy–based nanocomposites. The decoration of GNPs and MWCNTs with nanoparticles involved three steps: functionalization of GNPs or MWCNTs with diazonium salt (–D1), impregnation with bismuth precursor, and calcination. The hybrid material, PPy-GNPs–Bi_2O_3, showed an eleven–fold increase in power factor (1 $\mu Wm^{-1}K^{-2}$) compared to pure PPy (0.087 $\mu Wm^{-1}K^{-2}$). This improvement was attributed to enhanced charge transport and π–π stacking interactions between the PPy chains and the GNPs surfaces, with Bi_2O_3 playing a crucial role in binding both PPy and GNPs and improving the overall thermoelectric behavior.

Moreover, the inclusion of Bi_2O_3 in PPy–MWCNTs composites was examined, revealing that the PPy–MWCNTs–Bi_2O_3 nanocomposite exhibited a higher power factor (0.843 $\mu Wm^{-1}K^{-2}$) than both pure PPy (0.087 $\mu Wm^{-1}K^{-2}$) and PPy–MWCNTs (0.21 $\mu Wm^{-1}K^{-2}$). This underlines the significant role of Bi_2O_3 in enhancing charge transport within the composite matrix.

Lastly, the study explored the impact of nickel oxide (NiO) decorated MWCNTs in a PPy nanocomposite on its thermoelectric properties at room temperature. The customized method for incorporating NiO–decorated MWCNTs involved three steps: functionalizing MWCNTs with diazonium salt grafting (–D3), generating NiO nanoparticles on their surfaces, and chemically polymerizing pyrrole using methyl orange as a template and dopant.

This resulted in a nanocomposite with significantly higher Seebeck coefficient, electrical conductivity, and power factor (5.82 $\mu Wm^{-1}K^{-2}$) compared to both PPy and PPy–MWCNTs–D3 (0.62 $\mu Wm^{-1}K^{-2}$ and 0.78 $\mu Wm^{-1}K^{-2}$). The presence of NiO acted as a dopant, increasing charge carrier density and contributing to the highest recorded figure of merit ($ZT = 1.51 \times 10^{-2}$) among the studied materials. Given that there are few research on hybrid organic metal oxide composites for thermoelectric energy conversion, the power factor and ZT, at room temperature, of PPy/MWCNTs/Metal oxide nanocomposites achieved in this work was highly superior to reported values with metal oxides PPy/MWCNTs/$Ni(OH)_2$ at 0.2 $\mu Wm^{-1}K^{-2}$ [153], PPy/Graphene/NiO at 0.435 $\mu Wm^{-1}K^{-2}$ (at 60 °C) [229], PPy/Te (1 wt.%) at 1.064 $\mu Wm^{-1}K^{-2}$ (at 100 °C) [230], and for PPy/SnS (20 wt.%), the PF and ZT values at 100 °C are 6 $\mu Wm^{-1}K^{-2}$ and 0.86×10^{-2}, respectively [264].

The third part encompasses all the aforementioned contributions, examining the materials, the effects of matrices, fillers, and the synthesis methods of conducting polymers, resulting in various morphologies and their impact on thermoelectric properties.

Moving forward, it is crucial to study the relationship between charge carrier concentration and mobility with the thermoelectric properties of the developed materials and how these parameters evolve at different temperatures as in this work evaluation of TE properties has been done at room temperature. This will provide validation for the use of these materials in thermoelectric systems in applications, such as photovoltaic cells. Additionally, the exploration of other fillers, such as MXene, and their role in enhancing thermoelectric properties or the performance of other conducting polymers should be considered. A techno–economic analysis and a comprehensive study of the stability of the synthesized polymers and their composites, considering environmental conditions, should be investigated. This approach will ensure that the materials are not only high-performing but also viable for practical, large–scale applications.

Part IV

Appendix

APPENDIX A

ELECTRIC CONDUCTIVITY MEASUREMENTS USING FOUR–POINT PROBE METHOD

Electrical conductivity measurement was assessed with a Jandel Universal Probe station four–point probe, Figure A.1a. Composite powders were cold pressed at 7 tons into pellets using a hydraulic press (Specac) with 13 mm in diameter, and a loading duration of about 20–30 s each, Figure A.1b.

The four–point probe method is a widely used experimental technique for measuring the sheet resistance and/or resistivity of bulk semiconductor materials. This method is advantageous due to its simplicity and accuracy in determining these electrical properties, which are critical for evaluating semiconductor performance.

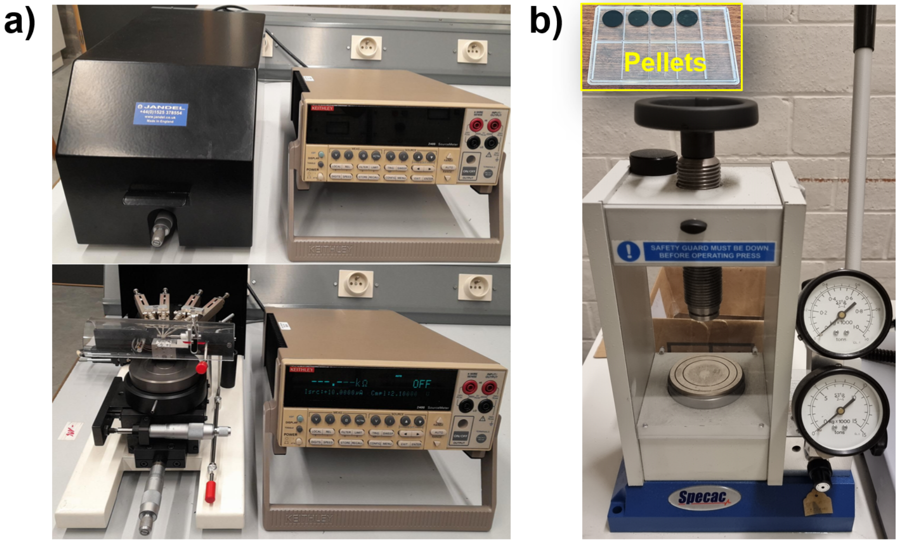

Figure A.1: a) Jandel Universal Probe station, b) hydraulic press Specac.

A.1 Setup and Procedure

The setup consists of four aligned and equidistant probes, which are pressed against the surface of the semiconductor sample. The distance (s) between the probes is designed to be small compared to the overall dimensions of the sample. This ensures that the measurements are focused on a localized area, minimizing edge effects and other potential sources of error.

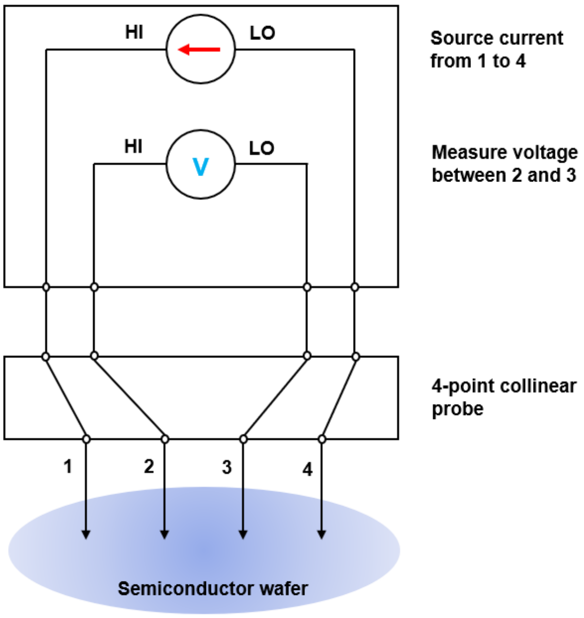

Figure A.2: Schematic representation for a four–point probe instrument.

A.1.1 Probe Arrangement

The four probes are arranged in a straight line, with equal spacing between each probe. The probes are usually spring–loaded to ensure consistent contact pressure on the sample surface.

A.1.2 Current Application

A current (I) is injected into the sample through the outermost probes (probe 1 and probe 4). This current flows through the sample, creating a voltage drop across it.

A.1.3 Voltage Measurement

The voltage difference (ΔV) is measured between the two inner probes (probe 2 and probe 3). This voltage measurement is crucial as it reflects the potential difference caused by the current flowing through the sample's resistive material.

A.2 Calculation of Resistivity and Conductivity

The key measurement in the four–point probe method is the voltage–to–current ratio ($\Delta V/I$). This ratio is directly related to the sample's resistivity (ρ), which can be calculated using the following formula, provided the sample is a thin film or has a uniform thickness:

$$\rho = \frac{\pi \cdot s}{\ln(2)} \cdot \frac{\Delta V}{I} \tag{A.1}$$

Where: ρ is the resistivity of the material, s is the distance between adjacent probes. ΔV is the measured voltage difference between probes 2 and 3. I is the current applied between probes 1 and 4.

For bulk materials, the formula may need adjustments to account for the sample thickness and other geometrical factors.

$$\rho = \frac{\pi \cdot s}{\ln(2)} \cdot \frac{\Delta V}{I} \cdot t \cdot k \tag{A.2}$$

Where: t is the sample thickness and k a correction factor based on the ratio of the probe to wafer diameter and on the ratio of wafer thickness to probe separation.

A.3 Estimation of Electrical Conductivity

Electrical conductivity (σ) is the reciprocal of resistivity:

$$\sigma = \frac{1}{\rho} \tag{A.3}$$

This calculation provides an estimation of how easily electrical current can flow through the material, a critical property for many electronic applications.

APPENDIX B

HOMEMADE EXPERIMENTAL DEVICE FOR SEEBECK COEFFICIENT MEASUREMENT

The Seebeck effect is a crucial parameter for determining the thermoelectric power of a material. Due to the lack of equipment capable of directly measuring this parameter, we developed an experimental setup tailored to the specific nature of the materials under study. This technique is based on measuring the potential difference (ΔV) between two terminals subjected to a temperature difference (ΔT).

In this context, we designed a device at the **Laboratory of Macromolecular Chemistry** at the **École Militaire Polytechnique, Algeria**, to determine the Seebeck coefficient for all the synthesized samples.

B.1 Principle of the Seebeck Effect

The Seebeck effect occurs when there is a temperature gradient across a material, which causes a voltage difference to develop between the hot and cold ends. This effect is used to measure the thermoelectric power or efficiency of a material.

B.2 Experimental Setup

The device was conceptualized using SolidWorks software, and was constructed in the **Laboratory of Macromolecular Chemistry** at the **École Militaire Polytechnique, Algeria**, specifically to measure the Seebeck coefficient, Figure B.1.

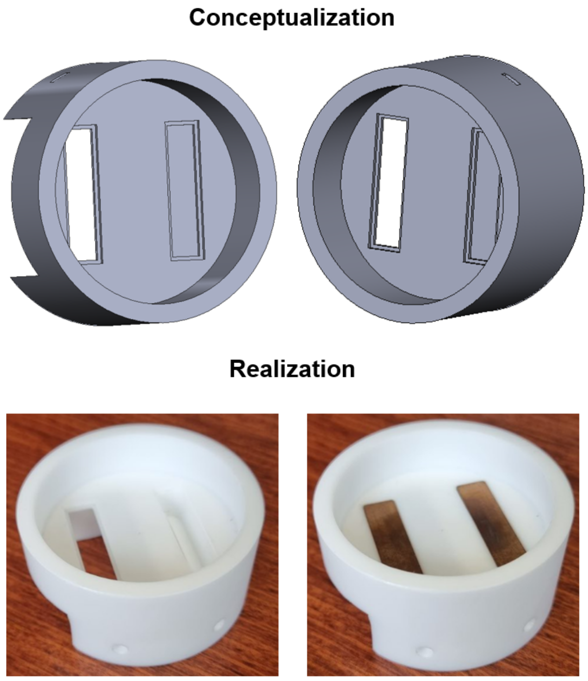

Figure B.1: Conceptualization and realization of a measurement cell of Seebeck coefficient.

The setup measures the voltage difference (ΔV) created when a temperature difference (ΔT) is applied across the sample. A controlled temperature difference is applied across the sample using heat sources and sinks to create a gradient. The resulting voltage difference (ΔV) between the two ends of the sample is then measured and $S = \Delta V / \Delta T$.

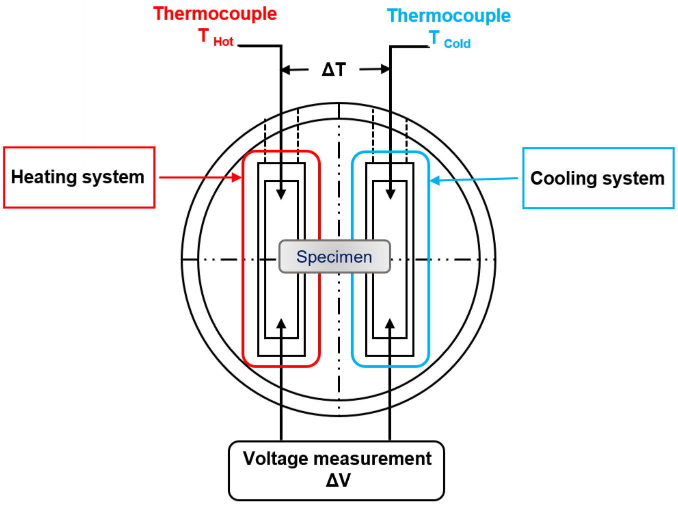

Figure B.2: Schematic presentation of homemade apparatus.

APPENDIX

C

HOMEMADE EXPERIMENTAL DEVICE FOR THERMAL CONDUCTIVITY MEASUREMENT

Thermal conductivity is a critical property for evaluating the thermoelectric performance of a material and calculating its figure of merit ZT. High thermal conductivity can reduce the efficiency of thermoelectric materials, as it allows heat to pass through without contributing to the electrical power output.

To measure the thermal conductivity of materials, a homemade setup was conceptualized and fabricated at the **Laboratory of Macromolecular Chemistry** at the **École Militaire Polytechnique, Algeria**. This device was calibrated using reference measurements obtained from a HOT–Disk device, ensuring the reliability of our results.

C.1 Design and Construction

The device was calibrated using reference measurements from a HOT–Disk device, which is known for its accuracy and reliability in thermal conductivity measurement. This step ensures that the custom setup provides results that are consistent with standard techniques, Figure C.1.

The hot ribbon method is a stationary regime technique developed for the thermal characterization of powders and porous materials. It focuses on determining the thermal conductivity (κ) of the materials in use. This method is recognized for its speed and precision, enabling the characterization of small–sized powders at ambient temperature and atmospheric pressure.

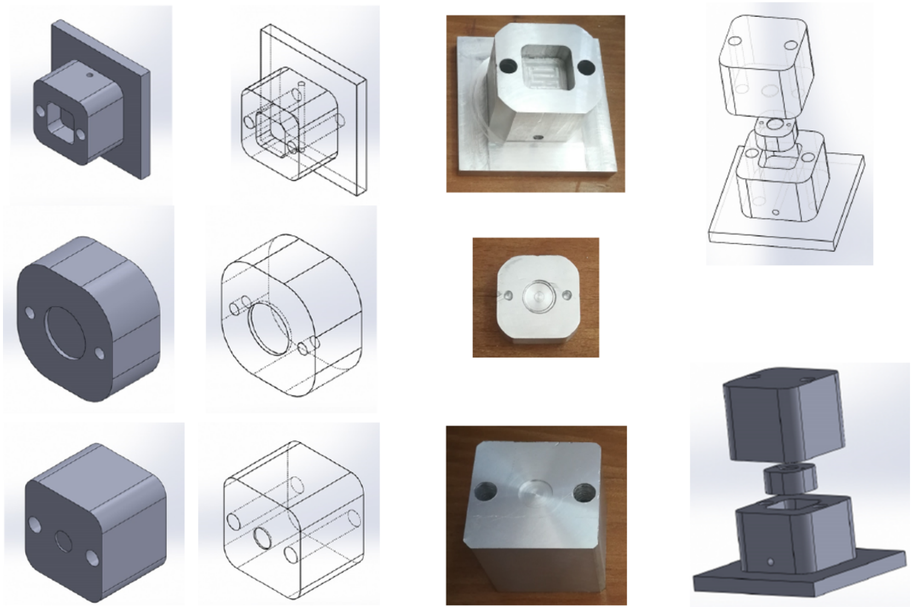

Figure C.1: Conceptualization and realization of the components of thermal conductivity measurements.

C.2 Principle of Operation

The sample to be characterized is placed in contact with a heating element made of a micro–ribbon composed of a Nickel–Chrome alloy. This ribbon is heated by the passage of an electric current. This method measures the thermal conductance K between the heating ribbon and the device. This is done by using the following relationship:

$$K = \frac{Q}{\Delta T} \tag{C.1}$$

Where ΔT is the temperature difference between the ribbon and the surrounding environment, and Q is the power supplied to the heating ribbon which can be calculated using the following equation:

$$Q = V \cdot I = \frac{V \cdot I}{R} \tag{C.2}$$

With V as the potential difference circulating through the hot ribbon, and I as the current intensity. This intensity is deduced by measuring the potential difference obtained between the two terminals of a calibrated 50 Ω resistor.

To obtain the thermal conductivity (κ), it is necessary to use a relationship that connects it to the thermal conductance (K). This relationship is characteristic of the measurement device and is established through prior calibration.

$$K = A + \kappa \cdot B \tag{C.3}$$

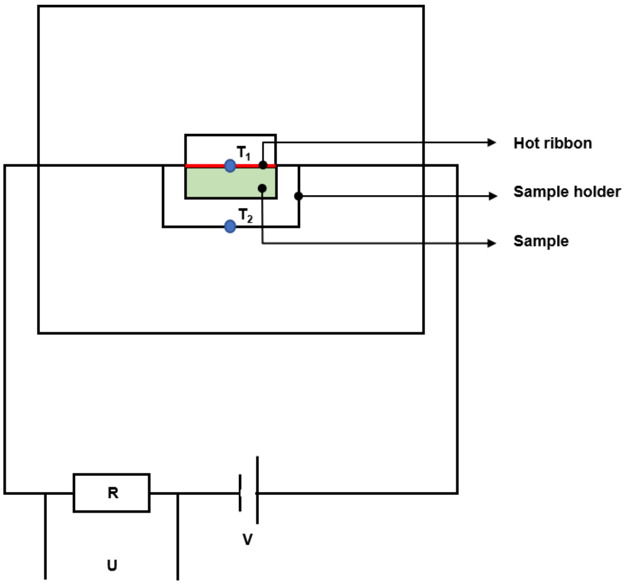

Figure C.2: Principle of operation of the hot ribbon technique.

A and B are calibration constants specific to the device, determined through the calibration process.

The calibration curve plotted will be used subsequently to determine the thermal conductivities of all the materials, once their conductance have been measured using the device we constructed. The calibration plot resulted in determining both constants A and B, which leads to the relation between the conductance and the thermal conductivity by the following equation:

$$\kappa = \frac{K + 0.0355}{0.6266} \tag{C.4}$$

BIBLIOGRAPHY

[1] Vladimir S. Arutyunov and Georgiy V. Lisichkin. Energy resources of the 21st century: problems and forecasts. Can renewable energy sources replace fossil fuels†. **Russian Chemical Reviews**, 86(8):777, August 2017. ISSN 0036-021X. doi: 10.1070/RCR4723. URL https://iopscience.iop.org/article/10.1070/RCR4723/meta. Publisher: IOP Publishing.

[2] N. L. Panwar, S. C. Kaushik, and Surendra Kothari. Role of renewable energy sources in environmental protection: A review. **Renewable and Sustainable Energy Reviews**, 15(3):1513–1524, April 2011. ISSN 1364-0321. doi: 10.1016/j.rser.2010.11.037. URL https://www.sciencedirect.com/science/article/pii/S1364032110004065.

[3] Hayati Mamur, Ömer Faruk Dilmaç, Jahanara Begum, and Mohammad Ruhul Amin Bhuiyan. Thermoelectric generators act as renewable energy sources. **Cleaner Materials**, 2:100030, December 2021. ISSN 2772-3976. doi: 10.1016/j.clema.2021.100030. URL https://www.sciencedirect.com/science/article/pii/S2772397621000307.

[4] D. M. Rowe. **Thermoelectrics Handbook: Macro to Nano**. CRC Press, October 2018. ISBN 978-1-4200-3890-3. Google-Books-ID: 0iwERQe5IKQC.

[5] Matteo d'Angelo, Carmen Galassi, and Nora Lecis. Thermoelectric Materials and Applications: A Review. **Energies**, 16(17):6409, January 2023. ISSN 1996-1073. doi: 10.3390/en16176409. URL https://www.mdpi.com/1996-1073/16/17/6409. Number: 17 Publisher: Multidisciplinary Digital Publishing Institute.

[6] Xiao Zhang and Li-Dong Zhao. Thermoelectric materials: Energy conversion between heat and electricity. **Journal of Materiomics**, 1(2):92–105, June 2015. ISSN 2352-8478. doi: 10.1016/j.jmat.2015.01.001. URL https://www.sciencedirect.com/science/article/pii/S2352847815000258.

[7] Nesrine Jaziri, Ayda Boughamoura, Jens Müller, Brahim Mezghani, Fares Tounsi, and Mohammed Ismail. A comprehensive review of Thermoelectric Generators: Technologies and common applications. **Energy Reports**, 6:264–287, December 2020. ISSN 2352-4847. doi: 10.1016/j.egyr.2019.12.011. URL https://www.sciencedirect.com/science/article/pii/S2352484719306997.

[8] H. Beyer, J. Nurnus, H. Böttner, A. Lambrecht, E. Wagner, and G. Bauer. High thermoelectric figure of merit ZT in PbTe and Bi2Te3-based superlattices by a reduction of the thermal conductivity. **Physica E: Low-dimensional Systems and Nanostructures**, 13(2):965–968, March 2002. ISSN 1386-9477. doi: 10.1016/S1386-9477(02)00246-1. URL https://www.sciencedirect.com/science/article/pii/S1386947702002461.

[9] Qing Shi, Juan Li, Xuanwei Zhao, Yiyuan Chen, Fujie Zhang, Yan Zhong, and Ran Ang. Comprehensive Insight into p-Type Bi2Te3-Based Thermoelectrics near Room Temperature. **ACS Applied Materials & Interfaces**, 14(44):49425–49445, November 2022. ISSN 1944-8244. doi: 10.1021/acsami.2c13109. URL https://doi.org/10.1021/acsami.2c13109. Publisher: American Chemical Society.

[10] Zhuang-Hao Zheng, Xiao-Lei Shi, Dong-Wei Ao, Wei-Di Liu, Meng Li, Liang-Zhi Kou, Yue-Xing Chen, Fu Li, Meng Wei, Guang-Xing Liang, Ping Fan, Gao Qing (Max) Lu, and Zhi-Gang Chen. Harvesting waste heat with flexible Bi2Te3 thermoelectric thin film. **Nature Sustainability**, pages 1–12, November 2022. ISSN 2398-9629. doi: 10.1038/s41893-022-01003-6. URL https://www.nature.com/articles/s41893-022-01003-6. Publisher: Nature Publishing Group.

[11] Md. Nazibul Hasan, Herman Wahid, Nafarizal Nayan, and Mohamed Sultan Mohamed Ali. Inorganic thermoelectric materials: A review. **International Journal of Energy Research**, 44(8):6170–6222, 2020. ISSN 1099-114X. doi: 10.1002/er.5313. URL https://onlinelibrary.wiley.com/doi/abs/10.1002/er.5313. _eprint: https://onlinelibrary.wiley.com/doi/pdf/10.1002/er.5313.

[12] Shengduo Xu, Xiao-Lei Shi, Matthew Dargusch, Chongan Di, Jin Zou, and Zhi-Gang Chen. Conducting polymer-based flexible thermoelectric materials and devices: From mechanisms to applications. **Progress in Materials Science**, 121:100840, August 2021. ISSN 0079-6425. doi: 10.1016/j.pmatsci.2021.100840. URL https://www.sciencedirect.com/science/article/pii/S0079642521000645.

[13] Emiliano Bilotti, Oliver Fenwick, Bob C. Schroeder, Mark Baxendale, Prospero Taroni-Junior, Thibault Degousée, and Zilu Liu. 6.14 Organic Thermoelectric Composites Materials. In Peter W. R. Beaumont and Carl H. Zweben, editors, **Comprehensive Composite Materials II**, pages 408–430. Elsevier, Oxford, January 2018. ISBN 978-0-08-100534-7. doi: 10.1016/B978-0-12-803581-8.10024-4. URL https://www.sciencedirect.com/science/article/pii/B9780128035818100244.

[14] Guangming Chen, Wei Xu, and Daoben Zhu. Recent advances in organic polymer thermoelectric composites. **Journal of Materials Chemistry C**,

5(18):4350–4360, May 2017. ISSN 2050-7534. doi: 10.1039/C6TC05488A. URL https://pubs.rsc.org/en/content/articlelanding/2017/tc/c6tc05488a. Publisher: The Royal Society of Chemistry.

[15] Jiwon Kim, Jae-Hong Lim, Jiwon Kim, and Jae-Hong Lim. Organic-Inorganic Hybrid Thermoelectric Material Synthesis and Properties. **Journal of the Korean Ceramic Society**, 54(4):272–277, July 2017. ISSN 1229-7801, 2234-0491. doi: 10.4191/kcers.2017.54.4.12. URL http://www.jkcs.or.kr/journal/view.php?doi=10.4191/kcers.2017.54.4.12. Publisher: Korean Ceramic Society.

[16] Jia Liang, Shujia Yin, and Chunlei Wan. Hybrid Thermoelectrics. **Annual Review of Materials Research**, 50(Volume 50, 2020):319–344, July 2020. ISSN 1531-7331, 1545-4118. doi: 10.1146/annurev-matsci-082319-111001. URL https://www.annualreviews.org/content/journals/10.1146/annurev-matsci-082319-111001. Publisher: Annual Reviews.

[17] Yong Du, Shirley Z. Shen, Kefeng Cai, and Philip S. Casey. Research progress on polymer–inorganic thermoelectric nanocomposite materials. **Progress in Polymer Science**, 37(6):820–841, June 2012. ISSN 0079-6700. doi: 10.1016/j.progpolymsci.2011.11.003. URL https://www.sciencedirect.com/science/article/pii/S0079670011001286.

[18] Richard Gulotty, Micaela Castellino, Pravin Jagdale, Alberto Tagliaferro, and Alexander A. Balandin. Effects of Functionalization on Thermal Properties of Single-Wall and Multi-Wall Carbon Nanotube–Polymer Nanocomposites. **ACS Nano**, 7(6):5114–5121, June 2013. ISSN 1936-0851. doi: 10.1021/nn400726g. URL https://doi.org/10.1021/nn400726g. Publisher: American Chemical Society.

[19] Momath Lo, Rémi Pires, Karim Diaw, Diariatou Gningue-Sall, Mehmet A. Oturan, Jean-Jacques Aaron, and Mohamed M. Chehimi. Diazonium Salts: Versatile Molecular Glues for Sticking Conductive Polymers to Flexible Electrodes. **Surfaces**, 1(1):43–58, December 2018. ISSN 2571-9637. doi: 10.3390/surfaces1010005. URL https://www.mdpi.com/2571-9637/1/1/5. Number: 1 Publisher: Multidisciplinary Digital Publishing Institute.

[20] Marco Liebscher, Titus Gärtner, Lazaros Tzounis, Matej Mičušík, Petra Pötschke, Manfred Stamm, Gert Heinrich, and Brigitte Voit. Influence of the MWCNT surface functionalization on the thermoelectric properties of melt-mixed polycarbonate composites. **Composites Science and Technology**, 101:133–138, September 2014. ISSN 0266-3538. doi: 10.1016/j.compscitech.2014.07.009. URL https://www.sciencedirect.com/science/article/pii/S0266353814002395.

[21] T. M. Tritt. Thermoelectric Materials: Principles, Structure, Properties, and Applications. In K. H. Jürgen Buschow, Robert W. Cahn, Mer-

ton C. Flemings, Bernhard Ilschner, Edward J. Kramer, Subhash Mahajan, and Patrick Veyssière, editors, **Encyclopedia of Materials: Science and Technology**, pages 1–11. Elsevier, Oxford, January 2002. ISBN 978-0-08-043152-9. doi: 10.1016/B0-08-043152-6/01822-2. URL https://www.sciencedirect.com/science/article/pii/B0080431526018222.

[22] Kok S. Ong, Liben Jiang, and Koon C. Lai. 4.20 Thermoelectric Energy Conversion. In Ibrahim Dincer, editor, **Comprehensive Energy Systems**, pages 794–815. Elsevier, Oxford, January 2018. ISBN 978-0-12-814925-6. doi: 10.1016/B978-0-12-809597-3.00433-8. URL https://www.sciencedirect.com/science/article/pii/B9780128095973004338.

[23] V. Subramanian and D. Varade. 5 - Thermoelectric Properties of Biopolymer Composites. In K. K. Sadasivuni, D. Ponnamma, J. Kim, J. J. Cabibihan, and M. A. AlMaadeed, editors, **Biopolymer Composites in Electronics**, pages 155–183. Elsevier, January 2017. ISBN 978-0-12-809261-3. doi: 10.1016/B978-0-12-809261-3.00005-X. URL https://www.sciencedirect.com/science/article/pii/B978012809261300005X.

[24] I. Terasaki. Thermal Conductivity and Thermoelectric Power of Semiconductors. In **Reference Module in Materials Science and Materials Engineering**. Elsevier, January 2016. ISBN 978-0-12-803581-8. doi: 10.1016/B978-0-12-803581-8.00771-2. URL https://www.sciencedirect.com/science/article/pii/B9780128035818007712.

[25] Huisheng Peng, Xuemei Sun, Wei Weng, and Xin Fang. 5 - Energy Harvesting Based on Polymer. In Huisheng Peng, Xuemei Sun, Wei Weng, and Xin Fang, editors, **Polymer Materials for Energy and Electronic Applications**, pages 151–196. Academic Press, January 2017. ISBN 978-0-12-811091-1. doi: 10.1016/B978-0-12-811091-1.00005-7. URL https://www.sciencedirect.com/science/article/pii/B9780128110911000057.

[26] J. Yeom, M. A. Shannon, and T. Singh. Micro-Coolers. In **Reference Module in Materials Science and Materials Engineering**. Elsevier, January 2017. ISBN 978-0-12-803581-8. doi: 10.1016/B978-0-12-803581-8.00568-3. URL https://www.sciencedirect.com/science/article/pii/B9780128035818005683.

[27] P. P. Pradyumnan and T. Parvathy. 7 - Thermoelectric nanomaterials for temperature gradient sensing (heat nose). In Ram K. Gupta, Tuan Anh Nguyen, Muhammad Bilal, and Mazaher Ahmadi, editors, **Nanotechnology-Based E-noses**, Woodhead Publishing Series in Electronic and Optical Materials, pages 165–192. Woodhead Publishing, January 2023. ISBN 978-0-323-91157-3. doi: 10.1016/B978-0-323-91157-3.00009-X. URL https://www.sciencedirect.com/science/article/pii/B978032391157300009X.

[28] J. M. Honig. Irreversible Thermodynamics and Basic Transport Theory in Solids. In Franco Bassani, Gerald L. Liedl, and Peter Wyder, editors, **Encyclopedia of Condensed Matter Physics**, pages 34–43. Elsevier, Oxford, January 2005. ISBN 978-0-12-369401-0. doi: 10.1016/B0-12-369401-9/00712-9. URL https://www.sciencedirect.com/science/article/pii/B0123694019007129.

[29] Rajkumar Modak, Masayuki Murata, Dazhi Hou, Asuka Miura, Ryo Iguchi, Bin Xu, Rulei Guo, Junichiro Shiomi, Yuya Sakuraba, and Ken-ichi Uchida. Phase-transition-induced giant Thomson effect for thermoelectric cooling. **Applied Physics Reviews**, 9(1):011414, February 2022. ISSN 1931-9401. doi: 10.1063/5.0077497. URL https://doi.org/10.1063/5.0077497.

[30] Hong Wang and Choongho Yu. Organic Thermoelectrics: Materials Preparation, Performance Optimization, and Device Integration. **Joule**, 3(1): 53–80, January 2019. ISSN 2542-4351. doi: 10.1016/j.joule.2018.10.012. URL https://www.sciencedirect.com/science/article/pii/S2542435118305038.

[31] Peter A. Finn, Ceyla Asker, Kening Wan, Emiliano Bilotti, Oliver Fenwick, and Christian B. Nielsen. Thermoelectric Materials: Current Status and Future Challenges. **Frontiers in Electronic Materials**, 1, August 2021. ISSN 2673-9895. doi: 10.3389/femat.2021.677845. URL https://www.frontiersin.org/articles/10.3389/femat.2021.677845. Publisher: Frontiers.

[32] Moinak Dutta, Tanmoy Ghosh, and Kanishka Biswas. Electronic structure modulation strategies in high-performance thermoelectrics. **APL Materials**, 8(4):040910, April 2020. ISSN 2166-532X. doi: 10.1063/5.0002129. URL https://doi.org/10.1063/5.0002129.

[33] Anne M. Glaudell, Justin E. Cochran, Shrayesh N. Patel, and Michael L. Chabinyc. Impact of the Doping Method on Conductivity and Thermopower in Semiconducting Polythiophenes. **Advanced Energy Materials**, 5(4):1401072, 2015. ISSN 1614-6840. doi: 10.1002/aenm.201401072. URL https://onlinelibrary.wiley.com/doi/abs/10.1002/aenm.201401072. _eprint: https://onlinelibrary.wiley.com/doi/pdf/10.1002/aenm.201401072.

[34] Jae-Hyun Lee, Dong-Seok Leem, and Jang-Joo Kim. Effect of host organic semiconductors on electrical doping. **Organic Electronics**, 11(3):486–489, March 2010. ISSN 1566-1199. doi: 10.1016/j.orgel.2009.12.002. URL https://www.sciencedirect.com/science/article/pii/S1566119909003644.

[35] Yanzhong Pei, Xiaoya Shi, Aaron LaLonde, Heng Wang, Lidong Chen, and G. Jeffrey Snyder. Convergence of electronic bands for high performance

bulk thermoelectrics. **Nature**, 473(7345):66–69, May 2011. ISSN 1476-4687. doi: 10.1038/nature09996. URL https://www.nature.com/articles/nature09996. Publisher: Nature Publishing Group.

[36] Yanzhong Pei, Heng Wang, and G. J. Snyder. Band Engineering of Thermoelectric Materials. **Advanced Materials**, 24(46):6125–6135, 2012. ISSN 1521-4095. doi: 10.1002/adma.201202919. URL https://onlinelibrary.wiley.com/doi/abs/10.1002/adma.201202919. _eprint: https://onlinelibrary.wiley.com/doi/pdf/10.1002/adma.201202919.

[37] Chenxi Zhao, Zhou Li, Tianjiao Fan, Chong Xiao, and Yi Xie. Defects Engineering with Multiple Dimensions in Thermoelectric Materials. **Research**, 2020, May 2020. doi: 10.34133/2020/9652749. URL https://spj.science.org/doi/10.34133/2020/9652749. Publisher: American Association for the Advancement of Science.

[38] Effects of Annealing Temperature on the Thermoelectric Properties and Microstructure of Ag0.6Pb18Sb5Te20. **Sensors and Materials**, page 1637, 2017. ISSN 0914-4935. doi: 10.18494/SAM.2017.1737. URL http://myukk.org/SM2017/article.php?ss=1737.

[39] Junbin Zang, Yuexuan Ma, Yaxin Zhao, Rui Guo, Yantao Liu, Dan Liu, and Chenyang Xue. Effect of post-annealing treatment on the thermoelectric properties of Ag2Se flexible thin film prepared by magnetron sputtering method. **Results in Physics**, 45:106222, February 2023. ISSN 2211-3797. doi: 10.1016/j.rinp.2023.106222. URL https://www.sciencedirect.com/science/article/pii/S2211379723000153.

[40] Xin Zhang, Hongliang Liu, Qingmei Lu, Jiuxing Zhang, and Feipeng Zhang. Enhanced thermoelectric performance of Mg2Si0.4Sn0.6 solid solutions by in nanostructures and minute Bi-doping. **Applied Physics Letters**, 103 (6):063901, August 2013. ISSN 0003-6951. doi: 10.1063/1.4816971. URL https://doi.org/10.1063/1.4816971.

[41] Heng Wang, Yanzhong Pei, Aaron D. LaLonde, and G. Jeffrey Snyder. Weak electron–phonon coupling contributing to high thermoelectric performance in n-type PbSe. **Proceedings of the National Academy of Sciences**, 109(25):9705–9709, June 2012. doi: 10.1073/pnas.1111419109. URL https://www.pnas.org/doi/abs/10.1073/pnas.1111419109. Publisher: Proceedings of the National Academy of Sciences.

[42] Shen Jia-Jun, Fang Teng, F. U. Tie-Zheng, X. I. N. Jia-Zhan, Zhao Xin-Bing, and Z. H. U. Tie-Jun. Lattice Thermal Conductivity in Thermoelectric Materials. **Journal of Inorganic Materials**, 34(3):260, March 2019. ISSN 1000-324X. doi: 10.15541/jim20180320. URL https://www.jim.org.cn/EN/10.15541/jim20180320.

[43] Euripides Hatzikraniotis, George S. Polymeris, Theodora Kyratsi, Euripides Hatzikraniotis, George S. Polymeris, and Theodora Kyratsi. Thermal Conductivity in Thermoelectric Materials. In **Novel Applications of Piezoelectric and Thermoelectric Materials**. IntechOpen, August 2022. ISBN 978-1-83768-397-0. doi: 10.5772/intechopen.106168. URL https://www.intechopen.com/chapters/83062.

[44] H. A. Eivari, Z. Sohbatzadeh, P. Mele, and M. H. N. Assadi. Low thermal conductivity: fundamentals and theoretical aspects in thermoelectric applications. **Materials Today Energy**, 21:100744, September 2021. ISSN 2468-6069. doi: 10.1016/j.mtener.2021.100744. URL https://www.sciencedirect.com/science/article/pii/S246860692100109X.

[45] Li-Dong Zhao, Shih-Han Lo, Yongsheng Zhang, Hui Sun, Gangjian Tan, Ctirad Uher, C. Wolverton, Vinayak P. Dravid, and Mercouri G. Kanatzidis. Ultralow thermal conductivity and high thermoelectric figure of merit in SnSe crystals. **Nature**, 508(7496):373–377, April 2014. ISSN 1476-4687. doi: 10.1038/nature13184. URL https://www.nature.com/articles/nature13184. Publisher: Nature Publishing Group.

[46] Woochul Kim, Joshua Zide, Arthur Gossard, Dmitri Klenov, Susanne Stemmer, Ali Shakouri, and Arun Majumdar. Thermal Conductivity Reduction and Thermoelectric Figure of Merit Increase by Embedding Nanoparticles in Crystalline Semiconductors. **Physical Review Letters**, 96(4):045901, February 2006. doi: 10.1103/PhysRevLett.96.045901. URL https://link.aps.org/doi/10.1103/PhysRevLett.96.045901. Publisher: American Physical Society.

[47] Rapaka S. C. Bose and K. Ramesh. Study of anisotropic thermal conductivity in textured thermoelectric alloys by Raman spectroscopy. **RSC Advances**, 11(39):24456–24465, July 2021. ISSN 2046-2069. doi: 10.1039/D1RA04886D. URL https://pubs.rsc.org/en/content/articlelanding/2021/ra/d1ra04886d. Publisher: The Royal Society of Chemistry.

[48] Hee Seok Kim, Weishu Liu, Gang Chen, Ching-Wu Chu, and Zhifeng Ren. Relationship between thermoelectric figure of merit and energy conversion efficiency. **Proceedings of the National Academy of Sciences**, 112(27):8205–8210, July 2015. doi: 10.1073/pnas.1510231112. URL https://www.pnas.org/doi/full/10.1073/pnas.1510231112. Publisher: Proceedings of the National Academy of Sciences.

[49] G. Jeffrey Snyder and Alemayouh H. Snyder. Figure of merit ZT of a thermoelectric device defined from materials properties. **Energy & Environmental Science**, 10(11):2280–2283, November 2017. ISSN 1754-5706. doi: 10.1039/C7EE02007D. URL https://pubs.rsc.org/en/content/articlelanding/2017/ee/c7ee02007d. Publisher: The Royal Society of Chemistry.

[50] H. Julian Goldsmid. Improving the thermoelectric figure of merit. **Science and Technology of Advanced Materials**, 22(1):280–284, December 2021. ISSN 1468-6996. doi: 10.1080/14686996.2021.1903816. URL https://doi.org/10.1080/14686996.2021.1903816. Publisher: Taylor & Francis _eprint: https://doi.org/10.1080/14686996.2021.1903816.

[51] Nuzul Hesty Pranita, Kiki Azura, Abrar Ismardi, Tri Ayodha Ajiwiguna, and I.P. Handayani. Implementing thermoelectric generator on CPU processor. In **2015 International Conference on Control, Electronics, Renewable Energy and Communications (ICCEREC)**, pages 108–111, August 2015. doi: 10.1109/ICCEREC.2015.7337026. URL https://ieeexplore.ieee.org/document/7337026.

[52] Kun-Quan Ma and Jing Liu. Heat-driven liquid metal cooling device for the thermal management of a computer chip. **Journal of Physics D: Applied Physics**, 40(15):4722, July 2007. ISSN 0022-3727. doi: 10.1088/0022-3727/40/15/055. URL https://dx.doi.org/10.1088/0022-3727/40/15/055.

[53] Yaoguang Shi, Yancheng Wang, Deqing Mei, Bo Feng, and Zichen Chen. Design and Fabrication of Wearable Thermoelectric Generator Device for Heat Harvesting. **IEEE Robotics and Automation Letters**, 3(1):373–378, January 2018. ISSN 2377-3766. doi: 10.1109/LRA.2017.2734241. URL https://ieeexplore.ieee.org/document/7997880. Conference Name: IEEE Robotics and Automation Letters.

[54] Yancheng Wang, Yaoguang Shi, Deqing Mei, and Zichen Chen. Wearable thermoelectric generator for harvesting heat on the curved human wrist. **Applied Energy**, 205:710–719, November 2017. ISSN 0306-2619. doi: 10.1016/j.apenergy.2017.08.117. URL https://www.sciencedirect.com/science/article/pii/S030626191731142X.

[55] Choong Sun Kim, Gyu Soup Lee, Hyeongdo Choi, Yong Jun Kim, Hyeong Man Yang, Se Hwan Lim, Sang-Gug Lee, and Byung Jin Cho. Structural design of a flexible thermoelectric power generator for wearable applications. **Applied Energy**, 214:131–138, March 2018. ISSN 0306-2619. doi: 10.1016/j.apenergy.2018.01.074. URL https://www.sciencedirect.com/science/article/pii/S0306261918300874.

[56] V. Leonov, P. Fiorini, T. Torfs, R. J. M. Vullers, and C. Van Hoof. Thermal matching of a thermoelectric energy harvester with the environment and its application in wearable self-powered wireless medical sensors. In **2009 15th International Workshop on Thermal Investigations of ICs and Systems**, pages 95–100, October 2009. URL https://ieeexplore.ieee.org/abstract/document/5340045.

[57] Aime Lay-Ekuakille, Giuseppe Vendramin, Amerigo Trotta, and Gabriella Mazzotta. Thermoelectric generator design based on power from body heat for biomedical autonomous devices. In **2009 IEEE International Workshop on Medical Measurements and Applications**, pages 1–4, May 2009. doi: 10.1109/MEMEA.2009.5167942. URL https://ieeexplore.ieee.org/abstract/document/5167942.

[58] Y. Y. Hsiao, W. C. Chang, and S. L. Chen. A mathematic model of thermoelectric module with applications on waste heat recovery from automobile engine. **Energy**, 35(3):1447–1454, March 2010. ISSN 0360-5442. doi: 10.1016/j.energy.2009.11.030. URL https://www.sciencedirect.com/science/article/pii/S0360544209005192.

[59] Chen Changhe. Experimental study of thermoelectric generation from automobile exhaust. **Journal of Tsinghua University**, 2010. URL https://www.semanticscholar.org/paper/Experimental-study-of-thermoelectric-generation-Changhe/14a316db925770d677fbd6e32810e477ef4ebad2.

[60] Jungsoo Lee, Seungjun Choo, Hyejin Ju, Jaehyung Hong, Seong Eun Yang, Fredrick Kim, Da Hwi Gu, Jeongin Jang, Gyeonghun Kim, Sangjoon Ahn, Ji Eun Lee, Sung Youb Kim, Han Gi Chae, and Jae Sung Son. Doping-Induced Viscoelasticity in PbTe Thermoelectric Inks for 3D Printing of Power-Generating Tubes. **Advanced Energy Materials**, 11(20):2100190, 2021. ISSN 1614-6840. doi: 10.1002/aenm.202100190. URL https://onlinelibrary.wiley.com/doi/abs/10.1002/aenm.202100190. _eprint: https://onlinelibrary.wiley.com/doi/pdf/10.1002/aenm.202100190.

[61] Neha Dimri, Arvind Tiwari, and G. N. Tiwari. Thermal modelling of semitransparent photovoltaic thermal (PVT) with thermoelectric cooler (TEC) collector. **Energy Conversion and Management**, 146:68–77, August 2017. ISSN 0196-8904. doi: 10.1016/j.enconman.2017.05.017. URL https://www.sciencedirect.com/science/article/pii/S0196890417304491.

[62] A. Rezania and L. A. Rosendahl. Feasibility and parametric evaluation of hybrid concentrated photovoltaic-thermoelectric system. **Applied Energy**, 187:380–389, February 2017. ISSN 0306-2619. doi: 10.1016/j.apenergy.2016.11.064. URL https://www.sciencedirect.com/science/article/pii/S030626191631649X.

[63] Samson Shittu, Guiqiang Li, Yousef Golizadeh Akhlaghi, Xiaoli Ma, Xudong Zhao, and Emmanuel Ayodele. Advancements in thermoelectric generators for enhanced hybrid photovoltaic system performance. **Renewable and Sustainable Energy Reviews**, 109:24–54, July 2019. ISSN 1364-0321. doi: 10.1016/j.rser.2019.04.023. URL https://www.sciencedirect.com/science/article/pii/S1364032119302357.

[64] Miguel Fisac, Francesc X. Villasevil, and Antonio M. López. High-efficiency photovoltaic technology including thermoelectric generation. **Journal of Power Sources**, 252:264–269, April 2014. ISSN 0378-7753. doi: 10.1016/j.jpowsour.2013.11.121. URL https://www.sciencedirect.com/science/article/pii/S0378775313019678.

[65] Mohamed Bashir Ali Bashir, Suhana Mohd Said, Mohd Faizul Mohd Sabri, Dhafer Abdulameer Shnawah, and Mohamed Hamid Elsheikh. Recent advances on Mg2Si1xSnx materials for thermoelectric generation. **Renewable and Sustainable Energy Reviews**, 37:569–584, September 2014. ISSN 1364-0321. doi: 10.1016/j.rser.2014.05.060. URL https://www.sciencedirect.com/science/article/pii/S1364032114003852.

[66] George S. Nolas, Jeffrey Sharp, and H. Julian Goldsmid. The Phonon—Glass Electron-Crystal Approach to Thermoelectric Materials Research. In George S. Nolas, Jeffrey Sharp, and H. Julian Goldsmid, editors, **Thermoelectrics: Basic Principles and New Materials Developments**, pages 177–207. Springer, Berlin, Heidelberg, 2001. ISBN 978-3-662-04569-5. doi: 10.1007/978-3-662-04569-5_6. URL https://doi.org/10.1007/978-3-662-04569-5_6.

[67] Lijun Wu, Qingping Meng, Christian Jooss, Jin-Cheng Zheng, H. Inada, Dong Su, Qiang Li, and Yimei Zhu. Origin of Phonon Glass–Electron Crystal Behavior in Thermoelectric Layered Cobaltate. **Advanced Functional Materials**, 23(46):5728–5736, 2013. ISSN 1616-3028. doi: 10.1002/adfm.201301098. URL https://onlinelibrary.wiley.com/doi/abs/10.1002/adfm.201301098. _eprint: https://onlinelibrary.wiley.com/doi/pdf/10.1002/adfm.201301098.

[68] Yintu Liu, Hanhui Xie, Chenguang Fu, G. Jeffrey Snyder, Xinbing Zhao, and Tiejun Zhu. Demonstration of a phonon-glass electron-crystal strategy in (Hf,Zr)NiSn half-Heusler thermoelectric materials by alloying. **Journal of Materials Chemistry A**, 3(45):22716–22722, November 2015. ISSN 2050-7496. doi: 10.1039/C5TA04418A. URL https://pubs.rsc.org/en/content/articlelanding/2015/ta/c5ta04418a. Publisher: The Royal Society of Chemistry.

[69] Vaishali Taneja, Subarna Das, Kapildeb Dolui, Tanmoy Ghosh, Animesh Bhui, Usha Bhat, Dinesh Kumar Kedia, Koushik Pal, Ranjan Datta, and Kanishka Biswas. High Thermoelectric Performance in Phonon-Glass Electron-Crystal Like AgSbTe2. **Advanced Materials**, 36(6):2307058, 2024. ISSN 1521-4095. doi: 10.1002/adma.202307058. URL https://onlinelibrary.wiley.com/doi/abs/10.1002/adma.202307058. _eprint: https://onlinelibrary.wiley.com/doi/pdf/10.1002/adma.202307058.

[70] Jiangtao Wei, Liangliang Yang, Zhe Ma, Peishuai Song, Mingliang Zhang, Jing Ma, Fuhua Yang, and Xiaodong Wang. Review of current high-ZT

thermoelectric materials. **Journal of Materials Science**, 55(27):12642–12704, September 2020. ISSN 1573-4803. doi: 10.1007/s10853-020-04949-0. URL https://doi.org/10.1007/s10853-020-04949-0.

[71] Yinong Yin, Bharati Tudu, and Ashutosh Tiwari. Recent advances in oxide thermoelectric materials and modules. **Vacuum**, 146:356–374, December 2017. ISSN 0042-207X. doi: 10.1016/j.vacuum.2017.04.015. URL https://www.sciencedirect.com/science/article/pii/S0042207X17300544.

[72] Shunjin Peng, Dengjing Wang, Jianduo Lu, Min He, Chao Xu, Ying Li, and Sicong Zhu. A Review on Organic Polymer-Based Thermoelectric Materials. **Journal of Polymers and the Environment**, 25(4):1208–1218, December 2017. ISSN 1572-8900. doi: 10.1007/s10924-016-0895-z. URL https://doi.org/10.1007/s10924-016-0895-z.

[73] Boris Russ, Anne Glaudell, Jeffrey J. Urban, Michael L. Chabinyc, and Rachel A. Segalman. Organic thermoelectric materials for energy harvesting and temperature control. **Nature Reviews Materials**, 1(10):1–14, August 2016. ISSN 2058-8437. doi: 10.1038/natrevmats.2016.50. URL https://www.nature.com/articles/natrevmats201650. Publisher: Nature Publishing Group.

[74] Hongyan Yao, Zeng Fan, Hanlin Cheng, Xin Guan, Chen Wang, Kuan Sun, and Jianyong Ouyang. Recent Development of Thermoelectric Polymers and Composites. **Macromolecular Rapid Communications**, 39(6): 1700727, 2018. ISSN 1521-3927. doi: 10.1002/marc.201700727. URL https://onlinelibrary.wiley.com/doi/abs/10.1002/marc.201700727. _eprint: https://onlinelibrary.wiley.com/doi/pdf/10.1002/marc.201700727.

[75] Canlin Ou, Abhijeet L. Sangle, Anuja Datta, Qingshen Jing, Tommaso Busolo, Thomas Chalklen, Vijay Narayan, and Sohini Kar-Narayan. Fully Printed Organic–Inorganic Nanocomposites for Flexible Thermoelectric Applications. **ACS Applied Materials & Interfaces**, 10(23):19580–19587, June 2018. ISSN 1944-8244. doi: 10.1021/acsami.8b01456. URL https://doi.org/10.1021/acsami.8b01456. Publisher: American Chemical Society.

[76] Naoki Toshima, Keisuke Oshima, Hiroaki Anno, Takahiko Nishinaka, Shoko Ichikawa, Arihiro Iwata, and Yukihide Shiraishi. Novel Hybrid Organic Thermoelectric Materials:Three-Component Hybrid Films Consisting of a Nanoparticle Polymer Complex, Carbon Nanotubes, and Vinyl Polymer. **Advanced Materials**, 27(13):2246–2251, 2015. ISSN 1521-4095. doi: 10.1002/adma.201405463. URL https://onlinelibrary.wiley.com/doi/abs/10.1002/adma.201405463. _eprint: https://onlinelibrary.wiley.com/doi/pdf/10.1002/adma.201405463.

[77] Naoki Toshima. Recent progress of organic and hybrid thermoelectric materials. **Synthetic Metals**, 225:3–21, March 2017. ISSN 0379-6779. doi: 10.1016/j.synthmet.2016.12.017. URL https://www.sciencedirect.com/science/article/pii/S0379677916304532.

[78] Pan Ren, Yamei Liu, Jian He, Tu Lv, Junling Gao, and Guiying Xu. Recent advances in inorganic material thermoelectrics. **Inorganic Chemistry Frontiers**, 5(10):2380–2398, October 2018. ISSN 2052-1553. doi: 10.1039/C8QI00366A. URL https://pubs.rsc.org/en/content/articlelanding/2018/qi/c8qi00366a. Publisher: The Royal Society of Chemistry.

[79] Jun Pei, Bowen Cai, Hua-Lu Zhuang, and Jing-Feng Li. Bi2Te3-based applied thermoelectric materials: research advances and new challenges. **National Science Review**, 7(12):1856–1858, December 2020. ISSN 2095-5138. doi: 10.1093/nsr/nwaa259. URL https://doi.org/10.1093/nsr/nwaa259.

[80] Lei Yang, Zhi-Gang Chen, Min Hong, Guang Han, and Jin Zou. Enhanced Thermoelectric Performance of Nanostructured Bi2Te3 through Significant Phonon Scattering. **ACS Applied Materials & Interfaces**, 7(42):23694–23699, October 2015. ISSN 1944-8244. doi: 10.1021/acsami.5b07596. URL https://doi.org/10.1021/acsami.5b07596. Publisher: American Chemical Society.

[81] Ching-Hua Su. Design, growth and characterization of PbTe-based thermoelectric materials. **Progress in Crystal Growth and Characterization of Materials**, 65(2):47–94, May 2019. ISSN 0960-8974. doi: 10.1016/j.pcrysgrow.2019.04.001. URL https://www.sciencedirect.com/science/article/pii/S0960897419300087.

[82] Abanti Nag and V. Shubha. Oxide Thermoelectric Materials: A Structure–Property Relationship. **Journal of Electronic Materials**, 43(4):962–977, April 2014. ISSN 1543-186X. doi: 10.1007/s11664-014-3024-6. URL https://doi.org/10.1007/s11664-014-3024-6.

[83] Michitaka Ohtaki, Kazuhiko Araki, and Kiyoshi Yamamoto. High Thermoelectric Performance of Dually Doped ZnO Ceramics. **Journal of Electronic Materials**, 38(7):1234–1238, July 2009. ISSN 1543-186X. doi: 10.1007/s11664-009-0816-1. URL https://doi.org/10.1007/s11664-009-0816-1.

[84] Woosuck Shin and Norimitsu Murayama. High performance p-type thermoelectric oxide based on NiO. **Materials Letters**, 45(6):302–306, October 2000. ISSN 0167-577X. doi: 10.1016/S0167-577X(00)00122-1. URL https://www.sciencedirect.com/science/article/pii/S0167577X00001221.

[85] P. S Patil and L. D Kadam. Preparation and characterization of spray pyrolyzed nickel oxide (NiO) thin films. **Applied Surface Science**, 199(1): 211–221, October 2002. ISSN 0169-4332. doi: 10.1016/S0169-4332(02)00839-5. URL https://www.sciencedirect.com/science/article/pii/S0169433202008395.

[86] Thanh-Hai Le, Yukyung Kim, and Hyeonseok Yoon. Electrical and Electrochemical Properties of Conducting Polymers. **Polymers**, 9(4): 150, April 2017. ISSN 2073-4360. doi: 10.3390/polym9040150. URL https://www.mdpi.com/2073-4360/9/4/150. Number: 4 Publisher: Multidisciplinary Digital Publishing Institute.

[87] Chun Li, Hua Bai, and Gaoquan Shi. Conducting polymer nanomaterials: electrosynthesis and applications. **Chemical Society Reviews**, 38(8): 2397–2409, July 2009. ISSN 1460-4744. doi: 10.1039/B816681C. URL https://pubs.rsc.org/en/content/articlelanding/2009/cs/b816681c. Publisher: The Royal Society of Chemistry.

[88] Jorge G. Ibanez, Marina. E. Rincón, Silvia Gutierrez-Granados, M'hamed Chahma, Oscar A. Jaramillo-Quintero, and Bernardo A. Frontana-Uribe. Conducting Polymers in the Fields of Energy, Environmental Remediation, and Chemical–Chiral Sensors. **Chemical Reviews**, 118(9):4731–4816, May 2018. ISSN 0009-2665. doi: 10.1021/acs.chemrev.7b00482. URL https://doi.org/10.1021/acs.chemrev.7b00482. Publisher: American Chemical Society.

[89] Jiri Janata and Mira Josowicz. Conducting polymers in electronic chemical sensors. **Nature Materials**, 2(1):19–24, January 2003. ISSN 1476-4660. doi: 10.1038/nmat768. URL https://www.nature.com/articles/nmat768. Publisher: Nature Publishing Group.

[90] Tobias Abrahamsson. Synthetic Functionalities for Ion and Electron Conductive Polymers : Applications in Organic Electronics and Biological Interfaces. 2021. URL https://urn.kb.se/resolve?urn=urn:nbn:se:liu:diva-181717. Publisher: Linköping University Electronic Press.

[91] Chandrani Nath, Ashok Kumar, Yung-Kang Kuo, and Gunadhor Singh Okram. High thermoelectric figure of merit in nanocrystalline polyaniline at low temperatures. **Applied Physics Letters**, 105(13):133108, September 2014. ISSN 0003-6951. doi: 10.1063/1.4897146. URL https://doi.org/10.1063/1.4897146.

[92] Alessia Famengo, Alberto Ferrario, Stefano Boldrini, Simone Battiston, Stefania Fiameni, Cesare Pagura, and Monica Fabrizio. Polyaniline carbon nanohorn composites as thermoelectric materials. **Polymer International**, 66(12):1725–1730, 2017. ISSN 1097-0126. doi: 10.1002/pi.5366.

URL https://onlinelibrary.wiley.com/doi/abs/10.1002/pi.5366. _eprint: https://onlinelibrary.wiley.com/doi/pdf/10.1002/pi.5366.

[93] Mousumi Mitra, Kajari Kargupta, Saibal Ganguly, Shyamaprosad Goswami, and Dipali Banerjee. Facile synthesis and thermoelectric properties of aluminum doped zinc oxide/polyaniline (AZO/PANI) hybrid. **Synthetic Metals**, 228:25–31, June 2017. ISSN 0379-6779. doi: 10.1016/j.synthmet.2017.03.017. URL https://www.sciencedirect.com/science/article/pii/S0379677917300887.

[94] Yu-Yun Hsieh, Yu Zhang, Lu Zhang, Yanbo Fang, Sathya Narayan Kanakaraaj, Je-Hyeong Bahk, and Vesselin Shanov. High thermoelectric power-factor composites based on flexible three-dimensional graphene and polyaniline. **Nanoscale**, 11(14):6552–6560, April 2019. ISSN 2040-3372. doi: 10.1039/C8NR10537E. URL https://pubs.rsc.org/en/content/articlelanding/2019/nr/c8nr10537e. Publisher: The Royal Society of Chemistry.

[95] M. Culebras, C. M. Gómez, and A. Cantarero. Enhanced thermoelectric performance of PEDOT with different counter-ions optimized by chemical reduction. **Journal of Materials Chemistry A**, 2(26):10109–10115, June 2014. ISSN 2050-7496. doi: 10.1039/C4TA01012D. URL https://pubs.rsc.org/en/content/articlelanding/2014/ta/c4ta01012d. Publisher: The Royal Society of Chemistry.

[96] Ioannis Petsagkourakis, Nara Kim, Klas Tybrandt, Igor Zozoulenko, and Xavier Crispin. Poly(3,4-ethylenedioxythiophene): Chemical Synthesis, Transport Properties, and Thermoelectric Devices. **Advanced Electronic Materials**, 5(11):1800918, 2019. ISSN 2199-160X. doi: 10.1002/aelm.201800918. URL https://onlinelibrary.wiley.com/doi/abs/10.1002/aelm.201800918. _eprint: https://onlinelibrary.wiley.com/doi/pdf/10.1002/aelm.201800918.

[97] Dan Ni, Haijun Song, Yuanxun Chen, and Kefeng Cai. Free-standing highly conducting PEDOT films for flexible thermoelectric generator. **Energy**, 170:53–61, March 2019. ISSN 0360-5442. doi: 10.1016/j.energy.2018.12.124. URL https://www.sciencedirect.com/science/article/pii/S0360544218324964.

[98] Yuwei Xu, Yanhua Jia, Peipei Liu, Qinglin Jiang, Dehua Hu, and Yuguang Ma. Poly(3,4-ethylenedioxythiophene) (PEDOT) as promising thermoelectric materials and devices. **Chemical Engineering Journal**, 404:126552, January 2021. ISSN 1385-8947. doi: 10.1016/j.cej.2020.126552. URL https://www.sciencedirect.com/science/article/pii/S1385894720326802.

[99] Zeng Fan and Jianyong Ouyang. Thermoelectric Properties of PEDOT:PSS. **Advanced Electronic Materials**, 5(11):1800769, 2019. ISSN 2199-160X. doi: 10.1002/aelm.201800769. URL https://onlinelibrary.wiley.com/doi/abs/10.1002/aelm.201800769. _eprint: https://onlinelibrary.wiley.com/doi/pdf/10.1002/aelm.201800769.

[100] Ningxuan Wen, Zeng Fan, Shuaitao Yang, Yongpeng Zhao, Tianze Cong, Shihong Xu, Hao Zhang, Jianzhen Wang, Hui Huang, Chengwei Li, and Lujun Pan. Highly conductive, ultra-flexible and continuously processable PEDOT:PSS fibers with high thermoelectric properties for wearable energy harvesting. **Nano Energy**, 78:105361, December 2020. ISSN 2211-2855. doi: 10.1016/j.nanoen.2020.105361. URL https://www.sciencedirect.com/science/article/pii/S2211285520309381.

[101] Zeng Fan, Donghe Du, Zhimeng Yu, Pengcheng Li, Yijie Xia, and Jianyong Ouyang. Significant Enhancement in the Thermoelectric Properties of PEDOT:PSS Films through a Treatment with Organic Solutions of Inorganic Salts. **ACS Applied Materials & Interfaces**, 8(35):23204–23211, September 2016. ISSN 1944-8244. doi: 10.1021/acsami.6b07234. URL https://doi.org/10.1021/acsami.6b07234. Publisher: American Chemical Society.

[102] Kazuhiro Kirihara, Qingshuo Wei, Masakazu Mukaida, and Takao Ishida. Thermoelectric power generation using nonwoven fabric module impregnated with conducting polymer PEDOT:PSS. **Synthetic Metals**, 225:41–48, March 2017. ISSN 0379-6779. doi: 10.1016/j.synthmet.2017.01.001. URL https://www.sciencedirect.com/science/article/pii/S0379677917300012.

[103] Jiajia Zhang, Guangjie Song, Lin Qiu, Yanhui Feng, Jie Chen, Jie Yan, Liyao Liu, Xing Huang, Yutao Cui, Yimeng Sun, Wei Xu, and Daoben Zhu. Highly Conducting Polythiophene Thin Films with Less Ordered Microstructure Displaying Excellent Thermoelectric Performance. **Macromolecular Rapid Communications**, 39(16):1800283, 2018. ISSN 1521-3927. doi: 10.1002/marc.201800283. URL https://onlinelibrary.wiley.com/doi/abs/10.1002/marc.201800283. _eprint: https://onlinelibrary.wiley.com/doi/pdf/10.1002/marc.201800283.

[104] Lirong Liang, Guangming Chen, and Cun-Yue Guo. Polypyrrole nanostructures and their thermoelectric performance. **Materials Chemistry Frontiers**, 1(2):380–386, February 2017. ISSN 2052-1537. doi: 10.1039/C6QM00061D. URL https://pubs.rsc.org/en/content/articlelanding/2017/qm/c6qm00061d. Publisher: The Royal Society of Chemistry.

[105] Chen Li, Hao Ma, and Zhiting Tian. Thermoelectric properties of crystalline and amorphous polypyrrole: A computational study. **Applied**

Thermal Engineering, 111:1441–1447, January 2017. ISSN 1359-4311. doi: 10.1016/j.applthermaleng.2016.08.154. URL https://www.sciencedirect.com/science/article/pii/S1359431116315137.

[106] Meng Li, Chan Luo, Jiang Zhang, Jiaji Yang, Jingkun Xu, Wenqian Yao, Rongri Tan, Xuemin Duan, and Fengxing Jiang. Electrochemical doping tuning of flexible polypyrrole film with enhanced thermoelectric performance. **Surfaces and Interfaces**, 21:100759, December 2020. ISSN 2468-0230. doi: 10.1016/j.surfin.2020.100759. URL https://www.sciencedirect.com/science/article/pii/S2468023020307513.

[107] Meng Xiang, Zhou Yang, Jianxiang Chen, Shilong Zhou, Wenjuan Wei, and Shuang Dong. Polymeric Thermoelectric Composites by Polypyrrole and Cheap Reduced Graphene Oxide in Towel-Gourd Sponge Fibers. **ACS Omega**, 5(46):29955–29962, November 2020. doi: 10.1021/acsomega.0c04356. URL https://doi.org/10.1021/acsomega.0c04356. Publisher: American Chemical Society.

[108] Zhiming Liang, Hyun Ho Choi, Xuyi Luo, Tuo Liu, Ashkan Abtahi, Uma Shantini Ramasamy, J. Andrew Hitron, Kyle N. Baustert, Jacob L. Hempel, Alex M. Boehm, Armin Ansary, Douglas R. Strachan, Jianguo Mei, Chad Risko, Vitaly Podzorov, and Kenneth R. Graham. n-type charge transport in heavily p-doped polymers. **Nature Materials**, 20(4):518–524, April 2021. ISSN 1476-4660. doi: 10.1038/s41563-020-00859-3. URL https://www.nature.com/articles/s41563-020-00859-3. Publisher: Nature Publishing Group.

[109] Kan Ueji, Masahiro Ohno, Jun Takeya, and Shun Watanabe. Correlation between coherent charge transport and crystallinity in doped -conjugated polymers. **Applied Physics Express**, 12(1):011004, December 2018. ISSN 1882-0786. doi: 10.7567/1882-0786/aaf2cf. URL https://dx.doi.org/10.7567/1882-0786/aaf2cf. Publisher: IOP Publishing.

[110] G.M. Sessler. Charge distribution and transport in polymers. **IEEE Transactions on Dielectrics and Electrical Insulation**, 4(5):614–628, October 1997. ISSN 1558-4135. doi: 10.1109/94.625648. URL https://ieeexplore.ieee.org/document/625648. Conference Name: IEEE Transactions on Dielectrics and Electrical Insulation.

[111] E. F. Aziz, A. Vollmer, S. Eisebitt, W. Eberhardt, P. Pingel, D. Neher, and N. Koch. Localized Charge Transfer in a Molecularly Doped Conducting Polymer. **Advanced Materials**, 19(20):3257–3260, 2007. ISSN 1521-4095. doi: 10.1002/adma.200700926. URL https://onlinelibrary.wiley.com/doi/abs/10.1002/adma.200700926. _eprint: https://onlinelibrary.wiley.com/doi/pdf/10.1002/adma.200700926.

[112] Tsu-Hsien Ku, Ju-Hung Hsu, Heh-Nan Lin, Hsin-Fei Meng, Ming-Chih Chen, and Show-An Chen. Study of charge transport in conducting polymer between electrodes with nanogaps. **Nanotechnology**, 17(9): 2279, April 2006. ISSN 0957-4484. doi: 10.1088/0957-4484/17/9/035. URL https://dx.doi.org/10.1088/0957-4484/17/9/035.

[113] Siegmar Roth, Hartmut Bleier, and Wojciech Pukacki. Charge transport in conducting polymers. **Faraday Discussions of the Chemical Society**, 88 (0):223–233, January 1989. ISSN 0301-7249. doi: 10.1039/DC9898800223. URL https://pubs.rsc.org/en/content/articlelanding/1989/dc/dc9898800223. Publisher: The Royal Society of Chemistry.

[114] Mukulika Jana Chatterjee, Prasenjit Chakraborty, and Dipali Banerjee. Charge Transport Through Polypyrrole and Single-Walled Carbon Nanotube Composite: A Thermoelectric Material. **Journal of Electronic Materials**, 51(10):5956–5964, October 2022. ISSN 1543-186X. doi: 10.1007/s11664-022-09812-3. URL https://doi.org/10.1007/s11664-022-09812-3.

[115] Hideki Shirakawa, Edwin J. Louis, Alan G. MacDiarmid, Chwan K. Chiang, and Alan J. Heeger. Synthesis of electrically conducting organic polymers: halogen derivatives of polyacetylene, (CH)x. **Journal of the Chemical Society, Chemical Communications**, (16):578–580, January 1977. ISSN 0022-4936. doi: 10.1039/C39770000578. URL https://pubs.rsc.org/en/content/articlelanding/1977/c3/c39770000578. Publisher: The Royal Society of Chemistry.

[116] Sam Rudd, Juan F. Franco-Gonzalez, Sandeep Kumar Singh, Zia Ullah Khan, Xavier Crispin, Jens W. Andreasen, Igor Zozoulenko, and Drew Evans. Charge transport and structure in semimetallic polymers. **Journal of Polymer Science Part B: Polymer Physics**, 56(1):97–104, 2018. ISSN 1099-0488. doi: 10.1002/polb.24530. URL https://onlinelibrary.wiley.com/doi/abs/10.1002/polb.24530. _eprint: https://onlinelibrary.wiley.com/doi/pdf/10.1002/polb.24530.

[117] L. Zuppiroli, M. N. Bussac, S. Paschen, O. Chauvet, and L. Forro. Hopping in disordered conducting polymers. **Physical Review B**, 50(8):5196–5203, August 1994. doi: 10.1103/PhysRevB.50.5196. URL https://link.aps.org/doi/10.1103/PhysRevB.50.5196. Publisher: American Physical Society.

[118] G. Pfister. Hopping transport in a molecularly doped organic polymer. **Physical Review B**, 16(8):3676–3687, October 1977. doi: 10.1103/PhysRevB.16.3676. URL https://link.aps.org/doi/10.1103/PhysRevB.16.3676. Publisher: American Physical Society.

[119] P. Röhl. Electronic hopping transport mechanism in polyethylene. In **1984 IEEE International Conference on Eletrical Insulation**, pages 186–

189, June 1984. doi: 10.1109/EIC.1984.7465175. URL https://ieeexplore.ieee.org/document/7465175?denied=.

[120] S. Capaccioli, E. Butta, S. Corezzi, M. Lucchesi, and P. Rolla. Hopping charge transport in conducting polymers studied by dc conduction and dielectric response analysis. 3471, 1998. doi: 10.1117/12.328156. URL https://consensus.app/papers/hopping-charge-transport-conducting-polymers-studied-capaccioli/679713f23164597c9194e4a1a82a901c/.

[121] Duong Nguyen Nguyen and Hyeonseok Yoon. Recent Advances in Nanostructured Conducting Polymers: from Synthesis to Practical Applications. **Polymers**, 8(4):118, April 2016. ISSN 2073-4360. doi: 10.3390/polym8040118. URL https://www.mdpi.com/2073-4360/8/4/118. Number: 4 Publisher: Multidisciplinary Digital Publishing Institute.

[122] Namsheer K and Chandra Sekhar Rout. Conducting polymers: a comprehensive review on recent advances in synthesis, properties and applications. **RSC Advances**, 11(10):5659–5697, January 2021. ISSN 2046-2069. doi: 10.1039/D0RA07800J. URL https://pubs.rsc.org/en/content/articlelanding/2021/ra/d0ra07800j. Publisher: The Royal Society of Chemistry.

[123] Pravesh Kumar Yadav, Sunil Kumar, and Pralay Maiti. 12 - Conjugated polymers for solar cell applications. In Vijay Kumar, Kashma Sharma, Rakesh Sehgal, and Susheel Kalia, editors, **Conjugated Polymers for Next-Generation Applications**, volume 2 of **Woodhead Publishing Series in Electronic and Optical Materials**, pages 367–401. Woodhead Publishing, January 2022. ISBN 978-0-12-824094-6. doi: 10.1016/B978-0-12-824094-6.00004-2. URL https://www.sciencedirect.com/science/article/pii/B9780128240946000042.

[124] Michał Gocki, Agnieszka Jakubowska-Ciszek, and Piotr Pruski. Comparative Analysis of a New Class of Symmetric and Asymmetric Supercapacitors Constructed on the Basis of ITO Collectors. **Energies**, 16(1):306, January 2023. ISSN 1996-1073. doi: 10.3390/en16010306. URL https://www.mdpi.com/1996-1073/16/1/306. Number: 1 Publisher: Multidisciplinary Digital Publishing Institute.

[125] Yusuf Yagci, Steffen Jockusch, and Nicholas J. Turro. Photoinitiated Polymerization: Advances, Challenges, and Opportunities. **Macromolecules**, 43(15):6245–6260, August 2010. ISSN 0024-9297. doi: 10.1021/ma1007545. URL https://doi.org/10.1021/ma1007545. Publisher: American Chemical Society.

[126] David Bird, Elbert Caravaca, Joseph Laquidara, Keith Luhmann, and Nuggehalli M. Ravindra. Formulation of Curable Resins Utilized in Stereolithography. In **TMS 2019 148th Annual Meeting & Exhibition Supplemental Proceedings**, pages 1575–1587, Cham, 2019. Springer Interna-

tional Publishing. ISBN 978-3-030-05861-6. doi: 10.1007/978-3-030-05861-6_148.

[127] Sobhan Bahraeian, Khatereh Abron, Fatemeh Pourjafarian, and Rohah A. Majid. Study on Synthesis of Polypyrrole via Chemical Polymerization Method. **Advanced Materials Research**, 795:707–710, 2013. ISSN 1662-8985. doi: 10.4028/www.scientific.net/AMR.795.707. URL https://www.scientific.net/AMR.795.707. Publisher: Trans Tech Publications Ltd.

[128] Yong Du, Hao Niu, Jun Li, Yunchen Dou, Shirley Shen, Runping Jia, and Jiayue Xu. Morphologies Tuning of Polypyrrole and Thermoelectric Properties of Polypyrrole Nanowire/Graphene Composites. **Polymers**, 10(10): 1143, October 2018. ISSN 2073-4360. doi: 10.3390/polym10101143. URL http://www.mdpi.com/2073-4360/10/10/1143.

[129] Lu Hao, Changyi Dong, Lifeng Zhang, Kaiming Zhu, and Demei Yu. Polypyrrole Nanomaterials: Structure, Preparation and Application. **Polymers**, 14(23):5139, January 2022. ISSN 2073-4360. doi: 10.3390/polym14235139. URL https://www.mdpi.com/2073-4360/14/23/5139. Number: 23 Publisher: Multidisciplinary Digital Publishing Institute.

[130] Xinyi Chen, Wen Shi, and Kun Zhang. Observation of Energy-Dependent Carrier Scattering in Conducting Polymer Nanowire Blends for Enhanced Thermoelectric Performance. **ACS Applied Materials & Interfaces**, 12(30): 34451–34461, July 2020. ISSN 1944-8244. doi: 10.1021/acsami.0c09907. URL https://doi.org/10.1021/acsami.0c09907. Publisher: American Chemical Society.

[131] Chang'an Li, Chengwei Shan, Dou Luo, Xiaoyu Gu, Qiujian Le, Aung Ko Ko Kyaw, Zhen Dong, Kuan Sun, and Jianyong Ouyang. Great Enhancement in the Seebeck Coefficient of PEDOT:PSS by Polaron Level Splitting via – Overlapping with Nonpolar Small Aromatic Molecules. **Advanced Functional Materials**, 34(9):2311578, 2024. ISSN 1616-3028. doi: 10.1002/adfm.202311578. URL https://onlinelibrary.wiley.com/doi/abs/10.1002/adfm.202311578. _eprint: https://onlinelibrary.wiley.com/doi/pdf/10.1002/adfm.202311578.

[132] Zeng Fan, Pengcheng Li, Donghe Du, and Jianyong Ouyang. Significantly Enhanced Thermoelectric Properties of PEDOT:PSS Films through Sequential Post-Treatments with Common Acids and Bases. **Advanced Energy Materials**, 7(8):1602116, 2017. ISSN 1614-6840. doi: 10.1002/aenm.201602116. URL https://onlinelibrary.wiley.com/doi/abs/10.1002/aenm.201602116. _eprint: https://onlinelibrary.wiley.com/doi/pdf/10.1002/aenm.201602116.

[133] Hui Shi, Congcong Liu, Jingkun Xu, Haijun Song, Baoyang Lu, Fengxing Jiang, Weiqiang Zhou, Ge Zhang, and Qinglin Jiang. Facile Fabrication of

PEDOT:PSS/Polythiophenes Bilayered Nanofilms on Pure Organic Electrodes and Their Thermoelectric Performance. **ACS Applied Materials & Interfaces**, 5(24):12811–12819, December 2013. ISSN 1944-8244. doi: 10.1021/am404183v. URL https://doi.org/10.1021/am404183v. Publisher: American Chemical Society.

[134] Xinfei Liu, Deqi Wang, Peng Wei, Lijun Zhu, and Jing Shi. Effect of carrier mobility on magnetothermoelectric transport properties of graphene. **Physical Review B**, 86(15):155414, October 2012. doi: 10.1103/PhysRevB.86.155414. URL https://link.aps.org/doi/10.1103/PhysRevB.86.155414. Publisher: American Physical Society.

[135] Deqi Wang and Jing Shi. Effect of charged impurities on the thermoelectric power of graphene near the Dirac point. **Physical Review B**, 83(11):113403, March 2011. doi: 10.1103/PhysRevB.83.113403. URL https://link.aps.org/doi/10.1103/PhysRevB.83.113403. Publisher: American Physical Society.

[136] Mingyu Sang, Jongwoon Shin, Kiho Kim, and Ki Jun Yu. Electronic and Thermal Properties of Graphene and Recent Advances in Graphene Based Electronics Applications. **Nanomaterials**, 9(3):374, March 2019. ISSN 2079-4991. doi: 10.3390/nano9030374. URL https://www.mdpi.com/2079-4991/9/3/374. Number: 3 Publisher: Multidisciplinary Digital Publishing Institute.

[137] Saeed Mardi, Marco Risi Ambrogioni, and Andrea Reale. Developing printable thermoelectric materials based on graphene nanoplatelet/ethyl cellulose nanocomposites. **Materials Research Express**, 7(8):085101, August 2020. ISSN 2053-1591. doi: 10.1088/2053-1591/ababc0. URL https://dx.doi.org/10.1088/2053-1591/ababc0. Publisher: IOP Publishing.

[138] Nguyen T. Hung, Ahmad R. T. Nugraha, and Riichiro Saito. Thermoelectric Properties of Carbon Nanotubes. **Energies**, 12(23):4561, January 2019. ISSN 1996-1073. doi: 10.3390/en12234561. URL https://www.mdpi.com/1996-1073/12/23/4561. Number: 23 Publisher: Multidisciplinary Digital Publishing Institute.

[139] Neazar Baghdadi, M. Sh Zoromba, M. H. Abdel-Aziz, A. F. Al-Hossainy, M. Bassyouni, and Numan Salah. One-Dimensional Nanocomposites Based on Polypyrrole-Carbon Nanotubes and Their Thermoelectric Performance. **Polymers**, 13(2):278, January 2021. ISSN 2073-4360. doi: 10.3390/polym13020278. URL https://www.mdpi.com/2073-4360/13/2/278. Number: 2 Publisher: Multidisciplinary Digital Publishing Institute.

[140] M. Almasoudi, Numan Salah, Ahmed Alshahrie, Abdu Saeed, Mutabe Aljaghtham, M. Sh Zoromba, M. H. Abdel-Aziz, and Kunihito Koumoto. High Thermoelectric Power Generation by SWCNT/PPy Core Shell

Nanocomposites. **Nanomaterials**, 12(15):2582, January 2022. ISSN 2079-4991. doi: 10.3390/nano12152582. URL https://www.mdpi.com/2079-4991/12/15/2582. Number: 15 Publisher: Multidisciplinary Digital Publishing Institute.

[141] Yihan Wang, Siqi Wu, Qinjian Yin, Bo Jiang, and Site Mo. Poly (3,4-ethylenedioxythiophene)/ polypyrrole/ carbon nanoparticle ternary nanocomposite films with enhanced thermoelectric properties. **Polymer**, 212:123131, January 2021. ISSN 0032-3861. doi: 10.1016/j.polymer.2020.123131. URL https://www.sciencedirect.com/science/article/pii/S0032386120309563.

[142] Yihan Wang, Jie Yang, Lingyu Wang, Kai Du, Qiang Yin, and Qinjian Yin. Polypyrrole/Graphene/Polyaniline Ternary Nanocomposite with High Thermoelectric Power Factor. **ACS Applied Materials & Interfaces**, 9(23): 20124–20131, June 2017. ISSN 1944-8244. doi: 10.1021/acsami.7b05357. URL https://doi.org/10.1021/acsami.7b05357. Publisher: American Chemical Society.

[143] Choongho Yu, Kyungwho Choi, Liang Yin, and Jaime C. Grunlan. Light-Weight Flexible Carbon Nanotube Based Organic Composites with Large Thermoelectric Power Factors. **ACS Nano**, 5(10):7885–7892, October 2011. ISSN 1936-0851. doi: 10.1021/nn202868a. URL https://doi.org/10.1021/nn202868a. Publisher: American Chemical Society.

[144] H. Anno, M. Fukamoto, Y. Heta, K. Koga, H. Itahara, R. Asahi, R. Satomura, M. Sannomiya, and N. Toshima. Preparation of Conducting Polyaniline–Bismuth Nanoparticle Composites by Planetary Ball Milling. **Journal of Electronic Materials**, 38(7):1443–1449, July 2009. ISSN 1543-186X. doi: 10.1007/s11664-009-0786-3. URL https://doi.org/10.1007/s11664-009-0786-3.

[145] X. B Zhao, S. H Hu, M. J Zhao, and T. J Zhu. Thermoelectric properties of Bi0.5Sb1.5Te3/polyaniline hybrids prepared by mechanical blending. **Materials Letters**, 52(3):147–149, January 2002. ISSN 0167-577X. doi: 10.1016/S0167-577X(01)00381-0. URL https://www.sciencedirect.com/science/article/pii/S0167577X01003810.

[146] Ajit Debnath, Jayanta Das, Krishna Deb, Kartick L. Bhowmik, and Biswajit Saha. Camphor sulfonic acid incorporation in SnO2/polyaniline nanocomposites for improved thermoelectric energy conversion. **Sustainable Energy & Fuels**, 6(5):1332–1344, March 2022. ISSN 2398-4902. doi: 10.1039/D1SE01909K. URL https://pubs.rsc.org/en/content/articlelanding/2022/se/d1se01909k. Publisher: The Royal Society of Chemistry.

[147] Sagarika Bhagade, Ajit Debnath, Dipankar Das, and Biswajit Saha. Thermoelectric composite material of CuBO2 incorporated PANI powders

with enhanced Seebeck coefficient. **Journal of Polymer Research**, 29(12): 505, November 2022. ISSN 1572-8935. doi: 10.1007/s10965-022-03306-w. URL https://doi.org/10.1007/s10965-022-03306-w.

[148] Naoki Toshima, Masahiro Imai, and Shoko Ichikawa. Organic–Inorganic Nanohybrids as Novel Thermoelectric Materials: Hybrids of Polyaniline and Bismuth(III) Telluride Nanoparticles. **Journal of Electronic Materials**, 40(5):898–902, May 2011. ISSN 1543-186X. doi: 10.1007/s11664-010-1403-1. URL https://doi.org/10.1007/s11664-010-1403-1.

[149] Eun Jin Bae, Young Hun Kang, Kwang-Suk Jang, and Song Yun Cho. Enhancement of Thermoelectric Properties of PEDOT:PSS and Tellurium-PEDOT:PSS Hybrid Composites by Simple Chemical Treatment. **Scientific Reports**, 6(1):18805, January 2016. ISSN 2045-2322. doi: 10.1038/srep18805. URL https://www.nature.com/articles/srep18805. Publisher: Nature Publishing Group.

[150] Y. Y. Wang, K. F. Cai, J. L. Yin, B. J. An, Y. Du, and X. Yao. In situ fabrication and thermoelectric properties of PbTe–polyaniline composite nanostructures. **Journal of Nanoparticle Research**, 13(2):533–539, February 2011. ISSN 1572-896X. doi: 10.1007/s11051-010-0043-y. URL https://doi.org/10.1007/s11051-010-0043-y.

[151] Ajit Debnath, Krishna Deb, Kamanashis Sarkar, and Biswajit Saha. Improved Thermoelectric Performance in TiO2 Incorporated Polyaniline: A Polymer-Based Hybrid Material for Thermoelectric Generators. **Journal of Electronic Materials**, 49(8):5028–5036, August 2020. ISSN 1543-186X. doi: 10.1007/s11664-020-08241-4. URL https://doi.org/10.1007/s11664-020-08241-4.

[152] Ying Li, Xuehui Wang, Ding Luo, Yong Shi, Yong Ren, and Yuying Yan. Recent development in structural designs and thermal enhancement technologies of thermoelectric generator with different types of heat sources: A review. **e-Prime - Advances in Electrical Engineering, Electronics and Energy**, 4:100180, June 2023. ISSN 2772-6711. doi: 10.1016/j.prime.2023.100180. URL https://www.sciencedirect.com/science/article/pii/S277267112300075X.

[153] Atif Al-Otaibi, Alaa Attar, Neazar Baghdadi, Numan Salah, Mohamed Shafick Zoromba, and Mohamed Helmy Abdel-Aziz. Ternary composites of PPy/MWCNTs/metals hydroxide for thermoelectric applications. **Journal of Materials Science: Materials in Electronics**, 35(13): 924, May 2024. ISSN 1573-482X. doi: 10.1007/s10854-024-12654-w. URL https://doi.org/10.1007/s10854-024-12654-w.

[154] Chhatrasal Gayner and Yaron Amouyal. Energy Filtering of Charge Carriers: Current Trends, Challenges, and Prospects for Thermoelec-

tric Materials. **Advanced Functional Materials**, 30(18):1901789, 2020. ISSN 1616-3028. doi: 10.1002/adfm.201901789. URL https://onlinelibrary.wiley.com/doi/abs/10.1002/adfm.201901789. _eprint: https://onlinelibrary.wiley.com/doi/pdf/10.1002/adfm.201901789.

[155] Xin Guan and Jianyong Ouyang. Enhancement of the Seebeck Coefficient of Organic Thermoelectric Materials via Energy Filtering of Charge Carriers. **CCS Chemistry**, 3(10):2415–2427, August 2021. doi: 10.31635/ccschem.021.202101069. URL https://www.chinesechemsoc.org/doi/10.31635/ccschem.021.202101069. Publisher: Chinese Chemical Society.

[156] Zizhen Lin, Hao Dang, Chunyu Zhao, Yanzheng Du, Cheng Chi, Weigang Ma, Yinshi Li, and Xing Zhang. The cross-interface energy-filtering effect at organic/inorganic interfaces balances the trade-off between thermopower and conductivity. **Nanoscale**, 14(26):9419–9430, July 2022. ISSN 2040-3372. doi: 10.1039/D2NR02432B. URL https://pubs.rsc.org/en/content/articlelanding/2022/nr/d2nr02432b. Publisher: The Royal Society of Chemistry.

[157] Shichao Wang, Yan Zhou, Yijia Liu, Lei Wang, and Chunmei Gao. Enhanced thermoelectric properties of polyaniline/polypyrrole/carbon nanotube ternary composites by treatment with a secondary dopant using ferric chloride. **Journal of Materials Chemistry C**, 8(2):528–535, January 2020. ISSN 2050-7534. doi: 10.1039/C9TC06300E. URL https://pubs.rsc.org/en/content/articlelanding/2020/tc/c9tc06300e. Publisher: The Royal Society of Chemistry.

[158] Kun Zhang, Yue Zhang, and Shiren Wang. Enhancing thermoelectric properties of organic composites through hierarchical nanostructures. **Scientific Reports**, 3(1):3448, December 2013. ISSN 2045-2322. doi: 10.1038/srep03448. URL https://www.nature.com/articles/srep03448. Number: 1 Publisher: Nature Publishing Group.

[159] N. I. Zaaba, K. L. Foo, U. Hashim, S. J. Tan, Wei-Wen Liu, and C. H. Voon. Synthesis of Graphene Oxide using Modified Hummers Method: Solvent Influence. **Procedia Engineering**, 184:469–477, January 2017. ISSN 1877-7058. doi: 10.1016/j.proeng.2017.04.118. URL https://www.sciencedirect.com/science/article/pii/S1877705817316235.

[160] William S. Jr. Hummers and Richard E. Offeman. Preparation of Graphitic Oxide. **Journal of the American Chemical Society**, 80(6):1339–1339, March 1958. ISSN 0002-7863. doi: 10.1021/ja01539a017. URL https://doi.org/10.1021/ja01539a017. Publisher: American Chemical Society.

[161] Jeong Yun Kim and Jeffrey C. Grossman. High-Efficiency Thermoelectrics with Functionalized Graphene. **Nano Letters**, 15(5):2830–2835, May 2015.

ISSN 1530-6984. doi: 10.1021/nl504257q. URL https://doi.org/10.1021/nl504257q. Publisher: American Chemical Society.

[162] Huarui Zhu, Ping Huang, Long Jing, Taisen Zuo, Yuliang Zhao, and Xueyun Gao. Microstructure evolution of diazonium functionalized graphene: A potential approach to change graphene electronic structure. **Journal of Materials Chemistry**, 22(5):2063–2068, January 2012. ISSN 1364-5501. doi: 10.1039/C1JM14862A. URL https://pubs.rsc.org/en/content/articlelanding/2012/jm/c1jm14862a. Publisher: The Royal Society of Chemistry.

[163] Dongyu Cai and Mo Song. Recent advance in functionalized graphene/polymer nanocomposites. **Journal of Materials Chemistry**, 20 (37):7906–7915, September 2010. ISSN 1364-5501. doi: 10.1039/C0JM00530D. URL https://pubs.rsc.org/en/content/articlelanding/2010/jm/c0jm00530d. Publisher: The Royal Society of Chemistry.

[164] Lirong Liang, Jueshuo Fan, Miaomiao Wang, Guangming Chen, and Guoxing Sun. Ternary thermoelectric composites of polypyrrole/PEDOT:PSS/carbon nanotube with unique layered structure prepared by one-dimensional polymer nanostructure as template. **Composites Science and Technology**, 187:107948, February 2020. ISSN 0266-3538. doi: 10.1016/j.compscitech.2019.107948. URL https://www.sciencedirect.com/science/article/pii/S0266353819327988.

[165] Younes Bourenane Cherif, Nawel Matmat, Zakaria Bekkar Djelloul Sayah, Ahmed Mekki, Jean-Félix Durastanti, and Zineb Mekhalif. Influence of graphene oxide surface treatment by diazonium salts on thermoelectrical behavior of polypyrrole-based composites. **Journal of Materials Science: Materials in Electronics**, 33(18):14938–14950, June 2022. ISSN 1573-482X. doi: 10.1007/s10854-022-08410-7. URL https://doi.org/10.1007/s10854-022-08410-7.

[166] Betelu S, Tijunelyte I, Boubekeur-Lecaque L, Ignatiadis I, Schnepf Ac, Guenin E, Bouchemal N, Felidj N, Rinnert E, and Lamy de la Chapelle M. Raman Characterization of Phenyl-Derivatives: From Primary Amine to Diazonium Salts. **Journal of Organic & Inorganic Chemistry**, 3(1), March 2017. ISSN ISSN No. 2472-1123. doi: 10.21767/2472-1123.100021. Publisher: iMedPub.

[167] Jean-Philippe Jasmin, Caroline Cannizzo, Eddy Dumas, and Annie Chaussé. Fabrication and characterization of all-covalent nanocomposite functionalized screen-printed voltammetric sensors. **Electrochimica Acta**, 133:467–474, July 2014. ISSN 0013-4686. doi: 10.1016/j.electacta.2014.04.069. URL https://www.sciencedirect.com/science/article/pii/S0013468614008160.

[168] Deepshikha Shahdeo, Akanksha Roberts, Naina Abbineni, and Sonu Gandhi. Chapter Eight - Graphene based sensors. In Chaudhery Mustansar Hussain, editor, **Comprehensive Analytical Chemistry**, volume 91 of **Analytical Applications of Graphene for Comprehensive Analytical Chemistry**, pages 175–199. Elsevier, January 2020. doi: 10.1016/bs.coac.2020.08.007. URL https://www.sciencedirect.com/science/article/pii/S0166526X2030060X.

[169] Sasha Stankovich, Dmitriy A. Dikin, Richard D. Piner, Kevin A. Kohlhaas, Alfred Kleinhammes, Yuanyuan Jia, Yue Wu, SonBinh T. Nguyen, and Rodney S. Ruoff. Synthesis of graphene-based nanosheets via chemical reduction of exfoliated graphite oxide. **Carbon**, 45(7):1558–1565, June 2007. ISSN 0008-6223. doi: 10.1016/j.carbon.2007.02.034. URL https://www.sciencedirect.com/science/article/pii/S0008622307000917.

[170] Jay R. Lomeda, Condell D. Doyle, Dmitry V. Kosynkin, Wen-Fang Hwang, and James M. Tour. Diazonium Functionalization of Surfactant-Wrapped Chemically Converted Graphene Sheets. **Journal of the American Chemical Society**, 130(48):16201–16206, December 2008. ISSN 0002-7863. doi: 10.1021/ja806499w. URL https://doi.org/10.1021/ja806499w. Publisher: American Chemical Society.

[171] Zakaria Bekkar Djelloul Sayah, Ahmed Mekki, Fabien Delaleux, Olivier Riou, and Jean-Felix Durastanti. Response Surface Methodology as a Powerful Tool for the Synthesis of Polypyrrole-Doped Organic Sulfonic Acid and the Optimization of its Thermoelectric Properties. **Journal of Electronic Materials**, 48(6):3662–3675, June 2019. ISSN 1543-186X. doi: 10.1007/s11664-019-07124-7. URL https://doi.org/10.1007/s11664-019-07124-7.

[172] R. Corradi and S. P. Armes. Chemical synthesis of poly(3,4-ethylenedioxythiophene). **Synthetic Metals**, 84(1):453–454, January 1997. ISSN 0379-6779. doi: 10.1016/S0379-6779(97)80828-4. URL https://www.sciencedirect.com/science/article/pii/S0379677997808284.

[173] S. Munusamy, R. Suresh, K. Giribabu, R. Manigandan, S. Praveen Kumar, S. Muthamizh, C. Bagavath, A. Stephen, J. Kumar, and V. Narayanan. Synthesis and characterization of GaN/PEDOT–PPY nanocomposites and its photocatalytic activity and electrochemical detection of mebendazole. **Arabian Journal of Chemistry**, 12(8):3565–3575, December 2019. ISSN 1878-5352. doi: 10.1016/j.arabjc.2015.10.012. URL https://www.sciencedirect.com/science/article/pii/S1878535215003081.

[174] H. J. Kharat, K. P. Kakde, P. A. Savale, K. Datta, P. Ghosh, and M. D. Shirsat. Synthesis of polypyrrole films for the development of ammonia sensor. **Polymers for Advanced Technologies**, 18(5):397–402,

2007. ISSN 1099-1581. doi: 10.1002/pat.903. URL https://onlinelibrary.wiley.com/doi/abs/10.1002/pat.903. _eprint: https://onlinelibrary.wiley.com/doi/pdf/10.1002/pat.903.

[175] Mária Omastová, Miroslava Mravcáková, Ivan Chodák, Jürgen Pionteck, and Liane Häussler. Conductive polypropylene/clay/polypyrrole nanocomposites. **Polymer Engineering & Science**, 46(8):1069–1078, 2006. ISSN 1548-2634. doi: 10.1002/pen.20551. URL https://onlinelibrary.wiley.com/doi/abs/10.1002/pen.20551. _eprint: https://onlinelibrary.wiley.com/doi/pdf/10.1002/pen.20551.

[176] Qin Zhao, Ruxangul Jamal, Li Zhang, Minchao Wang, and Tursun Abdiryim. The structure and properties of PEDOT synthesized by template-free solution method. **Nanoscale Research Letters**, 9(1):557, October 2014. ISSN 1556-276X. doi: 10.1186/1556-276X-9-557. URL https://doi.org/10.1186/1556-276X-9-557.

[177] Firdaus Abd-Wahab, Habibah Farhana Abdul Guthoos, and Wan Wardatul Amani Wan Salim. Solid-State rGO-PEDOT:PSS Transducing Material for Cost-Effective Enzymatic Sensing. **Biosensors**, 9(1):36, March 2019. ISSN 2079-6374. doi: 10.3390/bios9010036. URL https://www.mdpi.com/2079-6374/9/1/36. Number: 1 Publisher: Multidisciplinary Digital Publishing Institute.

[178] Ahmed Mekki, Soumen Samanta, Ajay Singh, Zakaria Salmi, Rachid Mahmoud, Mohamed M. Chehimi, and Dinesh K. Aswal. Core/shell, protuberance-free multiwalled carbon nanotube/polyaniline nanocomposites via interfacial chemistry of aryl diazonium salts. **Journal of Colloid and Interface Science**, 418:185–192, March 2014. ISSN 0021-9797. doi: 10.1016/j.jcis.2013.11.077. URL https://www.sciencedirect.com/science/article/pii/S0021979713010709.

[179] Afarin Bahrami, Zainal Abidin Talib, Wan Mahmood Mat Yunus, Kasra Behzad, Mahnaz M. Abdi, and Fasih Ud Din. Low Temperature Hall Effect Investigation of Conducting Polymer-Carbon Nanotubes Composite Network. **International Journal of Molecular Sciences**, 13(11):14917–14928, November 2012. ISSN 1422-0067. doi: 10.3390/ijms131114917. URL https://www.mdpi.com/1422-0067/13/11/14917. Number: 11 Publisher: Multidisciplinary Digital Publishing Institute.

[180] Mousumi Mitra, Chiranjit Kulsi, Krishanu Chatterjee, Kajari Kargupta, Saibal Ganguly, Dipali Banerjee, and Shyamaprosad Goswami. Reduced graphene oxide-polyaniline composites—synthesis, characterization and optimization for thermoelectric applications. **RSC Advances**, 5(39):31039–31048, March 2015. ISSN 2046-2069. doi: 10.1039/C5RA01794G. URL https://pubs.rsc.org/en/content/articlelanding/2015/ra/c5ra01794g. Publisher: The Royal Society of Chemistry.

[181] Qin Yao, Lidong Chen, Wenqing Zhang, Shengcong Liufu, and Xihong Chen. Enhanced Thermoelectric Performance of Single-Walled Carbon Nanotubes/Polyaniline Hybrid Nanocomposites. **ACS Nano**, 4(4):2445–2451, April 2010. ISSN 1936-0851. doi: 10.1021/nn1002562. URL https://doi.org/10.1021/nn1002562. Publisher: American Chemical Society.

[182] Nelson E. Coates, Shannon K. Yee, Bryan McCulloch, Kevin C. See, Arun Majumdar, Rachel A. Segalman, and Jeffrey J. Urban. Effect of Interfacial Properties on Polymer–Nanocrystal Thermoelectric Transport. **Advanced Materials**, 25(11):1629–1633, 2013. ISSN 1521-4095. doi: 10.1002/adma.201203915. URL https://onlinelibrary.wiley.com/doi/abs/10.1002/adma.201203915. _eprint: https://onlinelibrary.wiley.com/doi/pdf/10.1002/adma.201203915.

[183] Weijie Wang, Qihao Zhang, Jianlin Li, Xia Liu, Lianjun Wang, Juanjuan Zhu, Wei Luo, and Wan Jiang. An efficient thermoelectric material: preparation of reduced graphene oxide/polyaniline hybrid composites by cryogenic grinding. **RSC Advances**, 5(12):8988–8995, January 2015. ISSN 2046-2069. doi: 10.1039/C4RA12051E. URL https://pubs.rsc.org/en/content/articlelanding/2015/ra/c4ra12051e. Publisher: The Royal Society of Chemistry.

[184] Younes Bourenane Cherif, Zineb Mekhalif, Ahmed Mekki, and Zakaria Bekkar Djelloul Sayah. Effect of MWCNTs surface functionalization group nature on the thermoelectric power factor of PPy/MWCNTs nanocomposites. **Synthetic Metals**, 291:117196, December 2022. ISSN 0379-6779. doi: 10.1016/j.synthmet.2022.117196. URL https://www.sciencedirect.com/science/article/pii/S0379677922001904.

[185] Arvind K. Bhakta, S. Detriche, P. Martis, R. J. Mascarenhas, J. Delhalle, and Z. Mekhalif. Decoration of tricarboxylic and monocarboxylic aryl diazonium functionalized multi-wall carbon nanotubes with iron nanoparticles. **Journal of Materials Science**, 52(16):9648–9660, August 2017. ISSN 1573-4803. doi: 10.1007/s10853-017-1100-z. URL https://doi.org/10.1007/s10853-017-1100-z.

[186] Pisan Chungchamroenkit, Sumaeth Chavadej, Ummarawadee Yanatatsaneejit, and Boonyarach Kitiyanan. Residue catalyst support removal and purification of carbon nanotubes by NaOH leaching and froth flotation. **Separation and Purification Technology**, 60(2):206–214, April 2008. ISSN 1383-5866. doi: 10.1016/j.seppur.2007.08.009. URL https://www.sciencedirect.com/science/article/pii/S1383586607003802.

[187] P. Martis, B. R. Venugopal, J. F. Seffer, J. Delhalle, and Z. Mekhalif. Infrared irradiation controlled decoration of multiwalled carbon nanotubes with copper/copper oxide nanocrystals. **Acta Materialia**, 59(12):5040–5047,

July 2011. ISSN 1359-6454. doi: 10.1016/j.actamat.2011.04.061. URL https://www.sciencedirect.com/science/article/pii/S135964541100317X.

[188] Le Thi Mai Hoa. Characterization of multi-walled carbon nanotubes functionalized by a mixture of HNO3/H2SO4. **Diamond and Related Materials**, 89:43–51, October 2018. ISSN 0925-9635. doi: 10.1016/j.diamond.2018.08.008. URL https://www.sciencedirect.com/science/article/pii/S092596351830325X.

[189] Arvind K. Bhakta, Simon Detriche, Sunita Kumari, Sahid Hussain, Praveen Martis, Ronald J. Mascarenhas, Joseph Delhalle, and Zineb Mekhalif. Multi-wall Carbon Nanotubes Decorated with Bismuth Oxide Nanocrystals Using Infrared Irradiation and Diazonium Chemistry. **Journal of Inorganic and Organometallic Polymers and Materials**, 28(4):1402–1413, July 2018. ISSN 1574-1451. doi: 10.1007/s10904-018-0800-4. URL https://doi.org/10.1007/s10904-018-0800-4.

[190] Jiao Wang, Kefeng Cai, Shirley Shen, and Junlin Yin. Preparation and thermoelectric properties of multi-walled carbon nanotubes/polypyrrole composites. **Synthetic Metals**, 195:132–136, September 2014. ISSN 0379-6779. doi: 10.1016/j.synthmet.2014.06.003. URL https://www.sciencedirect.com/science/article/pii/S0379677914001994.

[191] Choongho Yu, Advaith Murali, Kyungwho Choi, and Yeontack Ryu. Air-stable fabric thermoelectric modules made of N- and P-type carbon nanotubes. **Energy & Environmental Science**, 5(11):9481–9486, October 2012. ISSN 1754-5706. doi: 10.1039/C2EE22838F. URL https://pubs.rsc.org/en/content/articlelanding/2012/ee/c2ee22838f. Publisher: The Royal Society of Chemistry.

[192] Tongzhou Wang, Congcong Liu, Fengxing Jiang, Zhaofen Xu, Xiaodong Wang, Xia Li, Changcun Li, Jingkun Xu, and Xiaowei Yang. Solution-processed two-dimensional layered heterostructure thin-film with optimized thermoelectric performance. **Physical Chemistry Chemical Physics**, 19(27):17560–17567, July 2017. ISSN 1463-9084. doi: 10.1039/C7CP02011B. URL https://pubs.rsc.org/en/content/articlelanding/2017/cp/c7cp02011b. Publisher: The Royal Society of Chemistry.

[193] M. Satyanarayana, K. Yugender Goud, K. Koteshwara Reddy, V. Sunil Kumar, and K. Vengatajalabathy Gobi. Silver nanoparticles impregnated chitosan layered carbon nanotube as sensor interface for electrochemical detection of clopidogrel in-vitro. **Materials Science and Engineering: C**, 101:103–110, August 2019. ISSN 0928-4931. doi: 10.1016/j.msec.2019.03.083. URL https://www.sciencedirect.com/science/article/pii/S0928493118337111.

[194] Susana L. H. Rebelo, Alexandra Guedes, Monika E. Szefczyk, André M. Pereira, João P. Araújo, and Cristina Freire. Progress in the Raman spectra analysis of covalently functionalized multiwalled carbon nanotubes: unraveling disorder in graphitic materials. **Physical Chemistry Chemical Physics**, 18(18):12784–12796, May 2016. ISSN 1463-9084. doi: 10.1039/C5CP06519D. URL https://pubs.rsc.org/en/content/articlelanding/2016/cp/c5cp06519d. Publisher: The Royal Society of Chemistry.

[195] Intan Syaffinazzilla Zaine, N. a. M. Napiah, Azmi Mohamad Yusof, A. N. Alias, A. M. M. Ali, and Siti Hajar Khalid. Study on Dispersion and Characterization of Functionalized MWCNTs Prepared by Wet Oxidation. **Applied Mechanics and Materials**, 661:8–13, 2014. ISSN 1662-7482. doi: 10.4028/www.scientific.net/AMM.661.8. URL https://www.scientific.net/AMM.661.8. Publisher: Trans Tech Publications Ltd.

[196] Hugo Bares. **Fonctionnalisation chimique du graphène, : vers des matériaux bidimentionnels photo actifs pour la reconnaissance et l'électronique moléculaire**. These de doctorat, Bordeaux, December 2015. URL https://www.theses.fr/2015BORD0400.

[197] Xin Fan, Zhewei Yang, and Nan He. Hierarchical nanostructured polypyrrole/graphene composites as supercapacitor electrode. **RSC Advances**, 5(20):15096–15102, January 2015. ISSN 2046-2069. doi: 10.1039/C4RA15258A. URL https://pubs.rsc.org/en/content/articlelanding/2015/ra/c4ra15258a. Publisher: The Royal Society of Chemistry.

[198] Jean Luc Bredas and G. Bryan Street. Polarons, bipolarons, and solitons in conducting polymers. **Accounts of Chemical Research**, 18(10):309–315, October 1985. ISSN 0001-4842. doi: 10.1021/ar00118a005. URL https://doi.org/10.1021/ar00118a005. Publisher: American Chemical Society.

[199] Sanjay G. Bachhav and Dilip R. Patil. Study of Polypyrrole-Coated MWCNT Nanocomposites for Ammonia Sensing at Room Temperature. **Journal of Materials Science and Chemical Engineering**, 3(10): 30–44, October 2015. doi: 10.4236/msce.2015.310005. URL https://www.scirp.org/journal/paperinformation.aspx?paperid=60855. Number: 10 Publisher: Scientific Research Publishing.

[200] Yesi Yesi, Indrajit Shown, Abhijit Ganguly, Trung Truc Ngo, Li-Chyong Chen, and Kuei-Hsien Chen. Directly-Grown Hierarchical Carbon Nanotube@Polypyrrole Core–Shell Hybrid for High-Performance Flexible Supercapacitors. **ChemSusChem**, 9(4):370–378, 2016. ISSN 1864-564X. doi: 10.1002/cssc.201501495. URL https://onlinelibrary.wiley.com/doi/abs/10.1002/cssc.201501495. _eprint: https://onlinelibrary.wiley.com/doi/pdf/10.1002/cssc.201501495.

[201] Thaís Larissa do Amaral Montanheiro, Fernando Henrique Cristóvan, João Paulo Barros Machado, Dayane Batista Tada, Nelson Durán, and Ana Paula Lemes. Effect of MWCNT functionalization on thermal and electrical properties of PHBV/MWCNT nanocomposites. **Journal of Materials Research**, 30(1):55–65, January 2015. ISSN 2044-5326. doi: 10.1557/jmr.2014.303. URL https://doi.org/10.1557/jmr.2014.303.

[202] Ayush Chowdhry, Jasreen Kaur, Madhu Khatri, Veena Puri, Rakesh Tuli, and Sanjeev Puri. Characterization of functionalized multiwalled carbon nanotubes and comparison of their cellular toxicity between HEK 293 cells and zebra fish in vivo. **Heliyon**, 5(10):e02605, October 2019. ISSN 2405-8440. doi: 10.1016/j.heliyon.2019.e02605. URL https://www.sciencedirect.com/science/article/pii/S2405844019362656.

[203] Shiao-Wen Tsai, Jiunn-Woei Liaw, Fu-Yin Hsu, Yi-Yun Chen, Mei-Jhih Lyu, and Ming-His Yeh. Surface-Modified Gold Nanoparticles with Folic Acid as Optical Probes for Cellular Imaging. **Sensors**, 8(10):6660–6673, October 2008. ISSN 1424-8220. doi: 10.3390/s8106660. URL https://www.mdpi.com/1424-8220/8/10/6660. Number: 10 Publisher: Molecular Diversity Preservation International.

[204] S. K. Swathi, T. Jeevananda, and Praveen C. Ramamurthy. Fabrication of device quality films of high loaded PPy/MWCNT nanocomposites using pulsed laser deposition. **Organic Electronics**, 11(9):1489–1499, September 2010. ISSN 1566-1199. doi: 10.1016/j.orgel.2010.06.013. URL https://www.sciencedirect.com/science/article/pii/S1566119910002016.

[205] Pavol Gemeiner, Jaroslav Kuliček, Milan Mikula, Michal Hatala, Ľubomír Švorc, Lenka Hlavatá, Matej Mičušík, and Mária Omastová. Polypyrrole-coated multi-walled carbon nanotubes for the simple preparation of counter electrodes in dye-sensitized solar cells. **Synthetic Metals**, 210: 323–331, December 2015. ISSN 0379-6779. doi: 10.1016/j.synthmet.2015.10.020. URL https://www.sciencedirect.com/science/article/pii/S0379677915301247.

[206] G. Zerbi, C. Castiglioni, J. T. Lopez Navarrete, T. Bogang, and M. Gussoni. A molecular viewpoint of lattice dynamics and spectra of conducting polymers. **Synthetic Metals**, 28(3):D359–D368, February 1989. ISSN 0379-6779. doi: 10.1016/0379-6779(89)90715-7. URL https://www.sciencedirect.com/science/article/pii/0379677989907157.

[207] C.R.K. Rao, R. Muthukannan, J. Adriel Jebin, T. Antony Raj, and M. Vijayan. Synthesis and properties of polypyrrole obtained from a new Fe(III) complex as oxidizing agent. **Indian Journal of Chemistry - Section A Inorganic, Physical, Theoretical and Analytical Chemistry**, 52(6):744–748, 2013. ISSN 0975-0975.

[208] E. Titus, N. Ali, G. Cabral, J. Gracio, P. Ramesh Babu, and M. J. Jackson. Chemically functionalized carbon nanotubes and their characterization using thermogravimetric analysis, fourier transform infrared, and raman spectroscopy. **Journal of Materials Engineering and Performance**, 15 (2):182–186, April 2006. ISSN 1544-1024. doi: 10.1361/105994906X95841. URL https://doi.org/10.1361/105994906X95841.

[209] Jiang Li, Alayna Brieann Huckleby, and Mei Zhang. The enhanced power factor of multi-walled carbon nanotube/stabilized polyacrylonitrile composites due to the partially conjugated structure. **Journal of Materiomics**, 7(1):51–58, January 2021. ISSN 2352-8478. doi: 10.1016/j.jmat.2020.08.002. URL https://www.sciencedirect.com/science/article/pii/S235284782030349X.

[210] Jijun Zhao, Hyoungki Park, Jie Han, and Jian Ping Lu. Electronic Properties of Carbon Nanotubes with Covalent Sidewall Functionalization. **The Journal of Physical Chemistry B**, 108(14):4227–4230, April 2004. ISSN 1520-6106. doi: 10.1021/jp036814u. URL https://doi.org/10.1021/jp036814u. Publisher: American Chemical Society.

[211] Théodore Olla. **Ingénierie moléculaire de polymères semi-conducteurs halogénés : influence de la nature et de la position des halogènes**. These de doctorat, Strasbourg, August 2019. URL https://www.theses.fr/2019STRAE018.

[212] Younes Bourenane Cherif, Zineb Mekhalif, Ahmed Mekki, Zakaria Bekkar Djelloul Sayah, and Souleymen Rafai. Enhanced thermoelectric power factor of PPy-based nanocomposites: effect of decorated graphene nanoplatelets by bismuth oxide nanoparticles. **Journal of Materials Science**, 58(11):4809–4823, March 2023. ISSN 1573-4803. doi: 10.1007/s10853-023-08334-5. URL https://doi.org/10.1007/s10853-023-08334-5.

[213] Younes Bourenane Cherif, Zineb Mekhalif, Ahmed Mekki, and Zakaria Bekkar Djelloul Sayah. Effect of decorated MWCNTs by bismuth oxide nanoparticles on the thermoelectric properties of polypyrrole-based nanocomposites. page 3, Ouargla, Algeria, October 2022. URL https://icrme2022.sciencesconf.org/.

[214] Hafiz Muhammad Sajid, Hafsa Afzal, Muhammad Irfan, Mohsin Saleem, Rahim Jan, Sofia Javed, and Muhammad Aftab Akram. Design of Multilayered 2D Nanomaterial Composite Structures for EMI Shielding Analysis. **ACS Omega**, 7(40):35586–35594, October 2022. doi: 10.1021/acsomega.2c03186. URL https://doi.org/10.1021/acsomega.2c03186. Publisher: American Chemical Society.

[215] Raji Atchudan, Arumugam Pandurangan, and Jin Joo. Effects of Nanofillers on the Thermo-Mechanical Properties and Chemical Resistiv-

ity of Epoxy Nanocomposites. **Journal of Nanoscience and Nanotechnology**, 15(6):4255–4267, June 2015. doi: 10.1166/jnn.2015.9706.

[216] Martin R. Ward, Shatha Younis, Aurora J. Cruz-Cabeza, Craig L. Bull, Nicholas P. Funnell, and Iain D. H. Oswald. Discovery and recovery of delta p-aminobenzoic acid. **CrystEngComm**, 21(13):2058–2066, March 2019. ISSN 1466-8033. doi: 10.1039/C8CE01882K. URL https://pubs.rsc.org/en/content/articlelanding/2019/ce/c8ce01882k. Publisher: The Royal Society of Chemistry.

[217] P. Karuppasamy, T. Kamalesh, V. Mohankumar, S. Abdul Kalam, Muthu Senthil Pandian, P. Ramasamy, Sunil Verma, and S. Venugopal Rao. Synthesis, growth, structural, optical, thermal, laser damage threshold and computational perspectives of 4-nitrophenol 4-aminobenzoic acid monohydrate (4NPABA) single crystal. **Journal of Molecular Structure**, 1176: 254–265, January 2019. ISSN 0022-2860. doi: 10.1016/j.molstruc.2018.08.074. URL https://www.sciencedirect.com/science/article/pii/S0022286018310238.

[218] Xinwei Li, Yanjuan Sun, Ting Xiong, Guangming Jiang, Yuxin Zhang, Zhongbiao Wu, and Fan Dong. Activation of amorphous bismuth oxide via plasmonic Bi metal for efficient visible-light photocatalysis. **Journal of Catalysis**, 352:102–112, August 2017. ISSN 0021-9517. doi: 10.1016/j.jcat.2017.04.025. URL https://www.sciencedirect.com/science/article/pii/S002195171730146X.

[219] Milena Šetka, Raúl Calavia, Lukáš Vojkůvka, Eduard Llobet, Jana Drbohlavová, and Stella Vallejos. Raman and XPS studies of ammonia sensitive polypyrrole nanorods and nanoparticles. **Scientific Reports**, 9 (1):8465, June 2019. ISSN 2045-2322. doi: 10.1038/s41598-019-44900-1. URL https://www.nature.com/articles/s41598-019-44900-1. Number: 1 Publisher: Nature Publishing Group.

[220] Mei Li, Yunqiang Zhang, Lanlan Yang, Yingkai Liu, and Jingyun Ma. Excellent electrochemical performance of homogeneous polypyrrole/-graphene composites as electrode material for supercapacitors. **Journal of Materials Science: Materials in Electronics**, 26(1):485–492, January 2015. ISSN 1573-482X. doi: 10.1007/s10854-014-2425-x. URL https://doi.org/10.1007/s10854-014-2425-x.

[221] Amr Alatawna, Matan Birenboim, Roey Nadiv, Matat Buzaglo, Sivan Peretz-Damari, Alva Peled, Oren Regev, and Raghu Sripada. The effect of compatibility and dimensionality of carbon nanofillers on cement composites. **Construction and Building Materials**, 232:117141, January 2020. ISSN 0950-0618. doi: 10.1016/j.conbuildmat.2019.117141. URL https://www.sciencedirect.com/science/article/pii/S0950061819325899.

[222] Arvind K. Bhakta, Sunita Kumari, Sahid Hussain, Simon Detriche, Joseph Delhalle, and Zineb Mekhalif. Differently substituted aniline functionalized MWCNTs to anchor oxides of Bi and Ni nanoparticles. **Journal of Nanostructure in Chemistry**, 9(4):299–314, December 2019. ISSN 2193-8865. doi: 10.1007/s40097-019-00319-8. URL https://doi.org/10.1007/s40097-019-00319-8.

[223] Jianyun Cao, Yaming Wang, Junchen Chen, Xiaohong Li, Frank C. Walsh, Jia-Hu Ouyang, Dechang Jia, and Yu Zhou. Three-dimensional graphene oxide/polypyrrole composite electrodes fabricated by one-step electrodeposition for high performance supercapacitors. **Journal of Materials Chemistry A**, 3(27):14445–14457, June 2015. ISSN 2050-7496. doi: 10.1039/C5TA02920A. URL https://pubs.rsc.org/en/content/articlelanding/2015/ta/c5ta02920a. Publisher: The Royal Society of Chemistry.

[224] L. Gence, S. Faniel, C. Gustin, S. Melinte, V. Bayot, V. Callegari, O. Reynes, and S. Demoustier-Champagne. Structural and electrical characterization of hybrid metal-polypyrrole nanowires. **Physical Review B**, 76(11):115415, September 2007. doi: 10.1103/PhysRevB.76.115415. URL https://link.aps.org/doi/10.1103/PhysRevB.76.115415. Publisher: American Physical Society.

[225] T. S. Sreeprasad and Vikas Berry. How Do the Electrical Properties of Graphene Change with its Functionalization? **Small**, 9(3):341–350, 2013. ISSN 1613-6829. doi: 10.1002/smll.201202196. URL https://onlinelibrary.wiley.com/doi/abs/10.1002/smll.201202196. _eprint: https://onlinelibrary.wiley.com/doi/pdf/10.1002/smll.201202196.

[226] Yichuan Zhang, Qichun Zhang, and Guangming Chen. Carbon and carbon composites for thermoelectric applications. **Carbon Energy**, 2(3):408–436, 2020. ISSN 2637-9368. doi: 10.1002/cey2.68. URL https://onlinelibrary.wiley.com/doi/abs/10.1002/cey2.68. _eprint: https://onlinelibrary.wiley.com/doi/pdf/10.1002/cey2.68.

[227] Manal Alsalama, Hicham Hamoudi, and Khaled M. Youssef. The effect of graphene structural integrity on the power factor of tin selenide nanocomposite. **Journal of Alloys and Compounds**, 872:159584, August 2021. ISSN 0925-8388. doi: 10.1016/j.jallcom.2021.159584. URL https://www.sciencedirect.com/science/article/pii/S0925838821009932.

[228] Weon Ho Shin, Kyunghan Ahn, Mahn Jeong, Jeong Seop Yoon, Jae Min Song, Soonil Lee, Won Seon Seo, and Young Soo Lim. Enhanced thermoelectric performance of reduced graphene oxide incorporated bismuth-antimony-telluride by lattice thermal conductivity reduction. **Journal of Alloys and Compounds**, 718:342–348, September 2017. ISSN 0925-8388. doi: 10.1016/j.jallcom.2017.05.204. URL https://www.sciencedirect.com/science/article/pii/S0925838817318212.

[229] Ajit Debnath, Krishna Deb, Kartick L. Bhowmik, and Biswajit Saha. Reduced Hopping Barrier Potential in NiO Nanoparticle-Incorporated, Polypyrrole-Coated Graphene with Enhanced Thermoelectric Properties. **ACS Applied Energy Materials**, 3(8):7772–7781, August 2020. doi: 10.1021/acsaem.0c01174. URL https://doi.org/10.1021/acsaem.0c01174. Publisher: American Chemical Society.

[230] Ajit Debnath, Krishna Deb, Kamanashis Sarkar, and Biswajit Saha. Low Interfacial Energy Barrier and Improved Thermoelectric Performance in Te-Incorporated Polypyrrole. **The Journal of Physical Chemistry C**, 125 (1):168–177, January 2021. ISSN 1932-7447. doi: 10.1021/acs.jpcc.0c09100. URL https://doi.org/10.1021/acs.jpcc.0c09100. Publisher: American Chemical Society.

[231] Younes Bourenane Cherif, Zineb Mekhalif, Slimane Abdous, Linda Nedjar, Ahmed Mekki, Zakaria Bekkar Djelloul Sayah, and Souleymen Rafai. Nickel Oxide Decorated MWCNTs Wrapped Polypyrrole: One Dimensional Ternary Nanocomposites for Enhanced Thermoelectric Performance. **ChemNanoMat**, 10(3):e202300486, 2024. ISSN 2199-692X. doi: 10.1002/cnma.202300486. URL https://doi.org/10.1002/cnma.202300486.

[232] M. Almasoudi, M. Sh. Zoromba, M. H. Abdel-Aziz, M. Bassyouni, Ahmed Alshahrie, Abdullah M. Abusorrah, and Numan Salah. Optimization preparation of one-dimensional polypyrrole nanotubes for enhanced thermoelectric performance. **Polymer**, 228:123950, July 2021. ISSN 0032-3861. doi: 10.1016/j.polymer.2021.123950. URL https://www.sciencedirect.com/science/article/pii/S0032386121005735.

[233] Hosam El-Din Saleh and Said Moawad Mohamed El-Sheikh. **Perspective of Carbon Nanotubes**. BoD – Books on Demand, December 2019. ISBN 978-1-78984-401-6. Google-Books-ID: W0P8DwAAQBAJ.

[234] Sedigheh Abbasi, Seyed Mojtaba Zebarjad, and Seyed Hossein Noie Baghban. Decorating and Filling of Multi-Walled Carbon Nanotubes with TiO2 Nanoparticles via Wet Chemical Method. **Engineering**, 5 (2):207–212, February 2013. doi: 10.4236/eng.2013.52030. URL https://www.scirp.org/journal/paperinformation.aspx?paperid=27820. Number: 2 Publisher: Scientific Research Publishing.

[235] Farnaz Fazlali, Ali reza Mahjoub, and Reza Abazari. A new route for synthesis of spherical NiO nanoparticles via emulsion nano-reactors with enhanced photocatalytic activity. **Solid State Sciences**, 48:263–269, October 2015. ISSN 1293-2558. doi: 10.1016/j.solidstatesciences.2015.08.022. URL https://www.sciencedirect.com/science/article/pii/S129325581530042X.

[236] Zhiqiang Wei, Hongxia Qiao, Hua Yang, Cairong Zhang, and Xiaoyan Yan. Characterization of NiO nanoparticles by anodic arc plasma method. **Journal of Alloys and Compounds**, 479(1):855–858, June 2009. ISSN 0925-8388. doi: 10.1016/j.jallcom.2009.01.064. URL https://www.sciencedirect.com/science/article/pii/S0925838809001480.

[237] T. Navaei Diva, K. Zare, F. Taleshi, and M. Yousefi. Synthesis, characterization, and application of nickel oxide/CNT nanocomposites to remove Pb2+ from aqueous solution. **Journal of Nanostructure in Chemistry**, 7 (3):273–281, September 2017. ISSN 2193-8865. doi: 10.1007/s40097-017-0239-0. URL https://doi.org/10.1007/s40097-017-0239-0.

[238] Lingyu Wang, Fangzhuan Liu, Cheng Jin, Taoran Zhang, and Qinjian Yin. Preparation of polypyrrole/graphene nanosheets composites with enhanced thermoelectric properties. **RSC Advances**, 4(86):46187–46193, September 2014. ISSN 2046-2069. doi: 10.1039/C4RA07774A. URL https://pubs.rsc.org/en/content/articlelanding/2014/ra/c4ra07774a. Publisher: The Royal Society of Chemistry.

[239] Shalini Kulandaivalu, Nadhrah Suhaimi, and Yusran Sulaiman. Unveiling high specific energy supercapacitor from layer-by-layer assembled polypyrrole/graphene oxide|polypyrrole/manganese oxide electrode material. **Scientific Reports**, 9(1):4884, March 2019. ISSN 2045-2322. doi: 10.1038/s41598-019-41203-3. URL https://www.nature.com/articles/s41598-019-41203-3. Publisher: Nature Publishing Group.

[240] N. Su, H. B. Li, S. J. Yuan, S. P. Yi, and E. Q. Yin. Synthesis and characterization of polypyrrole doped with anionic spherical polyelectrolyte brushes. **Express Polymer Letters**, 6(9):697–705, 2012. ISSN 1788618X. doi: 10.3144/expresspolymlett.2012.75. URL http://www.expresspolymlett.com/letolt.php?file=EPL-0003325&mi=c.

[241] Huanhuan Wang, Linyi Bian, Peipei Zhou, Jian Tang, and Weihua Tang. Core–sheath structured bacterial cellulose/polypyrrole nanocomposites with excellent conductivity as supercapacitors. **Journal of Materials Chemistry A**, 1(3):578–584, December 2012. ISSN 2050-7496. doi: 10.1039/C2TA00040G. URL https://pubs.rsc.org/en/content/articlelanding/2013/ta/c2ta00040g. Publisher: The Royal Society of Chemistry.

[242] Sharique Ahmad, Imran Khan, Ahmad Husain, Anish Khan, and Abdullah M. Asiri. Electrical Conductivity Based Ammonia Sensing Properties of Polypyrrole/MoS2 Nanocomposite. **Polymers**, 12(12):3047, December 2020. ISSN 2073-4360. doi: 10.3390/polym12123047. URL https://www.mdpi.com/2073-4360/12/12/3047. Number: 12 Publisher: Multidisciplinary Digital Publishing Institute.

[243] Shalini Kulandaivalu and Yusran Sulaiman. Rational design of layer-by-layer assembled polypyrrole-based nanocomposite film for high-performance supercapacitor. **Journal of Materials Science: Materials in Electronics**, 31(6):4882–4894, March 2020. ISSN 1573-482X. doi: 10.1007/s10854-020-03051-0. URL https://doi.org/10.1007/s10854-020-03051-0.

[244] Abdulaziz Ali Alghamdi, Abdel-Basit Al-Odayni, Waseem Sharaf Saeed, Mohammed S. Almutairi, Fahad A. Alharthi, Taieb Aouak, and Abdullah Al-Kahtani. Adsorption of Azo Dye Methyl Orange from Aqueous Solutions Using Alkali-Activated Polypyrrole-Based Graphene Oxide. **Molecules**, 24 (20):3685, January 2019. ISSN 1420-3049. doi: 10.3390/molecules24203685. URL https://www.mdpi.com/1420-3049/24/20/3685. Number: 20 Publisher: Multidisciplinary Digital Publishing Institute.

[245] Jitka Kopecká, Dušan Kopecký, Martin Vrňata, Přemysl Fitl, Jaroslav Stejskal, Miroslava Trchová, Patrycja Bober, Zuzana Morávková, Jan Prokeš, and Irina Sapurina. Polypyrrole nanotubes: mechanism of formation. **RSC Advances**, 4(4):1551–1558, December 2013. ISSN 2046-2069. doi: 10.1039/C3RA45841E. URL https://pubs.rsc.org/en/content/articlelanding/2014/ra/c3ra45841e. Publisher: The Royal Society of Chemistry.

[246] Zohra Nazir Kayani, Mahek Zaheen Butt, Saira Riaz, and Shahzad Naseem. Synthesis of NiO nanoparticles by sol-gel technique. **Materials Science-Poland**, 36(4):547–552, December 2018. URL https://sciendo.com/article/10.2478/msp-2018-0088.

[247] Nurul Nadia Mohd Zorkipli, Noor Haida Mohd Kaus, and Ahmad Azmin Mohamad. Synthesis of NiO Nanoparticles through Sol-gel Method. **Procedia Chemistry**, 19:626–631, January 2016. ISSN 1876-6196. doi: 10.1016/j.proche.2016.03.062. URL https://www.sciencedirect.com/science/article/pii/S187661961600108X.

[248] Paras Dubey and Netram Kaurav. Synthesis and thermogravimetric analysis of non-stoichiometric nickel oxide compounds. **Journal of Physics: Conference Series**, 836(1):012040, April 2017. ISSN 1742-6596. doi: 10.1088/1742-6596/836/1/012040. URL https://dx.doi.org/10.1088/1742-6596/836/1/012040. Publisher: IOP Publishing.

[249] R. Greta Putri, Y. Syafera, F. Larasati, N. Rofiqoh Eviana Putri, M. Handayani, Rochmadi, and Y. Kusumastuti. Effect of Reaction Time on Modification of Multi-walled Carbon Nanotubes with HNO3. **IOP Conference Series: Materials Science and Engineering**, 742(1):012038, January 2020. ISSN 1757-899X. doi: 10.1088/1757-899X/742/1/012038. URL https://dx.doi.org/10.1088/1757-899X/742/1/012038. Publisher: IOP Publishing.

[250] Cao Guan, Yadong Wang, Yating Hu, Jilei Liu, Kuan Hung Ho, Wei Zhao, Zhanxi Fan, Zexiang Shen, Hua Zhang, and John Wang. Conformally deposited NiO on a hierarchical carbon support for high-power and durable asymmetric supercapacitors. **Journal of Materials Chemistry A**, 3(46):23283–23288, November 2015. ISSN 2050-7496. doi: 10.1039/C5TA06658A. URL https://pubs.rsc.org/en/content/articlelanding/2015/ta/c5ta06658a. Publisher: The Royal Society of Chemistry.

[251] Veeman Sannasi, K. Uma Maheswari, C. Karthikeyan, and S. Karuppuchamy. H2O2-assisted microwave synthesis of NiO/CNT nanocomposite material for supercapacitor applications. **Ionics**, 26(8):4067–4079, August 2020. ISSN 1862-0760. doi: 10.1007/s11581-020-03563-z. URL https://doi.org/10.1007/s11581-020-03563-z.

[252] Uisik Kwon, Bong-Gi Kim, Duc Cuong Nguyen, Jong-Hyeon Park, Na Young Ha, Seung-Joo Kim, Seung Hwan Ko, Soonil Lee, Daeho Lee, and Hui Joon Park. Solution-Processible Crystalline NiO Nanoparticles for High-Performance Planar Perovskite Photovoltaic Cells. **Scientific Reports**, 6(1):30759, July 2016. ISSN 2045-2322. doi: 10.1038/srep30759. URL https://www.nature.com/articles/srep30759. Publisher: Nature Publishing Group.

[253] Wei Huang, Shujiang Ding, Yong Chen, Wanjun Hao, Xiaoyong Lai, Juan Peng, Jinchun Tu, Yang Cao, and Xiaotian Li. 3D NiO hollow sphere/reduced graphene oxide composite for high-performance glucose biosensor. **Scientific Reports**, 7(1):5220, July 2017. ISSN 2045-2322. doi: 10.1038/s41598-017-05528-1. URL https://www.nature.com/articles/s41598-017-05528-1. Publisher: Nature Publishing Group.

[254] Guangmin Zhou, Da-Wei Wang, Li-Chang Yin, Na Li, Feng Li, and Hui-Ming Cheng. Oxygen Bridges between NiO Nanosheets and Graphene for Improvement of Lithium Storage. **ACS Nano**, 6(4):3214–3223, April 2012. ISSN 1936-0851. doi: 10.1021/nn300098m. URL https://doi.org/10.1021/nn300098m. Publisher: American Chemical Society.

[255] ChunHui Wu, SiXu Deng, Hao Wang, YuXiu Sun, JingBing Liu, and Hui Yan. Preparation of Novel Three-Dimensional NiO/Ultrathin Derived Graphene Hybrid for Supercapacitor Applications. **ACS Applied Materials & Interfaces**, 6(2):1106–1112, January 2014. ISSN 1944-8244. doi: 10.1021/am404691w. URL https://doi.org/10.1021/am404691w. Publisher: American Chemical Society.

[256] Ashique Kotta, Eun-Bi Kim, Sadia Ameen, Hyung-Shik Shin, and Hyung Kee Seo. Communication—Ultra-Small NiO Nanoparticles Grown by Low-Temperature Process for Electrochemical Application. **Journal of The Electrochemical Society**, 167(16):167517, December 2020. ISSN

1945-7111. doi: 10.1149/1945-7111/abcf51. URL https://dx.doi.org/10.1149/1945-7111/abcf51. Publisher: IOP Publishing.

[257] Andrew P. Grosvenor, Mark C. Biesinger, Roger St. C. Smart, and N. Stewart McIntyre. New interpretations of XPS spectra of nickel metal and oxides. **Surface Science**, 600(9):1771–1779, May 2006. ISSN 0039-6028. doi: 10.1016/j.susc.2006.01.041. URL https://www.sciencedirect.com/science/article/pii/S0039602806001336.

[258] Zahra Roohi, Frej Mighri, and Ze Zhang. A Simple Trick to Increase the Areal Specific Capacity of Polypyrrole Membrane: The Superposition Effect of Methyl Orange and Acid Treatment. **Polymers**, 14(21):4693, January 2022. ISSN 2073-4360. doi: 10.3390/polym14214693. URL https://www.mdpi.com/2073-4360/14/21/4693. Number: 21 Publisher: Multidisciplinary Digital Publishing Institute.

[259] Mukulika Jana Chatterjee, Mousumi Mitra, and Dipali Banerjee. Thermoelectric Performance of Polypyrrole and Single Walled Carbon Nanotube Composite. **Materials Today: Proceedings**, 5(3, Part 3):9743–9748, January 2018. ISSN 2214-7853. doi: 10.1016/j.matpr.2017.10.161. URL https://www.sciencedirect.com/science/article/pii/S2214785317321867.

[260] Pinaki Mandal, Soumyajit Maitra, Mukulika Jana Chatterjee, Mausumi Chattopadhyaya, Kajari Kargupta, and Dipali Banerjee. Polypyrrole-bismuth selenide (PPY-Bi2Se3) composite-thermoelectric characterization and effect of nickel doping. **Synthetic Metals**, 289:117119, September 2022. ISSN 0379-6779. doi: 10.1016/j.synthmet.2022.117119. URL https://www.sciencedirect.com/science/article/pii/S0379677922001138.

[261] Yiyu Feng, Hongpo Liu, Wen Luo, Enzuo Liu, Naiqin Zhao, Katsumi Yoshino, and Wei Feng. Covalent functionalization of graphene by azobenzene with molecular hydrogen bonds for long-term solar thermal storage. **Scientific Reports**, 3(1):3260, November 2013. ISSN 2045-2322. doi: 10.1038/srep03260. URL https://doi.org/10.1038/srep03260.

[262] Haijun Song, Kefeng Cai, Jiao Wang, and Shirley Shen. Influence of polymerization method on the thermoelectric properties of multi-walled carbon nanotubes/polypyrrole composites. **Synthetic Metals**, 211:58–65, January 2016. ISSN 0379-6779. doi: 10.1016/j.synthmet.2015.11.013. URL https://www.sciencedirect.com/science/article/pii/S0379677915301454.

[263] Mario Culebras, You-young Byun, Junho Jang, Tae Kwon Lee, Dongwhi Choi, Aleksandra Serafin, Maurice N. Collins, Jung Sang Cho, and Chungyeon Cho. Enhanced Thermoelectric Performance in Polypyrrole-Based Multilayer Nanoarchitectures via Thermal Reduction. **ACS Applied Energy Materials**, 7(6):2351–2361, March 2024. doi: 10.1021/acsaem.3

c03060. URL https://doi.org/10.1021/acsaem.3c03060. Publisher: American Chemical Society.

[264] Medha Rakshit, Supriya Ghosal, Debnarayan Jana, and Dipali Banerjee. Polypyrrole/tin sulfide hybrid nanocomposites as promising thermoelectric materials: A combined experimental and dft study. **ACS Applied Energy Materials**, 7(9):3983–3995, 2024. doi: 10.1021/acsaem.4c00271. URL https://doi.org/10.1021/acsaem.4c00271.